Introductio to
Cosmic Radiation

OTTO CLAUS ALLKOFER

University of Kiel
Germany

CONTENTS

PREFACE

There exist about dozens of books on the subject of cosmic radiation. A reason to add one more is that some of them are partly obsolete, because in some areas an enormous amount of progress has taken place. Another mason is that the books available describe only certain aspects of the whole field of cosmic radiation. The reason for this book is to give an up-to-date survey of the whole field of cosmic radiation. In addition, it has been my intention to write a book which has more the character of a textbook, so that it can be used by students as an introduction to this topic; but it may also be useful as a small reference book for graduate students already working in this field. Because of the nature of the book, there are no references to publications but the survey articles and books referred to are quoted at the end of each chapter. For a few very new results, specific publications have been used. The quo ted literature also provides the basis for a deeper study. This book does not acknowledge the large amount of effort made by the numerous scientists working in this field. I thought that it might be useful to include at the end of the book, a comprehensive survey of relevant books and review articles. Since the field of cosmic radiation is becoming less and less a coherent topic, this would then be a last effort to show younger people the historical development of the com- plete field of cosmic radiation.

I would like to acknowledge the help of Dr. W. D. Dau. and Dr. D. Reimers who have read some of the chapters and given valuable advise. In addition, I wish to thank Dr. H. Jokisch who was nice enough to have a critical look at the whole text and showed me that some passages needed to be changed. Finally, I like to acknowledge the help of Dr. R. Clifft who not only gave the final text an English image but also gave me valuable advise. Finally, I thank Mrs. B. Sierau who made the drawings for the book.

Kiel, July 1975   **Otto Claus Allkofer**

1. Introduction

Cosmic radiation, defined as the high-energy radiation coming from the universe, has been bombarding our earth for millions of years, although we have only had any knowledge of it for about 60 years. During this time,it has added stimulus to many fields of research and created new ones, like no other phenomenon. This is particularly true when we consider the extensive fields of particle physics and space physics.

The cosmic-ray era started with the manned balloon flights of Hess,which resulted in the revolutionary statement that a high-energy radiation from space was falling on the earth.

Today, four different aspects of cosmic radiation are studied. Firstly, there is astrophysics,which is concerned with the origin of cosmic radiation, the acceleration mechanisms of charged particles up to very high energies, the shape of the energy spectra of the different components, and their chem- ical composition. The new field of high-energy astrophysics, where X- and T-radiation of diffuse and point-source character is investigated, has added a new dimension to this exciting area of cosmic radiation.

Secondly there is geophysics. Cosmic radiation interacts with the atmos- phere, producing secondary components with different composition and intensity at different levels. The influence of the geomagnetic field on charged particles leads to the well known geomagnetic effects. The solar wind,continuously transporting plasma with frozen-in magnetic fields from the sun, modulates the intensity of the galactic cosmic radiation. This interaction between sun and earth,via the solar plasma has created the field of solar-terrestrial physics which is extensively studied by baloon borne detectors, with rockets and satellites.

The third area is particle physics. Elementary-particle physics started with cosmic radiation. The first elementary particles were detected in the atmosphere, namely the positron, the muon, the pion, the kaon, and some of the baryons. This was long before the first accelerators were built. Today, particle physics is best done with high precision and high statistics at the large machines. However, there still remains an energy region to be studied by cosmic radiation in the future, because the energies of cosmic- ray particles still extend many orders of magnitude higher, although the statistics decrease with energy. If there is a need for interaction physics at very high energy, then development of very large detectors must go ahead.

Finally, there is the area of biophysics. Primary and secondary cosmic radiation produces a radiation dose in man due to its ionizing properties.

This dose is relatively constant at sea level, far below the legally permissible dose rate,but increases with altitude. Already, at the level of supersonic transport, crew members can receive on average,almost the specified permissible dose for radiation workers. In addition, small numbers of heavy nuclei produce locally high dose rates and sporadic solar flares are sometimes present with high intensity. For long-term missions of astronauts in free space the radiation hazard is particularly important.

Thus,cosmic radiation is a manifold field of research with a common source as the only link between the different fields. Although in past this link was strong enough to hold the different components together it seems that this will no longer be true in the future.

2. Historical survey

In contrast to many other fields of physics, cosmic radiation created a great deal of excitement from the very beginning. This new phenomenon very soon showed up new geophysical effects, new particles were discovered, and astrophysicists were attracted to understand its origin. Without the discovery of cosmic radiation,the rapid scientific development in nuclear and particle physics and to a lesser extent in space and solar-terrestrical physics would not have occurred. The story started at the beginning of the century with the study of the electric conductivity of gases. Although a dielectric-like behaviour was expected,there existed a residual conductivity which was not understood. Amongst the explanations for this conductivity which included radioactivity and spontaneous ionization of the gas, was the possibility that it could be due to a new phenomenon. The altitude dependence of the residual conductivity was studied using a balloon-borne ionization chamber with the scientist accompanying the instrument since telemetry was not yet feasible. After some preliminary misinterpretation of the results Hess finally showed in 1912, in Austria, that beyond an altitude of about 1 000 m the conductivity increased and he made the revolutionary statement that a new penetrating radiation from outside the earth must be responsible. Since no difference in intensity between day and night balloon flights was found he concluded that the sun was not the source of this new radiation.

The subsequent discoveries associated with this new phenomenon created such interest and excitement that the most important of them are mentioned below.

1900 *Wilson* in England and independently Geitel and *Elster* in Germany measured the residual conductivity in air; both found a residual current equivalent to the production of about 20 ion pairs per second per cm^3.

1903 *Rutherford* shielded an electroscope with lead and found that there was a reduction of the conductivity.

1910 *Wulf* constructed a sensitive electrometer with which he measured a reduction of the ionization at the top of the Eiffel Tower in Paris. This was in fact due to a reduction of environmental radioactivity.

1912 Hess reached a height of 5 km by balloon flights and was able to show that the current in an ion chamber increased with altitude. In addition, he established that there was no difference between the day and night intensity from which he concluded that a new penetrating

radiation from outside was responsible and gave it the name Hohen-strahlung.

1914 *Kohlhorster* confirmed that the radiation increased up to an altitude of 9 000 m.

1925 *Millican* and *Cameron* started a study of the absorption of the radiation by measuring the intensity at different heights in the atmosphere.

1926 *Hoffmann* studied absorbtive behaviour using an ionization chamber and found an increase of intensity with increase of absorber thickness (Hoffmannsche StoBe bursts; transition effect).

1927 *Clay,* by means of ionization chamber measurements, on a voyage from Amsterdam to Java, found the intensity near the equator to be less than at higher latitudes (latitude effect).

1929 *Bothe* and *Kohlhorster* measured a charged component of the radiation using Geiger-Miiller counters in coincidence.

1929 Skobelzyn from Leningrad identified the first cosmic ray tracks by their weak deflection in a cloud chamber.

1930 *Stormer* developed a theory about the motion of charged particles in the earth's magnetic field (originally proposed as an explanation of aurorae).

1932 *Anderson* identified the positron in a cloud chamber, a particle predicted theoretically by *Dirac.*

1932 *Compton* measured a decrease of cosmic-ray intensity with latitude during a Pacific expedition.

1933 *Lemaitre* and *Vallarta* carried out an extensive analysis of the behaviour of particles in the geomagnetic field.

1933 *Johnson* and independently *Alvarez* and *Compton* measured the sign of the charged particles by observing that the intensity from the west was higher than the intensity from the east. Because this effect was due to the geomagnetic field the concluded that the primary cosmic radiation was composed of positively charged particles.

1933 *Rossi* measured the frequency of showers in an array of Geiger-Miiller counters for different thicknesses of absorber materials and found a maximum for approximately 2 cm of lead (transistion or Rossi effect); this local shower effect he interpreted as the result of particle multiplication.

1935 Rossi used a telescope of Geiger-Miiller counters with absorbers of varying thickness interposed to establish that there were two

components of the radiation; a soft component which decreased rapidly with increase of absorber thickness (mostly electrons) and a hard component which was very penetrating (mostly muons).

1935 *Yukawa* postulated the existance of an intermediate particle for strong interactions called the meson,and using Fermi's theory for beta decay predicted a mass of about 200 m_e and a lifetime of about 10^{-6} s.

1936 *Pfotzer* using a balloon-borne counter telescope found that the cosmic-ray intensity had a maximum at an altitude of about 15 km (Pfotzer-maximum), which was interpreted as the transition effect in the atmosphere.

1937 *Forbush* observed worldwide decreases in cosmic ray intensity in coincidence with geomagnetic storms *(Forbush* decrease).

1937 *Anderson and Neddermeyer* identified the muon in a cloud chamber. This particle was originally thought to be the Yukawa meson but subsequently found to have no strongly interacting properties.

1937 *Bhabha* and *Heitler* and independently *Carlson* and *Oppenheimer* developed the cascade theory which explained the multiplication of electrons and photons at high energies due to bremsstrahlung and pair-production processes (cascade showers).

1938 *Auger* and collaborators and independently *Kohlhorster* and collaborators first observed the lateral distribution of Extensive Air Showers (EAS) by measuring coincidences in widely separated Geiger-Miiller counters (decoherence curve).

1941 *Schein, Jesse,* and *Wollan* using balloon-borne equipment, measured directly that the primary cosmic radiation consisted of protons.

1947 *Lattes, Occhialini* and *Powell* discovered the pion in nuclear emulsions exposed at mountain altitudes. They showed that the charged pion decayed into a muon,and so finally 12 years later the *Yukawa* particle was found.

1947 *Rochester* and *Butler* found tracks in a cloud chamber which were due to charged particles with a mass around 1 $000 m_e$ (kaons).

1948 *Freier. Bradt* and *Peters* discovered heavy nuclei in the primary cosmic radiation using nuclear emulsions.

1949 *Fermi* proposed a theory of the statistical acceleration of cosmic ray particles resulting from interactions with interstellar clouds *(Fermi* mechanism).

1950 *Haar* discussed explosions of supernovae as a possible mechanism for producing cosmic-ray particles.

1951 *Armenteros* observed at mountain altitudes, unstable particles heavier than nucleons which decayed into protons and pions (hyperons).

1958 *Van Allen* and co-workers using Geiger-Muller counters on board satellites (Explorer I and III) measured high count rates in confined regions beyond an altitude of about 1000 km due to trapped charged particles (radiation belts, van Allen belts).

1961 *Meyer* and *Vogt,* and independently *Earl* identified electrons and positrons in cosmic radiation.

1962 *Giaconi, Gursky, Paolini,* and *Rossi* observed cosmic X-radiation using rocket borne detectors.

1967 *Fowler, Adams, Cowen,* and *Kidd* using nuclear emulsions, measured cosmic ray nuclei up to uranium and perhaps even transuranic nuclei.

1968 *Kraushaar, Clark,* and *Garmire* observed cosmic gamma radiation using satellite-borne detectors.

3. Basic data of astrophysics

Cosmic radiation is mainly a phenomenon of our galaxy, the milky way. An outline of its most important features is given below. Other astrophysical phenomena which are related to the origin and propagation of cosmic radiation are also discussed. These include some special types of stars which are regarded as sources and stellar processes which produce the different elements in the universe.

3.1. The milky way

The main constituents of the universe are the galaxies, which themselves are composed of stars and gas clouds. The galaxies vary considerably in size, a large galaxy containing between 10^{11} and 10^{12} stars with a mass of about $10^{11} M_{\odot}$ ($M_{\odot}$ is the solar mass). Galaxies have dimensions of the order of 10^{24} cm. They are not uniformly distributed throughout the universe; definite clusters of galaxies exist. The most distant galaxies observed are at several times 10^{29} cm. Galaxies are classified mainly according to their morphology. Three classes exist;

(a) elliptical galaxies — these show a smooth variation of structure from bright center to indefinite edges,

(b) spiral galaxies — these have typical spiral arms or whorls extending from a central nucleus,

(c) irregular galaxies.

Our galaxy is a rotating system composed of stars, clusters, nebulae, absorbing clouds, atomic and molecular gases, ions, and dust particles. The stars are believed to have been formed out of interstellar material and therefore have different ages and behaviour. Due to its rotation, the galaxy has the shape of an ellipsoid of revolution. The galactic disc is surrounded by a spherical region of halo. Most of the young stars which originated at a late stage in the life of the universe are arranged in the disc. They were formed out of the gas of the rotating disc and consequently are circulating around the galactic center. Many of the stars are members of clusters, which are groupings of stars for which mutual gravitational attraction is stronger than the disruptive forces. They are of two types. *Globular clusters,* which have a compact circular appearance; these are spread throughout the galaxy and each contain 10^5 to 10^6 stars. *Galactic clusters,* which are formed in the disc and contain fewer stars. Our sun is one of these stars, with an orbital velocity of about 250 km s^{-1}. It completes one

revolution about the galactic center in some 10^8 years. The sun together with the earth have completed about 20 to 25 revolutions around the milky way since their formation about 5 x 10^9 years ago.

At the center of the galactic disc there is thought to be a galactic nucleus which is a source of radio waves.This nucleus could also be a powerful source of non-thermal radio emission. It is postulated that gas flowing out radially from the nucleus at a rate of mass loss of about 1 solar mass per year would empty the nucleus within 10^8 years if no matter were supplied. Such matter could be obtained from the halo.

In addition to the young stars,the galactic disc contains old stars which do not move in orbits. These are thought to have been formed during the first stages of the galaxy, before it developed a disc structure. These old stars show no systematic velocity behaviour. They are also present in the halo.

Most of the mass of the galaxy is contained in the flat disc and central nucleus. The total mass of stars is estimated to be about 1.5 x $10^{11}\,M_{\odot}$. Five to ten percent of the mass is interstellar gas and dust, concentrated in the disc and particularly in the spiral arms.
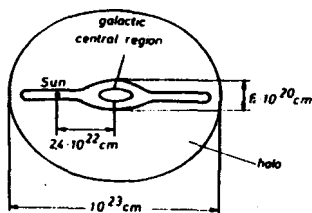
Fig. 3.1: Schematic representation of the milky way
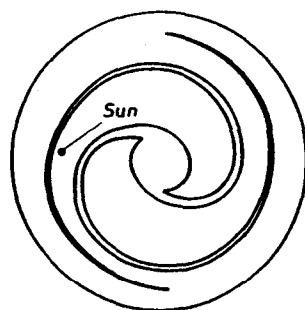
Fig. 3.2: Spiral structure of the milky way

The milky way has a spiral form as a result of its rotation. The angular velocity depends on the radial distance from the galactic center. Neutral hydrogen is concentrated in the spiral arms. Schematic representations of the milky way are shown in Figs. 3.1 and 3.2. The spiral structure of the galactic disc is indicated.

The interstellar medium within the galaxy is composed mainly of neutral hydrogen atoms (H I regions[1]). These clouds occupy about 90 % of the disc volume; the average density is $\sim 1\ cm^{-3}$ and the temperature ~ 100 K. The other 10% of the volume is occupied by ionized gases (H II regions[2]). The particle density of the ions is $\sim 10\ cm^{-3}$ and the mean temperature $\sim 10^4$ K. Molecular hydrogen is probably as abundant as atomic hydrogen. The following atoms, ions and molecules have been detected: Na, K, Ca, Ti, Fe, CH, CN, OH, H,, HD, C^+, O and N. The mass of the galaxy is about $M = 2.8$ x 10^{44} g corresponding to 1.4 x $10^{11}\ M_{\odot}$.The ionzied intergalactic hydrogen corresponds to -- 6 x 1 $0^7\ M_{\odot}$ and the neutral hydrogen to ~ 1.5 x $10^9\ M_{\odot}$, about 1 % of the galactic mass. Intergalactic: dust particl es with a wide range of size and composition (silicates, graphite, ice) have been detected. From measurements of the polarization of light it is calcu- lated that the particles are oriented in a galactic magnetic field with a strength of about 10^{-5} Gauss, the field lines being oriented along the spiral arms. The density of the dust particles is- 1.3 x 10^{-26} g cm^{-3} which corresponds to about 1 % of the total interstellar matter. The most important parameters of the galaxy are given in Table 3.1.

In Fig. 3.3 the mass distribution, density, and periods of revolution in the galactic disc are presented as a function of distance from the galactic center.

Table 3.1: Principal parameters of the milky way
(Adapted from Allen, C.W.: Astrophysical Quantities. London: The Athlone Press of the University of London 19731

number of stars	10^{11}
total mass of the galaxy	1.4 x IO" $M_{\cdot}$ = 2.8 10^{44} g
total density of the galaxy	10.0 x 10^{-24} g cm$^{-:3}$
star density in the disc (near the sun)	10^{-56} cm$^{-3} \cong 6$ x 10 ^{24} g cm$^{-:3}$
star density in the nucleus	10^{-53} cm^{-3}
density of interstellar gas	1.7 x 10^{-24} g cm$^{-3} \cong 1$ atom cm
density of dust particles	1.3 x 10^{-26} g cm^{-3}
density of interstellar gas in the halo	$10^{-2} - 10^{-3}$ atoms cm^{-3}
mean velocity (population I stars)	180 $-$ 250 km s^{-1}
random velocity Ipopulation II stars)	10 km s^{-1}
magnetic field strength in the disc	10^{-5} Gauss
magnetic field strength in the halo	$10^{-5} - 10^{-6}$ Gauss

[1] H I neutral hydrogen.
[2] H II ionized hydrogen.
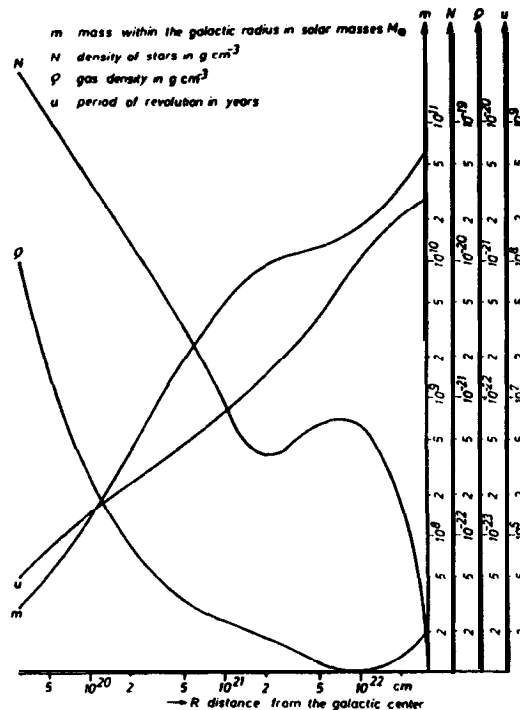
Fig. 3.3: Distribution of mass. density. and periods of revolution in the milky way
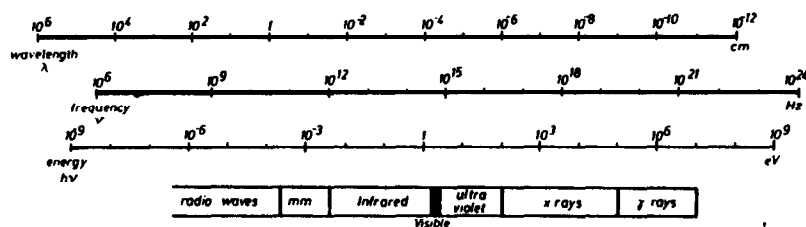
Fig. 3.4: Spectrum of electromagnetic radiation

3.2. Radiation and energy density

Stars, nebulae, and the interstellar medium emit a broad spectrum of electromagnetic radiation extending from the gamma-ray region, through the regions of X-rays, ultraviolet, visible and infrared to the radio-frequency region. The radiation is characterized by its direction, its origin, its inten-
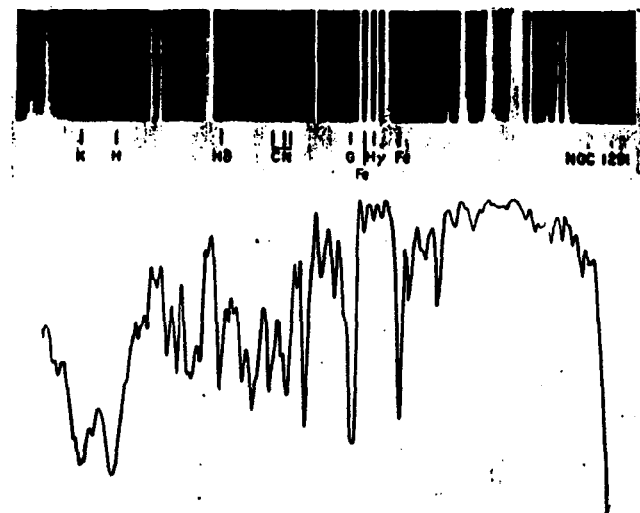
Fig. 3.5: Typical galaxy spectrum
(Reproduced from Menzel, D. H.. F. L. Whipple. G. de Vancouleurs Survey of the Universe. Englewood Cliffs: Prentice-Hall. New Jersey 1970)

sity or brightness, its frequency or color in the visible region and its polarization. Fig. 3.4 shows the electromagnetic spectrum in units of frequency, wave length and energy. Different spectra are observed from galaxies with different morphologies. Fig. 3.5 shows a typical galaxy spectrum. The energy density of radiation is defined as the amount of radiation energy per unit volume. If I is the intensity of the radiation, the energy density u is given by

$$u = 1/c \int d\ w$$

where c is the velocity of light and do the solid angle. The dimensions are erg cm^{-3}. The density of radiation in interstellar space due to star light is $\sim 7 \times 10^{-13}$ erg cm^{-3}. The total radiation emitted by the stars as measured on the earth is $\sim 1.4 \times 10^{-23}$ erg $cm^{-3}\ s^{-1}$.

3.3. Cosmic abundance of the elements

Information about the relative abundances of elements in the universe has been obtained from many different sources. Although there appears to be a surprising consistency in composition, differences do exist between

different types of stars. Discrepancies arise due to errors in the determination of spectral lines and due to the fact that some elements are not excited to emission of light because the surface temperature of the star is too low. The principal sources of information are:

The earth. The chemical composition of the earth's crust is studied by mineralogical and geological means. Information about the interior of the earth is obtained from studies of earthquake waves and the earth's magnetic field. Only non-volatile constituents are measured.

Meteorites. These extraterrestrial objects can be investigated by chemical analysis. There are three basic types known as iron, stone and stony iron meteorites; the first type being mainly metallic, the second type mainly rock and the third type a mixture. Because meteorites lose mass as a result of heating when they pass through the atmosphere, the relative abundances can be changed due to the different heats of vaporization of the different constituents. The most abundant subgroup of meteorites are the carbon aceous chondrites which constitute 90% of all meteorites reaching the earth. They are stony meteorites containing chondrules which are small spheroidal bodies; they also contain more carbon and water than other meteorites.

The *sun.* The abundance of a chemical element in a star is calculated from the existance and behaviour of characteristic spectral lines, which may appear as absorption or emission lines, although mainly as absorption lines. The intensity of a spectral line depends on the temperature, density and chemical composition of the stellar atmosphere and on the cross-section for absorption of photons (f-value). An uncertainty factor of 2 or 3 is typical.

Other stars. Other stars of the milky way can be divided into two classes, those with abundances like the sun, and those with quite different composition. Some stars (subdwarfs, high-velocity stars) have a ratio of metals to hydrogen appreciably smaller than in sun and others have a ratio which is actually greater. There is some evidence that the heavy elements were produced within the galactic nucleus during the formation of the galaxy. The concentration of heavy elements may be higher in the galactic center than in the outer regions.

Interstellar medium and gaseous *nebulae.* The measured values are less reliable than those for stars.

Outside the galaxy. Stars in other galaxies are generaly too faint for their spectra to be studied. There is however, some information about groups of stars and large gaseous nebulae. It appears that the composition of nearby galaxies is similar to that of the milky way.

Moon and planets.

An overall similarity in the abundances of detectable elements is found from different sources,from which it is concluded that it is the same throughout the universe. A composite abundance distribution is represented in Fig.3.6. The abundance is given on a logarithmic scale normalized to silicon (Si = 10^6), as a function of the mass number. The following characteristic features are seen:

− The most abundant element is hydrogen. About three quarters of the mass of the sun appears to be composed of hydrogen and most of the remainder of He 4.
− The light elements D, He 3, Li, Be, B are rare.
− Carbon, nitrogen and oxygen are very abundant compared with their neighbours.
− A huge abundance peak is centered at Fe 56.
− Between *A* = 20 and *A* = 100 the abundance is fairly constant but rises to a final peak in the region of lead and bismuth.
− There are sharp peaks near the mass numbers 90, 140 and 208. These peaks correspond to magic numbers of neutrons (50.82, 126). configurations which are extremely stable.
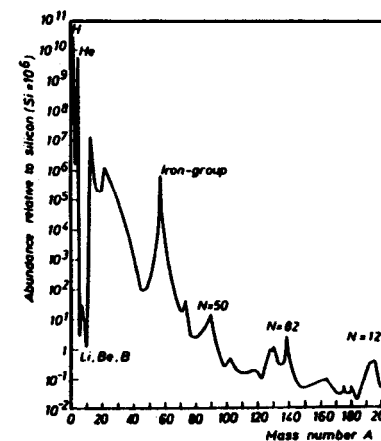
Fig. 3.6: Abundance distribution of elements

3.4. The galactic magnetic field

The existance of a galactic magnetic field has been established from measurements of the polarization of star light. Light from almost all stars is up to several percent polarized in a direction lying approximately within the plane of the galaxy. The observed polarization in the plane of the galaxy is shown in Fig.3.7; the dashes give a vectorial representation. Polarization is produced in the interstellar medium, by the scattering of the light on oriented dust grains. An admixture of metallic constituents in the dust is magnetized by any external magnetic field. Since the dust particles are concentrated in the spiral arms, the magnetic field lines which orientate the magnetic moments of the grains are directed along the spiral arms. The strength of the magnetic field in the galaxy, in the neighbourhood of the sun, is of the order of 10^{-5} to 10^{-6} Gauss. The polarization increases with the amount of matter traversed.
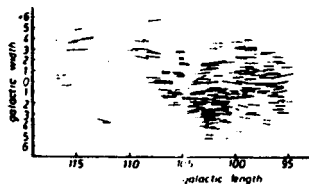
Fig. 3.7: Polarization of the light from stars observed perpendicular to the spiral arms

3.5. The 3 K-radiation

In 1965 a background radiation with a wavelength of about 7 cm was observed. The radiation was arriving uniformly from all directions of space and was observable at several wave lengths between 0.26 to 20.7 cm. It showed the spectral energy distribution of black-body radiation for a temperature of about 3 K. Fig.3.8 shows the observed distribution together with the black-body radiation curve for 3 K. The distribution for star light which can be regarded as black-body radiation of about 10^4 K is also shown.

According to the big-bang theory, the background ratliation is likely to be a remnant radiation from the beginning of the universe. Within a primeval fireball of extremely high temperature, energy and intense radiation were produced by nuclear reactions in a short time interval resulting in an expansion of the fireball and a drastic drop in the temperature. This expansion can still be observed as the universal redshift of photons. If $E_0 = h\nu_0 = hc/\lambda_0$ is the energy emitted by a source with a redshift
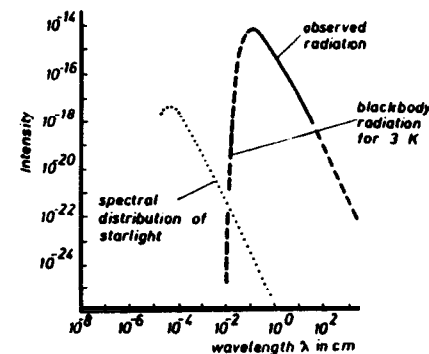
Fig. 3.6: Spectral energy distribution of the 3 K-radiation
(From Menzel, D. H., F. L. Whipple, G. de Vancouleurs: Survey of the Universe, Enslewood Cliffs, New Jersey: Prentice-Hall 1970)

$$z = \frac{\lambda - \lambda_0}{\lambda_0},$$ the oberserved energy is

$$E = h\nu = E_0 \frac{\nu}{\nu_0} = E_0 \frac{\lambda_0}{\lambda} = \frac{E_0}{1 + z}$$

An additional effect of the universal redshift is a reduction in the density of photons in space. If No photons are emitted and travel a distance I to an observer without expansion, then in an expanding universe the distance is increased by

$$s = I \frac{\lambda - \lambda_0}{\lambda_0} = Iz.$$

The photons emitted in one second by the source and spread over length I are thus spread over the length $I + s$. Since the number of photons per unit volume is inversely proportional to length, $I + s$, the relation

$$N/N_0 = I/(I + s) = (1 + z)^{-1}$$

is obtained.

Hence, the expansion produces similar energy and density effects. The energy density of the 3 K-radiation has an equivalent mass density of $\rho = 5 \times 10^{-34}$ g cm^{-3}, corresponding to a photon density of 10^3 cm^{-3}

3.6. Nucleosynthesis

The energy radiated by the stars is derived from the conversion of matter into radiation by nuclear interactions. Stars are gaseous throughout with interior temperatures high enough for thermonuclear reactions to take

place. Such reactions alter the chemical composition of the stars. Since hydrogen is the most abundant element, the predominant process is the proton-proton interaction. The number of interactions per unit volume and unit time z depends upon the densities of the interacting nuclei, n_1 and n_2, and on the average value of the product of reaction cross-section $\sigma (v)$ and the relative velocity of the nuclei v,

$$z = n_1 \, n_2 \, \langle \sigma (v) \, v \rangle .$$

Both resonant and non-resonant reactions take place. The former may be described by the Breit-Wigner resonance formula. A wide range of variation in the above mentioned parameters allow both slow and rapid processes to occur. The nuclei produced may be stable or radioactive with a wide range of half-lives.

Although the mean energy in the stellar interior is lower than the threshold energy for most of the processes (the mean temperature in the interior of the sun corresponds to about 2×10^3 eV $\cong 1.4 \times 10'$ K), they occur due to the tail of the Maxwell distribution.

Starting with a star composed of pure hydrogen, the basic reaction is the proton-proton interaction which forms deuterium

$$p + p \rightarrow d + e^+ + \nu_e + \gamma \qquad (1.44 \text{ MeV}) .$$
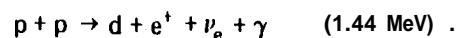
An energy of 1.44 MeV is released in this exothermic process. The p-p reaction is extremely slow; in the center of the sun it takes an average time of 5×10^9 years. The deuteron can react with a further proton to produce helium

$$d + p \rightarrow {}^3He + \gamma \qquad (5.49 \text{ MeV}) ,$$

This is a rapid process taking about 4 s for conditions like those in the interior of the sun. The He 3 nuclei can react with one another by a relatively slow process ($\approx 4 \times 10^6$ years).

$$^3He + {}^3He \rightarrow {}^4He + 2\,p \qquad (12.86 \text{ MeV}) .$$
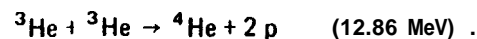
As a result of the above reactions, 4 protons in the p-p chain have formed a He 4 nucleus. The total energy released is

$$E = 2 \, (1.44 \text{ MeV} + 5.49 \text{ MeV}) + 12.86 \text{ MeV} = 26 \text{ MeV}$$

This is the main source of stellar energy. The proton cycle may continue by further reactions again creating Helium.

$$^3He + {}^4He \rightarrow {}^7Be + \gamma \qquad (1.58 \text{ MeV})$$
$$^7Be + e^- \rightarrow {}^7Li + \nu_e \qquad (0.86 \text{ MeV})$$

$$^7Li + p \rightarrow 2\,{}^4He \qquad (17.35 \text{ MeV})$$
$$^7Be + p \rightarrow {}^8B + \gamma \qquad (0.10 \text{ MeV})$$
$$^8B \rightarrow {}^8Be + e^+ + \nu_e \quad (18.01 \text{ MeV})$$
$$^8Be \rightarrow 2\,{}^4He \qquad (0.10 \text{ MeV})$$

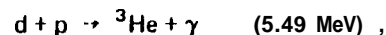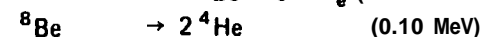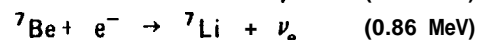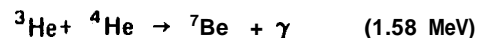In this latter cycle the elements Li, Be, and B appear only temporally. Be 7 is radioactive with a half life of 53 days. The reactions (^{7}Li, p) is of special interest because it has a low threshold energy, of the order of 10^6 K. The low cosmic abundance of lithium is explained in this way.

The production of heavier elements occurs by means of the carbon cycle. Shrinkage of the star creates sufficiently high temperature for the fusion of alpha particles to take place; in this cycle carbon plays the role of a catalyst. The basic reaction is the combination of 3 alpha particles to form C 12

$$3\,{}^4He \rightarrow {}^{12}C \qquad (7.26 \text{ MeV})$$
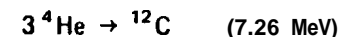
The carbon or CNO-cycle consists of six steps

$$
\begin{array}{llll}
^{12}C + p \rightarrow {}^{13}N + \gamma & (1.95 \text{ MeV}) & 10^6 \text{ a} \\
^{13}N \rightarrow {}^{13}C + e^+ + \nu_e & (2.22 \text{ MeV}) & 10 \text{ min} \\
^{13}C + p \rightarrow {}^{14}N + \gamma & (7.55 \text{ MeV}) & 2 \times 10^5 \text{ a} \\
^{14}N + p \rightarrow {}^{15}O + \gamma & (7.28 \text{ MeV}) & < 3 \times 10^7 \text{ a} \\
^{15}O \rightarrow {}^{15}N + e^+ + \nu_e & (2.76 \text{ MeV}) & 2 \text{ min} \\
^{15}N + p \rightarrow {}^{12}C + {}^4He & (4.97 \text{ MeV}) & 10^4 \text{ a}
\end{array}
$$
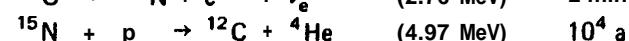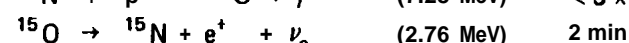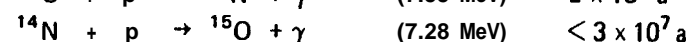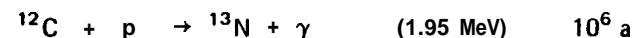
The intermediate nuclei N 13 and O 18 are radioactive with short half-lives.

A second CNO-cycle occurs much less frequently, in which O 16, F 17, and O 17 are produced.

After helium burning, the central region of the star contracts again and raises the temperature and density sufficiently for the following reactions to take place. Whether or not such processes do occur, however, is still uncertain.

$$
\begin{array}{ll}
^{12}C + {}^4He \rightarrow {}^{16}O & \qquad ^{36}Ar + {}^4He \rightarrow {}^{40}Ca \\
^{16}O + {}^4He \rightarrow {}^{20}Ne & \qquad ^{40}Ca + {}^4He \rightarrow {}^{44}Ti \\
^{20}Ne + {}^4He \rightarrow {}^{24}Mg & \qquad ^{44}Ti + {}^4He \rightarrow {}^{48}Cr \\
^{24}Mg + {}^4He \rightarrow {}^{28}Si & \qquad ^{48}Cr + {}^4He \rightarrow {}^{52}Fe \\
^{28}Si + {}^4He \rightarrow {}^{32}S & \qquad ^{52}Fe + {}^4He \rightarrow {}^{56}Ni \\
^{32}S + {}^4He \rightarrow {}^{36}Ar & \qquad ^{56}Ni + {}^4He \rightarrow {}^{60}Zn
\end{array}
$$
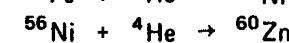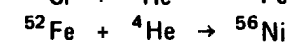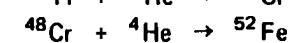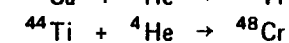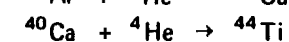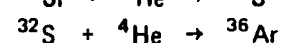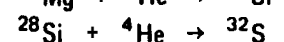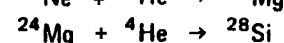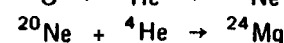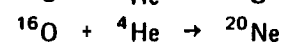
Si 28 is a stable Isotope which can undergo photodisintegration by star light to produce Mg 24. The latter may undergo further photodisintegration giving rise to lighter nuclei and more alpha particles.

$$\gamma + {}^{28}Si \rightarrow {}^{24}Mg + {}^{4}He$$
$$\gamma + {}^{24}Mg \rightarrow {}^{20}Ne + {}^{4}He \qquad etc.$$
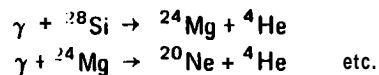
Some of the nuclides undergo beta decay producing, for instance, Ti 48, Cr 52, and the stable Fe 56. Alpha-particle capture leads to nuclides with even atomic number, which are more stable in nature than those with odd number.

C 12 can react with itself in an exothermic reaction,

$$^{12}C + {}^{12}C \rightarrow p + {}^{23}Na$$
$$^{12}C + {}^{12}C \rightarrow {}^{4}He + {}^{20}Ne$$
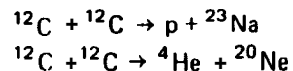
Oxygen burning occurs by a similar process,

$$^{16}O + {}^{16}O \rightarrow p + {}^{31}P$$
$$^{16}O + {}^{16}O \rightarrow n + {}^{31}S$$
$$^{16}O + {}^{16}O \rightarrow {}^{4}He + {}^{28}Si$$
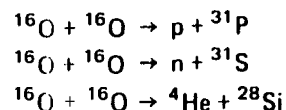
Heavier elements, between iron and lead, are produced by successive capture of neutrons and beta decay. Neutrons are produced by the reactions

$$^{3}He + {}^{13}C \rightarrow {}^{15}O + n$$
$$^{3}He + {}^{15}N \rightarrow {}^{17}F + n$$
$$^{17}O + {}^{4}He \rightarrow {}^{20}Ne + n$$
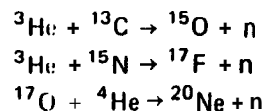
Both. slow processes (s-process), when the neutron flux is weak and rapid processes (r-process), when the neutron flux is strong, occur. The latter are important when the nuclei which capture neutrons are unstable with relatively short lifetimes.

3.7. Supernovae

A supernova is a cosmic explosion which is observed by the sudden increase in the brightness of a star followed by a less rapid decline. Such phenomena last from a few to several hundred days. At its maximum the brightness can reach the brightness of the whole galaxy to which the supernova belongs; this can be 10' to 10^9 times the luminosity of the sun. In our own galaxy a supernova event is estimated to occur once every 30 years. On the average, a supernova is expected every 360 years per galaxy. Only three supernova

explosions have definitely been observed in our galaxy. In 1054 one was seen by Chinese and Japanese astronomers which left the crab nebula as a remnant. Tcyho Brahe observed one in 1572 and *Kepler* in 1604. At present about 300 extragalactic supernovae have been found by systematic observations. .

In a supernova explosion large amounts of energy are released, in the region of 10^{50} to 10^{51} erg. The energy is radiated as visible light, radio waves and X-rays. Some energy produces acceleration of particles. A distinction is made between two types, I and II, of supernova explosions according to luminosity, spectral behaviour, and frequency of observation. Type I supernovae are believed to have low mass since they occur in stellar systems which contain mainly low-mass stars,whereas type II supernovae are believed to be massive stars, because they are observed in regions of galaxies which contain massive stars.

The supernova explosion is a dramatic event in the development of a star. Conflicting theories exist about the processes involved. One supernova model for massive stars suggests that at the end of thermonuclear processes in the interior of the star, heavy elements like iron and nickel are the dominant components. This region continues to contract by gravitation, which produces heat and decomposes the heavy elements into mixtures of helium and neutrons by the reaction

$$^{56}Fe \rightarrow 13\,{}^{4}He + 4\,n \,.$$
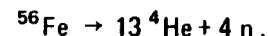
The star becomes unstable leading to a collapse in the interior region. Material further out is heated rapidly to high temperatures and thermonuclear processes are explosively ignited. As a result the outside of the star

Fig. 3.9: Picture of the crab nebula in H_α

may be ejected and the inside imploded. Most of the energy will be carried outwards by these processes in strong compression waves which create shock waves further out. Heavy elements may be synthesized. Fig. 3.9 shows the crab nebula which is considered to be the remnant of a type I supernova. Spectral analysis reveals that the nebula is expanding from the central star with a velocity of about 1,300 km s^{-1}. The emitted light is polarized. Radio emission has been observed from the central region and the expanding filaments. The radio waves are produced by electrons moving relativistically in spiral paths within a magnetic field (synchrotron radiation). The crab nebula is also a source of X- and r-radiation.

3.8. White dwarfs

White dwarfs are stars with relatively low brightness and relatively high temperature. Their sizes are comparable to earthlike planets with masses between 0.1 and 1 $M_\odot$. The densities of these stars are extremely high with values of 10^4 to 10^5 g cm^{-3} leading to high gravitation forces. The densities of the atmospheres are also very high and so they strongly absorb light. White dwarf stars are limited in mass; a theoretical maximum value of 1.2 $M_\odot$ is calculated.

Within the interior of the star, an equilibrium is assumed to exist between gravitation and gas pressure produced by a degenerated electron gas; this means that most quantum states are occupied. The pressure of such a gas is therefore independent of the temperature. The interior is mostly composed of He 4 so that no thermonuclear reactions take place anymore. The star cools down by radiation; the temperature of the surface decreasing in about 10^9 years to a value which renders the star unobservable.

The birth rate of these stars is about 7 x 10^{-77} s^{-1} cm^{-3}. Approximately 100 white dwarfs have been detected within a distance of about 10^{19} cm from the sun.

3.9. Neutron stars

If extreme compression exists within a star, the electrons of the electron gas unite with the protons to form neutrons. Since neutrons are unstable particles which decay with a mean lifetime of 10 min. into protons, electrons and electron-neutrinos, the neutrons in a neutron star are in equilibrium with protons and electrons. Such a state is possible only if the density of the electron gas is high enough. In a neutron star the neutrons

are a gas in a degenerate state similar to the electron gas in white dwarfs. However, the density is higher, in the region of about 10^{14} g cm^{-3}.

Neutron stars are considered to be stars in the final stages of development. During this development, the star is heated enormously by compression, the heat being carried away by neutrinos which are produced by the interaction of protons and electrons ($p + e \rightarrow n + \nu_e$). The star cools down to 10^9 K in about 10 years. After the temperature has fallen below this value further cooling occurs by radiation of photons. The theoretical upper limit for the mass of a neutron star is about 2 $M_\odot$.

A medium-heavy neutron star could have the following typical parameters: density 5 x 10^{14} g cm^{-3}, radius 12 km, mass 0.25 $M_\odot$ and temperature 10^8 K. In the interior, superfluid neutrons, protons and electrons exist while further out, at lower pressure, neutron-rich nuclei formed by interactions of nuclei with electrons may be dominant. An equilibrium is maintained between the degenerate neutron gas and the gravitational forces.

Fig. 3.10: Observed example of a pulsar (CP 0329; P = 0.712, λ = 11 cml

(From Pfleiderer. J.: Gross Properties of Pulsars in Lecture on Space Physics (A. Bruzek, f-f. Pilkuhn Eds.). Dusseldorf: Bertelsmann Universitatsverlag 1973)
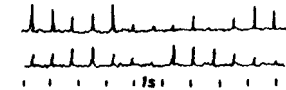
3.10. Pulsars

Pulsars are sources of radiation lying in the radio-frequency region, mainly in the meter range. They periodically emit pulsed radiation with a period of the order of seconds or less. Fig. 3.10 shows an observed example. If many pulses are superimposed, the resulting pulse has constant shape as illustrated in Fig. 3.11. The radiation is emitted in pulses which have only a small fraction, $\sim 10^{-1}$, of the total period of the pulsar. The periods are very exact and can be measured very precisely. They range from 0.033 s to 3.74 s. Some of them display an increase of the period P with time, for these dP/dt ranges from 36 ns d^{-1} to 0.01 ns d^{-1}.
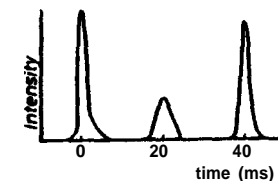
Fig. 3.11: Characteristic average pulse shape from a pulsar

The average distancesof pulsars have been estimated from their distribution in the sky. They lie at distances between 0.5×10^{21} cm and 6×10^{21} cm and are concentrated in the galactic disc. The absolute number in the galaxy is estimated to be $\sim 5 \times 10^6$. Their ages can be deduced from the ratio $T = P/\dot{P}$. These range from about 10^3 to about 3×10^8 years. Most pulsars have ages of several million years. Since the detection of the first pulsar in 1967, about 150 have been found.

Pulsars are generally believed to be neutron stars with extremely rapid rotations resulting from supernova explosions. However, not every supernova explosion produces a pulsar. If a star, the size of the sun, were to collapse to a much smaller star of radius about 10 km, this star would spin with high velocity due to angular momentum conservation. For an original radiusr, $= 7 \times 10^{10}$ cm and an original angular velocity $\dot{\varphi}_1 = 3 \times 10^{-6} s^{-1}$, conservation of angular momentum implies a final angular velocity $\dot{\varphi}_2 = \dot{\varphi}_1 (r_1/r_2)^2$. In this way the angular velocity is increased by a factor 10^3. If in addition there was an original magnetic field of 10^2 Gauss, after contraction a field of 10^{12} Gauss is produced. When the axis of the angular momentum and the magnetic field do not coincide, which is usually the case, electromagnetic radiation is emitted with a frequency of $\nu = I/P$.

The character of the pulses can be understood in terms of emission from a relatively small extended source. If the radiation is emitted simultaneously from a region of finite extent the arrival time at an observer varies because of the different distances from different parts of the source. Even if a sharp pulse was emitted,it would be spread out due to the different transit times from different points of the source.

When a mass-rich star contracts to a pulsar, a rotation energy of about 10^{51} erg can be derived from the gravitation energy. The energy of the emitted radiation is removed from the rotation energy which leads to the slowing-down process observed as $\dot{P}$ for some pulsars.

The crab nebula has a pulsar at its center which emits radiation throughout. the electromagnetic spectrum, radio waves, visible light, X- and T-radiation. The total energy output is of the order of 10^{38} erg s^{-1}. If the crab pulsar is the remnant of a normal star (radius 10^5 km, magnetic field 10^2 Gauss) then the resulting magnetic field should be about 10^{12} Gauss. If the magnetic axis is markedly inclined to the rotation axis, a strong magnetic dipole radiation with a frequency of 30 Hz and an energy output of about 4×10^{38} erg s^{-1} will exist. Such radiation would be completely absorbed in the vicinity of the pulsar. It is reasonable to suppose that the pulsar provides the energy input for the crab nebula. From the change in the

period of the pulses, the age of the crab nebula is calculated to be about 1,200 years which is in good agreement with the actual known age of 920 years.

3.11. Black holes

Stars with masses of less than about 2 $M_\odot$ are able to end their lives in stable final configurations such as white dwarfs or neutron stars. However, stars with much larger masses can become white dwarfs or neutron stars only if they eject a considerable fraction of their mass into space during an unstable period in their history. According to general relativity theory they may also become black holes as a result of gravitational collapse, which in their final states are stars with zero radius and infinite density. The radiation from such hypothetical objects would suffer energy loss in the high-gravitational field increasing the wavelength by gravitational red shift so that the objects become invisible. Anything that approaches a black hole too closely will fall into it and lose its separate identity. If such objects exist, a considerable amount of hidden matter could be present in the universe.

3.12. Synchrotron radiation

A charged particle moving along a circular orbit in a magnetic field of strength H emits electromagnetic radiation. This radiation is produced by continuous centrifugal acceleration, and is called magneto-bremsstrahlung. It is usually associated with electrons. If the motion is non-relativistic,one speaks of cyclotron radiation, but in the relativistic region it is called synchrotron radiation. (Fig. 3.12). The energy carried away by the radiation originates in the kinetic energy of the electrons. Its frequency depends on the velocity of the electron and the strength of the magnetic field. The radiation is produced in the radio-frequency, ultraviolet, visible, infrared, and gamma ray regions.

Synchrotron radiation is almost completely polarized, the electric field vector of the wave lying perpendicular to the magnetic field vector and the
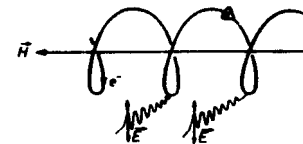
Fig. 3.12: Production mechanism for synchrotron radiation

velocity vector, The angular frequency of the emitted wave is equal the angular frequency of the particle rotation. A non-relativistic electron emits a fundamental frequency

$$\omega = 8.8 \times 10^{12} \times H/E.$$

H magnetic field (Gauss)
E total energy of the electron (eV)

Fig. 3.13: Direction of emission of synchrotron radiation

In the ultra-relativistic range $E \gg m\,c^2$ (= 0.51 MeV), the electron emits waves predominantly in the direction of the velocity vector (Fig. 3.13) and the fundamental frequency is given by

$$\omega = \frac{e\,H_\perp}{2\,mc}\left(\frac{E}{m\,c^2}\right)^2,$$

ω frequency of the emitted radiation
$H_\perp$ magnetic field
E total energy of the electron
m electron mass

The radiation is concentrated within a cone of angle $\Theta \approx m\,c^2/E \ll 1$. An observer in the orbital plane observes bursts of radiation at intervals $t = 2\,\pi/\omega$. The duration of a burst is

$$\Delta t \approx \frac{r\Theta}{c}\left(\frac{m\,c^2}{E}\right)^2,$$

where $r = c/\omega$ is the radius of the orbit and $(m\,c^2/E)^2$ is a factor due to the Doppler effect.

References

Aller, L. H.: Astrophysics (2nd ed.). New York: The Ronald Press Company 1963

Hess, W. N., G. D. Mead feds.): Introduction to Space Science (2nd ed.). New York: Gordon and Breach, Science Publishers 1968

Menzel, D. H., F. L. Whipple, G. De Vaucouleurs: Survey of the Universe. New Jersey: Prentice-Hall 1970

Hayakawa, S.: Cosmic-Ray Physics. New York: Wiley-interscience 1969

Unsold, A.: Der Neue Kosmos (2nd ed.). Berlin: Springer-Verlag 1974

Taylor, R.J.: The Origin of the Chemical Elements. London: Wykeham Publications 1972

Taylor, R.J.: The Stars: Their Structure and Evolution. London: Wykeham Publications 1972

Bruzek, A., H. Pilkuhn feds.): Lectures on Space Physics. Diisseldorf: Bertelsrnann Universitatsverlag 1973

4. Galactic cosmic radiation

In this chapter, the principal observed features of the primary galactic cosmic radiation are presented. The unmodified components of charged cosmic radiation are not observed even when measurements are made outside the terrestrial atmosphere. This is mainly the result of interactions with interstellar matter and the effects of the magnetic fields of the solar wind which perturb the low-energy particles. The modulation effect in the magnetosphere will be discussed later. The main properties characterizing primary cosmic radiation are intensity, chemical composition, i.e. intensity as a function of particle charge, energy spectra and isotropy.

4.1. Basic definitions

Intensify. The intensity or directional intensity j, is defined as the number of particles, dN, incident upon an area, dF, per time, d t, per solid angle, $d\Omega$ (Fig. 4.11,

$$J = \frac{dN}{dF \cdot dt \cdot d\Omega} \quad (cm^{-2} s^{-1} sr^{-1}).$$
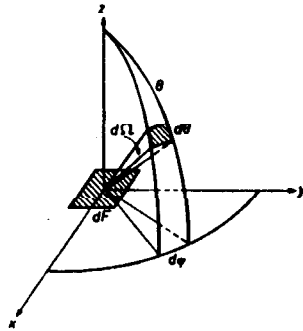
Fig. 4.1: Definition of intensity

Fig. 4.2: Integrated intensity

This quantity depends upon the polar and azimuthal angles 0 and φ, the time t and the energy E, $j = j (\Theta, \varphi, E, t)$. The total intensity integrated over all energies is usually used. When $\Theta = 0$ the vertical intensity $i_v = j (\Theta = 0)$ is obtained. The intensity integrated over all φ gives the isotropic distribution (Fig. 4.2).

Flux. The particle flux J_1, is defined as the total number of particles per unit time passing through unit horizontal area in a downward direction. thus

$$J_1 = \int_{\substack{upper \\ half-space}} j \cos \Theta \, d\Omega \quad (cm^{-2} s^{-1}).$$

Omnidirectional intensity. This is obtained by integrating the directional intensity j over all angles

$$J_2 = \int_{\substack{upper \\ half-space}} j \, d\Omega.$$

Since $d\Omega = \sin \Theta \, d\Theta \, d\varphi$,

$$J_2 = \int_{\Theta=0}^{\pi/2} \int_{\varphi=0}^{2\pi} j (\Theta) \sin \Theta \, d\Theta \, d\varphi$$

$$= 2\pi \int_0^{\pi/2} (\Theta) \sin \Theta \, d\Theta$$

if no azimuthal dependence is given. The omnidirectional intensity J_2 is per definition always greater than the particle flux J_1.

Differential energy spectrum. This energy spectrum is defined as the number of particles, dN, per area, dF, per time, d t, per solid angle, $d\Omega$ and per energy interval d E,

$$D = \frac{dN}{dF \cdot d\Omega \cdot dt \cdot dE}.$$

It is usually expressed in units of $cm^{-2} s^{-1} sr^{-1} (GeV)^{-1}$. Instead of energy (GeV), one may use momentum (GeV/c) or rigidity, S, defined as

$$S = \frac{pc}{ze}$$

where pc is the kinetic energy in units of GeV, and ze is the charge of the particle. The unit of rigidity is GV. The reason for using this unit is that particles with the same rigidity follow identical paths in magnetic fields.

Integral energy spectrum. This quantity, M, is defined for all particles with an energy greater than E_j per unit area, unit solid angle and unit time

$$M (> E) = \frac{dN}{dF \cdot d\Omega \cdot dt} \quad (cm^{-2} sr^{-1} s^{-1})$$

The integral spectrum is derived from the differential spectrum by integration

$$M(>E) = \int_E^\infty D\,dE .$$

Alternatively D is derived from M as

$$D = -\,dM/dE .$$

4.2. Primary intensity

Due to modulation of the intensity of charged particles by the magnetic fields of the solar wind in the interplanetary space, the primary intensity which is composed mainly of low energetic particles, varies with time following the time variations of the magnetic fields (Chapter 13). A further influence is the geomagnetic field, which leads to an increase of intensity with increasing latitude (Chapter 12). During 1949/50 at the geomagnetic latitudes of 0° and 60°, intensities of $0.03\,\text{cm}^{-2}\,\text{s}^{-1}\,\text{sr}^{-1}$ and $0.3\,\text{cm}^{-2}\,\text{s}^{-1}\,\text{sr}^{-1}$ respectively, were measured. The effects due to the interplanetary magnetic field follow an 11-year cycle and give rise to intensity variations of a factor 1 to 4, depending on the geomagnetic latitude. For particles of energy $\geqslant 10^{12}$ eV no significant modulation exists. The intensity of particles with energy $> 10^{15}$ eV is, approximately

$$j \approx 5 \times 10^{-10}\,\text{cm}^{-2}\,\text{s}^{-1}\,\text{sr}^{-1} .$$

4.3. Chemical composition

The chemical composition of the primary cosmic radiation as measured at a particular geographical location above the earth's atmosphere depends upon,

(a) the interstellar space, due to interactions with interstellar gas and the interstellar magnetic field,

(b) the interplanetary space, due to interactions with the solar wind,

(c) the energy of the radiation. At present information is only available for energies $E < 10^{12}$ eV.

Heavy nuclei are classified into groups with the following nomenclature,

$3 \leqslant Z \leqslant 5$ light nuclei	L-group	Li, Be, B
$6 \leqslant Z \leqslant 9$ medium nuclei	M-group	C, N, O, F
$10 \leqslant Z \leqslant 19$ heavy nuclei	H-group	Ne – K
$20 \leqslant Z \leqslant 30$ very heavy nuclei	VH-group	Ca – Zn
$Z > 30$ ultra-heavy nuclei	VVH-group	Ga – U
$Z > 92$ superheavy nuclei	SH-group	

The nuclei with $Z \geqslant 10$ are also classified as,

$10 \leqslant Z \leqslant 15$	H_1-nuclei
$16 \leqslant Z \leqslant 19$	H_2-nuclei
$20 \leqslant Z \leqslant 28$	Ho-nuclei
$29 \leqslant Z \leqslant 80$	$H_,$-nuclei
$80 < Z$	H_5-nuclei

The following composition has been measured at the top of the atmosphere: 86% protons; 13% alpha particles; 1.4% heavy nuclei ($Z \geqslant 3$). There are in addition about 1 % electrons. During solar minima at a geomagnetic latitude of 40°. the values given in Table 4.1 have been measured.

Table 4.1: Composition of heavy nuclei

charge	integral flux $(m^2\,s\,sr)^{-1}$	relat. frequency %	relat. mass %	relet. total energy %
1	610 ± 30	86.0	54.6	10.7
2	90 ± 2	12.7	32.2	21 .0
3 - 5	2 ± 0.2			
6 - 9	5.6 ± 0.2	1.3	13.2	8.3
10 – 19	1.4 ± 0.2			
20-29	0.4 ± 0.1			

Fig. 4.3 shows the chemical composition arriving at the top of atmosphere, and for comparison the composition of the elements in the solar system, sometimes called the universal composition. Both diagrams are normalized to carbon. It is seen that H and He are less abundant in cosmic rays, but elements between $18 \leqslant Z \leqslant 24$ are more abundant. The most striking disparity occurs for the elements Li, Be, B, which are found to be about five orders of magnitude more abundant in cosmic rays than in the universal abundance (see Section 4.6).
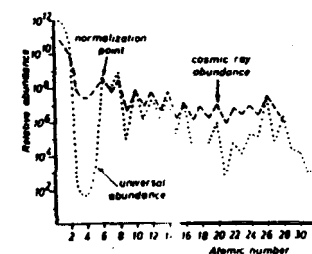
Fig. 4.3: Comparison of cosmic-ray chemical composition with the universal composition (normalized to carbon)
(From Shapiro. M. M.. R. Silberberg: Ann. Rev. Nucl. Sci. 20 (1970) 323)

Deuterons are also found to be present. They are assumed to be the result of spallation of higher mass nuclei in interstellar space due to collisions with hydrogen nuclei. The ratio D^2/H^1 which has a value of $\sim$ 7% is not appreciably affected by solar modulation. Tritium nuclei have not been found in cosmic rays.

Several attempts have been made to detect anti-nuclei in cosmic rays, but none have been found; only upper limits for various energies can be given, thus $N(\bar{p})/N(p) \approx 5 \times 10^{-2}$ to 3×10^{-4}

4.4. Energy spectra

The energy spectrum of the primary cosmic-ray particles has been measured in different energy regions by a variety of observational techniques. At low energies, up to about 10^{12} eV, the spectra have been measured directly outside the earth's atmosphere. At higher energies, indirect methods have been used. The low-energy part of the spectrum is strongly modulated by solar effects. The spectrum extends smoothly from about 10^7 eV to 10^{20} eV, and covers approximately 32 decades in intensity. Fig. 4.4 shows the
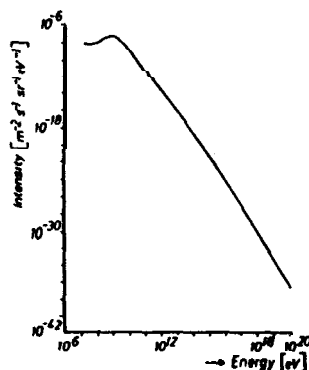
Fig. 4.4: Primary differential energy spectrum (From Wolfendale, A. W.: Cosmic Rays at Ground Level. London: The Institute of Physics (1973))

primary differential energy spectrum of protons. The energy spectra of alpha particles and heavier nuclei have not been measured to such high energies. Since the total energy E of a nucleus is shared equally amongst its A nucleons, the energy per nucleon E/A, is used when comparing different nuclei. The energy spectra of alpha particles and heavier nuclei are shown in Fig. 4.5. The shapes are seen to be comparable.
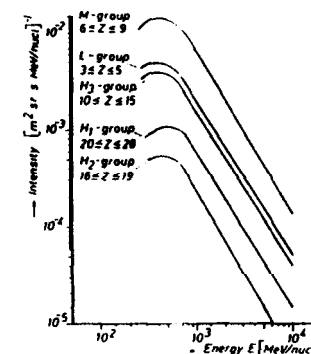
Fig. 4.5: Differential energy spectra of different charge groups of heavy nuclei

The primary proton spectrum may be represented by a power law. If the integral spectrum is written as

$$M(>E) = K \cdot E^{-\gamma} \qquad \text{particles cm}^{-2} \text{ s}^{-1} \text{ sr}^{-1}$$

where K is a constant

the differential spectrum is then

$$D = -\frac{dM}{dE} = K \gamma E^{-(\gamma+1)} = A \cdot e^{-\gamma}$$
$$\text{particles cm}^{-2} \text{ s}^{-1} \text{ sr}^{-1} (\text{GeV/c})^{-1}$$

Here A is the intensity and δ the slope. The slope of the differential spectrum is seen to be steeper than that of the integral one. The following values of the slope and the intensity have been measured:

energy range (eV)	δ	A (cm^{-2} s^{-1} sr^{-1} eV^{-1})
$10" < E < 10^{15}$	≈ 2.6	3.1×10^{14}
$3 \times 10^{15} < E < 10^{20}$	≈ 3.2	1.0×10^{24}

4.5. Primary electrons and positrons

Cosmic-ray electrons are about 1 % as abundant as the primary protons. The positrons on the other hand are about 10 % as abundant as the electrons. The energy spectrum is strongly modulated in the low-energy region. The observed data extend up to about 10^{12} eV. Fig. 4.6 shows the integral energy spectrum of the primary electrons. There is a signifirant change in the slope between 100 MeV and 2 GeV. The spectrum follows a power law similar to the proton spectrum but with a slightly different exponent.

Fig. 4.6: Differential energy spectrum of electrons (From Meyer. P.: Ann. Rev. Astron. Astrophysics 7, (1969) 1)

The energy spectrum of positrons has been measured crudely from 10^8 to 10^{10} eV. It also may be fitted by a power law, with $\delta = 2.6$.

Cosmic-ray electrons are likely to come from one of two principal sources. They could have the same origin as protons and heavy nuclei, or they could be generated in secondary processes by interactions with interstellar matter. If the latter process was responsible one would expect an excess of positrons over electrons, because primary protons produce an excess of π^+ over π^- and hence, μ^+ over μ^-, and finally e^+ over e^-. However, since a large excess of e^- is observed, the bulk of them probably come from the same source as the protons and nuclei.

4.6. Source composition and spectra

On their long journeys through space, the source nuclei of cosmic radiation suffer modifications both in energy and composition due to interactions with the interstellar and interplanetary matter and with magnetic fields. The amount of interstellar matter traversed by cosmic-ray particles is about 4 g cm^{-2}. They can suffer energy loss by ionization and undergo nuclear interactions leading to fragmentation. The magnetic fields modify the energy spectra in the low- energy region.

The abundance of the nuclei Li, Be, B was shown in Fig. 4.3, to be several orders of magnitudes higher than in the universal composition. The reason for this is that heavy nuclei undergo spallation producing lighter nuclei.

The mean free path, λ_i, for the collision of a particle of type i, is related to the cross-section σ_i by

$$\lambda_i = \frac{\rho}{n \, \sigma_i} \quad (g \, cm^{-2}).$$

ρ matter density (g cm^{-3})
n particle density (cm^{-3})

Using the geometrical cross-section

$$\sigma_i = \pi \, r_i^2 \quad (cm^2)$$

$r_i = 1.26 \times 10^{-13} A^{1/3}$ (cm)
A = atomic weight

the values of σ_i and λ_i given in Table 4.2 are obtained. The time between collisions τ_i for relativistic particles $(v \approx c)$ is given by the relation

$$\tau_i = \frac{\lambda_i}{\rho \cdot c} = 108 \, \lambda_i \quad (years)$$

for $n = 1 \, cm^{-3}$. Values of τ_i are also given in Table 4.2.

Table 4.2: Cross-sections for fragmentation and mean free paths for heavy nuclei (From Grewino. M. in Lectures on Space Physics (Eds. C.A. Bruzek. H. Pilkuhn) Dusseldorf: Bertelsmann Universitats-Verlag 197e)

particle	A mean atomic number	σ_i $(10^{-26} cm^2)$	λ_i (g cm^{-2})	τ_i (years)
P	1	2.3	17	4.8×10^7
α	4	9.3		1.2×10^7
L	10	23	7	4.8×10^6
M	14	29	5.	3.8×10^6
H	36	54	3.	2.1×106
Fe	56	73	2.	1.5×10^6

In order to calculate the primordial composition of cosmic rays, the cross-sections, σ_i, for fragmentation at high energies have to be known. Due to a lack of data, present calculations are inaccurate.

The slab model assumes that all cosmic rays have traversed the same mean thickness of about 4 g cm^{-2} of matter between source and earth. To obtain better agreement between universal and cosmic-ray chemical compositions, a distribution function for the path length is introduced. Good agreement is obtained if an exponential form is assumed for this distribution.

$$dN/dx = a \cdot \exp(-bx/\Lambda); \quad \Lambda = \Lambda(E).$$
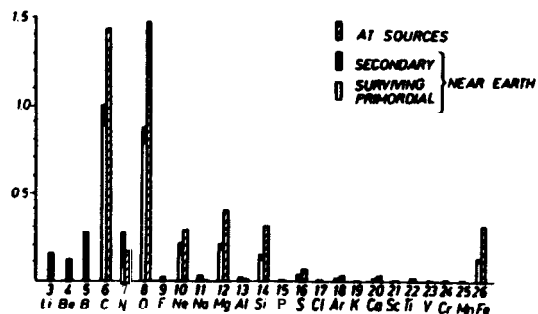
Fig. 4.7: Comparison of the chemical composition of heavy nuclei at the source and near the earth (From Shapiro, M. M., R. Silberberg: Ann. Rev. Nucl. Sci. 20 (1970) 323)

The fraction of primordial nuclei and the number of fragmentation products in the observed composition near earth can then be calculated, giving the results as shown in Fig. 4.7. Elements like Li, Be, B, Ti, V, Cr and Mn need not be present at the source.

The energy spectrum observed at the top of the atmosphere is not the same as the one existing outside of the solar system. The fluxes of cosmic-ray particles reaching the earth from the galaxy are attenuated within the interplanetary space by the magnetic fields of the solar wind. These modulations are produced by convection and diffusion processes in the solar corona (see Section 13.4). The continuous flow of the solar wind de-termines the interplanetary magnetic field. The galactic cosmic-ray particles diffuse through this field,and a steady state exists between outward con-vection and inward diffusion. The spectra outside the solar system can be
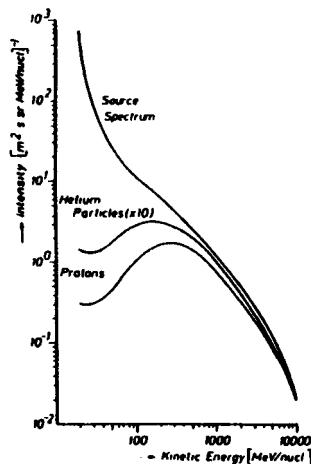
Fig. 4.8: The energy spectra of protons and nuclei and their extrapolation to interstellar space (From Meyer, P.: Ann Rev. Astron. Astrophysics 7, (1969) 1)

estimated by taking these effects into account. The spectra of protons and alpha particles extrapolated to interstellar space are shown in Fig. 4.8. Both spectra have the same shape but are very different from the spectra observed at low energies.

4.7. X- and v-radiation

High-energy astronomy is the study of X- and y-radiation in space. It is important because high-energy photons provide information about pro-duction processes,and in contrast to the charged cosmic-ray particles are not influenced by the interstellar magnetic fields. High-energy photons in the range from 1 keV to about 1 MeV are called X-rays, and photons with energies above 1 MeV are called γ-rays. A distinction is made for both X- and γ-rays,between diffuse radiation and radiation sources.

The following processes are responsible for the production of high-energy photons.

Synchrotron radiation. Electrons spiral in magnetic fields emitting strongly polarized electromagnetic radiation. The emitted quanta have frequencies clustered around a characteristic frequency w (see Section 3.12). If the electrons have a differential energy spectrum $D_e \sim E^{-\delta}$, the resulting fre-quency spectrum is

$$D \sim \nu^{-\alpha}, \qquad = \frac{-1}{2} .$$

Bremsstrahlung. Electrons traverse matter and lose energy due to Coulomb interactions. The probability, Φ, of emitting a photon by this process, in a frequency interval, $d\nu$, within a path length, dx, is given by

$$\Phi \, d\nu \, dx = \frac{dv}{\nu} \cdot \frac{dx}{X_0}.$$

X_0 radiation length of the matter

Inverse Compton effect. Low-energy photons can interact with high-energy electrons with subsequent energy gain, in contrast to the usual Compton process, in which a high-energy photon loses energy. The process is of considerable astrophysical significance, because as electrons travel through space they interact with the photons of star light and the 3 K-radiation.

Nuclear interactions. Cosmic-ray particles interact with the nuclei of in-terstellar matter raising them to excited states which then decay by gamma emission. These processes are induced by low-energy particles with $E \lesssim 100$ MeV. The energy of the emitted gamma rays is $\lesssim 10$ MeV.

High-energy interactions. At high energies π^o mesons are produced by the interaction of the protons with interstellar matter. The π^o mesons decay immediately into two gamma rays.

Annihilation processes. If nucleons interact with antimatter, π^o mesons will be produced and hence gamma rays. Such gamma rays will have energies concentrated around 100 MeV.
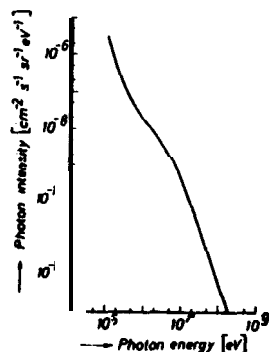
Fig. 4.9: Diffuse X-ray spectrum
(From Pinkau, K.: X-Rays and
Gamma Rays: Rapporteur
Paper at the 13. Conference
on Cosmic Rays, Denver (1973))

An approximately isotropic, diffuse background radiation is observed in both the X-ray and the γ-ray regions (Fig. 4.9). Diffuse gamma radiation is observed up to an energy of $\sim$ 100 MeV. Measurements indicate that the intensity is peaked towards the direction of the galactic equator which suggests that the radiation comes from the galactic center. The intensity from the direction of the galactic center is

$$N_\gamma = 1.2 \times 10^{-4} \text{ photons cm}^{-2} \text{ s}^{-1} \text{ sr}^{-1}.$$

A number of specific X-ray sources have been detected; one of them in the crab nebula. In the gamma-ray region, point sources have been observed but there is no general agreement about them. There is, however, no doubt that the crab nebula emits both, pulsed and unpulsed gamma radiation in addition to X-radiation.

Recently, the occurence of intense, several-second duration bursts of 0.1 to 1.2 MeV cosmic gamma rays has been observed by measurements with Vela satellites. Multiple-pulse events have been measured simultaneously by three satellites at different orbital positions, enabling the direction of the gamma bursts to be determined. These events have distinct pulses of one or two seconds duration separated by several seconds. Their energy

spectra have been measured and can be expressed in terms of an exponential relation of the form

$$dN/dE = \text{Io} \exp\left(-E/E_0\right) \text{ photons cm}^{-2} \text{keV}^{-1} \text{cm}^{-2} \text{ burst-'}$$

The characteristic energies at maximum intensity appear to cluster around 150 keV.

Various hypotheses concerning the possible origin of these bursts have been put forward. One interpretation assumes a correlation with neutron star formation from white dwarfs. Another model proposes that the bursts are similar to flare events from the sun (stellar superflare hypothesis). It is suggested that the photons of the bursts in the X-ray region are produced by inverse Compton scattering with electrons, and in another model that dust grains produced by pulsars, break up during their approach to the sun and scatter solar photons. Yet another model proposes that the bursts are due to comets falling onto a neutron star.

4.6. Neutrinos

When cosmic-ray particles interact with matter, unstable particles can be produced which decay into one of the four types of neutrinos ν_e, $\bar{\nu}_e$, ν_μ, $\bar{\nu}_\mu$. Such parent particles might be neutrons, mesons or hyperons. Neutrinos are expected from cosmic-ray sources such as the sun, pulsars and supernovae, and also from interactions in intergalactic and even extragalactic space.

Solar neutrinos. The nuclear reactions responsible for the production of the solar energy which occur in the solar core, also produce electron-neutrinos ν_e. The main process is hydrogen burning

$$4\,^1\text{H} \rightarrow {}^4\text{He} + 2\,\nu_e + 26.7 \text{ MeV} .$$
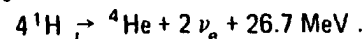
The detailed reactions have already been considered in Chapter 3.6. Electron neutrinos are produced in the various reactions with different intensities and with energies ranging from 100 keV to about 10 MeV. Table 4.3 gives some calculated fluxes and the corresponding energies. The values, however, are not too reliable; they have been revised many times during recent years. Underground measurements of solar neutrinos have not been very successful.

Other sources of extraterrestrial neutrinos are:

Discrete sources: In rapidly evolving stars, there are certain stages during which neutrinos are expected to be responsible for energy loss from the Interiors.

Table 4.3: **Solar** neutrino fluxes
(From Young, E. C. M. in Cosmic Rays at Ground Level (Ed. A. W. Wolfendale)
London: The Institute of **Physics, 19731**

source	neutrino energy (MeV)	flux on earth $(cm^{-2} s^{-1})$
$p + p \to d + e^{+} + \nu_e$	$0 - 0.42$	6.0×10^{10}
$p + e^{-} + p \to d + \nu_e$	1.44	1.5×10^8
^7Be decay	0.86	4.5×10^9
^8B decay	$0 - 14.06$	5.4×10^8
^{13}N decay	$o - 1.19$	3.3×10^8
^{15}O decay	$o - 1.74$	3.7×10^8

Galactic *neutrinos:* They are produced as secondary particles in interactions of primary cosmic-ray particles with interstellar matter. The main processes are the decay of π^{+} and π^{-} which are produced by these interactions. Since π^{o} mesons which decay into gamma rays, are produced in similar reactions, there is a correlation between the fluxes of neutrinos and gamma rays. Using the measured gamma-ray flux, a neutrino flux of $i_\nu = 2 \times 10^{-6}$ $cm^{-2} s^{-1} sr^{-1}$ is estimated for neutrinos with $E \geqslant 1$ GeV.
Extragalactic neutrinos: They come from discrete sources or from interactions with intergalactic matter.

Additional reactions which could give rise to neutrino pairs are

$$e^{+} + e^{-} \to \nu_e + \bar{\nu}_e$$
$$e^{+} + e^{-} \to \nu_\mu + \bar{\nu}_\mu.$$
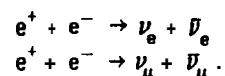
The normal process for the annihilation of electron pairs is the electromagnetic process

$$e+ + e^{-} \to \gamma + \gamma.$$
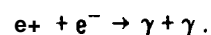
Annihilation into neutrinos isgoverned by the weak interaction coupling constant and so is a factor of roughly twenty orders of magnitude less than the annihilation into gamma rays. In highly evolved stars, with extreme temperatures of about 10^9 K, electron pairs are created from photons by

$$\gamma + \gamma \to e^{+} + e^{-}.$$
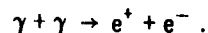
Here the probability of neutrino production is greatly enhanced due to the high electron densities.

In order to detect astrophysical neutrinos, detectors of very large size with high sensitivity, good angular resolution and good time resolution must be developed.

4.9. Energy densities

The energy density of charged cosmic ray particles can be calculated from the differential energy spectrum $D(E)$ using the relationship

$$\rho = \frac{4n}{c} \int ED(E)\ dE.$$

For a mean energy of the primary cosmic rays of about 1 GeV,the particle density in interstellar space is about 10^{-9} cm^{-3}. This corresponds to an energy density of $\rho_{CR} = 1$ eV cm^{-3}. The energy density as a function of energy can be derived from the equation

$$\rho(> E) = \frac{4\pi}{c} \int_E ED(E)\ dE.$$

The resultant curve is shown in Fig. 4.10. Integration gives the more precise value of $\rho_{CR} = 0.6$ eV cm^{-3}. The energy density of star light is found to be $\rho_{SL} = 0.6$ eV cm-^{3}.

The turbulent gas motion of the interstellar gas has an energy density of $\rho_{GM} = 0.5$ eV cm^{-3} and the energy density of the 3 K-radiation has a value of $\rho_{BR} \approx 0.25$ eV cm^{-3}. Finally the energy content of the interstellar magnetic field is found to be $\rho_{MF} \approx 0.6$ eV cm-^{3}. Hence, a rough approximation gives

$$\rho_{CR} \approx \rho_{SL} \approx \rho_{GM} \approx \rho_{BR} \approx \rho_{MF} \approx 1\ eV\ cm-^3,$$

from which it is concluded that these quantities are in some way correlated and a coupling between plasma, magnetic field and particle motion exists.

Finally, it should be noted that the energy density of X- and y-radiation is about 3×10^{-5} eV cm^{-3} and of neutrinos $\lesssim 10^4$ eV cm^{-3}.
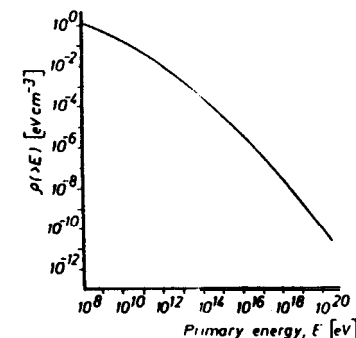
Fig. 4.10: Energy density of cosmic radiation (From Wolfendale. A. W.: Cosmic Revs at Ground Level, The Institute of Physics. London (1973))

4.10. Cosmic-ray lifetime

An estimate of cosmic-ray lifetime is obtained by calculating the shapes of electron and positron energy spectra. Electrons undergo energy loss by several processes: synchrotron radiation, ionization loss, bremsstrahlung and Compton collisionswith photons. The source spectrum is therefore modified and steepened; the energy where a steepening occurs is depending on the average transit time between source and observer. The dominant mechanism by which electrons are lost at energies beyond about 100 GeV, is leakage from the galaxy. For each of the above processes,a lifetime can be defined by

$$\tau_i = \frac{E}{(dE/dt)},$$

i   specific loss process

The total lifetime is given by

$$\frac{1}{\tau} = \sum_i 1/\tau_i.$$

If it is assumed that the electrons are injected into the galactic disc with the spectral form $D(E) = D_0 \cdot E^{-\beta}$, the observed equilibrium density is

$$J(E) = D(E)\,\tau(E),$$

where $\tau(E)$ is the storage time of the electrons. If the amount of matter traversed is 2 to 4 g cm^{-3}, the effective storage time is $\tau \approx 2 \times 10^6$ years.

Positrons are not considered to be source particles,but the result of inter-actions of protons with interstellar matter giving rise to π^+ and hence, μ^+, which finally decays as $\mu^+ \rightarrow e^+ + \nu_e + \overline{\nu}_\mu$. A storage time of about 2×10^6 years is also obtained for positrons.

Another method of deriving the storage time of cosmic-ray particles is to examine the spectra and fluxes of secondary particles such as Li, Be, B, which are produced by fragmentation of heavier primary nuclei. For a uniform source distribution and a mean disc density of 2 to 4 g cm^{-3}, a storage time of about 2×10^6 years is obtained.

References

Bruzek, A., H. Pilkuhn (eds.):   Lectures on Space Physics. Diisseldorf: Bertelsmann Universitatsverlag, 1973

Hess. W.N., G.D. Mead lads.): Introduction to Space Science (2nd ed.).   New York: Gordon and Breach. Science Publishers 1966

Meyer, P.: Cosmic Rays in the Galaxy. Ann. Rev. Astron, Astrophysics 7 (1969) 1

Wolfendale, A.W.: Cosmic Rays at Ground Level. London: The Institute of Physics 1973

Shapiro, M. M., R. Silberberg: Heavy Cosmic-Ray Nuclei. Ann. Rev. Nucl. Sci. 20, (1970) 323

Hayakawa, S.: Cosmic-Ray Physics. New York: Wiley-Interscience 1969

Pinkau. K.: X-Rays and Gamma Rays. Rapporteur Paper at the 13th Conference on Cosmic Rays, Denver 1973

Klebesadel, R. W., I. B. Strong, R. A. Olson: Ap. J. (letters), 182 (1973) L 85

5. The origin of cosmic radiation

There is still no definite answer to the question of the origin of cosmic-ray particles; they are certainly not of solar origin. The remaining possibilities are a universal origin or an origin confined to our galaxy.

The local theories of galactic origin can be divided into point-source models and statistical models. A further classification depends upon whether or not strong electromagnetic fields are involved. However, whichever model is used the following facts must be taken into account:

(1) The energy density of cosmic radiation is about 1 eV cm^{-3}. This is the same order of magnitude as the energy densities of star light, universal black-body radiation, turbulent gas motion of interstellar gas and the energy content of the interstellar magnetic field, demonstrating a correlation between the different energy components.

(2) The differential energy spectrum obeys a power law $D(E) \sim E^{-\delta}$, which shows a change in tha slope at about 3×10^{15} eV from $\delta \sim 2.6$ to $\delta \sim 3.2$ for higher energies.

(3) For some nuclei, the charge spectrum shows strong deviations from the universal distribution.

(4) Up to the highest energies observed, no significant anisotropies have been found. For energies up to 10^{14} eV the measured anisotropy is less than 0.5%, increasing to about 3% at an energy of 3×10^{17} eV.

(5) The particle flux remains constant over long periods of time.

The point sources which have been considered include the sun, supernova explosions, magnetic A-stars, white dwarfs and pulsars. The universal model gets into difficulties because an energy density of 1 eV cm^{-3} throughout the whole universe cannot be explained.

5.1. Supernova explosions

It is postulated that supernova explosions are the principal source of cosmic rays. Since observations tell us that on average one supernova explosion occurs in our galaxy ever 30 to 50 years and that 10^{50} to 10^{51} erg are liberated per event, such explosions would maintain the cosmic-ray flux in a quasi-stationary state with an energy content of about 10^{56} erg. This energy supply would be sufficient to replace those particles which escape from the galaxy or disappear as a result of energy losses.

In supernova explosions a huge amount of energy is liberated during the gravitational collapse of the star. If r_1 and r_2 denote the radii of the star before and after the collapse, the gravitational energy produced is given by

$$E = G_N M^2 (1/r_2 - 1/r_1).$$

M mass of the star
G_N gravitational constant

Taking $r_2 \sim 10^6$ cm, $r_2 \ll r_1$, and $M = 1\, M_\Theta \approx 2 \times 10^{33}$ g, as for the case of a neutron star, then

$$E = 3 \times 10^{53} \text{ erg}.$$

Using the values for the density of cosmic radiation in the galaxy $\rho = 10^{-12}$ erg cm^{-3}, for the galactic volume $V = 10^{67}$ cm^3, and for the lifetime of cosmic radiation in the galaxy $\tau = 10^7$ years $= 10^{15}$ s, then the energy injection rate is

$$\Delta E_1 / \Delta t = \frac{V \cdot \rho}{\tau} = \frac{10^{67} \cdot 10^{-12}}{10^{15}} = 10^{40} \text{ erg s}^{-1}.$$

It is estimated that $E_s = 10^{49}$ erg of the energy released during a supernova explosion is converted into cosmic rays. For a supernova explosion occuring every 30 years ($\tau_s = 10^9$ s), this gives an injection rate of

$$\Delta E_2 / \Delta t = E_s / \tau_s = \frac{10^{49}}{10^9} = 10^{40} \text{ erg s}^{-1}.$$

Comparing E_1 / t and $E_2 / \Delta t$ it can be concluded that the energy required for cosmic radiation could indeed be provided by supernova explosions.

After the initial explosion of the supernova, a shock wave goes out from the core which accelerates the particles in the outer layers to relativistic energies of 10^8 to 10^{21} eV. Neutrons are produced which in turn create heavier nuclei by rapid capture processes. Radio waves, visible light and X-radiation have been observed from the direction of supernova remnants, which may be attributed to synchrotron acceleration. Electrons and even protons and other nuclei may be continuously accelerated there; electrons perhaps up to 10^{13} eV. The crab nebula is regarded as a supernova remnant.

5.2. Batatron and Fermi mechanisms

In statistical models, cosmic-ray particles are assumed to be accelerated by electromagnetic fields. An increase or decrease of energy can occur in a

single process, but for a large number of events an overall energy gain results. There are two basically different processes,

(a) acceleration in homogeneous magnetic fields which increase with time (betatron acceleration),

(b) acceleration due to interactions with moving magnetic-field inhomogeneities in magnetic clouds (Fermi mechanism).

Betatron mechanism. Consider a particle with velocity $v_\perp$ and mass m moving in a plane perpendicular to a magnetic field $H = H(t)$. The changing field induces an electric field $\vec{E}$, curl $\vec{E} = -1/c\dot{H}$, which causes a change in the kinetic energy of the particle. For slowly varying fields the magnetic moment $\mu = \dfrac{\pi a^2}{c}$ ($a = \dfrac{v_\perp}{\omega_g}$ Larmor radius, $\omega_g = \dfrac{eH}{mc}$ gyrofrequency) is a constant of motion, and so it follows that

$$1/2\, m v_\perp^2 = \mu H$$

i.e. $v_\perp$ is proportional to H. By this means an overall gain in velocity results, because during the time the particles travel from a region with positive H to a region with negative H, some redistribution of $v_\perp$ to $v_=$ occurs due to interactions with the interstellar gas. As a result, the energy gain is partly transferred to $v_=$ and so in the next deceleration process which effects only $v_\perp$, not all of the energy gain is cancelled out.

Fermi mechanism. A charged particle interacting with a moving magnetic cloud gains or loses kinetic energy depending upon whether the cloud velocity u is added to the velocity v of the particle or subtracted from it. After many such processes a net energy gain results.

In the simplest non-relativistic approach (Fig. 5.1), the energy gain in a head-on collision is the same as the energy loss in an overtaking collision. However, because head-on collisions are more probable, a net gain results.
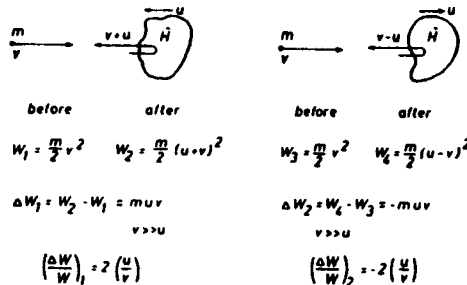
Fig. 5.1 The explanation of the Fermi mechanism

Let m be the number of magnetic clouds per unit volume and σ the cross-section for a collision between particle and magnetic cloud. Then assuming that $m/2$ clouds are moving in one direction, and $m/2$ in the opposite direction, the numbers of collisions per unit time will be

$$N_1 = m/2 \cdot \sigma (v + u) \quad \text{for head-on collisions} \quad \xrightarrow{v} \quad \xleftarrow{u}$$

$$N_2 = m/2 \cdot \sigma (v - u) \quad \text{for overtaking collisions} \quad \xrightarrow{v} \quad \xrightarrow{u}$$

The relative energy gain per unit time will be

$$\Delta W/W = (\Delta W/W)_1 N_1 + (\Delta W/W)_2 N_2$$
$$\Delta W/W = 2\,(u/v)\, m/2 \cdot \sigma (v + u) - 2\,(u/v)\, m/2 \cdot \sigma (v - u)$$
$$\Delta W/W = 2\, m \cdot \sigma \cdot u\, (u/v)^2$$

and the energy gain per collision

$$\Delta E = \frac{(\Delta W/W)}{N_1 + N_2} = 2\,(u/v)^2 \cdot E.$$

In the relativistic case it turns out that the energy gain is the same, i.e.

$$\Delta E = 2\,E\, u^2/c^2 = 2\,E\,\beta^2 .$$

After n collisions this becomes

$$\Delta E = 2\, n\, \beta^2\, E.$$

The average time between collisions, τ_c, is given by $\tau_c = l/v$, where l is the mean distance between two interstellar clouds and $v = c$ is the velocity of the particle. This leads to a change in energy between two collisions

$$dE/dt = 2\,\beta^2\, E\, (l/v) .$$

The number of collisions in time t is $n = t/\tau_c$, and the energy after the time t is given by

$$E(t) = E_0 \cdot \exp (2\, n\, \beta^2) = E_0 \cdot \exp (2\,\beta^2\, t/\tau_c) = E_0 \cdot \exp (t/t_c)$$

where $t_c = \tau_c / 2\,\beta^2 .$

As well as energy-gain processes, there are loss processes due to interactions with the interstellar matter and leakage out of the galaxy. If t_1 is the mean time for whichever is the dominant process, the probability of surviving to an age greater than t is

$$P(> t) = \exp (-t/t_1) .$$

Taking $u = 10^6$ cm s^{-1} as a typical cloud velocity and $l = 3 \times 10^{19}$ cm, then

$$dE/dt = 2 \times 10^{-18}\, E .$$

Assuming $E = 10^{12}$ eV. $dE/dt = 2 \times 10^{-6}$ eV s^{-1} or approximately
60 eV per year, the mean time between collisions is calculated to be

$$\tau_c = \frac{3 \times 10^{19}}{3 \times 10^{10}} = 10^9 \text{ s}.$$

If strong interactions with interstellar matter are the main energy-loss
process. then the interaction length λ is the dominant parameter. For an
interstellar density of $\rho = 10^{-25}$ g cm^{-3} λ is about 10^{26} cm, which
leads to a mean interaction time of $t_1 = \lambda/c \approx 3 \times 10^{16}$ s. If ionization is
regarded as the main process for energy loss, then the loss per unit time
dE/dt will be

$$- (dE/dt)_{ion} = - v\,(dE/dx)_{ion}$$

which for a proton of 10^{11} eV, leads to

$$- (dE/dt)_{ion} = 3 \times 10^{-7} \text{ eV s}^{-1}.$$

For high-energy particles an overall energy gain is possible. But at lower
energies the energy loss due to ionization exceeds the energy gain due to
the Fermi mechanism. For each particle, a minimum incident energy exists
above which the energy gain exceeds the loss. For protons this minimum
energy is $\sim$ 200 MeV and for iron $\sim$ 300 GeV.

5.3. Pulsars

A rotating neutron star with a high magnetic field induces strong electric
fields in which charged particles can be accelerated to high energies. Dur-
ing the evolution of a neutron star, the electrical conductivity of the stellar
material remains sufficiently high to maintain the original magnetic field.
This magnetic-flux conservation leads to intense surface fields of up to
10^{13} Gauss. If r_i denotes the initial radius and r_f the final radius of the
neutron star, and if H_i and H, denote the corresponding magnetic fields,
the following relation holds

$$H, = H_i\,(r_i/r_f)^2$$

which is approximately $H_f = 10^{10}\,H,$.

If the magnetic axis is inclined to the rotation axis by an angle α the star
will emit electromagnetic radiation and lose energy according to'

$$(- dE/dt)_1 = \frac{2}{3c^2}\,\mu_\perp^2\,\omega^4.$$

$\mu_\perp = \mu \sin\alpha$
μ magnetic moment
ω rotation frequency

This energy loss is balanced by a change in the rotational energy

$$(dE/dt)_2 = d/dt\,(I/2\,\omega^2) = I\omega\dot\omega.$$

I moment of inertia

Introducing the rotation period $P = T^{-1} = 2\,\pi/\omega$, the above equation
leads to

$$\mu_i^2 = \left(\frac{3c^2}{8\pi^2}\right) I \cdot P \cdot \dot P$$

and a surface magnetic field

$$H_s^2 = \frac{1}{\sin^2 -} \cdot \frac{6c^3}{4\pi^2} I \cdot P \cdot \dot P.$$

Calculations relating to neutron stars find that the moments of inertia lie
within the range $5 \times 10^{43} \leqslant I \leqslant 10^{45}$ g cm^2, and pulsar observations find
the limits $0.033 \leqslant P \leqslant 3.14$ s and $4 \times 10^{-13} \leqslant \dot P \leqslant 10^{-16}$.

Hence, surface magnetic fields of $10^{11} \leqslant H_s \leqslant 10^{13}$ Gauss are predicted.
The strong magnetic fields induce equally strong electric fields

$$\vec E = - 1/c\,[(\vec r, \vec\omega), \vec H].$$

in which cosmic-ray particles can be accelerated. In the case of the crab
pulsar with $P = 3.3 \times 10^{-2}$ s and $\dot P = 35$ ns/d, electric fields of 10^{10}
$\leqslant E \leqslant 10^{12}$ V cm^{-1} are calculated, which would be sufficient to accelerate
particles to cosmic-ray energies by linear acceleration.

A second acceleration mechanism is possible, because a rotating pulsar
generates intense low-frequency electromagnetic radiation which carries
away an enormous amount of energy. In the case of the crab pulsar
$(- dE/dt)_1 \approx 10^{38}$ erg s^{-1}. Particles can very efficiently couple to such
waves and obtain high relativistic energies. Modifications of this mecha-
nism by the inclusion of additional field components could accelerate
particles up to energies of 10^{21} e V.

Although the highest energies can be explained, many questions remain
unanswered;

(1) The electric field around the pulsar should pull charged particles
out of the surface leading to a dense magnetosphere. What changes
will this induce in the acceleration mechanism?

(2) Can the slope of the energy spectrum be reproduced by such a
model?

(3) Can the observed chemical composition of cosmic radiation be explained?

(4) Are the number of active pulsars enough to sustain the observed cosmic-ray flux?

(5) Are the majority of cosmic-ray particles below about 10^{11} eV produced by such processes?

5.4. Extragalactic origin

It would be very strange, indeed, if the milky way was the only galaxy containing cosmic radiation. If radio waves are a sign that cosmic radiation is present in a galaxy, then it can be concluded that other galaxies produce even more cosmic radiation. In addition to radio galaxies, the quasars are regarded as powerful sources of cosmic rays. It is possible that cosmic rays leak into intergalactic space from the various galactic sources (normal galaxies, radiogalaxies, quasars). Since such sources produce energy in the form of synchrotron radiation amounting to $\sim 10^{43}$ erg s^{-1}, which is about 10^5 more than is produced in the milky way, it can be concluded that cosmic radiation is a universal phenomenon, i.e. the cosmic-ray energy density is roughly constant throughout the whole universe. For an energy density of ~ 1 eV cm^{-3}, inside as well as outside the galaxy, a cosmic-ray production rate of $\sim 5 \times 10^{30}$ erg cm^{-3} s^{-1} is necessary if all losses are ignored. It follows that each cosmic-ray source has to generate about 10^{49} erg s^{-1} for the production of relativistic particles. This is about a factor 10^2 less than the energy emitted in the form of electromagnetic radiation. The universal model encounters difficulties in explaining such large amounts of energy.

It is not possible moreover, to regard the electron component to be of universal origin. The charge ratio of electrons to positrons has shown that the electrons should have the same origin as the protons and nuclei. However, if the hadronic component is of extragalactic origin, this source can. not be common to both hadrons and electrons. The extragalactic electrons interact with the photons of the intergalactic space and lose energy by the inverse Compton effect. This interaction takes place with the photons of the 3 K-radiation, producing X-radiation, with the photons of the star light, producing gamma radiation, and with the intergalactic gas producing gamma radiation via π^0-production. Electrons would lose all their energy by these processes and could not reach our galaxy. For example, an electron of 10^{10} eV loses about 50% of its energy in about 10^7 years by in-

teraction with the 3 K-radiation and therefore cannot travel more than about 10^{25} cm, a relatively small distance. If the electrons were produced in extragalactic sources, their energy spectrum would be expected to steepen rapidly above 10^{11} eV.

It is believed in some circles, that cosmic-ray particles with energies beyond 10^{17} eV are of extragalactic origin. A proton of momentum p, moving in a magnetic field H, travels along circular orbit perpendicular to the field with a Larmor radius

$$r = \frac{p\,(eV/c)}{300\,H\,(\text{Gauss})}\ \text{cm}.$$

For an interstellar field of 5×10^{-6} Gauss, a proton of 6×10^{17} eV has a Larmor radius of 6×10^{20} cm, which is comparable with the dimensions of the milky way, and so the particles cannot be stored within the magnetic field ot the galaxy. Furthermore, if they were of galactic origin they would show some anisotropy, indicating the direction of the source, in contrast to observations made with poor statistics.

It is plausible therefore, to construct a two-component model. The low-energy part of the cosmic-ray spectrum is of galactic origin and there is an extragalactic component which predominates at high energies as shown in Fig. 5.2.
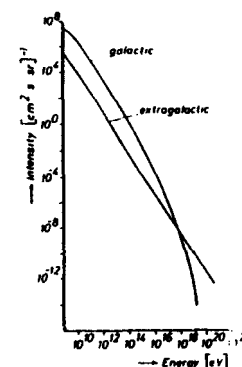

fig. 5.2 Two-component explanation of the primary emergy spectrum

5.5. Other sources

Magnetic A-stars. From observations of the Zeeman splitting of their ab-sorption lines, it can be deduced that objects of this kind have surface magnetic field strengths of $\geq 10^3$ Gauss. The rotation of such stars could

accelerate cosmic-ray particles in their electromagnetic fields, in a similar manner to pulsars. The maximum energy produced by such an acceleration mechanism would be around 10^{10} eV. These stars could he partly responsible for low-energy cosmic-ray particles.

White dwarfs. If white dwarfs are the early stages of pulsars, they could contribute to the low-energy part of the cosmic-ray spectrum in in a similar manner to magnetic A-stars if their magnetic fields are high enough. Since there are many such sources widely distributed throughout the galaxy, they could produce an appreciable amount of the low-energy component.

Novae. These objects could produce cosmic radiation by similar mechanism to supernovae. Although the energy released is only about 10^{-4} that of supernovae, they could make an appreciable contribution because they occur more frequently, about 100 per year.

Galactic center. Emission of radiation in several regions of the frequency spectrum is stronger from the galactic center than from other directions in the galaxy. In addition,there is evidence of violent emission of material from the galactic nucleus and so that this part of the galaxy is considered to be an important source of cosmic radiation,produced by a kind of supernova mechanism. If explosions occur in the galactic core every few times 10^7 years, a cosmic-ray production rate of about 10^{40} erg s^{-1} is possible.

References

Meyer. P.: Cosmic Rays in the Galaxy. Ann. Rev. Astron. Astrophys. 7 (1969) 1

Grewing. M., H. Heintzmann: The Origin of Cosmic Rays – New Interest in an Old Ouestion. Z. Naturwissenschaften 28a (1973) 369

Bruzek, A., H. Pilkuhn (eds.): Lectures on Space Physics. Dusseldorf: Bertelsmann Universitatsverlag 1973

Wolfendale, A.W.: Cosmic Rays at Ground Level. London: The fnstitute of Physics 1973

Coswik. R., P.6. Price: Origin of Cosmic Rays. Physics Today. Okt. 11971) 30

Hillas, A.M.: Cosmic Rays. Oxford: Pergamon Press 1973

Ginzburg. V. L.: The Astrophysics of Cosmic Rays. Scientific American 220 (1969) 51

Ginzburg. V. L., S. T. Syrovatskii: The Origin of Cosmic Rays. Oxford: Pergamon Press 1964

Ginrburg, V. L.: The Astrophysics of Cosmic Rays. Israel Program for Scientific Translations, Jerusalem (1969)

Pinkau, K.: Kosmische Gammastrahlen. Munchen: MPI-PAE/Extraterr. 83 (1973)

6. Interactions with matter

The behaviour of cosmic radiation in the earth's atmosphere and beneath its surface can be fully understood, only by an understanding of the basic interaction processes themselves. When primary cosmic-ray particles enter the atmosphere, strong interactions are predominant. Nuclear fragmentation processes also take place, similar to those which occur when the primary nuclei interact with interstellar matter. Some of the secondary particles produced in the atmosphere initiate multiple electromagnetic processes, which lead to widely distributed air showers. Most of the secondary particles are unstable and decay via weak interactions. A basic knowledge of interaction processes is clearly necessary, to understand cosmic-ray development .

6.1. Survey of the basic interaction processes

Interaction processes can be divided into four classes which involve,

(a)   the strong interaction, which is responsible for the binding of nucleons in nuclei and for many production processes,

(b)   the electromagnetic interaction,which exists between all particles with electric charges or magnetic moments,

(c)   the weak interaction, which is responsible for the radioactive decay of nuclei and the decay of many unstable particles, and

(d)   gravitation, which applies to all particles existing in the universe.

Interactions are characterized by their strength, i.e. the crosssection, their interaction time and their range. Typically, strong interactions correspond to the production of resonance particles, e.g.

$$\pi^+ + p \rightarrow N^* (1236) .$$

Examples of electromagnetic interactions are Compton scattering and pair production, whereas the most well-known weak interaction is beta decay.

Strong interactions are characterized by the coupling constant g, which is related to the Yukawa potential in the nucleus. Hence, the dimensionless coupling constant

$$K_s = g^2 / \hbar c \approx 10$$

is derived. The lifetime, τ, of strong interaction states is about 10^{-23} s and they have widths $= \hbar / \tau$ of 10 to 1000 MeV.

interaction	coupling constant	typical cross-section	typical interaction time	example
strong	$g^2/\hbar c \approx 10$	10^{-26} cm²	10^{-23} s	$p + n \to d$
electromagnetic	$e^2/\hbar c \approx 137^{-1}$	10^{-29} cm²	10^{-16} s	$e^- + e^+ \to 2\gamma$
weak	$G_F/\hbar c \approx 10^{-7}$	10^{-38} cm²	10^{-8} to 10^{-13} s	$n \to p + e^- + \bar{\nu}_e$
gravitation	$G_N m_p^2/\hbar c \approx 10^{-39}$			

Electromagnetic interactions are characterized by the Sommerfeld constant α, which corresponds to the coupling strength

$$K_e = \alpha = e^2/\hbar c = 1/137 .$$

Weak interactions involve the Fermi constant $G_F = 1.4 \times 10^{-49}$ erg cm^{-3} from which the dimensionless coupling constant

$$K_w = G_F/\hbar c \approx 10^{-7}$$

is derived. Finally, the coupling constant for the gravitational interaction, which is related to the Newton constant $G_N = 6.7 \times 10^{-8}$ cgs units, is given by

$$K_g = G_N m_p^2/\hbar c \approx 10^{-39} .$$

The principal parameters of the different types of interactions are given in the following table (Table 6.1).

6.2. Reaction kinematics

A comparison is often made of kinematical quantities in the Laboratory System (LS) and the Center-of-Mass System (CMS). Consider the interaction of an incident particle of momentum p, velocity v, and rest mass m_0, with a particle of the same rest mass (Fig.6.1). In the non-relativistic case, the kinetic energy available is

$$E_{LS} = 1/2 \, m_0 v^2 ,$$
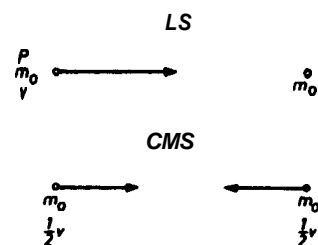
Fig.6.1: Transformation in a non-relativistic frame

in the Lab System, and

$$E_{CMS} = 1/2 \, m_0 (v/2)^2 + 1/2 \, m_0 (v/2)^2 = 1/4 \, m_0 v^2$$

in the Center-of-Mass System, thus

$$E_{CMS}/E_{LS} = 1/2 .$$

Only half of the energy of the incident particle is available for inelastic processes, i.e. for production of new particles.

In the relativistic case, which is more relevant to cosmic-ray interactions, the momentum of the incident particle is

$$p = mv = m_0 \gamma v ,$$

where

$$\gamma = \frac{1}{\sqrt{1 - \beta^2}}$$

is the Lorentz factor and $\beta = v/c$.

For an equivalent kinematical procedure, the following Lorentz-invariant relation will be used

$$\frac{1}{1 - \beta^2} - \frac{\beta^2}{1 - \beta^2} = 1$$

or

$$\gamma^2 - \beta^2 \gamma^2 = 1 .$$

Hence,

$$m_0^2 c^4 (\gamma^2 - \beta^2 \gamma^2) = m_0 c^4$$

or

$$m_0^2 c^4 \gamma^2 - p^2 c^2 = m_0^2 c^4 .$$

Since m_0 and c are constants, this equation is Lorentz-invariant. Now using the mess-energy equality

$$E = m c^2 = m_0 \gamma c^2 \approx m_0 c^2 + 1/2 \, m_0 v^2$$

it follows that

$$E^2 - p^2 c^2 = m_0^2 c^4 .$$

This relation is also Lorentz-invariant. Hence, for two systems

$$E'^2 - p'^2 c^2 = E^2 - p^2 c^2 = m_0 c^4 .$$

Consider now the two-body interaction in the relativistic case (Fig.6.2).

52
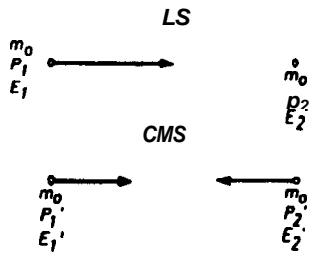
Fig.6.2: Transformation in a relativistic frame

We have

$$(E_1 + E_2)^2 - (p_1 + p_2)^2 c^2 = (E_1' + E_2')^2 - (p_1' + p_2')^2 c^2 .$$

Conservation of momentum gives

$$p_1' + p_2' = 0$$

and since the target particle is at rest in the Laboratory System, $p_2 = 0$.

Therefore, in the Laboratory System, it follows that

$$(E_1 + E_2)^2 - (p_1 + p_2)^2 c^2 = (E_1 + m_0 c^2)^2 - p_1^2 c^2$$
$$= E_1^2 - p_1^2 c^2 + m_0^2 c^4 + 2 m_0 E_1 c^2$$
$$= 2 (m_0 c^2)^2 + 2 m_0 E_1 c^2 .$$

From conservation of energy

$$E_1' + E_2' = E_{tot}' = E_{tot}^{CMS}$$

and since

$$E_1 + m_0 c^2 = E_{tot}^{LS}$$

the following relation is obtained

$$E_{tot}^{LS} = \frac{(E_{tot}^{CMS})^2}{2 m_0 c^2}$$

Example for pp-scattering:

$$m_0 c^2 \approx 1 \text{ GeV}$$

$$E_{tot}^{LS} = 30 \text{ GeV}$$

thus $E_{tot}^{CMS} = \sqrt{30 \cdot 2} \approx 8$ GeV. So only $E = E_{tot}^{CMS} - 2 m_p c^2 \approx 8 - 2 \approx$ ≈ 6 GeV is available for production processes.

At relativistic energies, the four-momentum $q = (p_x, p_y, p_z, iE)$ is the kinematical quantity usually used ($c = 1$). The four-momentum transfer in an inelastic reaction is derived in the following way. Assume that $P_0 (\vec{p}_0, iE)$ is the four-momentum of the incident particle, $P = (\vec{p}, iE)$ the
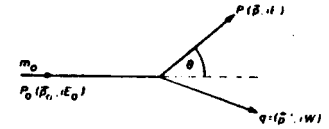
Fig.6.3: Four-momentum transformation

value for the scattered particle and $q = (\vec{p}', iW)$ the corresponding value for the target particle (Fig. 6.3). Using the relation

$$p^2 = (\vec{p})^2 + (iE)^2 = p^2 - E^2 = - m_0^2 c^4$$

the four-momentum transfer is

$$q^2 = (\vec{p}_0 - \vec{p})^2 - (E_0 - E)^2$$
$$q^2 = p_0^2 - 2 p_0 p \cos \Theta + p^2 - E_0^2 + 2 E E_0 - E^2$$
$$q^2 = (p_0^2 - E_0^2) + (p^2 - E^2) - 2 p_0 p \cos \Theta + 2 E E_0$$
$$q^2 = - 2 m_0^2 c^4 - 2 p p_0 \cos \Theta + 2 E E_0 .$$

For the case

$$m_0^2 c^4 \ll q^2 \text{ and } p^2 \approx E^2$$

it follows that

$$q^2 = - 2 p p_0 \cos \Theta + 2 p p_0$$
$$q^2 = 2 p p_0 (1 - \cos \Theta) = 4 p p_0 \sin^2 \frac{\Theta}{2} .$$

The four-momentum transfer to the target particle of mass, M_0, is also calculated ($c = 1$) as

$$q^2 = (0 - \vec{p}')^2 - (M_0 - W)^2$$
$$q^2 = (p'^2 - W^2) - M_0^2 + 2 M_0 W = - 2 M_0^2 + 2 M_0 W .$$

The kinetic energy of the target particle $T = W - M_0$ can be expressed in terms of the four-momentum transfer, q^2, as $T = q^2 / 2 M_0$.

6.3. Coulomb scattering

When a charged particle traverses matter, it undergoes electromagnetic interactions with both electrons and nuclei. The resultant angle of deflection in the CM-systems, Θ can be calculated by introducing an impact parameter b, which corresponds to the minimum distance of approach of the particle and the nucleus during the scattering process,

$$\tan \frac{\Theta}{2} = \frac{Z z e^2}{m v^2 b} .$$

Z   charge of the nucleus
ze, m, v   charge, mass and velocity of the incident particle

The differential cross-section for this elastic process is given by the Rutherford formula

$$d\sigma/d\Omega = 1/4 \left(\frac{Zz\,e^2}{pv}\right)^2 \left(\sin\frac{\Theta}{2}\right)^{-4} .$$

p momentum of the particle

In the relativistic case, the Rutherford formula is replaced by the Mott formula for spinless nuclei

$$\left(\frac{d\sigma}{d\Omega}\right)_{Mott} = \frac{Z^2 z^2 e^4 \cos^2\frac{\Theta}{2}}{4 p^2 \sin^4\frac{\Theta}{2}\left[1 + \frac{2p}{M_0}\sin^2\frac{\Theta}{2}\right]}$$

M_0 mess of the nucleus

The Rutherford formula regards the nucleus as point-like. When the spacial distribution of the electric charge and the magnetic moment of the target particle are taken into account, a form factor $F(q^2)$ is introduced and the cross-section becomes

$$d\sigma/d\Omega = \frac{Z^2 z^2 e^4 [F(q^2)]^2}{4 p^2 \sin^4\frac{\Theta}{2}}$$

For point-like nuclei $F(q^2) = 1$.

If the four-momentum transfer is mainly a function of momentum i.e. $E - E, \approx 0$, then

$$F(q^2) = \int \rho(r) \exp(i\vec{q}\vec{r}) \, d^3\vec{r}$$

where $\rho(r)$ is the charge distribution, the Fourier transform of $F(q^2)$. Thus

$$F(q^2) = \int \rho(r) \frac{\sin qr}{qr} 4\pi r^2 \, dr .$$

Taking a Yukawa distribution for $\rho(r)$,

$$\rho(r) = \rho_0 \exp(-\alpha r) \cdot \frac{1}{r},$$

the form factor becomes

$$F(q^2) - 4\pi \rho_0 \int \frac{e^{-\alpha r}}{2iq} (e^{iqr} - e^{-iqr}) \, dr$$

$$F(q^2) = 4\pi \rho_0 \frac{1}{a^2 + q^2} .$$

Normalization leads to

$$\alpha^2 = 4\pi \rho_0$$

and hence

$$F(q^2) = \frac{1}{1 + q^2/\alpha^2} .$$

For the scattering of an electron on a point-like proton with spin $s = 1/2\,\hbar$ and the magnetic moment $\mu = e\hbar/2 M_0 c$, the Dirac theory expresses the cross-section as

$$\left(\frac{d\sigma}{d\Omega}\right)_{Dirac} = \frac{e^4 \cos^2\frac{\Theta}{2}}{4 p^2 \sin^4\frac{\Theta}{2}\left(1 + \frac{2p}{M_0}\sin^2\frac{\Theta}{2}\right)} \cdot \left[1 + q^2/2 M_0^2 \cdot \tan\frac{\Theta}{2}\right] = \left(\frac{d\sigma}{d\Omega}\right)_{el} + \left(\frac{d\sigma}{d\Omega}\right)_{magn} .$$

This formula is an extension of the Mott formula. For large angles and large momentum transfers $(d\sigma/d\Omega)_{el} > (d\sigma/d\Omega)_{magn}$. Two form factors exist for each nucleon. An electric form factor, $G_E(q^2)$, due to the charge distribution, and a magnetic form factor $G_\mu(q^2)$, resulting from the distribution of anomalous magnetic moment. Thus, there are four nucleon form factors:

Electric form factor $G_E(q^2)$: $G_E^p(0) = 1$ G," (0) = 0

Magnetic form factor $G_M(q^2)$: $G_M^p(0) = \mu_p$ $G_M^n(0) = \mu_n$

where $\mu_p = 1.79\,\mu_B$, $\mu_n = -1.91\,\mu_B$ and $\mu_B = e\hbar/2 m_p c$, the nuclear magneto". The scattering formula which takes these form factors into account is the Rosenbluth formula

$$\frac{d}{d\Omega} = \frac{d}{d\Omega}\Big|_{Mott} \cdot \left[\frac{G_E^2 + q^2/4 M_0^2 \cdot G_M^2}{1 + q^2/4 M_0^2} + \frac{q^2}{4 M_0^2} \cdot 2 G_M^2 \tan\frac{\Theta}{2}\right]$$

$$\frac{d\sigma}{d\Omega} = \left(\frac{d\sigma}{d\Omega}\right)_{Mott} \cdot \left[A(q^2) + B(q^2) \tan^2\frac{\Theta}{2}\right]$$

where

$$A(q^2) = \frac{G_E^2 + q^2/4 M_0^2 \cdot G_M^2}{1 + q^2/4 M_0^2} \quad \text{and} \quad B(q^2) = \frac{q^2}{4 M_0^2} \cdot 2 G_M^2$$

Instead of the angular distribution of the scattered particle, the energy distribution of the recoil particle is sometimes measured. If an interaction occurs with an electron of an atom or molecule, the recoil electron is called a knock-on electron.

For the scattering of a particle of mass m and spin 1/2 on an atomic or molecular electron, the Bhabba formula is used

$$\sigma(E, E')\, dE' = 2\,\pi\,\frac{N}{A}\ Z\,\frac{m_0\, c^2}{\beta^2}\ \cdot\ ^{-1}\left[1-\beta^2\frac{E'}{E'_{max}}+\frac{1}{2}\left(\frac{E'}{E+\mu_0\, c^2}\right)^2\right] dE'.$$

E, μ_0 energy and mass of the incident particle
E' transferred energy
E'_{max} maximum energy transfer to the electron
m_0 mass of the electron
r_e classic electron radius

If the transferred energy E' is small compared with the maximum energy available, the following expression holds

$$(E, E')\, dE' = 0.3\,\frac{Z m_0 c^2}{A\,\beta^2}\ \frac{1}{E'^2}\, dE'$$

This formula is also called the Rutherford formula. Since $\sigma(E, E') \sim 1/E'^2$, the probability of producing high energy electrons is small. Electrons do exist, however, in the keV- and μeV-ranges called δ-rays and knock-on electrons respectively.

6.4. Bremsstrahlung

When a charged particle undergoes acceleration, electromagnetic radiation is emitted. Since the cross-section for this process, which is known as bremsstrahlung, is inversely proportional to the square of the mass of the particle, the process is important mainly for light particles such as electrons. However, in cosmic radiation and at high-energy accelerators, bremsstrah-' lung is important for heavier particles, such as muons. When a charged particle traverses matter, the mean energy loss due to bremsstrahlung is given by

$$\left(\frac{dE}{dx}\right)_{BS} = \frac{4\, e^4}{137\, c^4}\cdot\frac{N}{A}\ Z\,(Z+1)\,\frac{1}{\mu_0^2}\cdot E\,\ln\left(\frac{183}{Z^{1/3}}\right).$$

N Avogadro number
A, Z   atomic weight and atomic number of the medium
μ_0, E   mass and energy of the incident particle

This radiation loss increase; linearly with the energy E and inversely with the square of the mass μ_0. It is convenient to write

$$(-\, dE/dx)_{BS} = E\, X_0^{-1},$$

where

$$X_0^{-1} = \frac{4\, e^4}{137\, c^4}$$

$$\cdot\frac{N}{A}\ Z\,(Z+1)\,\frac{1}{\mu_0^2}\,\ln\left(\frac{183}{Z^{1/3}}\right).$$

If E_0 is the initial energy of the charged particle, its mean energy after travelling a distance x is given by

$$E = E_0\, \exp\,(-\, x/X_0).$$

Xo is called the radiation length, and is defined as the thickness of material in $g\,cm^{-2}$ required to reduce the energy E_0 by a factor e. Radiation lengths for electrons and muons in various materials are given in Table 6.2.

In the bremsstrahlung process, there is a high probability that a large fraction of the energy of the incident particle will be transferred to a single photon. It is possible for one particle to penetrate a given thickness of material without producing a bremsstrahlung photon, whereas another particle might dissipate a large amount of energy. Hence, large fluctuations occur in this process.

Independently of the energy of the emitted photon, the angular distribution of the bremsstrahlung is peaked about the value

$$\langle\Theta\rangle = 1/\gamma = \frac{M_0\, c^2}{E}$$

Table 6.2: Radiation length and critical energy for various materials

material	(units)	Fe	Cu	Pb	Al	Air
radiation length X_0 (e)	g cm^{-2}	13.8	12.8	6.3	23.9	37.8
	cm	1.75	1.43	0.55	8.91	2.93×10^4
critical energy ϵ (e)	MeV	24	22	7.8	49	84
radiation length X_0 (μ)	g cm^{-2}	5.9×10^5	5.5×10^5	2.7×10^5	1.0×10^6	1.6×10^6
	cm	7.5×10^4	6.1×10^4	2.4×10^3	3.8×10^5	1.3×10^8
critical energy ϵ (μ)	GeV	10^3	9.4×10^2	3.3×10^2	2.1×10^3	3.6×10^3

Ionization loss (see Chapter 6.11) and bremsstrahlung are the dominant mechanisms for the energy loss of charged particles. In the relativistic region, the ionization loss attains an approximately constant value while the bremsstrahlung loss continues to increase with energy. The energy at which both losses become equal, i.e.

$$(- dE/dx)_{ion} = (- dE/dx)_{BS}$$

is called the critical energy ϵ. Some values of ϵ for electrons and muons are given in Table 6.2.

6.5. Multiple scattering

For an elastic scattering process in which the angle of deflection is small, the Rutherford formula can be replaced by

$$\frac{d\sigma}{d\Omega} = \left(\frac{2 Z z e^2}{pv}\right)^2 \frac{1}{\Theta^4} \ .$$

A charged particle traversing a layer of material suffers many small angular deviations (Fig. 6.4), which combine to give an overall mean scattering

Fig.6.4: Explanation of multiple scattering

angle. The angular distribution of this multiple scattering process is approximately Gaussian, and given by

$$P(\Theta)\, d\Theta = \frac{\exp\left(-\dfrac{\Theta^2}{2 \langle \Theta^2 \rangle}\right)}{\sqrt{2 \pi \langle \Theta^2 \rangle}} \ d\Theta$$

The root mean square projected angle is

$$\langle \Theta^2 \rangle = \frac{z^2}{2}\left(\frac{E_s}{pc\beta}\right)^2 \frac{x}{X_0}$$

z charge of the particle
E_s = 21 MeV
x/X_0 thickness of material in radiation lengths

In addition to an angular deviation, a projected lateral deviation $\langle y^2 \rangle$ is produced (Fig.6.4), which also follows an approximately Gaussian distribution,

$$\langle y^2 \rangle = \frac{z^3}{3}\left(\frac{E_S}{pc\beta}\right)^2 \frac{x^3}{X_0} = \frac{x^2}{3} \langle \Theta^2 \rangle$$

6.6. Photoelectric effect

High-energy photons interact with matter by three main processes;

(1) Photoelectric Effect   (PE)
(2) Compton Scattering   (CS)
(3) Pair Production   (PP)

The interactions of photons with matter, differ from those of charged particles in that photons are completely absorbed or scattered by large angles. The attenuation of a beam of photons follows an exponential law

$$I = I_0 \exp (- \mu x) \ .$$

μ absorption coefficient
I_0 intensity of the incident beam

The absorption coefficient is the sum of 3 components corresponding to the above 3 processes

$$\mu = \mu_{PE} + \mu_{CS} + \mu_{PP} \ .$$

In the photoelectric effect, the photon is absorbed by an atom and an energy

$$E = h\nu - B$$

B binding energy

is transferred to an electron. For a K-shell electron in a heavy atom

$$B = B_K = \hbar R (Z - 1)^2 \ .$$

R Rydberg frequency
Z atomic number

The cross-section for the photoelectric process changes significantly as the incident energy crosses an absorption edge. Far from the absorption edge, the Born approximation for a K-shell electron gives

$$\sigma \propto Z^5/(\hbar\nu)^{3.5} \ .$$

This process is dominant in heavy elements.

6.7. Cornpton scattering

The photoelectric effect is most important in the low-energy region, i.e. for E = 0.01 to 1 MeV, but at energies above 1 MeV the Compton effect becomes dominant. The latter inelastic process involves a transfer of energy by means of a photon to an atomic electron. As a result, the wavelength of the photon is shifted to a lower value. The change in wavelength as a function of the scattering angle is given by

$$\Delta\lambda = \lambda' - \lambda = \frac{h}{m_e c}\,(1 - \cos\Theta)$$

$$\lambda' - \lambda = 2\,\Lambda\,\sin^2\frac{\Theta}{2}$$

where $\quad\dfrac{h}{m_e c} = \Lambda = 2.4 \times 10^{-10}\ \text{cm}$,

the Compton wavelength of the electron.

In the relativistic case, the cross-section is given by the Klein-Nishina formula

$$\sigma_{CS} = 2\,\pi\,r_e^2\left[\frac{1+\epsilon}{\epsilon^2}\left|\frac{2(1+\epsilon)}{1+2\epsilon} -- \frac{1}{\epsilon}\ln(1+2\epsilon)\right| + \frac{1}{2\epsilon}\ln(1+2\epsilon) - \frac{1+3\epsilon}{(1+2\epsilon)^2}\right]\ .$$

$\dfrac{e^2}{m_e c^2} = r_e = 2.8 \times 10^{-13}\ \text{cm}$ classical electron radius

$\epsilon = h\nu/m_e c^2$ reduced photon energy

At high energies, the cross-section varies roughly as $\sigma_{CS}\ \alpha\ Z/\epsilon$ and is proportional to the number of electrons Z.

Of considerable astrophysical significance is the inverse Compton effect. In this process, a high energy electron with energy E collides with a photon of energy $E_{ph} = h\nu$ and transfers some of its energy, thereby increasing the energy of the photon. In the rest frame of the electron, the final photon energy, E'_{ph}, is given by

$$E'_{ph} = E_{ph}\,(1 - \beta\cos\Theta)\,\frac{E}{m_e c^2}\ ,$$

β velocity of the electron
Θ angle between photon and electron

In the Thomson limit ($\gamma = E/m_e c^2 \gg 1$ and $\gamma E_{ph} \ll m_e c^2$), this expression becomes $E'_{ph} = \gamma^2 E_{ph}$. This process is equivalent to the usual Compton scattering of a photon of energy E'_{ph}.

In space, electrons interact with starlight and the 3 K-radiation by the inverse Compton effect. Using typical values of $E_{ph} = 10^{-3}$ eV for the 3 K-radiation and 1 eV for star light, it follows that electrons require an energy of 50 GeV in the case of the 3 K-radiation and 2 GeV in the case of star light to produce a photon of energy $\sim$ 10 MeV.

6.9. Pair production

If the energy of a photon is more than twice the rest energy of an electron, i.e. $E \geqslant 2\,m_e c^2 = 1.02$ MeV, electron-positron pair production can occur. In order to conserve momentum and energy, a nucleus or less frequently a bound electron is taking up the recoil.

The pair-production process is the inverse process of bremsstrahlung (Fig.6.5). The change from bremsstrahlung to pair production involves only a reversal of the sign of one electron and the momentum, and so the cross-sections differ only by kinematical factors.

The cross-section depends upon the screening effect of the atomic electrons. If this screening is neglected the cross-section is given by

$$\sigma_{PP} = \frac{1}{137}\,r_e^2\,Z^2\left(\frac{28}{9}\ln 2\,\epsilon - \frac{218}{27}\right)\ \text{in cm}^2/\text{atom}.$$

$$\sigma_{PP} \propto Z^2 \ln E_\gamma\ .$$

r_e classical electron radius
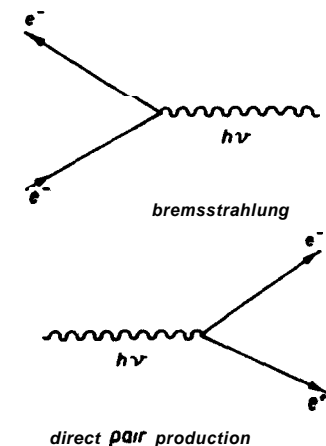ϵ reduced photon energy

Fig.6.6: Diagram of bremsstrahlung and pair-production processes

bremsstrahlung

direct pair production

When the screening is taken into account, the cross-section becomes

$$\sigma_{PP} = \frac{r_0^2}{137} Z^2 \left(\frac{1}{9} \ln \frac{183}{Z^{1/3}} - \frac{\sim}{27} \right) \text{ in cm}^2/\text{atom.}$$

$$\sigma_{PP} \propto Z^2 \ln Z^{1/3}$$

Here, there is no dependence on the photon energy.

In the case when an atomic electron is the recoil partner, the cross-section is given by

$$\sigma_{PP} = \frac{r_e^2}{137} \left(\frac{28}{9} \ln 2E_\gamma - 11.3 \right) \propto \ln E_\gamma \text{ in cm}^2/\text{atom.}$$

The total cross-section is approximately proportional to $\sim Z^2 \cdot \ln E_\gamma$.

The mean opening angle of an electron-positron pair is

$$\langle \Theta \rangle \approx m_e c^2 / E_\gamma .$$

Since the cross-section is proportional to $r_e^2 \sim e^4/m^2 c^4$, the muon pair production cross-section is a factor $m_e^2/m_\mu^2 = 4.28 \times 10^4$ smaller than for electron-pair production.

An energetic charged particle can also undergo pair production by means of virtual photons. In the simplest case, this is calculated by the Williams-Weizsacker method.

A moving charged particle carries with it, time-dependent electric and magnetic fields as considered from a fixed point in space, i.e. $\vec{E} = \vec{E}(t)$, $\vec{H} = \vec{H}(t)$. By means of a Fourier transformation the time dependence can be transformed to a frequency dependence $\vec{E} = \vec{E}(\nu)$, $\vec{H} = \vec{H}(\nu)$.

The electromagnetic energy of the field acting at a fixed point can be expressed in terms of the Poynting vector $\vec{S}$, which corresponds to an effective virtual photon field

$$|\vec{S}| = \frac{c}{4\pi} |[\vec{E}(\nu) \times \vec{H}(\nu)]| = \sum_\nu p(\nu) h\nu$$

$h\nu$ energy of the virtual photon
$p(\nu)$ probability of energy $h\nu$

The number of virtual photons with energy between E_γ ($= h\nu$) and $E_\gamma + dE_\gamma$ associated with a charged particle of energy E is given by

$$p(E_\gamma, E) \, dE_\gamma = \frac{2\alpha}{\pi} \frac{dE_\gamma}{E_\gamma} \left(\ln \left(\frac{E}{E_\gamma} \right) - 0.38 \right) .$$

The cross-section for energy transfer E_γ in the collision is thus

$$\frac{d(E, E_\gamma)}{dE_\gamma} = \sigma_\gamma(E_\gamma) \, p(E_\gamma, E) .$$

σ_γ cross-section for photo production

The cross-section for direct pair production by a charged particle is difficult to calculate, because there are four particles in the final state. For the case of no screening it can be expressed as

$$\sigma = \frac{4}{3\pi} Z^2 \alpha^2 r_e^2 \left[\frac{7}{9} \ln^3 \left(\frac{E, E_\gamma}{Mc^2} \right) - C_1 \ln^2 \left(\frac{E, E_\gamma}{Mc^2} \right) + \right.$$
$$\left. + C_2 \ln \left(\frac{E, E_\gamma}{Mc^2} \right) \right]$$

E, E_γ, M energy and mass of incident particle
C_1, C_2 constants

6.9 Cerenkov radiation

A particle moving through a dielectric medium with a velocity v, which is greater than the velocity of light in the medium $v_s = c/n$ (c velocity of light in vacuum, n refraction index) radiates and loses energy. This energy loss is due to a polarization of the neighbouring atoms and molecules along the particle trajectory. Electric dipoles are created and give rise to a resultant field which is zero for $v < c/n$ but finite for $v > c/n$.

When a particle moves from A to B (see Fig. 6.6) with a velocity $v > c/n$, Cerenkov radiation is emitted which, according to Huyghens' principle, adds up to form the wave front CB. During the time in which the particle moves from A to B, the electromagnetic radiation propagates from A to C. The time taken to traverse the distance AB is

$$t = AB/v ; \quad v > c/n = v_s ; \quad v < c$$

while for the propagation of the light from A to C, the time taken is
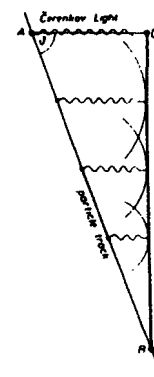
$$t = AC/v_s = (AC/c) \cdot n .$$

Fig.6.6: Explanation of Cerenkov radiation

Thus, the angular dependence follows

$$\cos \vartheta = 1/n\beta \; ; \quad \beta = v/c \; .$$

The velocity is a minimum for $\vartheta = 0$, i.e. $\beta_{min} = 1/n$. There exists a maximum emission angle for each medium

$$\vartheta_{max} = arc \, (\cos 1/n) \, .$$

Because $|\cos \vartheta| \leqslant 1$ then $n \geqslant 1/\beta$, and so the condition $\beta = 1$ leads to $n = n(\nu) > 1$. This condition is only fulfilled for a limited frequency range. The total energy radiated per unit length of trajectory, for frequencies with $\beta n \geqslant 1$, is given by

$$- dE/dx = \frac{4 \pi^2 z^2 e^2}{c^2} \int (1 - 1/\beta^2 n^2) \, \nu \, d\nu$$

ν frequency of the emitted radiation
ze charge of the incident particle

For $\beta = 1$, in water, $- dE/dx = 400$ eV/cm for visible light ($A = 4 \times 10^{-5}$ to 7×10^{-5} cm), which corresponds to the emission of about 200 photons per cm.

Because $- dE/dx \sim 1/\lambda$, the energy radiated per wavelength is $\sim 1/\lambda^2$, which is the reason why Cerenkov radiation is emitted preferably in the short wave region (blue light).

6.10.   Transition   radiation

In heterogeneous media, emission of photons is possible even when the conditions for emission of Cerenkov radiation do not exist. Such a process occurs when a charged particle crosses from one medium with dielectric constant ϵ_1 to another medium with value ϵ_2. At the interface of the two media, energy is lost and electromagnetic radiation, known as transition radiation, is emitted. This effect is due to a modification of the electromagnetic field at the interface, which causes some of the field energy to be shaken off as electromagnetic radiation. The energy of transition radiation emitted per unit solid angle and per unit frequency, from an interface between vacuum, $\epsilon_1 = 1$, and a medium of dielectric constant $\epsilon_2 = \epsilon$ is given by

$$\frac{d^2 E}{d\Omega \, d\omega} = \frac{e^2}{\pi^2 c} \frac{\beta^2 \sin^2 0 \, \cos^2 0}{(1 - \beta^2 \cos^2 \Theta)^2} \times$$

$$\left[\frac{(\epsilon - 1) (1 - \beta^2 \mp \beta \sqrt{\epsilon - \sin^2 \Theta}}{(\epsilon \cos \Theta + \sqrt{\epsilon - \sin^2 \Theta}) (1 \mp \beta \sqrt{\epsilon - \sin^2 \Theta}} \right]^2 ,$$

where

$$\epsilon (\omega) = 1 - \frac{\omega_p^2}{w + i\delta}$$

is the dielectric constant and

$$\omega_p^2 = \frac{4 \pi N_e^2}{m_e}$$

is the plasma frequency.

For   aluminium

$$(\hbar \omega_p)_{Al} \approx 3 \, 4 \; \text{eV}$$

$$\hbar \delta \approx 0 \, . \, 2 \; \text{eV}$$

N_e number of electrons per unit volume
m_e mass of electron
Θ angle between incident trajectory and emitted radiation
$-$ sign: forward emission
$+$ sign: backward emission

The dielectric constant ϵ is a complex quantity. The frequency of the transition radiation increases with γ, the Lorentz factor of the particle, up to a value of $\gamma \omega_p$. Thus, a particle with $\gamma = 10^3$ produces radiation with energies up to 34 keV for Al.

Integration over all angles for $\beta = 1$, gives the following expressions for the total energy emitted in the optical region E_{opt} and the X-ray region E_x :

$$E_{opt} = \frac{2 e^2}{c} \left(\ln \gamma - \frac{3}{2} \right) \Delta \omega$$

$$E_x = \frac{2 e^2 \omega_p}{3c} \gamma$$

The probability for emission of a photon from a single interface is extremely small, i.e. about 1%. The emission angle Θ_{max} for the maximum intensity is given by $\Theta_{max} \sim 1/ $.

A minimum thickness of material must be traversed before transition radiation can be created. This formation zone T_f is given by

$$T = \frac{c}{\omega} \frac{1}{(1/\gamma)^2 + \frac{1}{2}\left(\frac{\omega_p}{\omega}\right)^2}$$

6.11. Energy-loss relation

When charged particles traverse matter, they lose energy mainly by ionization and excitation, and in addition at higher energies, by direct pair production, bremsstrahlung, and nuclear interactions. The Bethe-Bloch formula gives the energy loss per unit thickness, due to ionization and excitation in collisions with atomic electrons

$$(- dE/dx)_{BB} = \frac{4 \pi N Z z^2 e^4}{m_e \beta^2 c^2 A} \left[\ln\left(\frac{2 m v^2}{I(1 - \beta^2)}\right) - \beta^2 - D \right]$$

N   Avogadro number
Z, A   atomic number and weight of the material traversed
ze, β charge and velocity of the incident particle
D   density effect
I   effective ionization potential averaged over all electrons. $I \approx 10\ Z$ in eV.

The Bethe-Bloch formula applies to heavy spinless particles. For electrons, the spin has to be taken into account which gives rise to an extra term, but the energy loss is only a few percent less than for heavy particles.

The following important facts can be deduced from the energy-loss relation:

(1) The energy loss is proportional to z^2 of the incident particle and inversely proportional to its velocity β^{-2}, i.e. $- dE/dx \propto z^2 / \beta^2$.

(2) There is only a weak dependence on the material traversed
$$- dE/dx \propto Z/A$$
Near the minimum of energy loss, $- dE/dx$ has the value 2 MeV g^{-1} cm^2 for singly charged particles.

(3) Expressed in terms of the velocity β, the energy-loss relation is the same for all particles, independent of their masses. **Fig.6.7a** shows the
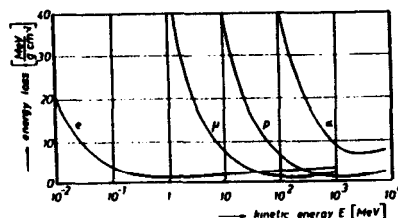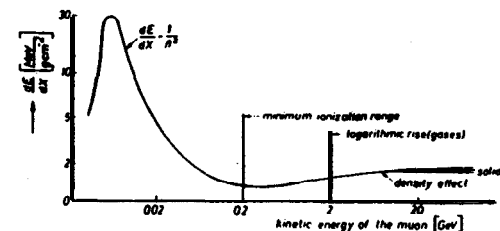
Fig.6.7a: Energy-loss relation for various particles

Fig.6.7b: Energy-loss relation for muons

energy-loss relation for different particles as function of energy and Fig.6.7b gives the detailed energy-loss relation for muons.

At low velocities, the energy loss is determined by the β^{-2} term, but at higher energies, the logarithmic term becomes important and leads to a weak rise beyond a minimum in the curve. The logarithmic rise flattens at even higher energies due to a polarization of the medium and produces shielding effects which reduce the rate of energy loss. This density effect is proportional to the electron concentration in the medium and is related to its dielectric properties. It is more important therefore for solids and liquids than for gases, and is expressed as

$$D = \ln \gamma^2 - \ln (I/\hbar \omega_p) - 1.$$

ω_p plasma frequency

The energy loss of a charged particle gives rise to a mean range in a homogeneous medium and hence by measuring this mean range, the energy of the particle can be obtained. The mean range is derived from the energy-loss relation

$$R = \int_E^0 \frac{dE}{(- dE/dx)} = \int_0^E \frac{dE}{f(E)}$$

where $f(E) = (+ dE/dx)_{BB}$.

For relativistic particles, the logarithmic rise can be neglected, so that $f(E) \approx$ const, and hence, $R =$ const $\cdot E$. In the non-relativistic region $f(E) \sim 1/v^2 \sim 1/E$ and so $R =$ const $\cdot E^2$. For intermediate velocities $(0.1 \leqslant \beta \leqslant 0.7)$ the empirical power-law relation $R =$ const $\cdot E^{1.75}$ holds for medium-weight elements.

At ultra-relativistic energies, in addition to the ionization loss, energy losses due to Cerenkov radiation, direct pair production (PP), bremsstrahlung (BS), and nclear interactions (NI) are important. In heavy elements, the energy loss due to Cerenkov radiation is less than 1% of the ionization

loss. The rate of energy loss, when these other effects are included can be expressed by the relation

$$-f(E) = -dE/dx = a + bE + c \cdot \ln E,$$

where $\quad a + c \cdot \ln E$ is the ionization loss

and $\quad b = b_{BS} + b_{PP} + b_{NI}$.

The values b_{BS}, b_{PP} and b_{NI} are related to the cross-sections for bremsstrahlung, direct pair production and nuclear interactions. Since these cross-sections depend on the mass of the incident particle, the energy loss due to b becomes important at increasingly higher energies for increasingly higher mass particles. The values of b are slowly varying functions of E, as shown in Fig.6.8 for high-energy muons.
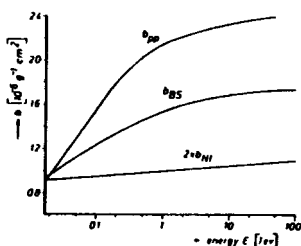

Fig.6.8: Energy dependence of b
(After Kobayakawa, K.: 13. Conference on Cosmic Rays. Denver (1973))

For standard rock, which is defined as a medium with $Z/A = 0.5$. $Z^2/A = 5.5, Z = 11$ and $\rho = 2.65$ g cm^{-3}, the approximate energy-loss relations are

$$(- dE/dx)_{BS} = 1.77 \times 10^{-6} E \quad \text{in MeV g}^{-1} \text{cm}^2$$
$$(- dE/dx)_{PP} = 2.40 \times 10^{-6} E \quad \text{in MeV g}^{-1} \text{cm}^2$$
$$(- dE/dx)_{NI} = 0.21 \times 10^{-6} E \quad \text{in MeV g}^{-1} \text{cm}^2$$
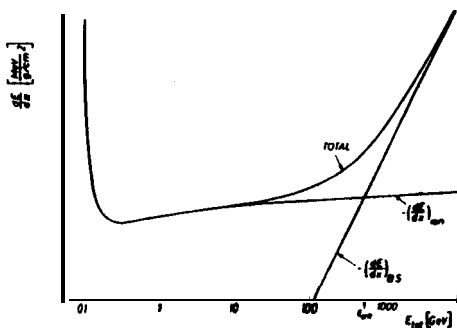

Fig.6.9: Total energy-loss relation

and the total energy-loss relation is

$$- dE/dx = 1.84 + 4.38 \times 10^{-6} E + 0.076 \log E.$$

It is shown in Fig.6.9.

When the logarithmic term in the total energy-loss relation is neglected, a relatively simple range-energy relation is obtained

$$R(E) = \int \frac{1}{f(E)} dE$$

$$R(E) = \int \frac{1}{a + bE} dE = (1/b) \ln (1 + b/a \cdot E)$$

or $\quad E = a/b [\exp (bR) - 1]$

$\quad\quad E \approx (a/b) \exp (bR)$.

The range-energy curves for standard rock and sea water $(Z/A = 0.553, Z^2/A = 3.26)$ are given in Fig.6.10.

The range-energy relation applies to mean values, whereas the actual rate of energy loss for a single particle, fluctuates considerably around this mean. Even at low energies, where only the Bethe-Bloch formula applies, fluctuations exist for large energy transfers, due to the small value of the cross-sections. These fluctuations are called Landau fluctuations and follow approximately a Gaussian distribution. At high energies, the fluctuations are mainly due to the bremsstrahlung process, because the energy loss in a single event can be a significant fraction of the total energy of the particle.
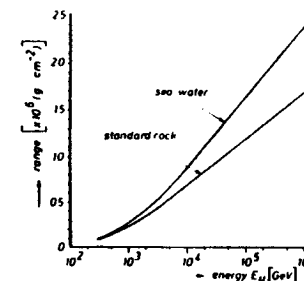

Fig. 6.10: Range-energy relation for standard rock
(After Kobayakawa. K.: 13. Conference on Cosmic Rays, Denver (1973))

References

Bruzek, A., H. Pilkuhn (eds): Lectures on Space Physics.
Dusseldorf: Bertelsmann Universitatsverlag 1973

Hayakawa. S.: Cosmic-Ray Physics.
New York: Wiley-Interscience 1969

Perkins, D. H.: Introduction to High-Energy Physics.
Reading. Massachusetts: Addison Wesley Publ. Comp. 1972

Yuan, Luke C. L.: Recent Progress in the Transition Radiation Detector Techniques.
Intern. Conf. on Instrumentation for High-Energy Physics, Frascati (1973)

Rossi, B.: High-Energy Particles.
Englewood Cliffs: Prentice-Hall 1954

7. Basic features of the elementary particles

This chapter contains a short review of the most important features of elementary particles and high energy interactions. It is intended only to give definitions, to summarize the relevant facts and to present the latest features of high-energy interactions measured at accelerators, in as far as they are relevant to cosmic ray physics.

7.1. Classification of elementary particles

Elementary particles are characterized by properties such as mass, lifetime, spin, parity, charge and interaction behaviour. On the basis of general arguments they can be classified according to their behaviour in terms of statistics. Particles with half-integer spin, fermions, obey Fermi-Dirac statistics, and those with integer spin, bosons, obey Bose-Einstein statistics.

The fermions include all the baryons, particles with mass $m \geqslant m_p$ (m_p proton mass), and the leptons, particles with mass $m \leqslant m_\mu$ (m_μ muon mass). The bosons include the photon and all the mesons. From this broad basis the following crude classification can be made:

(1) Photon. Mass zero, stable, spin = 1 A.

(2) *Leptons.* Electrons e^+, e^-; muons μ^+, μ^-; electron-neutrinos ν_e, $\bar{\nu}_e$; muon-neutrinos ν_μ, $\bar{\nu}_\mu$.

(3) *Mesons.* Pions π^+, π^o, π^-; kaons K^+, K"; eta particle η^o.

(4) *Baryons.* Nucleons (proton p, neutron n); lambda particle Λ^o; sigma particles Σ^+, Σ^o, Σ^-; xi particles Ξ^o, Ξ^-; omega particle Ω^-.

The elementary particles may be further grouped into different families according to their interaction behaviour. The photon takes part in all electromagnetic and some strong interactions. In the latter case it behaves as a mixture of vector mesons (ρ, ω, ϕ), a concept known as vector meson dominance. The family of leptons are responsible for weak interactions, and in addition the electron and muon interact electromagnetically.

The mesons are strongly interacting particles, with integer spin and masses greater than the muon mass. The baryons are also strongly interacting particles, with half-integer spin and masses greater than or equal to the nucleons. Particles in both families, the mesons and the barYons, are called hadrons.

Besides mass, lifetime, and decay mode, the particles have additional properties known as quantum numbers, which are characteristic of the differ-

ent families. Antiparticles have quantum numbers of the opposite sign to particles.

Baryon number. All baryons have an additive quantum number B, the baryon number which has the value + 1; the antibaryons have B = − 1; other particles have B = 0. This quantum number is additively conserved in all interactions, for example

$$p \ + \ \bar{p} \ \rightarrow \ \pi^+ \ + \ \pi^- \ + \ \pi^o$$

$$B = + 1 \qquad -1 \qquad 0 \qquad 0 \qquad 0$$

is an allowed interaction, whereas

$$p \ + \ \bar{p} \ \rightarrow \ p \ + \ \pi^-$$

$$B = + 1 \qquad -1 \qquad + 1 \qquad 0$$

is forbidden.

Lepton number. e^-, ν_e carry the lepton number $L_e = + 1$, whereas the anti-leptons $e^+, \bar{\nu}_e$ have $L_e = - 1$; all other particles have $L_e = 0$. Correspondingly, μ^-, ν_μ carry the lepton number $L_\mu = + 1$ and $\mu^+, \bar{\nu}_\mu$ have the number $L_\mu = - 1$. Lepton number must also be conserved, for example, the reaction $\pi^+ \rightarrow \mu^+ + \nu_\mu$ is allowed, but the reaction $\pi^+ \rightarrow \mu^+ + \gamma$ is forbidden. Also the reaction $\nu_e + n \rightarrow e^- + p$ is allowed, but the reaction $n \rightarrow p + e^-$ is forbidden.

Isotopic spin. Hadrons are further classified according to interaction behaviour, independently of their electric charge. Thus charge multiplets are introduced. The proton and the neutron are regarded as different states of the nucleon, characterized by the isotopic spin $I = 1/2$. The third component of I has different values for the proton $(I_3 = + 1/2)$ and the neutron $(I_3 = - 1/2)$. The charge multiplicity is given by

$$M_{ch} = 2 I + 1 .$$

The pion triplet π^+, π^o, π^- has $M_{ch} = 3$, corresponding to isotopic spin I = 1, and components $I_3 = + 1$ for $\pi^+, I_3 = 0$ for π^o, and $I_3 = - 1$ for π^-. The kaons like the nucleons, consist of a charge doublet K', K". In strong interactions, both I and I_3 are conserved as additive quantum numbers, for example

$$\pi^+ + p \rightarrow \Sigma^+ + K^+$$

I	1	1/2	1	1/2
I_3	+ 1	+ 1/2	+1	+ 1/2

In electromagnetic interactions only I_3 is conserved, for example

$$\Sigma^o \rightarrow \Lambda^o + \gamma$$

I	1	0	0
I_3	0	0	0

whereas for weak interactions, such as nonleptonic decays of strange particles, the selection rule I = 1/2, is generally obeyed, for example

I		$\rightarrow$ p	+ π^-
	0	1/2	1

I	Σ^-	$\rightarrow$ n	+ π^-
	1	1/2	1

Strangeness. Hadrons can be divided into two categories, strange and non-strange particles. Non-strange particles are the nucleons and the pions; strange particles are the kaons and the hyperons. Strangeness S, is an additive quantum number which is conserved in strong interactions. It is related to the charge Q, the baryon number B, and the third component of isotopic spin I_3, by

$$Q = 1/2 (B + S) + I_3 .$$

Thus, K^- has S = − 1, Λ has S = − 1 and Ω^- has S = − 3. The reaction

$$K^- + p \rightarrow \Lambda + \pi^o$$

$$S \quad -1 \quad 0 \quad -1 \quad 0$$

is an example of conservation of S. Instead of S, the hypercharge $Y = S + B$, is sometimes used.

For weak interactions of strange particles, the selection rule S = ΔQ (i.e. change in charge equals change in strangeness for hadrons) applies, for example the decay

$$K^o \rightarrow \pi^- + e^+ + \nu_e$$

$$S \quad +1 \qquad 0$$

$$Q \quad 0 \qquad -1$$

is allowed, but the decay

$$K^o \rightarrow \pi^+ + e^- + \nu_e$$

$$S \quad +1 \qquad 0$$

$$Q \quad 0 \qquad +1$$

is suppressed.

Parity. An important concept in physics is behaviour under inversion of all space coordinates or under reflection, i.e. inversion of just one coordinate. The laws of classical physics remain invariant under this operation. When the parity operation is applied to the wave function of a system by means of the parity operator P, its sign may or may not be changed, i.e. there exist two eigenvalues ± 1. Thus

$$P \psi(r) = \psi(-r) = (\pm 1) \psi(r)$$

For the wave function $\psi_l(r)$ describing a particle with orbital angular momentum hl, moving in a spherically symmetric potential

$$\psi_l(-r) = (-1)^l \psi_l(r)$$

The total parity of the system is composed of the orbital part $(-1)^l$ and the intrinsic parity of the particle. Intrinsic parities are determined via conservation laws for strong interactions. Parity is a multiplicative quantum number which is conserved in strong and electromagnetic interactions, but violated in weak interactions.

Charge conjucation. The operator C interchanges particles and antiparticles; it reverses the signs of the charge and the magnetic moment of a particle. When applied to the wave function, it gives the eigenvalues ± 1. Classical laws are invariant under charge conjugation, e.g. the Maxwell equations. The C-operator changes in addition to the charge the baryon number, the third component of isotopic spin and the strangeness. For a system of particles, $C = (-1)^{l+s}$, where l is angular momentum and s the spin of the total system. Charge conjugation is conserved in strong and electromagnetic interactions, but violated in weak interactions.

CP-invariance. If parity and charge conjugation are conserved, then their product CP is also conserved. This means that laws are invariant if they are inverted under parity and if simultaneously, particles are exchanged for antiparticles. CP-conservation holds for most weak interactions, but a weak violation is observed in K°-decay.

G-parity. The charge conjugation operator C, only has eigenvalues for neutral systems, such as π°, y, e^+ and e^-. It is useful therefore, to introduce an equivalent operator for charged systems, the G-operator, which corresponds to the C-operator acting in isotopic spin space.

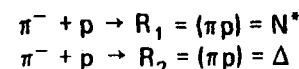$$G = C \, e^{i\pi I},$$

where I_2 is the second component of isotopic spin. For a system of particles, the G-operator may be expressed as

$$G = (-1)^{L+S+I}$$

where L is the total angular momentum, S the total spin and I the isotopic spin. The G-parity operator is only useful for strong interactions.

Lifetime. Most elementary particles are unstable and hence can be classified according to their mean lifetime. Three known particles π°, η° and Σ° decay electromangeticaly with lifetimes of 10^{-16} to 10^{-19} s, whereas the majority of the other particles decay by weak interactions, with lifetimes ranging from 918s for the neutron to 0.8×10^{-10} s for the Σ^+. Resonance particles decay by strong interactions with lifetimes of $\leq 10^{-23}$ s. States which decay by strong interactions are called resonances but those which decay by weak or electromagnetic interactions are merely termed particles. An example of resonance production is given in Fig. 7.1. It includes the reactions

$$\pi^- + p \rightarrow R_1 = (\pi p) = N^*$$
$$\pi^- + p \rightarrow R_2 = (\pi p) = \Delta$$

The N^*- and -resonances are both composed of pion plus nucleon. They differ in the total isotopic spin, which is $I = 1/2$ for N^* and $I = 3/2$ for .
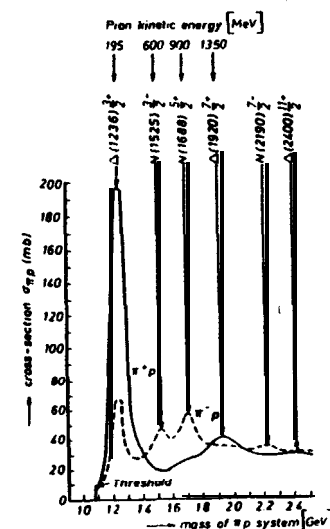

Fig. 7.1: **Cross-sections for production of baryon resonances**

Due to the Heisenberg uncertainty principle, a relationship exists between the mean lifetime τ and the width Γ of a particle, namely $\Gamma = h/\tau$. Often, widths are given instead of lifetimes; these are of the order of 10 to 100 MeV. Although resonance particles have very short lifetimes, they nevertheless have definite quantum numbers such as spin and isotopic spin, and are well-defined particle states.

Table 7.1 gives a summary of the elementary particles and their most important properties.

The following meson resonances have been detected with varying degrees of credibility. They are listed in order of mass (MeV) :

$$\rho(770); \omega(784); K^*(892); \delta(970); S(997); \Phi(1019);$$
$$A_1(1100); A_2(1310); E(1420); f'(1514); F_1(1540);$$
$$\rho'(1600); A_3(1640); \omega'(1675); g(1680) \text{ and } L(1770)$$

About 90 baryon resonances been found also with varying degrees of credibility. They may be classified according to isotopic spin and mass as follows:

N.-resonances $(I = 1/2)$ — 22 with masses between 939 and 3755 MeV;

A-resonances $(I = 3/2)$ — 12 with masses between 1232 and 3030 MeV;

Z-resonances — 5 with masses between 1780 and 2500;

A-resonances $(I = 0)$ — 17 with masses between 1116 and 2585 MeV;

C-resonances $(I = 1)$ — 24 with masses between 1193 and 3000 MeV and

E-resonances $(I = 1/2)$ — 8 with masses between 1317 and 2500 MeV.

Two new neutral particles have recently been found, ψ (3105 MeV) and ψ' (3695 MeV), both with very narrow widths, < 100 keV.

7.2. Interaction mean free path and cross-section

Information about the interaction behaviour of particles is obtained by means of scattering experiments, and the quantitative parameter involved is the cross-section. In an elastic interaction, only kinematic quantities are exchanged, but in an inelastic process new particles are created.

The cross-section was originally defined as a purely geometrical quantity. Suppose that there are n particles per cm^2 within an area F, and that each covers a geometrical area τ_g, then the total area presented to an incident particle is

$$A = nF\,\tau_g.$$

Table 7.1: Classification of the elementary particles
(Adapted from Barash-Schmidt, N., et al., Review of Particle Properties, Phys. Lett. 50 B (1974))

family	particle	Y	J^P	J	m (MeV)	τ (s)	decay modes
photon	γ	—	1^-	—	0	stable	—
leptons	ν_e	—	1/2	—	$< 5 \times 10^{-5}$	stable	—
	ν_μ	—	1/2	—	< 1	stable	—
	$e^\pm$	—	1/2	—	0.51	stable	—
	$\mu^\pm$	—	1/2	—	105.66	2.2×10^{-6}	$e\nu\bar{\nu}$
mesons	$\pi^\pm$	—	0^-	1^-	139.6	2.6×10^{-8}	$\mu\nu; e\nu; \mu\bar{\nu}\gamma; \pi^?e\nu; e\nu\gamma$
	π^0	—	0^-	1^-	135.0	0.9×10^{-16}	$\gamma\gamma; \gamma e^?e^-$
	$K^\pm$	—	0^-	1/2	493.8	1.24×10^{-8}	$\mu^\pm\nu; \pi^\pm\pi^0; \pi^\pm\pi^+\pi^-; \pi^\pm\pi^0\pi^0;$ $\mu^\pm\pi^\mp e^\pm\nu, e^\pm\nu$ and others
	$K^0, \bar{K}^0$	—	0^-	1/2	491.8	50 % K_s 50 % K_l	$\pi^+\pi^-; \pi^0\pi^0; \pi^+\pi^-\pi^0; \pi^+\pi^-\pi^0 \gamma$ $\pi^0\pi^0\pi^-; \pi^\pm\pi^-\pi^0; \pi\mu\nu; \pi e\nu;$ $\pi^+\pi^-$ and others
	K^0_s	—	0^-		548.8	0.86×10^{-10}	$\gamma\gamma; \gamma\gamma; \gamma; \pi^0\pi^0\pi^0; \pi^+\pi^-\pi^0; \pi^+\pi^-\gamma$
	$\bar{K}^0_l$	—	0^-		958	5.17×10^{-8}	$\eta\pi\pi; \rho^0\gamma; \gamma\gamma$
baryons	η	—	0^+	0^+	938.26	2.5×10^{-19}	—
	η'	—	0^+	0^+	939.55	23.8×10^{-16}	$pe^-\nu$
	p	1	$1/2^+$	1/2	115.60	stable	$p\pi^-; n\pi^?; pe\nu; p\mu\nu$
	n	1	$1/2^+$	1/2	1189.4	918	$p\pi^0; n\pi^+; \Lambda e^+\nu; p\gamma; n\pi^+\gamma$
	Λ	0	$1/2^+$	0	1192.5	2.51×10^{-10}	$\Lambda\gamma$
	Σ^+	0	$1/2^+$	1	1197.3	0.802×10^{-10}	$n\pi^-; \Lambda e^-\nu; n e^-\nu; n\mu^-\nu; n\pi^-\gamma$
	Σ^0	0	$1/2^+$	1	1314.7	$< 10^{-14}$	$\Lambda\pi^0$
	Σ^-	-1	$1/2^+$	1	1321.3	1.49×10^{-10}	$\Lambda\pi^-$
	Ξ^0	-1	$1/2^+$	1/2	1672.5	3.0×10^{-10}	$\Xi^0\pi^-; \Xi^?; \pi^?; \Lambda K^-$
	Ξ^-	-1	$1/2^+$	1/2		1.66×10^{-10}	
	Ω^-	-2	$3/2^+$	0		1.3×10^{-10}	

Y = S + B Hypercharge (S strangeness; B baryon number) J spin; P parity; I isotopic spin; G G-parity; m mass; τ lifetime; s short-lived; l long-lived.
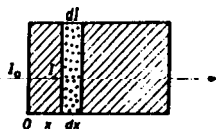
Fig. 7.2: Schematic representation of cross-section

This simple concept will now be developed in a more general manner (see Fig. 7.2). Consider a particle-flux I, incident on a layer of thickness dx, within a target. The differential intensity loss due to interactions is given by

$$dI = - I \sigma N \, dx \, ,$$

$$IN = \frac{dn}{dx} \text{volume density)}$$

and so

$$I = I_0 \, e^{-\sigma N x}$$

The transparency of the process is defined as

$$p_1 = I/I_0 = e^{-\sigma N x} \, ,$$

and the opacity as

$$p_2 = 1 - e^{-\sigma N x} \, .$$

The cross-section exists in several different forms as determined by experimental conditions and requirements:

Elastic cross-section σ_{el}. This cross-section relates to processes in which only kinematical exchanges occur.

Inelastic cross-section σ_{inel}. This cross-section relates to processes in which new particles are created.

Total cross-section σ_{tot}. This is the sum of elastic and inelastic cross-sections.

Differential cross-section. Often the experimental conditions are such that only values for particular angular, energy or momentum ranges are obtained, i.e.

$$\sigma(\Theta) = \frac{d\sigma}{d\Theta} \, ; \qquad (E) = \frac{d\sigma}{dE} \, ; \qquad (p) = \frac{d^3 a}{dp^3} \, ;$$

These are differential cross sections.

Integral cross-section σ_{int}. This is just the integral over the differential cross-section, i.e.

$$\sigma_{int} = \int \sigma(\Theta) \, d\Theta \, .$$

Partial cross-section σ_i. For an interaction in which several different processes can occur, the cross-section for a particular process is termed a partial cross-section.

The *total cross-section* is thus the sum

$$\sigma_{tot} = \sum \sigma_i \, .$$

Cross-sections are expressed in units of the barn, $1 \text{ b} = 10^{-24} \text{ cm}^2$. Using the concept of quantum mechanics, a beam of particles can be represented as a plane wave

$$\psi_i(x, t) = C \cdot \exp\left[i(\vec{x}, \vec{p}) - iEt\right] \, ,$$

where
p momentum
E energy
and $\hbar = 1$.

Consider this beam to be incident upon a scattering center, consisting of a potential well, which changes the phase and the amplitude of the wave. Thus, the scattered wave at a large distance from the scattering center, can be written, for an elastic process, as

$$\psi_s(x, t) = C \cdot f(\Theta) \cdot (1/x) \cdot \exp\left[i(\vec{x}, \vec{p}) - iEt\right] \, .$$

The scattered amplitude is attenuated as l/x and is proportional to the amplitude of the incident wave. The probability, dP, that the scattered wave traverses a differential area d F, at an angle Θ is given by

$$dP = k \, | \, \psi_s(x, t) \, |^2 \, dF$$
$$dP = k \, C^2 \, | \, f(\Theta) \, |^2 \, dF/x^2 \, ,$$

(where k is a constant)
or using the solid angle definition $d\Omega = dF/x^2$

$$dP = k \, C^2 \, | \, f(\Theta) \, |^2 \, d\Omega \, .$$

The probability P_i, that the incident wave traverses unit area before the scattering process is given by

$$P_i = k \, | \, \psi_i(x, t) \, |^2 = k \, C^2 \, ,$$

so that

$$\sigma_{int} = \int dP/P_i = \int | \, f(\Theta) \, |^2 \, d\Omega$$

and finally

$$\sigma(\Theta) = | \, f(\Theta) \, |^2 \, .$$
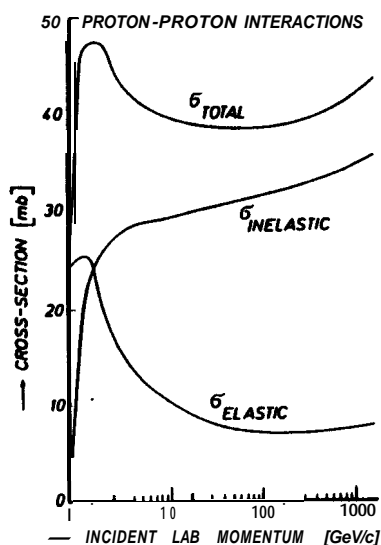
Fig. 7.3: Total. elastic, and inelastic cross-sections as a function of the laboratory momentum $\vec{p}$ for the proton-proton interaction.
(From Morrison, D. R. 0: CERN-Report D. Ph II/Phys. 7-46 (1973))

The total cross-section for pp-interactions has been measured up to energies of 1.5 TeV at the CERN Intersecting Storage Rings (ISR). Above this energy, the cross-section can only be measured using cosmic radiation. Fig. 7.3 shows the measured elastic, inelastic and total cross-sections. Above ~ 100 GeV, σ_{tot} rises monotonically, but at lower energies it decreases/due to the fact that σ_{el} falls faster than σ_{inel} rises. Once σ_{el} stops falling, the slow monotonous increase of σ_{inel} produces the increase in σ_{tot}.

When particles interact with nuclei, not all of the nucleons are involved. The cross-section can be parametrized as

$$\sigma = \sigma_0 (E)\, A^\alpha .$$

$\sigma_0(E)$ = 30 to 59 mb
A atomic number

a is predicted to have the value $2/3$ for a spherical nucleus, since $\sigma_g = \pi R^2$, and $R = R_0\, A^{1/3}$. For pion beams α is found to be ~ 0.75.

In cosmic-radiation, interaction probabilities are expressed in terms of the interaction mean free path λ. When a beam of intensity I_0, passes through matter the fraction of the beam existing after a thickness x is given by (see definition of cross section)

$$I = I_, e^{-x/\lambda} .$$

with
$\lambda = N\sigma/A$
N Avogadro number
N/A number of nuclei per gram

$\lambda = N\sigma/A$ is called the mean interaction length. Since the cross-section is a function of E and A, so is the mean free path $= \lambda(E, A)$. The intensity $I_,$ corresponds to the number of particles which have travelled a distance x (g cm^{-2}) without an interaction. Fig. 7.4 shows the variation of λ with atomic weight A and Table 7.2 gives values for various media.

Interaction mean free paths for heavy nuclei are smaller because of the higher cross-sections involved. Fig. 7.5 gives the variation with incident atomic weight A for air and for nuclear emulsions.

Table 7.2: Mean interaction lengths

material	Z	A	σ_g(b)	λ(g cm^{-2})	λ (cm)	density ρ
air	7.4	14.8		70.8	4.8×10^4	1.29×10^{-3}
water	6	14.3		62.4	62.4	1.00
Fe	26	55.8	0.84	110.8	14.0	7.9
Pb	82	207.2	2.0	171.6	16.1	11.34
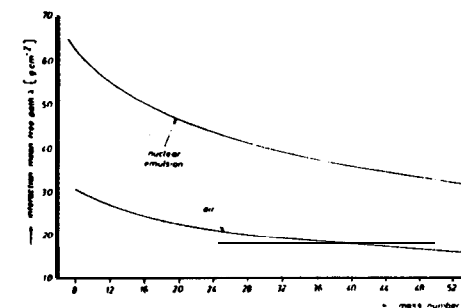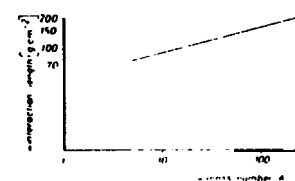
Fig. 7.4: Variation of the interaction length with the mass number (obtained from interactions of 24 GeV protons) (Adapted from Hayakawa, S.: Cosmic Ray Physics: New York: John Wiley and Sons 1969)

Fig.7.5: Variation of the interaction mean free Path with mass, for nuclei in air and nuclear emulsions
(Adapted from Allkofer. 0. C., W. Heinrich: Health Physics 27, (1974) 543)

An additional characteristic length , is used when the secondary particles produced in the interaction are taken into account. The relation

$$I = I_0 e^{-x/\Lambda}$$

applies to the attenuation of all nucleons produced in a hadron cascade, both primaries and secondaries. is called the attenuation length and is greater than the mean free path λ, due to the contribution of the secondary particles. For air $\lambda = 71\,g\,cm^{-2}$ and $\Lambda = 120\,g\,cm^{-2}$.

7.3. Some kinematical considerations

For a relativistic two-body interaction involving four momenta $P_i = (iE/c, p_1, p_2, p_3) = (iE/c, \vec{p})$, conservation of four momentum gives (see Fig. 7.6)

$$P_1 + P_2 = P_3 + P_4 .$$

Using the relations

$$P_i^2 = \vec{p}_i^2 - E^2$$

and

$$E_i = \sqrt{\vec{p}_i^2 + m_i^2}$$

one obtains

$$P_i^2 = -m_i^2 .$$

The Lorentz-invariant variables of the system (Mandelstam variables) are defined as

$$s = - (P_1 + P_2)^2$$
$$t = - (P_3 - P_1)^2$$
$$u = - (P_4 - P_1)^2$$

In the CM-system, momentum conservation gives

$$\vec{p}_1 + \vec{p}_2 = 0$$

and hence,

$$s = (E_1 + E_2)^2 - (\vec{p}_1 + \vec{p}_2)^2 = W^2 ,$$

where W is the total CMS-energy.

The following important expression relates the Mandelstam variables and the masses in the system,

$$s + t + u = \sum m_i^2 .$$

At high energies, strong interaction cross-sections are usually written in terms of the CMS-variables W, the total energy, p_T, the transverse momentum and p_L the longitudinal momentum. Introducing the maximum linear CMS-momentum as $p_{L,max}$, the variable x, known as the Feynman variable is defined as

$$x = (p_L/p_{L,max}) = 2 (p_L/W) = 2 p_L / \sqrt{s},$$

using $W=p$ for $p^2 \gg m^2$.

Another useful variable, the rapidity, is also defined in the CM-system as

$$y = 1/2 \log \frac{W + p_L}{W - P} = 1/2 \log \frac{\sqrt{s} + p_L}{\sqrt{s} - p_L}.$$

The reason for using rapidity is that it adds linearly in a relativistic frame. This corresponds to the linear addition of velocities in a non-relativistic frame (Galilei principle). At low energies where relativistic considerations do not apply, rapidity reduces to velocity.

Inelastic distributions are often expressed in terms of the Feynman variable x, by the function

$$f_1 = 2 E/\sqrt{s} (d^3 \sigma/d p^3) = 2 E/\sqrt{s} \frac{d^3 \sigma}{d x \ d p_T^2} ,$$

E incident energy

or in terms of rapidity, by the function

$$f_2 = 1/\pi \frac{d^3 \sigma}{d y \ d p_T^2} .$$
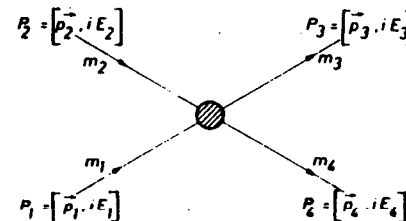
Fig. 7.6: Two-body interactions
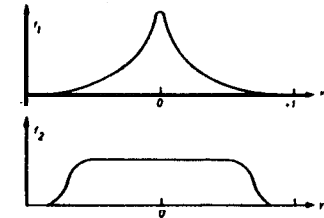
Fig. 7.7: Representation of cross-sections in terms of the Feynman variable x and the rapidity y
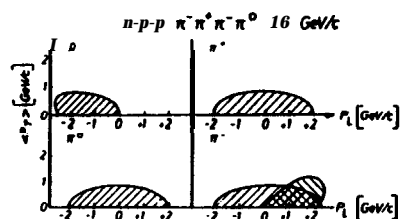
Fig. 7.8: Leading particle effect as shown in a $p_L - p_T$ distribution for the reaction $\pi^- p \ldots p \ \pi^- \pi^+ \pi^- \pi^\circ$

The x- and y-distributions for pion production in the pp-interaction are shown in Fig. 7.7. It is seen that plotting against y opens up the central region in contrast to using x.

7.4. Leading particle effect

In an inelastic process, the interacting particles and the secondary products have different momentum distributions. This is shown in Fig. 7.8 for the reaction

$$\pi^- p \rightarrow p \ \pi^- \pi^+ \pi^- \pi^\circ$$

involving 18 GeV/c pions. In this diagraqdistributionsarepresented on a $p_L - p_T$-plot for all the particles involved. It is seen that the distributions of particles not present before the interaction, namely the π^+ and π°, are symmetrically distributed about the CM, whereas the proton distribution is shifted to large negativep, and the n--distribution shows a region of large positive p_L values, in addition to a symmetric component. This effect can be interpreted in the following way. In the CM-system, the interacting particles have large longitudinal momentum being the leading particles of the interaction, whereas the secondary particles are emitted symmetrically, This is sometimes called pionization.

7.5. Two-body interaction

In an elastic two-body interaction, because of the leading particle effect, the particles leave the interaction volume travelling in their original directions with small exchange of momentum and energy. As a consequence, only small transverse momenta are involved. Fig. 7.9 gives a schematic representation of the elastic scattering process $\pi^+ p \rightarrow \pi^+ p$. The π^+ continues to travel from left to right with only a small deflection/and the proton does likewise in the opposite direction. This collision process is
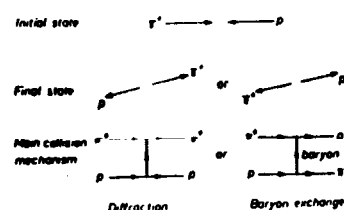
Fig. 7.9: Schematic representation of the elastic process $\pi^+ P \rightarrow \pi^+ P$
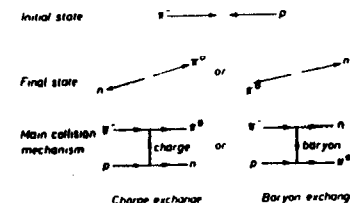
Fig. 7.10: Schematic representation of the two-body collision $\pi^- p \rightarrow n \ \pi^\circ$

called elastic diffraction and the cross-section is found to remain almost constant with energy. In the second process, the π^+ becomes a proton and the proton a π^+, by exchanging one unit of baryon number. For this baryon-exchange process, the cross-section is found to decrease with energy as E_{CM}^{-5}. In Fig. 7.10 the analogous process for the reaction $\pi^- p \rightarrow \pi^\circ n$ is shown. This process is explained as an exchange of charge plus a baryon. The cross-section decreases approximately as E_{CM}^{-2}.

In an inelastic process, new particles are produced (few-body or many-body interaction). In Fig. 7.11 the four-body interaction $\pi^+ p \rightarrow \pi^+ \pi^+ \pi^- p$ is illustrated. Here, the hadronic system travelling to the right is initially a π^+, but changes into a three-pion system conserving the total charge,+ 1. The proton continues to the left and suffers only a small change of momentum and energy. This collision mechanism is inelastic diffraction, and its cross-section becomes almost constant above an energy of $\sim$ 5 GeV.

Inelastic processes may produce new particles at both vertices allowing both charge exchange and baryon exchange to occur (Fig. 7.12).
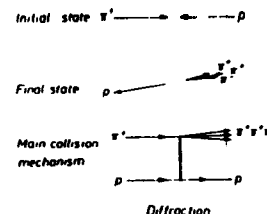
Fig. 7.11: Schematic representation of a many-body process
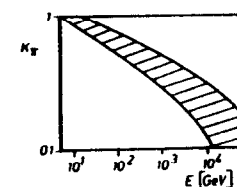
Fig. 7.12: Variation of the inelasticity for n-production with the energy of the interacting particles

7.6. Inelasticity

The inelasticity of a nuclear interaction is defined as the fraction of the kinetic energy of the incident particle which is lost. It is expressed as

$$K = \frac{\Sigma E_i}{(E_0 - m)}$$

$E_0 - m$ kinetic energy of the incident particle
$E_i = (E_i^{kin} + m_i)$ total energy of each additional particle produced

Correspondingly, the elasticity is defined as $\eta = 1 - K$. The energy loss in the collision is given by

$$\Delta E = K(E_0 - m) = (1 - \eta)(E_0 - m).$$

The energy transferred in the interaction is shared between charged particles, photons, coming mainly from the decay of neutral pions, and other neutral particles. Thus,

$$K = K_{charged} + K_\gamma + K_{neutral}$$

It follows that

$$\frac{K_{charged}}{K_\gamma} \approx \frac{\Sigma E_{charged}}{\Sigma E_{\pi^0}} \approx 2$$

because most of the secondaries are pions and these are produced with equal probabilities for π^+, π^0 and π^-.

The energy which goes into neutral particles other than π^0 s is small in comparison, thus $K_{neutral} < K_\gamma$ and hence,

$$K \approx 3/2 \, K_{charged}$$

Partial inelasticities are obtained by measuring the different secondary components. The total inelasticity for pion production K_{π}, decreases slightly with energy, although large fluctuations are observed for single events (Fig. 7.12). At energies of 10^5 to 10^6 GeV, the total mean inelasticity is found to be 0.4 to 0.5.

7.7. Multiplicity

The multiplicity of an interaction as defined in cosmic-ray physics is the number of secondary particles produced, e.g. the multiplicity of the interaction

$$p + p \rightarrow p + p + \pi^+ \, \pi^- \, \pi^0 \, \pi^+ \, \pi^-$$
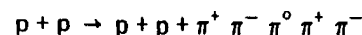
is $n = 5$. The total multiplicity is composed of the partial multiplicities for each of the different particles created, thus

$$n = n_{\pi^+} + n_{\pi^0} + n_K + n_{\Lambda^0} + \ldots$$
$$n = n_{neutral} + n_{charged}.$$

Another definition which is used in accelerator high-energy physics, states that the multiplicity of an interaction is the total number of outgoing particles. For the above reaction the charged multiplicity would be $n_{ch} = 6$ and the total multiplicity $n = 7$.
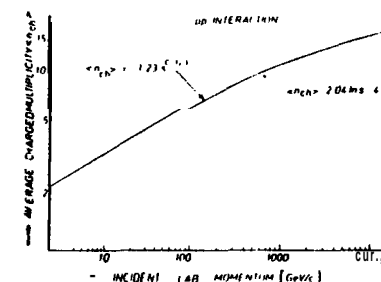
Fig. 7.13: Average charged multiplicity as a function of the incident momentum of the proton in a pp-interaction (Adapted from Morrison, D. R. 0.: CERN-Report D. Ph II/Phys. 73 · 46 (1973))

Multiplicities are weakly dependent on the energy of the interacting particles and fluctuate a large amount from reaction to reaction. Fig. 7.13 gives the mean charged multiplicity $\langle n_{ch} \rangle$ as a function of incident proton energy in the Laboratory System. At low energies, the data is consistent with a multiplicity of $n \approx s$, but at higher energies the multiplicity varies as log s.

7.6. Transverse momentum

In inelastic processes, energy and momentum are transferred to the secondary particles. The momentum of each final particle has an longitudinal component p_L along the direction of the incident particle, and a transverse component p_T. Measurements have shown that in general, the mean transverse momentum $\langle p_T \rangle$ is always small, of the order of 0.35 GeV/c, is independent of the longitudinal momentum p_L and varies only slightly with the mass of the particle. A small increase of $\langle p_T \rangle$ with energy has been observed in cosmic radiation (Fig. 7.14) and there is also evidence for a small increase in $\langle p_T \rangle$ with the mass of the final particle (Fig. 7.15).
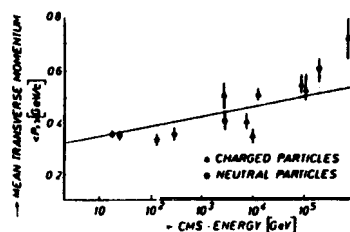
Fig. 7.14: Mean transverse momentum $\langle p_T \rangle$ versus CM-energy as observed in cosmic radiation
(Adapted from Morrison, D. R. 0.: CERN-Report D. Ph. II/Phys. 73 · 46 (1973))
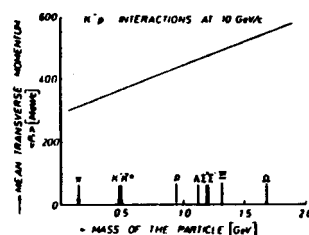
Fig. 7.15: Mean transverse momentum $\langle p_T \rangle$ as a function of the mass of the particle produced in K^- p reactions at 10 GeV/c
(Adapted from Morrison, D. R. 0.: CERN-Report D. Ph. II/Phys. 73 · 46 f1973))

For a specific process, the transverse momentum has a distribution which is independent of longitudinal momentum p_L and the Feynman variable $x = p_L / p_{L\,max}$. Hence, the distribution can be simplified by means of factorization

$$f(x, p_T) = G(x)\, H(p_T) .$$

Recent results have shown that the mean value $\langle p_T \rangle$ becomes smaller near $x = \pm 1$ and has a dip near $x = 0$, as shown in Fig. 7.16 (seagull effect).

Experiments at the CERN-ISR, measuring pion production in pp-collisions have found that the invariant cross-section shows an exponential decrease with p_T,

$$E \left(\frac{d^3 \sigma}{d p^3} \right) \propto e^{-6 p_T}$$
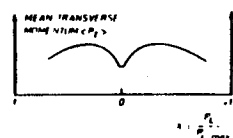
Fig. 7.16: Variation of $\langle p_T \rangle$ with the Feynman variable $x = p_L / p_{L,max}$ (seagull effect)
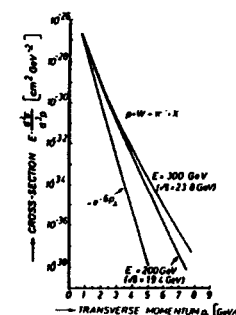
Fig. 7.17: Cross-section for the inclusive reaction $p + W \cdots \pi^- + X$ es a function of $\langle p_T \rangle$ near $\Theta_{CMS} = 90°$ (W tungsten)
(Adapted from Ellis, S. D., R. Thun: CERN Preprint Th. 1874 (1974))

In addition, some particles with large transverse momentum have been observed at large CMS-angles in disagreement with this exponential fall-off. This is seen in Fig. 7.17, which shows the measured distribution of π^- in the reaction p + Tungsten $\to \pi^- + X$ for different energies near $\Theta_{CMS} = 90°$. The figure also shows that the inclusive cross-section at fixed large p_T rises sharply with increasing CMS-energy.

The relative abundance of the different types of charged particles has been measured as a function of $\langle p_T \rangle$. It is found that at small $\langle p_T \rangle$ the pions are dominant (90 % pions, 10 % heavy particles), at about $\langle p_T \rangle$ = 1.5 GeV/c their contribution is somewhat less (64 % charged pions, 35 % heavier particles) and at the highest $\langle p_T \rangle$, the ratio of light to heavy particles is approximately independent of $\langle p_T \rangle$. In addition, it is found that the ratio of positive to negative particles is higher at larger $\langle p_T \rangle$.

7.9. Scaling laws

For some time in cosmic-ray physics and more recently in accelerator-particle physcs, the extrapolation of interaction results to higher energies by means of scale invariance has been discussed. Such scaling behaviour is expected both for strong interactions (Feynman scaling, Benecke scaling), and for electromagnetic interactions (Bjorken scaling).

High-energy interactions may be divided into two types, inclusive and exclusive'processes. In the interaction

$$a + b \to c + \text{anything}$$

when only one particle (c) is observed and its behaviour studied, the interaction is called an inclusive interaction, thus

$$p + p \to \pi^+ + X$$

is an inclusive interaction in which the π^+ is the measured particle; X could be a many-body system, e.g. X = p + n + π^o. In an inclusive interaction,the details of the final state are unknown.

When the behaviour of all particles in an interaction is taken into account, the process is termed an exclusive interaction.

The cross-section for an inclusive interaction depends upon the total energy $W = \sqrt{s}$ and the momentum p, with components p_L and p_T. By using the Feynman variable $x = p_L/p_{L,max}$ and the rapidity $y = 1/2 \log [W + p_L/(W - p_L)]$, the independent functions $f(s,p)$, $f_1(s, x, p_T)$ and f_2 ls, y, p_T) become available.

A useful expression involving the total cross-section and the multiplicity, for an inclusive interaction is

$$\int \frac{d^3 \sigma}{d p^3} \cdot \frac{d p^3}{W} = \langle n_{charged} \rangle \cdot \sigma_{tot} .$$

A physical quantity is said to scale, if its behaviour under unknown conditions can be deduced from its behaviour under known conditions using laws of similarity. Feynman scaling makes predictions about the behaviour of the cross-section at high energies in the CM-system

$$f_1 (s, x, p_T) \equiv E \frac{d^3 \sigma}{d p^3} \xrightarrow[s \to \infty]{} g(x, p_T) .$$

Benecke scaling makes similar predictions for the Lab System

$$f_2 (s, y, p_T) \equiv E \frac{d^3 \sigma}{d p^3} \Big|_{I} \implies h(y, p_T) .$$

In both cases, the cross-section is expected to become energy-independent at high energies.

For a rapidity plot of $E \frac{d^3 \sigma}{d p^3}$, scaling means that the height of the central plateau remains constant as the energy increases (Fig. 7.18).
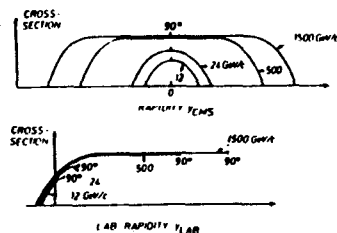
Fig, 7.18: Demonstration of Feynman scaling in a rapidity plot

Fig.7.19: The interactionp+p $\to \pi^+$ + X showing scaling behaviour for π^+ -production (Adapted from Morrison, D. R. O.: CERN-Report D. Ph. II/Phys. 73 · 46 (1973)
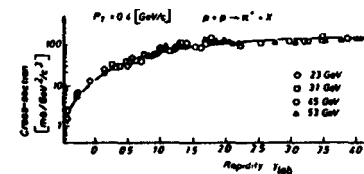
The latest results from CERN-ISR find that for some, but not all reactions, scale invariance is obeyed. Fig. 7.19 shows the cross-section for the inclusive interaction p + p $\to \pi^+$ + X at several energies; the results are consistent with scale invariance. An overall picture for different inclusive reactions is given in Fig. 7.20. It is seen that the cross-sections for π^+ are higher than for π^- and likewise for K^+ and K^-.
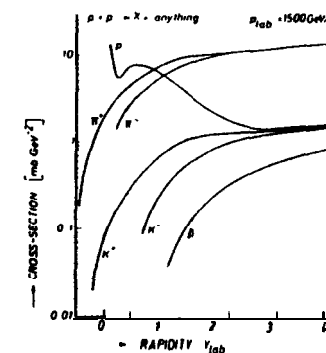
Fig. 7.20: Cross-sections for different inclusive reactions as a function of rapidity (Adapted from Morrison, D. R. 0.: CERN-Report D.Ph. II/Phys. 73.46 (1973))

7.10. Charge ratio of pions

In ppinteractions,a larger number of positive than negative mesons is always observed. This is shown in Fig. 7.20 where positive charge ratios for π^+/π^- and for K^+/K^- can be seen. The reason for this is that the inter-acting particles have a positive charge excess which is transferred to the secondary components. It is of interest to investigate the kinematical variation of the charge ratio. From the hypothesis of limited fragmentation, it follows that the secondaries are of two types, the fragments F coming from the leading particle and the other particles coming from the target region, CP. Fig. 7.21 shows the contribution of both types of particles and their sum. Thus the incident proton produces more π^+ than π^- since its charge is positive,but the target region produces equal numbers of π^+ and π^-. The variation of charge ratio with rapidity can be derived and shows that the ratio of particle to antiparticle cross-section tends to a limiting value at high energies.
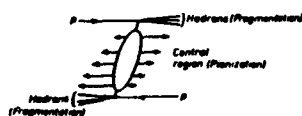
Fig.7.21: Schematic representation of the model of limited fragmentation

7.11. Particle models

Observations of high-energy interactions in cosmic radiation stimulated efforts to explain their main features by means of interaction models; quantitative explanations of the anisotropy in emission of secondary particles and the energy dependence of multiplicity were required. In the *Heisenberg model* (1952) the interaction volume expands after a collision and the mechanical analogy of shock waves is used. The *Fermi model* (1950) treats the interaction volume as a black body at high temperature and the *Landau model* (1953) introduces hydrodynamical considerations. The two-fireball model of *Cocconi* (1958) is able to explain the peaked anisotropic emission of secondary particles.

A widely used model which has had some success in explaining observed results is the *diffraction dissociation model.* Here, the incident particle undergoes diffractive scattering on the target particle which behaves like an opaque disc, as in the case of optical waves. A partial wave analysis shows that in the forward direction all the wavelets add up coherently to give a diffraction peak. This process can be elastic with exchange of energy, momentum and also charge, isospin, parity, virtual particles etc. or inelastic, in which case diffraction dissociation, i.e. the production of secondary particles, can occur at one or both vertices (Fig. 7.22).
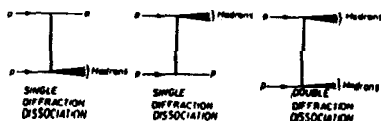
Fig. 7.22: Schematic representation of single and double diffraction dissociation

The *multiperipheral model* or *ABSFT-model* (1962) considers the production of many particles at many vertices (Fig. 7.23). The chain increases with energy and consequently also the multiplicity. A basic requirement is for small four-momentum transfer between neighbouring particles, resulting in a small average transverse momentum $\langle p_T \rangle$.

The *statistical thermodynamical model (Hadedorn* 1970) assumes that in the pp-interaction, a series of local centers in thermal equilibrium are
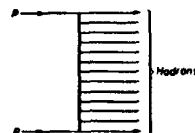
Fig. 7.23: Schematic representation of the multiperipheral model
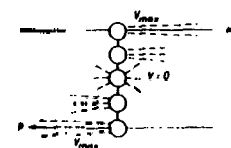
Fig. 7.24: Schematic representation of the statistical thermodynamical model

produced, (Fig.7.24). The peripheral centres have large velocities but in the interior the velocities are small. Thus all velocities between $v = 0$ and $v = v_p$ (v_p velocity of the leading particle) are possible. Each center emits secondary particles isotropically. The model makes predictions about the density of states (resonance particles) as a function of mass.

The parton model (Feynman 1969) suggests that the proton is composed of small particles which have large masses and are strongly bound. Thus, the hadron has a granular structure, and the constituent partons are considered to behave as pointlike objects. The model was developed from inelastic electron scattering data at high energies.

An earlier model which considered a subnuclear structure was the *quark model.* In this model, hadrons are considered to be compound states of three different quarks, which have spin $1/2$, baryon number $1/3$ and charge $1/3$ or $2/3$. The mesons are composed of quark − antiquark pairs. Such particles have not been detected in experiments. In order to understand new results in interaction physics a fourth quark has been introduced with a quantum number called charm.

In the *quark-parton-model,the* partons are identified as quarks. An extension of this model assumes a substructure of the nucleons composed of a core of partons plus additional valency partons. The spin of the particle is due to valency partons, the core having spin zero. The valency partons are responsible for all quantum numbers of the nucleons. Field quanta, called gluons, which describe the interaction between quark-partons, are also present.

The *model of limited fragmentation (Benecke* 1969) treats the hadronic interaction as a fragmentation process for both the incident and the target particles. Only a limited fraction of the total energy is given to the fragments and so their multiplicity is independent of the energy (scaling behaviour, see section 7.9).

References

Hayakawa, S.: Cosmic-Ray Physics. New York: John Wiley & Sons 1969

Morrison. D. R.O.: Experimental Review of Strong Interactions at High Energy.
CERN-Report D.Ph. II/Phys. 73-46 1973

Ellis, S.D., R. Thun: Large Transverse Momentum Phenomena: An Experimental and
Theoretical Review. CERN-Report Ref. Th. 1874 – CERN 1974

Perkins, D. H.: Introduction to High-Energy Physics. Reading: Addison-Wesley 1972

Barash-Schmidt, N., A. Barbaro-Galtieri, C. Brieman, et al.: Tables of Particle
Properties (1973)

Hove, L. van: Recent Development in High-Energy Physics. CERN-Report Ref. TH
1579 – CERN (1972)

Feinberg, E. L.: Multiple Production of Hadrons at Cosmic Ray Energies. Physics
Reports 6 c (1972) 240

8. Cascade showers

8.1. The phenomenon

When high-energy particles traverse matter, they create secondary particles,
which in turn create tertiary particles, and so on. The particles are scattered
and absorbed in the matter and also decay into other particles. The whole
phenomenon is termed a cascade. The number of particles increases up to
a maximum,and then decreases until the end of the cascade. As a result of
scattering in the various interactions, there is a lateral as well as a longitudi-
nal development.

Electromagnetic cascades are propagated by electrons and photons. The
basic cascading processes are bremsstrahlung and pair production (see
Chapter 6), which produce successive generations of photons and electrons
of both charges (Fig.8.1). The numbers of particles increase until their
energies become too low to multiply any further, and then the cascade de-
clines.

The development of an electromagnetic cascade depends upon the pro-
perties of the material traversed, i.e. on the atomic weight A, the atomic
number Z and the density ρ. Convenient parameters for describing this
dependence are radiation length X_0 (see Chapter 6) and critical energy ϵ.
Values of both are given in Table 8.1, for some important materials.

The hadron cascade is propagated by quite different processes. When a
high-energy hadron traverses matter, it undergoes nuclear interactions, and
loses energy corresponding to an inelasticity of 0.4 to 0.5. Nucleons, me-
sons and hyperons, are present in numbers determined by their relative
cross-sections; the pion triplet is dominant here. Alpha particles and frag
ments of heavier nuclei are also produced. Nuclei are raised to excited
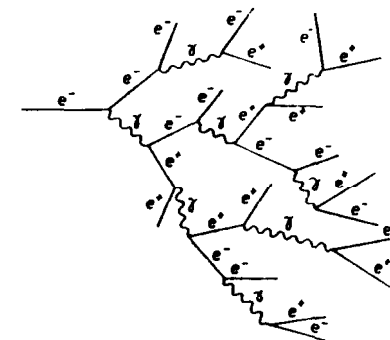
Fig. 8.1: Schematic representation of an
electromagnetic cascade

Table 8.1: Constants of materials relevant to cascade showers

material	Z	A	λ (g cm^{-2})	λ (cm)	X_0 (g cm^{-2})	X_0 (cm)	ϵ (MeV)	ρ (g cm^{-3})
H$_2$	1	1	43.0	607.4	62.8	887	350	0.0708
Be	4	9	55.4	30.0	66.0	35.7		1.848
C	6	12	58.7	28.9	43.3	27.0	79	1.55
Ne	10	20.6	64.4	53.7	29.1	24.3		1.207
Al	13	27	87.0	32.3	24.3	9.0	40	2.70
Fe	26	56	110.8	14.0	13.9	1.77	20.7	7.87
Cu	29	64	115.7	13.0	13.0	1.45	18.8	8.96
Pb	82	207	176.6	15.1	6.4	0.56	7.4	11.35
Air (20 °C)			70.8	5.49 × 10^4	37.2	3.1 × 10^4	81	1.21 × 10^{-3}
H$_2$O			62.4	62.4	36.4	36.4	73.0	1.00
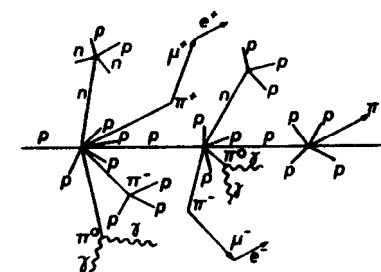
Fig. 8.2: Schematic representation of a hadron cascade

states and evaporate low-energy nucleons and gamma rays (Fig.8.2). The secondary hadrons either interact strongly or else decay; the π^0 mesons decay into gamma rays initiating electromagnetic cascades. All charged particles lose energy by ionization processes. The number of particles increases to a maximum, and then decreases, as in the case of the electromagnetic cascade.

The characteristic dependence on the material traversed has been described already, in Chapter 7. Values of the interaction length $\lambda \sim 1/$, i.e. the mean free path between strong interactions, are included in Table 8.1. The cross-section used here is the total cross-section $\sigma = \sigma_{el} + \sigma_{inel}$.

8.2. Longitudinal development of electromagnetic cascades

The number of electrons or photons in a cascade shower is a function of the primary energy Eo, and the thickness of matter traversed t, i.e. N = N (E_0, t). Often, it is of interest to know the numbers of electrons and photons with an energy greater than E, i.e. N = N (E_0, E, t). If E_0 and E are expressed in units of critical energy ϵ, and t in units of radiation length X,, then N is almost independent of the specific material traversed.

Calculations of shower development have been made by analytical and more precisely, by Monte Carlo methods. Analytical calculations only give correct results for light materials, and are performed under two approximations, A and B. In approximation A, the cross-sections for the main processes of pair production and bremsstrahlung are used in an approximate form, and the energy loss is neglected. The average number of shower particles is expressed as a function of E_0/E, thus N_A = N $(E_0/E, t)$.

Approximation B includes the ionization loss, which becomes important as E approaches the critical energy as a constant term, thus N_B = N (E_0, E, t).
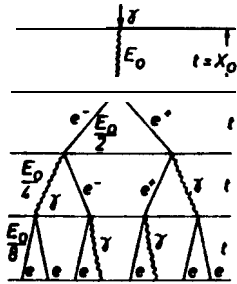
Fig. 8.3: Simplified quantitative model for an electromagnetic cascade

The basic features of shower development can conveniently be explained by means of the following simple model (Fig.8.3). A primary photon of energy Eo undergoes pair production during the first radiation length, and each electron gets half of the energy $E_0/2$. During the next radiation length, both electrons radiate giving half of their energy to the photons. These processes are repeated. The number of particles N, after t interaction lengths is given by

$$N(t) = 2^t.$$

Here, ionization loss and the energy dependence of the cross-sections are neglected. At a depth t, the energy $E(t)$ per particle is thus

$$E(t) = E_0 \cdot 2^{-t}.$$

The shower continues to develop until $E(t) = \epsilon$, and then ceases abruptly. The depth at which this occurs is given by

$$t = t_{max}(E_0) = \frac{\ln E_0/E}{\ln 2}$$

and the number of particles is

$$N_{max} = \exp[t_{max}\ln 2] = E_0/\epsilon.$$

The number of particles with energy greater than E is

$$N(>E) = \int_0^{t(E)} N\,dt = \int_0^{t(E)} e^{t\ln 2}\,dt$$

$$\approx \frac{e^{t\ln 2}}{\ln 2} = \frac{E_0/E}{\ln 2},$$

$t(E)$ is the depth at which the particle energy has fallen to E. Thus, the differential energy spectrum of particles varies as

$$dN/dE \propto 1/E^2.$$

For the complete shower, the total track length in radiation lengths of the charged particles is given by

$$L = \frac{2}{3} \int_0^{t_{max}} N\,dt = \frac{2}{3\ln 2}\frac{E_0}{\epsilon} \propto \frac{E_0}{\epsilon}$$

This simple model already shows the main features of electromagnetic shower development which are:

– the shower has a maximum at a depth which increases logarithmically with the primary energy E,; $t_{max} \propto \ln E_0/E$
– the number of shower particles at the maximum is proportional to the primary energy; $N_{max} \propto E_0$
– the total track length is proportional to E,; $L \propto E_0$.

Another important parameter which enters into analytical shower calculations is the age parameter s. This parameter represents the age of a shower, which starts at depth $t = 0$ with s = 0. At the maximum of the shower, s = 1. Expressed in terms of s, all shower curves become similar, independent of the incident energies. Thus, the slope of a shower curve can be expressed in terms of s alone; approximately

$$dN/dt \approx 1/2\,(s - 1 - 3\ln s).$$

The values of s are determined as the saddle points in inverse Mellin transformations. In terms of the age parameter, the energy spectrum of electrons in a shower has the approximate form

$$w_e(E_0, E, t) \propto E^{-s}.$$

In Fig. 8.4, the average number of electrons $N_e = N_e(E, E_0, t)$ expressed as a function of depth t, in iron, is given for five showers.
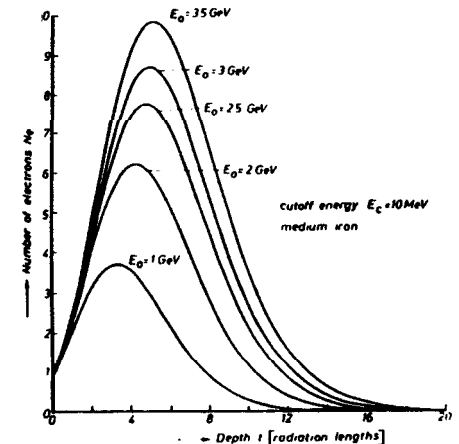
Fig. 8.4: Development of electromagnetic cascade showers in iron
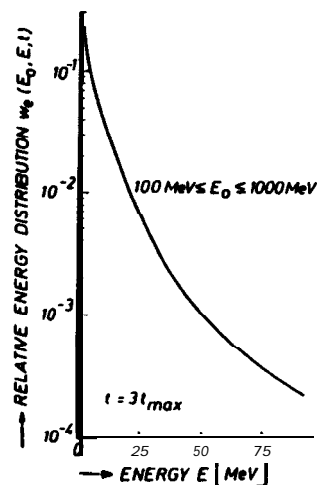
Fig. 8.5: Energy distribution of electrons in an electromagnetic cascade at a depth of $t = 3\,t_{max}$ in Pb
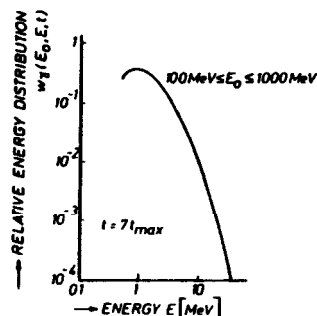(Adapted from Nagel, H. H.: Zeitschr. Phys. 186. 319 (1965))

Fig. 8.6: Energy distribution of photons in an electromagnetic cascade at the depth of $t = 7\,t_{max}$ in Pb
(Adapted from Nagel, H. H.: Zeitschr. Phys. 186, 319 (1965))

Energy spectra of electrons and photons in showers have also been calculated by Monte Carlo methods. Fig.8.5 shows the energy distribution of electrons in lead, at a depth $t = 3\,t_{max}$ as a function of E. In Fig. 8.6, the relative energy distribution of photons at the depth $t = 7\,t_{max}$ is given for the same values of the primary energy.

8.3. Lateral development of electromagnetic cascades

The cascade shower is not, as mentioned previously, only a one-dimensional phenomenon. Because the electrons receive transverse momenta as a result of Coulomb scattering, they are widely distributed in a three-dimensional cascade. Thus, the total number of shower particles depends upon the angle subtended at the origin with respect to the shower axis, or correspondingly on the lateral distance from the axis, r, i.e. $N = N\,(E_0, E, t, \Theta)$ or $N = N\,(E_0, E, t, r)$. It follows that

$$\int N(E_0, E, \Theta, t)\,d\Theta = \int N(E_0, E, r, t)\,dr = N(E_0, E, t)\,.$$

It is often important to know the number of particles with angles less than a particular value of Θ, or the number of particles whose lateral distance from the axis is less than a particular value of r. In these instances the differential angular and lateral distributions f( ) and f(r) are used,

$$f(\ ) = \frac{1}{N(E_0, E, t)\,\sin\Theta}\,\frac{dN(E_0, E, \Theta, t)}{d\Theta}$$

$$f(r) = \frac{1}{N(E_0, E, t)\,2\,\pi r}\,\frac{dN(E_0, E, r, t)}{dr}$$

The lateral distribution of a shower is almost independent of material traversed if the distance r is expressed in Moliere units

$$r_M = X_0\,\frac{E_s}{\epsilon}\,.$$

E_s is the characteristic energy for multiple scattering. For single charged particles $E_s = 21$ MeV. The lateral distribution varies with the age parameters approximately as

$$f(r) \propto (r/r_M)^{s-2}\,,$$

and so with increasing s it becomes flatter. This flatter region may be defined as the core of the shower and its radius is given by

$$r_c \approx r_M\,(\epsilon/E_0)\,e^{t/4}$$

Fig.8.7 shows the lateral distribution function $f(r)$ in air for three different age parameters. r is expressed in units of the Moliere radius r_M, which at sea level for air is

$$r_M^{\ air} = 21\ (\text{MeV})\ \frac{37.8\ (\text{g cm}^{-2})}{84\ (\text{MeV})} = 9.45\ (\text{g cm}^{-2}) = 79\ (\text{m})\,.$$
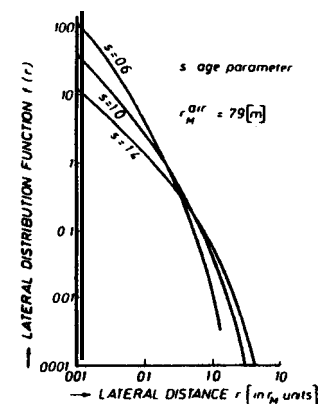
Fig. 8.7: Lateral distribution of electrons in a cascade in air
(From Cranshaw. T. E.: Cosmic Rays. Oxford Library of the Physical Science 1963)

8.4. Hadron cascades

Hadron showers have also been simulated both by analytical methods, using diffusion equations, and by Monte Carlo methods. The cross-sections for the inelastic processes, the inelasticity, the multiplicity, the ionization loss, and the nuclear excitation energy are used. Monte Carlo calculations following the thermodynamical model determine the momentum spectra of the secondary particles after each collision for pp- and p-nucleus interactions, for different primary momenta. Secondary spectra of $\pi^{\pm}$, $K^{\pm}$, $p^{\pm}$, A, Σ, Ξ are obtained. These data are widely used for estimates of shielding requirements. Fig.8.8 shows differential π^{+} spectra produced in a pp-interaction, at an incident lab momentum of 800 GeV/c and Fig.8.9 shows the corresponding π^{-} spectra. In **Fig.8.10** the proton momentum distribution also for an incident momentum of 800 GeV/c is given.

In a hadron cascade, the secondary particles either interact again, decay, or are absorbed as a result of ionization energy loss. The hadrons build up to a shower maximum as in an electromagnetic cascade after which the numbers decrease. Because decay muons do not interact by strong interactions, they only lose energy by ionization, and therefore have a slower decrease. In Fig.8.11 is shown the number of shower particles with energy greater than 100 MeV, produced by an incident proton of the energy 200 GeV in-
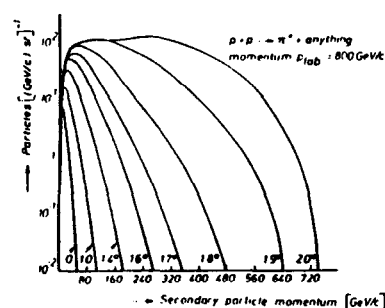
Fig. 8.8: The differential particle spectra of π^{+} in the pp-interaction at 800 GeV/c (Adapted from Grote[1], H., et al.: Particle Spectra, CERN 1970)
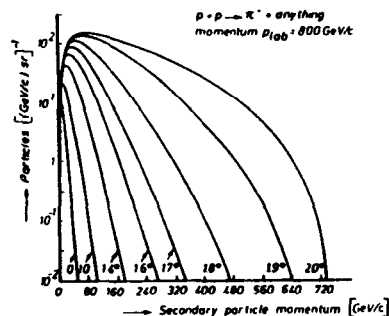
Fig. 8.9: The differential particle spectra of π^{-} in the pp-interaction at 800 GeV/c (Adapted from Grote', H. et al.: Particle Spectra, CERN 19701)

---

[1] New calculations give slightly different plots.
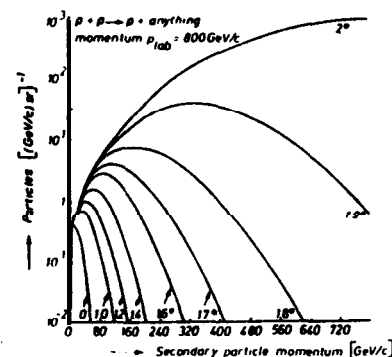
Fig. 8.10: The differential proton spectra in the pp-interaction at 800 GeV/c (Adapted from Grote[1], H. et al.: Particle Spectra, CE RN 19701
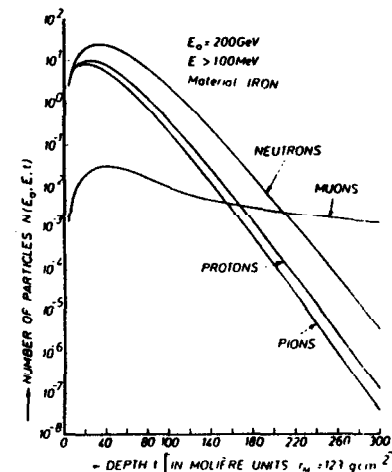
Fig. 8.11: Development of a hadron cascade in iron for protons of 200 GeV (Adapted from Alsmiller, R. G., J. Barish: Oak Ridge National Laboratory, Report ORNL-TM-1121 (1965))

cident on iron as a function of depth. The units are Moliere length, $r_M = 12.3$ g cm^{-2}. The curves are seen to be different for neutrons, protons, pions, and muons.

References

Rossi, 8.: High-energy particles. Englewood Cliffs: Prentice-Hall 1954

Hayakawa. S.: Cosmic-ray physics. New York: Willey-Interscience 1969

Nagel, H. H.: Electron-Photon-Kaskaden in Blei. Zeitschiift fur Physik 186 (1965) 319

Grote, H.. R. Hagedorn, J. Ranft: Atlas of particle production spectra. CERN 1970

Alsmiller, R. G., J. Barish: The nucleon-meson cascade initiated by 200 GeV protons. Oak Ridge National Laboratory. Report ORNL-TM-1121 (1965)

9. Transformation in the atmosphere

9.1 Introduction

The primary cosmic radiation is influenced by the earth's magnetic field, its flux is modulated by solar activity, and its composition is changed due to interactions with the atoms, molecules, and nuclei of the atmosphere.

Protons of the primary radiation interact with the electrons of atoms and molecules, and lose energy by excitation and ionization (Bethe-Bloch formula). The energy loss of a relativistic particle traversing the atmosphere, ~ 1000 g cm^{-2}, is ~ 2.2 GeV.

The incident particles undergo strong interactions with the nuclei of oxygen and nitrogen. Above an energy of a few GeV, local penetrating showers are produced by emission of nucleons and mesons. If the energy is high enough, the primary proton continues to interact with nuclei and produces further particles; the high-energy secondaries do likewise. The most numerous particles are pions, but kaons and hyperons are also present.

An average of 12 interactions take place through the atmosphere, corresponding to a mean interaction length of ~ 80 g cm^{-2}. Thus a hadron cascade is frequently created. The atmospheric nuclei become highly excited and then de-excite by emission of light nuclei, mainly alpha particles and nucleons of energy $\leqslant 10$ MeV.

The heavy nuclei of the primary radiation are fragmentated in their first interaction, which occurs at a higher altitude than for protons because of the shorter interaction length (see Fig. 7.51. For a nucleus with A = 25, the mean interaction length is ~ 20 g cm^{-2}, corresponding to about 50 interactions through the atmosphere. Hence, there is no chance for a heavy nucleus to penetrate down to sea level.

Amongst all the secondaries, the pion triplet π^+, π^o, π^- is the most important. The charged pions have a mean lifetime of 2.6×10^{-8} s, and decay via the processes $\pi^+ \rightarrow \mu^+ + \nu_\mu$ and $\pi^- \rightarrow \mu^- t\ \bar{\nu}_\mu$ into muons and neutrinos. When the energy is high enough, the mean lifetime τ_0 is significantly enhanced by the time dilatation effect

$$\tau = \tau_0 \frac{E}{m_0} = \gamma\ \tau_0 .$$

γ Lorentz factor
E total energy
m_0 rest mass

If $E \gtrsim 100$ GeV, the have the opportunity to interact with a nucleus before they decay, and in this way produce secondary particles which contribute to the hadron cascade. The $\pi^\pm$ decays give rise to a muonic component which is easily able to penetrate the atmosphere because muons lose only ~ 2 GeV of energy, by ionization, down to sea level. Although the muon lifetime is small, $\sim 2.2 \times 10^{-6}$ s, most of them survive to sea level because of time dilatation. However, some of them do decay

$$(\mu^+ \rightarrow e^+ + \nu_e + \bar{\nu}_\mu\ ;\ \mu^- \rightarrow e^- + \bar{\nu}_e + \nu_\mu)$$

producing electrons and neutrinos.

The neutral pions decay into gamma rays ($\pi^o \rightarrow 2\gamma$) with a mean lifetime of $\sim 10^{-16}$ s. If the energy is high enough, the gamma rays produce $e^+ e^-$ -pairs, which in turn undergo bremsstrahlung, and so on. In this way an electromagnetic cascade is built up through the atmosphere. A high-energy primary proton can create about a million of secondaries, which are spread out laterally on their way through the atmosphere. Such a cascade is called *extensive air shower.*

An increase in the number of particles occurs in the first 100 g cm^{-2}, after which there is a continuous decrease due to absorption and decay processes. This maximum was first detected by Pfotzer, at a height of about 20 km, and is called Pfotzer maximum (Fig. 9.1).
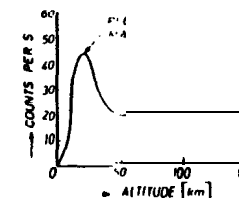

Fig. 9.1: Variation of the total cosmic ray flux with altitude

There are altogether, three components in the atmosphere: the *hadronic component,* which constitutes the core of the shower, the *electron-photon* component, corresponding to the electromagnetic cascade, and the *muonic component,* arising mainly from the decay of charged pions. The development of the three components is shown schematically in Fig. 9.2. Due to their different behaviour, the three components have different altitude dependences. This is shown in Fig. 9.3.

The fluxes and energy spectra of the different components in the atmosphere are discussed in the following sections. A general survey of
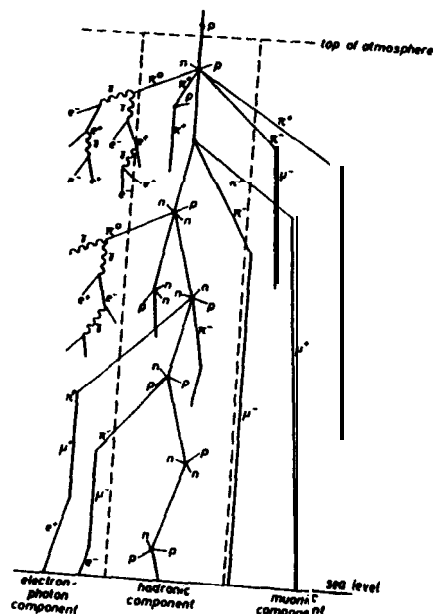
Fig. 9.2: Schematic representation of the development of particle production through the atmosphere

the field is given, but not the methods by which the results are obtained. No account is taken of the modulation of the fluxes and energy spectra at low energies, $\leq 10^{11}$ eV, by the magnetic fields transported by the solar wind, which lead to changes of intensity. For the primary radiation, the intensity around 1 GeV changes by approximately a factor 4 during the solar cycle. This effect will be considered later in Chapter 13.
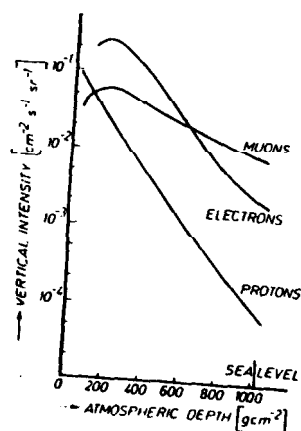
Fig. 9.3: Altitude variation of the main cosmic ray components

There is in addition,an effect due to the geomagnetic field, important at low energies, which will be treated in Chapter 12.

9.2. Basic data of the atmosphere

In order to provide a better understanding of the secondary processes which take place in the atmosphere, some of its basic features are outlined. The earth's atmosphere is a large volume of gas with a density of almost 10^{19} particles per cm^3, at sea level. As the distance from the earth increases, the density of the neutral particle concentration decreases,at the rate of about a factor of e for each 15 km, up to an altitude of 120 km.

The atmosphere is composed mainly of oxygen and nitrogen, although smaller amounts of other constituents are present. In the homosphere, which corresponds to the atmosphere up to a level of about 85 km,the composition remains fairly constant. Table 9.1 gives the number of molecules per cm^3, n, of each constituent at standard pressure (760 mm Hg) and standard temperature (273.2 K), and also, its relative percentage, c.

Table 9.1: Composition of the atmosphere
(Ratcliffe, J. A., (Ed.): Physics of the Upper Atmosphere. New York: Academic Press, 1960)

molecule	$n(cm^{-3})$	$C = n/n_{air}$ (%)
air	2.607×10^{19}	100 .
N_2	$2.098 \times 10^{'9}$	78.1
O_2	5.629×10^{18}	20.9
Ar	$2.510 \times 10^{''}$	0.9
CO_2	8.87×10^{15}	0.03
He	1.41×10^{14}	5×10^{-4}
Ne	4.89×10^{14}	1.8×10^{-3}
Kr	3.06×10^{13}	1×10^{-4}
Xe	2.34×10^{12}	9×10^{-6}

Specific regions are defined within the atmosphere according to their temperature variations. These include the troposphere, where the processes which constitute the weather take place, the stratosphere which is generally without clouds, where ozone is concentrated, the *mesosphere* which lies between 50 and 80 km, where the temperature decreases with increasing altitude, and the thermosphere, where the temperature increases with altitude up to about 130 km. A schematic representation of the atmosphere, with variation of temperature is shown in Fig.9.4. The layers between the different regions are calledpauses, i.e. tropopause, stratopause, and mesopause.
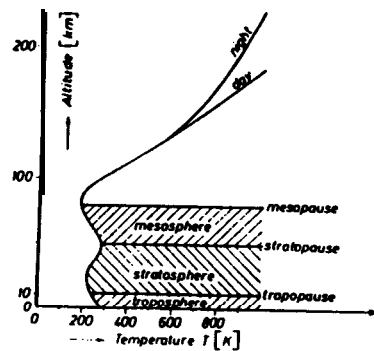
Fig. 9.4: Schematic representation of the atmosphere

The variation of density with altitude in the atmosphere is a changeable quantity which depends upon the meteorological parameters. The variation of each component may be represented by the barometric law

$$n_i\,(x,\,t) = n_0\,(x_0)\,\frac{T(x_0)}{T(x,\,t)}\,\exp\left[-\int_{x_0}^{x}\frac{dx}{H_i}\right].$$

$H_i = \dfrac{RT}{m_i\,g(x)}$ scale height for each component

n_i density of component i at height x and time t
x_0 sea level
T temperature
R gas constant
g gravity acceleration constant
m_i atomic mass of the i-th component

In a static isothermal atmosphere, for which complete mixing equilibrium of all constituents is assumed, the relation reduces to

$$n = n_0 \exp\,(-x/H_0)\,,$$

where H_0 is a mean scale height for the mixture.

For the real atmosphere, the same relation applies, if the scale height H_0 varies slightly with altitude. Table 9.2 gives some values of H_0 for different atmospheric depths. A similar relation applies to the variation of pressure with altitude.

Table 9.2: Scale heights at different depths in the atmosphere
(From Rossi, 9.: High-Energy Particles, Englewood Cliffs, N.J.: Prentice-Hall 1952)

x (g cm^{-2})	10	100	300	500	900
H_0 (10^5 cm)	6.94	6.37	-- 6.70	7.37	6.21

110
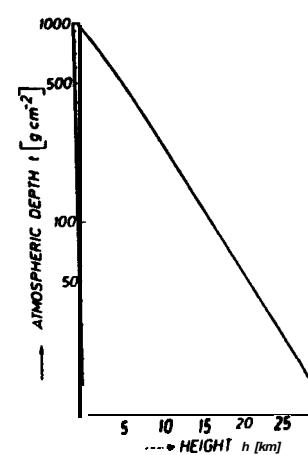
Fig. 9.5: Relation between atmospheric depth and altitude for an isothermal atmosphere (Reproduced from Rossi, 6.: High-Energy Particles. Englewood Cliffs, N.J.: Prentice-Hall 19521
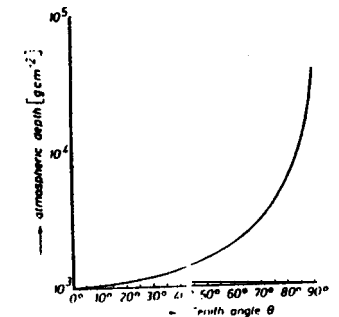
Fig. 9.6: Relation between zenith and atmospheric depth

Fig. 9.6 shows the relation between density and altitude in the real atmosphere, for the region which is important for cosmic-ray transformation processes. In an inclined direction, i.e. for non-zero zenith angle, the change of density per unit length is less than in the vertical clirection. Furthermore, the total thickness of atmosphere increases with increasing zenith angle. This is shown in Fig. 9.6, where in the horizontal direction, i.e. $\Theta = 90°$, the thickness is approximately 40 times greater.

9.3. General intensity considerations

Intensity and flux have already been defined in Chapter 4.1. In order to obtain the omnidirectional intensity, the angular variation of the intensity $j\,(\Theta,\,\varphi)$ must be known. Measurements have found that there is practically

111

no azimuthal dependence for any of the components (see Section 12.7 for east-west effect), and that the variation with zenith angle can be expressed as

$$j(\Theta) = j_\perp \cdot \cos^{n_i} \Theta,$$

where $j_\perp = j(\Theta = 0)$. The exponent n_i for the component i depends upon the depth x and the energy E, i.e. $n_i = n_i(x, E)$.

The hadronic component is attenuated in the atmosphere with an attenuation length Λ, and its altitude dependence is expressed as

$$N(x) = N_0 \cdot \exp(-x/\Lambda).$$

At a zenith angle Θ, the thickness traversed is $x \cdot \sec \Theta$ and so the angular dependence is

$$j(\Theta, x) = j_\perp \cdot \exp(-x \sec \Theta/\Lambda)$$

Assuming that cosmic radiation impinges isotropically on the top of the atmosphere, that the particle trajectories are not influenced by the earth's magnetic field, and that the intensity $j(\Theta, x)$ depends only on the thickness of the material traversed, then $j(x, \Theta)$ depends only on $x \sec \Theta$

$$j(x, \Theta) = j_\perp(x \cdot \sec \Theta).$$

Thus, the omnidirectional intensity J_2, is given by

$$J_2(x) = 2\pi \int_0^{\pi/2} j(\Theta, x) \sin \Theta \, d\Theta$$

$$J_2(x) = 2\pi \int_0^{\pi/2} j_\perp(x \sec \Theta) \sin \Theta \, d\Theta.$$

Differentiation of this expression leads to the Gross transformation

$$2\pi j_\perp(x) = J_2(x) - x \frac{dJ_2(x)}{dx}.$$

By means of this formula, the vertical intensity can be obtained from the omnidirectional intensity or vice versa.

For both practical and historical reasons, cosmic radiation is divided into two components, a hard component and a soft component. This classification is determined by an ability to penetrate 15 cm lead, which corresponds to a thickness of 167 g cm^{-2}. The soft component, which is unable to penetrate this thickness, is composed mainly of electrons, whereas the hard penetrating component consists of muons and hadrons, the dominant

one depending on the altitude. At sea level the hard component consists mostly of muons.

9.4. Secondary particles

The energy spectra of secondary particles produced by primary proton interactions can be calculated from a knowledge of the hadron-hadron interaction at high energies. The primary protons, which have an energy spectrum of the form

$$N(E_p) \propto E_p^{-\gamma_p},$$

produce secondary hadrons, pions and kaons, which either decay or interact further. The energy spectra of the secondary particles can be calculated, if the relevant cross-sections, the energy variation of the multiplicity, and the distribution of transverse momenta are known. Calculation of the energy spectra of secondary particles have been made by both analytical and Monte-Carlo methods using CERN ISR data up to 1.5 TeV. The secondary spectra produced in the first interaction have a similar form to the primary spectra. For secondary pions

$$N(E_s) \propto E_s^{-\gamma_\pi}$$

with an exponent, γ_π, very similar to the exponent of the primary spectrum, i.e.

$$\gamma_\pi \sim \gamma_p.$$

Because the secondary particles are able to decay on their way through the atmosphere, the decay probabilities must be known in order to calculate the energy spectra. The mean lifetime for a particle of energy E is given by

$$\tau(E) = E/m \, c^2 \cdot \tau_0 = \gamma \cdot \tau_0 .$$

The distance travelled during this time is

$$s = v\tau \approx c\beta\gamma\tau,$$

and the decay rate per unit length is

$$\frac{1}{l} = \frac{1}{c\beta\gamma\tau_0}.$$

In a medium of density ρ, the mean free path, λ_d, for spontaneous decay is given by

$$\frac{1}{\lambda_d} = \frac{1}{c\beta\gamma\tau_0\rho}.$$

The number of particles dN, which decay within a thickness dx, is given by

$$dN = -N \, dx/\lambda_d$$

and hence, the number remaining after a thickness x is

$$N = N_0 \cdot \exp\left[-\int \frac{dx}{\lambda_d}\right]$$

and the number of decays is

$$N' = N_0 - N = N_0\left[1 - \exp\left(-\int \frac{dx}{\lambda_d}\right)\right].$$

The decay probability $W = N'/N_0$ is given by

$$W = \left[1 - \exp\left(-\int \frac{m \, dx}{\rho p \, \tau_0}\right)\right] \approx \frac{mx}{\rho p \, \tau_0}$$

When the decaying particle is incident at an angle Θ, the decay probability is increased for the same atmospheric depth x, by the factor sec Θ, hence,

$$W \approx \frac{mx \sec \Theta}{PP \ \tau_0} \ .$$

m mass of the decaying particle
x thickness traversed
ρ density
Θ zenith angle
p momentum
τ_0 mean lifetime

From these formulae, it is seen that the decay probability depends on the mass, the mean lifetime, and the momentum or energy of the particle. The decay probabilities for pions and kaons in the atmosphere, as a function of energy, are given in Fig. 9.7.
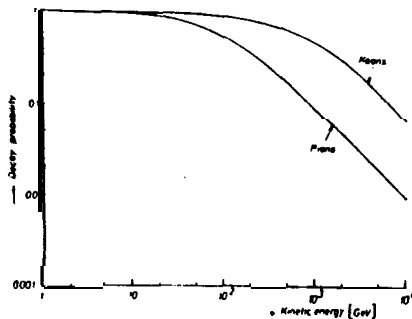
Fig. 9.7: Decay probabilities for charged pions and kaons as a function of kinetic energy

On their way through the atmosphere, charged pions and kaons decay into muons, which in turn can lose energy by ionization and also decay into electrons and neutrinos. The decay probability for muons W_μ, is derived in a similar manner to that for mesons. At a specific level in the atmosphere, the energy spectrum of muons is given by

$$N_\mu(E) = A \ W_\pi(E + \Delta E)^{-\gamma_\mu} (1 - W_\mu)$$

where

$$\gamma_\mu \approx \gamma_\pi \ .$$

A   absolute intensity normalization constant
E   energy loss by ionization
W_π meson decay probability
$(1 - W_\mu)$ survival probability of muons

At low energies, all mesons decay into muonos, which subsequently decay and lose energy at a rate which increases as the energy decreases. This leads to a maximum in the muon spectrum (Fig. 9.8).
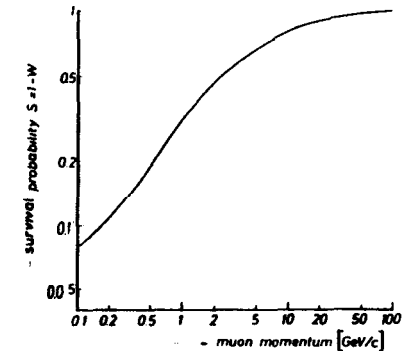
Fig. 9.8: Survival probability for muons from the depth 100 g cm^{-2} to sea level as a function of momentum

At higher energies, mesons not only decay but also interact strongly with the air nuclei. Thus, some pions decay into muons, while others interact and hence lose energy. These effects give rise to a steepening of the muon spectrum relative to the pion spectrum. The energy spectrum in this region can be expressed by the formula

$$N_\mu(E) = N_\pi(E) \ \frac{B}{B + E}$$

B   constant which takes account of the steepening.

$$B = \frac{m \, c^2}{c \, \tau_0} \ \frac{RT}{\langle m \rangle g} \ \frac{m_\mu}{m_{mes}}$$

m_{mes} mass of decaying meson

$\dfrac{RT}{\langle m \rangle g} = H_0$ scale height factor

$\langle m \rangle$ mean atomic mass of the atmosphere

τ_0 lifetime of decaying meson

B has values of 90 GeV for pions and 517 GeV for kaons. Since both, pion and kaon components are present, the energy spectrum is expressed as

$$N_\mu(E) = N_\pi(E)\left[\frac{\alpha B_\pi}{E + B_\pi} + \frac{(1-\alpha)\,B_K}{E + B_K}\right] ,$$

α fraction of pions

$\gamma = \gamma_\pi = \gamma_K$ at high energies.

For $B \gg E$, i.e. in the energy range 10 to 100 GeV, the above formula leads to

$$N_\mu(E) \propto N_\pi(E) .$$

For higher energies, $B \ll E$, the muon spectrum has the approximate form

$$N_\mu(E) \propto N_\pi(E)/E ,$$

which leads to a steepening of the energy spectrum as shown in Fig. 9.9.
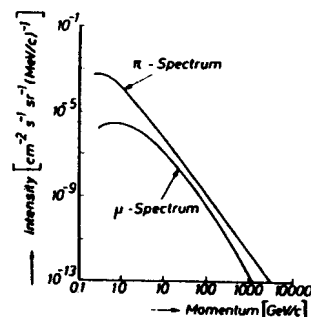
Fig. 9.9: Comparison of the shapes of pion and muon spectra

9.5. Protons

All cosmic-ray components in the atmosphere are supplied with energy by the hadron cascade. The energy of the primary proton after the first collision is

$$E_1 = E_0(1 - K)$$

K inelasticity

and therefore after the n-th collision is

$$E_n = E_0(1 - K)^n .$$

Assuming an inelasticity of 0.4, a primary proton with an energy of 10^{12} eV at the top of the atmosphere will arrive at sea level with an energy of $E_n = 10^{12} \times 0.6^{14} \approx 8 \times 10^8$ eV. Obviously, the proton component is strongly attenuated on its way through the atmosphere. Correspondingly, the charged pion component is reduced, since in addition to strong interactions, decays may also occur.

The attenuation resulting from strong interactions can be expressed as

$$I = I_0 \exp(-x/\Lambda) .$$

Λ 120 to 130g cm^{-2} attenuation length
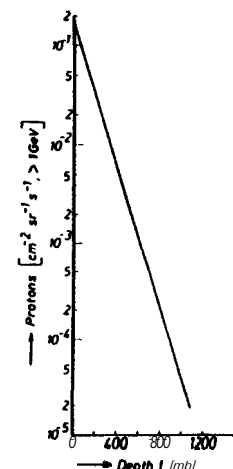
Fig. 9.10: Altitude variation of the proton flux in the atmosphere
(Adapted from J. Geophys. Res. 66 (1963) 5 487)
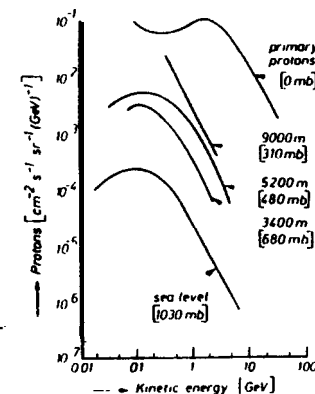
Fig. 9.11: Energy spectra of protons in the atmosphere

At the top of the atmosphere and at the geomagnetic latitude of 55°. the intensity for energies of $E \gtrsim 1$ GeV is about 0.2 protons $(\text{cm}^2 \text{ sr}^{-1})$. The variation with altitude has been measured, and is shown in Fig. 9.10 for protons with $E \gtrsim 1$ GeV.

Energy spectra of protons high up in the atmosphere have only been measured in the low-energy region. In Fig. 9.11, the differential energy spectra at 3,400 m, 5,200 m and 9,000 m are shown, together with the sea level spectrum. The energy spectra of protons and negative pions at sea level have been measured more precisely and to higher energies. Fig. 9.12 shows the differential energy spectra of both types of particles.
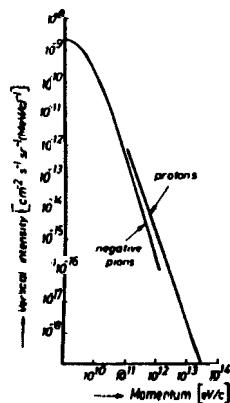
Fig. 9.12: Energy spectra of protons and π^- at sea level (Adapted from Brooke, G.: Protons and Pions. in Cosmic Rays at Ground Level (Ed. A. W. Wolfendale). London: The Institute of Physics 1973)

9.6. Muons

Muons are the principal cosmic-ray component both at sea level and underground, and will be discussed in more detail in Chapter 10. In this section only their general features and altitude dependence will be considered. At sea level, the vertical intensity $j_\parallel$, the total flux J_1, and the omnidirectional intensity J_2 (see Section 4.1) have been accurately measured, for both the soft and the hard components. Values of these quantities for the hard component, at high latitudes, are given in Table 9.3.

Table 9.3: Muon intensities at sea level
(Adapted from Allkofer, 0. C., K. Carstensen, W. D. Dau, H. Jokisch: J. Physics, G: Nucl. Phys. Vol 1. No. 6. L 1 (1975))

$j_\parallel$	$(0.94 \pm 0.05) \times 10^{-2} \text{ cm}^{-2} \text{ sr}^{-1} \text{ s}^{-1}$
J_1	$(1.44 \pm 0.09) \times 10^{-2} \text{ cm}^{-2} \text{ s}^{-1}$
J_2	$(1.90 \pm 0.12) \times 10^{-2} \text{ cm}^{-2} \text{ s}^{-1}$

The sea-level value of the vertical intensity at 1 GeV/c is an important standard, often used to normalize the momentum spectrum. Recent measurements have found a value 25 % higher than much earlier ones. The present value is

$$j_\parallel (1 \text{ GeV/c}) = 3.09 \times 10^{-3} \quad \text{cm}^{-2} \text{ sr}^{-1} \text{ s}^{-1} (\text{GeV}/c)^{-1}$$

Muon spectra have also been measured at mountain altitudes. Fig. 9.13 shows spectra measured at 3 000 m and 5 200 m.
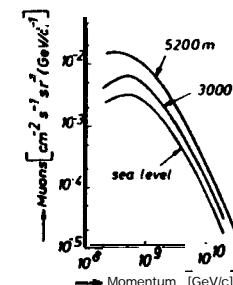
Fig. 9.13: Differential muon spectra in the atmosphere (From Allkofer, O. C.: Fortschritte der Physik 15. (1967) 1131

9.7. Electrons

Electrons contribute about 1% to the total intensity of the primary cosmic radiation. On entering the atmosphere, they initiate electromagnetic cascades. Small fluxes of X-rays and gamma rays are also present in the primary radiation, but the intensities are too weak to contribute significantly to the secondary intensities in the atmosphere.

The main sources of electrons in the atmosphere are processes initiated by the primary hadronic component. These are:

Decay of short-lived particles, created by the interactions of the hadronic component with air nuclei. Mesons, hyperons and resonance particles are produced, which decay directly or via other particles giving rise to electrons. The most important decay channel is

$$\pi^\pm \rightarrow \mu^\pm \rightarrow e^\pm .$$

Knock-on electrons. These are produced by interactions of the primary hadronic component and also secondary particles such as pions and muons. Near the top of the atmosphere the former process dominates, while deep in the atmosphere the muon contribution is dominant.
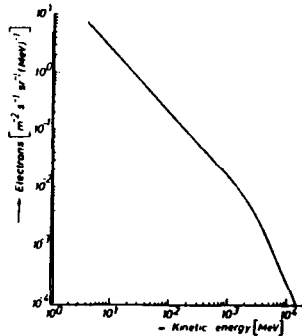
Fig. 9.14: Differential energy spectrum of electrons at the depth 2.5 g cm^{-2} during the night (0.21 GeV)
(Adapted from Daniel. R. R., S. A. Stephens: Review of Geophysics and Space Physics 12, (1974) 2331

Calculations of the energy spectra of electrons in the atmosphere have been performed using the cascade theory; the results agree fairly well with the measured values. Measurements have been made at mountain top and balloon altitudes. Fig. 9.14 shows the energy spectrum at an atmospheric depth of 2.5 g cm^{-2} and a geomagnetic latitude equivalent to a threshold energy of 0.21 GeV, measured during the night. Fig. 9.15 shows electron energy spectra (electrons and positrons combined) at different altitudes in the atmosphere.

Negative electrons are present in greater numbers than positive ones, because the latter are not produced in the knock-on process. In addition, the Compton effect produces only e^-. The charge ratio $N(e^+)/N(e^-)$ varies with altitude; at sea level, in the momentum range 0.05 to 1 GeV/c, a value of 0.5 to 0.6 has been measured.

9.8. Gamma radiation

The main source of gamma radiation in the atmosphere is neutral pion decay. If the number of neutral pions created per interaction is the same as the numbers of π^+ and π^-, the gamma spectrum should be similar to the muon spectrum, which is produced by decay of the charged pions. The differential energy spectrum of gamma rays is shown in Fig. 9.16. It includes data measured over a wide range of energy. In order to combine data from experiments carried out at different altitudes, the energy spectrum is expressed in g cm^{-2} of air. This spectrum is in agreement with theoretical predictions. In order to show the effect of the atmosphere, the calculated spectra are presented in Fig. 9.17 for different atmospheric depths, and at a latitude with a geomagnetic cut-off rigidity of 4.5 GV (see Section 12.3).

Decay of radioactive nuclei, which are created by interactions in the atmosphere or are emitted from the earth's surface. This process is not very important.

Compton effect. Energetic photons liberate electrons from air molecules.

Because electron spectra extend down to MeV energies, the fluxes as well as the spectra depend strongly on the geomagnetic latitude, the eleven-year cycle and meteorological parameters of the atmosphere. In particular, there are differences between day and night.

Fig. 9.15: Differential energy spectra of electrons in the atmosphere
(Adapted from Daniel, Ft. R., S. A. Stephens: Review of Geophysics and Space Physics 12. (1974) 233)

Fig. 9.16: Differential energy spectrum of gamma rays in the atmosphere
(Adapted from Daniel, R. R.. S. A. Stephens: Review of Geophysics and Space Physics 12, (1974) 233)
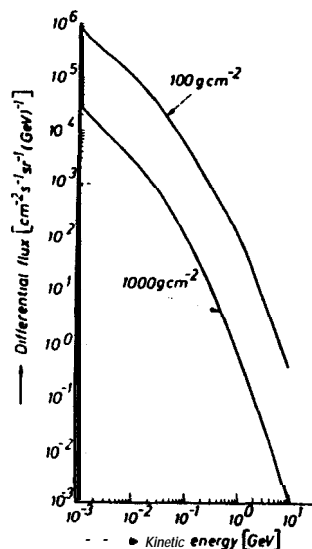
Fig. 9.17: Calculated energy spectra of gamma rays in the atmosphere
(Adapted from Daniel, R. R., S. A. Stephens: Review of Geophysics and Space Physics 12, (1974) 2331

9.9. Neutrons

As a result of the interaction of primary hadrons with atmospheric nuclei, the nuclei are left in highly excited states. These subsequently de-excite, with evaporation of nuclear matter including neutrons. Since the primary component is electrically charged,the secondary neutrons show a latitude effect (see Section 12.5). The neutrons have energies in the range $10^{-3} < E_n < 10$ MeV,with a maximum at around 1 MeV.

In addition to the evaporation neutrons, fast neutrons are produced by direct interactions of incident protons with nuclei. The latter neutrons have energies in the range $10 < E_n < 500$ MeV. The energy spectra of slow and fast neutrons have different slopes. Neutrons with very high energy contribute to the hadron cascade as a result of the charge exchange. interaction. Neutrons can not lose energy by ionization and are only
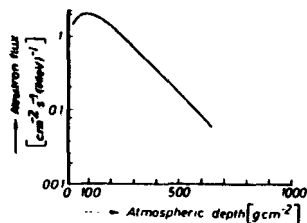
Fig. 9.18: Altitude variation of the neutron flux in the atmosphere for neutrons in the energy range $1 \leqslant E_n \leqslant 10$ MeV
(Adapted from Schopper, E.. E. Lohrmann, G. Mauck: Nukleonen in der Atmosphare, Hand-buch der Physik. Kosmische Strahlung II, 372 Berlin: Springer Verlag 1967)
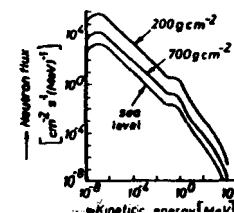
Fig. 9.19: Energy spectra of neutrons in the atmosphere in the low energy range
(Adapted from Schopper, E., E. Lohrmann, G. Mauck: Nukleonen in der Atmosphare, Handbuch der Physik, Kosmische Strahlung II. 372 Berlin: Springer Verlag 1967)

attenuated by strong interactions with air nuclei. Thus, the flux is attenuated like the proton flux, following an exponential law

$$N(x) = N_0 \cdot \exp(-x/\Lambda).$$

The attenuation length A, in the atmosphere is ~ 155 g cm^{-2}. Fig. 9.18 shows the measured neutron flux in the energy range $1 \lesssim E_n < 10$ MeV. It is seen that there is a build-up process as for the charged component of cosmic radiation,with a maximum at a depth of ~ 100 g cm^{-2}, i.e. the same value as for the charged component.

Energy spectra of neutrons at different altitudes are shown in Fig. 9.19. Maxima occur at an energy of less than 1 eV and at around 500 keV, the latter being due to the shape of the neutron evaporation spectrum.

The differential energy spectrum of fast neutrons as measured at sea level, up to energies of about 1 TeV, is shown in Fig. 9.20. It displays the average
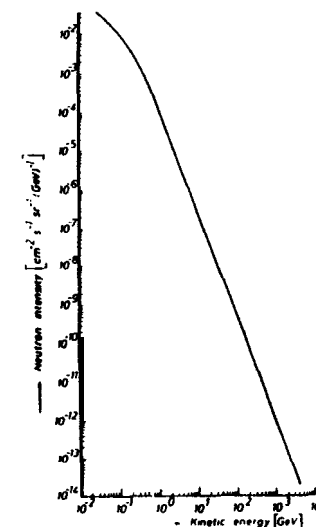
Fig. 9.20: Differential energy spectrum of fast neutrons at sea level
(Adapted from Brooke, G.: Protons and Pions in Cosmic Rays at Ground Level (Ed. A. W. Wolfendale), London: The Institute of Physics 1973)

characteristics of high-energy nucleon-nucleus interaction when compared with the shape of the primary proton spectrum. If the mean free path for a nucleon to undergo an interaction in air is λ, then the average number of collisions n, in an atmospheric thickness x, is x/λ, and the probability that m collisions will occur is given by the Poisson distribution

$$P(m) = \frac{e^{-n}n^m}{m!}$$

As the result of a collision, the incident nucleon of energy E emerges with a mean energy $(1 - K)E$ and loses an amount of energy KE. Now consider a nucleon of energy E, at depth x, produced by a primary proton of energy E_p, and suppose that it has made m interactions on its way through the atmosphere. Then $E = (1 - K)^m E_p$, df $= (1 - K)^m dE_p$ and the differential energy spectrum of nucleons at depth x is given by

$$N(E)\,dE = \sum_{m=0}^{\infty} \left(\frac{E}{\eta^m}\right)^{-\gamma} \frac{dE}{\eta^m} P(m)$$

$$= A \cdot E^{-\gamma}\,dE\, e^{-n} \sum \frac{\eta^{m(\gamma-1)} n^m}{m!}$$

$$= A \cdot E^{-\gamma}\,dE\, e^{-n} \left(1 + \frac{\eta^{(\gamma-1)} n}{1} + \frac{\eta^{2(\gamma-1)} n^2}{2} + \cdots\right)$$

$$= A \cdot E^{-\gamma}\,dE \cdot \exp\left[- n\left(1 - \eta^{\gamma-1}\right)\right]$$

$$= A \cdot \exp\left[-\left(\frac{x}{\lambda}\right)\left(1 - \eta^{\gamma-1}\right)\right] E^{-\gamma}\,dE$$

$$= A \left[\exp\left(-x/\Lambda\right)\right] E^{-\gamma}\,dE$$

where $\eta = 1 - K$.

The attenuation length Λ, is given by

$$\Lambda = \frac{\lambda}{1 - \eta^{\gamma-1}} = \frac{\lambda}{1 - (1 - K)^{\gamma-1}}.$$

λ interaction mean free path
γ exponent of the differential spectrum
K inelasticity

Thus, the differential energy spectrum of nucleons at a depth x has the same shape as the primary spectrum, and is of the form

$$N(E_p)\,dE_p = A \cdot E_p^{-\gamma}\,dE_p,$$

the difference is in the attenuation factor, exp (-x/A).

Neutrons in the atmosphere interact with the nitrogen isotope N 14, and produce carbon C 14 by the reaction

$$^{14}_{7}N + n \rightarrow {}^{14}_{6}C + p.$$
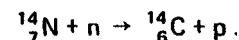
The isotope C 14 then decays by beta decay with a half-life of 5 570 years. Carbon is absorbed into plants as CO_2 and hence, also the nuclide C 14. The plants are then eaten by animals. When the plants or animals die, the assimilation ceases and from that time on, the C 14 content is reduced by radioactive decay. Hence, by measuring the C 14 content, the age of samples of vegetation or animal remains can be estimated.

9.10. Heavy nuclei

The primary flux of heavy nuclei is rapidly diminished by fragmentation in the upper atmosphere. In addition, the heavy nuclei suffer a high ionization loss because $(- dE/dx)_{ion} \propto Z^2$. The interaction mean free path in air lies between 30 and 15 g cm^{-2} and is dependent on the mass of the incident nucleus (see Fig.7.5). Thus, no heavy nuclei are able to penetrate to sea level. As a result of the fragmentation process, the numbers of some primary nuclei are strongly decreased while others are newly created. The change dN_j/dx, in the number of nuclei of charge j, within a layer dx (g cm^{-2}) due to fragmentation, can be described by the diffusion equation

$$dN_j(x)/dx = - N_j(x)/\lambda_j + \sum_{i>j} N_i(x)\, P_{ij}/\lambda_i$$

$\lambda_{i,j}$ interaction mean free path for the charge i, j
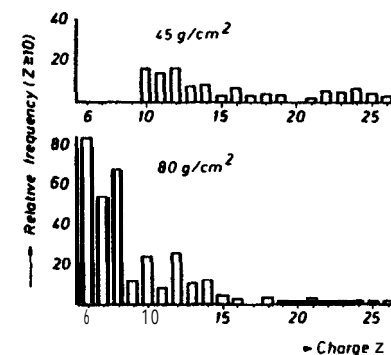P_{ij} fragmentation probability from charge i to charge j

Fig. 9.21: **Charge spectra** of heavy nuclei in the atmosphere (From Allkofer. O.C., W. Heinrich: Nucl. Phys. B 71, (1974) 429)
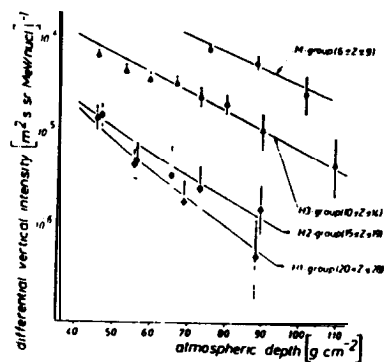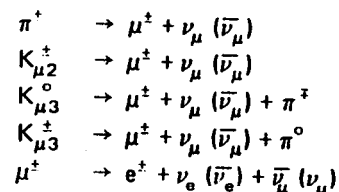
Fig. 9.22: Attenuation of the flux of heavy nuclei in the atmosphere (From Allkofer, 0. C., W. Heinrich: Nucl. Phys. B71, (1974) 429)

The change in the chemical composition of the primary flux due to fragmentation is shown in Fig. 9.21; the primary charge spectrum and the charge spectra at the depths 45 g cm^{-2} and 80 g cm^{-2}, are shown for nuclei with charges $Z \geqslant 10$.

The differential vertical intensities have been measured and also calculated down to a depth of about 100 g cm^{-2}. The attenuation of the flux is shown in Fig. 9.22 for some of the charge groups.

9.11. Neutrinos

Both, primary and secondary neutrinos are present in the atmosphere. The secondary neutrinos are decay products of unstable particles produced in the atmosphere. Muon-neutrinos are produced in the following interactions:

$$\pi^{\pm} \rightarrow \mu^{\pm} + \nu_\mu \, (\bar{\nu}_\mu)$$
$$K_{\mu 2}^{\pm} \rightarrow \mu^{\pm} + \nu_\mu \, (\bar{\nu}_\mu)$$
$$K_{\mu 3}^{o} \rightarrow \mu^{\pm} + \nu_\mu \, (\bar{\nu}_\mu) + \pi^{\mp}$$
$$K_{\mu 3}^{\pm} \rightarrow \mu^{\pm} + \nu_\mu \, (\bar{\nu}_\mu) + \pi^{o}$$
$$\mu^{\pm} \rightarrow e^{\pm} + \nu_e \, (\bar{\nu}_e) + \bar{\nu}_\mu \, (\nu_\mu)$$

Electron-neutrinos are produced in muon decay and to a lesser extent in kaon decay, via the decay mode $K^{\pm} \rightarrow e^{\pm} \pi^{o} \nu_e \, (\bar{\nu}_e)$, which has a branching ratio of about 5%. Electron-neutrinos are also produced in the earth's crust by beta decay of radionuclides. However, this flux is very low in comparison with fluxes from other sources; it has the approximate value of 7×10^6 cm^{-2} s^{-1}.
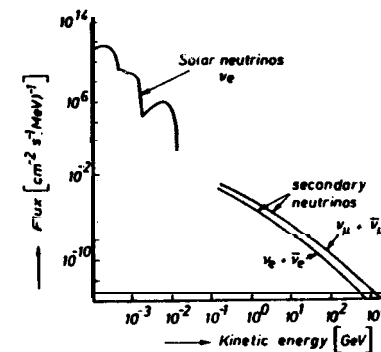
Fig. 9.23: Energy spectra of neutrinos in the atmosphere (Adapted from Wolfendale, A. W.: Cosmic Ray Neutrinos in Lecture on Space Physics (Eds. A. Bruzek, H. Pilkuhn) Diisseldorf: Bertelsmann Universitatsverlag 1973)

Hence, the neutrino flux in the atmosphere is composed of extraterrestrial neutrinos coming mainly from the sun, plus muon- and electron-neutrinos produced in the atmosphere. The principal component is the secondary muon-neutrino one. Spectra of the neutrinos present in the atmosphere have not been measured, but since the particles are produced by kinematically known decays of pions, kaons, and muons, the spectra can be calculated. In Fig. 9.23 are shown the energy spectra of secondary muon and electron-neutrinos, and for comparison the low-energy solar neutrinos. The total neutrino flux with energy $E > 1$ GeV at sea level, is about 2×10^{-6} cm^{-2} s^{-1} sr^{-1}.

9.12 Zenith angle dependence

The fluxes and energy spectra of all secondary particles in the atmosphere have an angular variation. There are two reasons for this; firstly, the atmospheric depth changes with zenith angle and so the thickness of matter traversed increases with increasing angle. This leads to the results that for all charged particles the ionization loss increases, the energies are shifted to lower values, and there is a low energy cut-off. Furthermore, the mean number of strong interaction collisions increases, so that even neutron fluxes are attenuated. The second reason is that for a fixed path length, the change of atmospheric density decreases with zenith angle. Hence, an unstable particle reaches a higher density more quickly at vertical incidence than at a larger zenith angle. The probability of interaction is higher for vertical incidence, and the probability of decay is higher at large zenith angles. Thus for unstable strongly interacting particles, there is a competition between interaction and decay; the interaction mean free path also being dependent on zenith angle. The above behaviour is discussed in
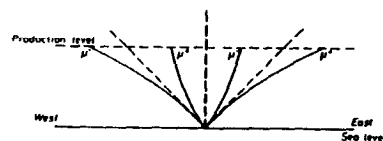
Fig. 9.24: Bending of particle trajectories by the geomagnetic field

Fig. 9.26: Variation of the exponent $n = n(E)$ in the expression $I(\Theta) = I(0)\cos^n(\Theta)$ at sea level for muons (From Flint, R. W., et al.: Canad. J. Phys. 50 (1972) 843)

Chapter 9.4, where it is seen that the decay probability increases with zenith angle Θ.

The mean lifetime τ_0 and the mass of the particle are of course also important. Since

$$W_K/W_\pi = (M_K/M_\pi)(\tau_\pi/\tau_K) \approx 6.6,$$

for equal momenta, the decay probability for kaons is higher than for pions by a factor of ~ 6.6.

For muons, a decrease of the atmospheric flux with angle is expected at low energies, but at higher energies an increase should occur due to the higher decay probability of mesons. At low energies there is a further reduction,because the particle trajactories are bent due to the geomagnetic field leading to aprolongation of the path lengths (Fig.9.24). The decrease of the muon flux with increasing zenith angle is shown for large zenith angles in Fig. 9.25.

The angular distribution of muons can be expressed as

$$I(\Theta) = I(0)\cos^n\Theta,$$

where the exponent n has the value 2 for the integral intensity at low energies, and depends upon the energy of the particle. The value of n decreases with energy as the effect of ionization loss becomes less important. The variation of $n = n(E)$ has been both measured and calculated and is shown in Fig. 9.26.

The increase of the sea-level muon flux with energy, at high energies,is shown in Fig 9.27. Here,the muon fluxes have been calculated assuming that muons are only decay products of charged pions.

The decrease of the intensity at low energies is shown in Fig. 9.28 where the measured sea level spectra are given for different zenith angles.
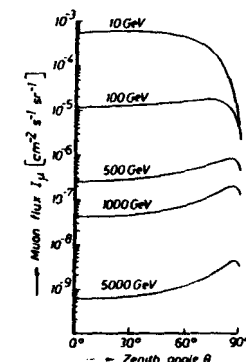
Fig. 9.27: Zenith angle variation of the muon flux at sea level for different production energies (Adapted from Maeda. K.: Fortschritte der Physik 21 (1973) 113)

Fig. 9.25: Zenith angle variation of the total muon flux at sea level (From Flint, R. W., et al.: Canad. J. Phys. 50, (1972) 843)
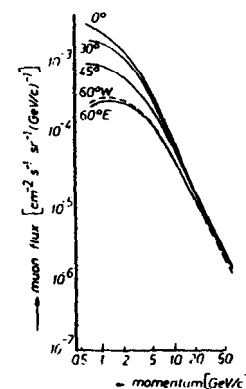
Fig. 9.28: Differential momentum spectra of muons at sea level for different zenith angles (From Judge, R. J. R., W. F. Nash: Nuov. Cim. 35 (1965) 999)

References

Wolfendale, A. W.: Cosmic Rays at Ground Level. The Institute of Physics, London (1973)

Schopper, E., E. Lohrmann, G. Mauck: Nukleonen in der Atmosphare. Handbuch der Physik: Kosmische Strahlung II (1967) 372

Allkofer, O.C.: Die Hohen- und Zenithwinkelabhangigkeit der Energiespektren von Ultrastrahlungsteilchen. Fortschritte der Physik 16 (1967) 113

Hayakawa. S.: Cosmic-Ray Physics. New York: Willey-Interscience 1969

Daniel R. R, S.A. Stephens: Cosmic-ray produced electrons and gamma rays in the atmosphere. Review of Geophysics and Space Physics 12 (1974) 233

Allkofer, 0. C., H. Jokisch: A Survey on the recent measurements of the absolute vertical cosmic-ray muon flux at sea level. Nuov. Cim. 15A (1973) 371

Maeda, K.: Energy and Zenith Angle Dependence of Atmospheric Muons. Fort-schritte der Physik 21 11973) 113

Allkofer. 0. C., W. Heinrich: Attenuation of cosmic ray heavy nuclei fluxes in the upper atmosphere by fragmentation. Nucl. Physics B71 (1974) 429

Flint, R. W.. R. B. Hicks, S. Standil: Variation with zenith angle of the integral Intensity of muons near sea level. Canad. J. Physics 50 (1972) 643

Kertz, W.: Einfuhrung in die Geophysik. B1 Hochschultaschenbiicher, Bd. 535. Mannheim: Bibliographisches Institut 1971

10. Leptons at sea level and underground

10.1.   Introduction

For a long time, cosmic ray muons at sea level and underground were the only charged high-energy leptons with which electromagnetic interact ions could be studied. The advent of electron accelerators changed this situation, and new results have subsequently been obtained. Powerful proton accelerators are also able to provide beams of muons and neutrinos up to energies of several hundred GeV, via the decay of pions and kaons. For higher ener-gies, $\geqslant$ 300 GeV, cosmic rays remain as the only source of incident muons, although their intensity is very low compared with accelerator beams.

The problems associated with the use of cosmic radiation for neutrino interactions are great because the cross-sections involved are very low, in the region of 10^{-40} to 10^{-36} cm^2. In addition, a serious shielding problem exists because the muons produced in the interactions have to be distinguished from the muonic cosmic-ray background. Neutrino interactions are conse-quently performed deep underground, mostly in mines.

The main component of cosmic radiation at and below the earth's surface is the muon. The fluxes and energy spectra of muons have been measured very precisely and are important geophysical standards.

In this chapter, the muonic component, at sea level and underground will be discussed and the depth-intensity relation of muons will be derived. The charge ratio of muons, i.e. the ratio of positively to negatively charged muons, which is strongly influenced by the fact that the primary cosmic radiation is predominatly positively charged, will also be considered. Finally, some measurements of electromagnetic interactions of muons, and weak interactions of muon-neutrinos will be discussed.

10.2. The muon spectrum at sea level

The general features of the muonic component at sea level have already been described,in Chapter 9. Here the form of the spectrum was derived, and the sea-level fluxes were given. The energy or momentum spectrum of muons at sea level has been measured many times mostly with magnetic spectrographs. Precision has improved with time, so that today the shape of the spectrum and the absolute normalization are accurately known. Measurements with magnetic spectrographs have been made up to an energy of $\sim$ 1 TeV. Fig. 10.1 shows the momentum spectrum of sea-level muons, both charges combined, in differential and integral form, meas-ured in the vertical direction.
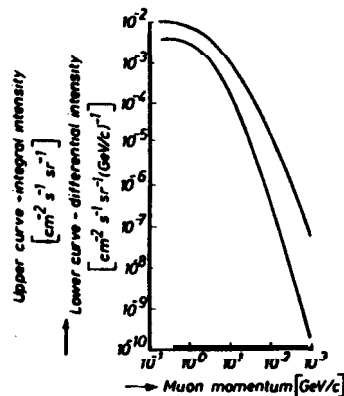
Fig. 10.1: The absolute differential and integral momentum spectra of muons at sea level
(From Allkofer, O. C.. K. Carstensen, W. D. Dau, Phys. Lett. 36B 119711 425)

The momentum spectrum has also been measured very precisely in the near horizontal direction. Its shape turns out to be different from the vertical one for two reasons. Because the atmosphere is appreciably thicker in the horizontal direction than in the vertical one, low-energy muons are more strongly absorbed and their fluxes are reduced. At high energies, the parent mesons can either decay or interact strongly. Which process occurs, is influenced by the density of the atmosphere. The interaction mean free path increases as $\sec \Theta$, and hence the probability of decay and consequently the flux of high-energy muons increases with zenith angle. In the low-energy region, the muon flux is reduced, compared with the vertical one, and in the high-energy region it is increased. The cross over occurs at ~ 170 GeV/c for the differential momentum spectrum. This behaviour has already been discussed in Section 9.4. Fig. 10.2 shows the differential momentum spectrum of muons at a zenith angle of 83° and in the vertical direction. The larger flux at inclined directions is used to obtain higher counting rates in high-energy muon experiments.
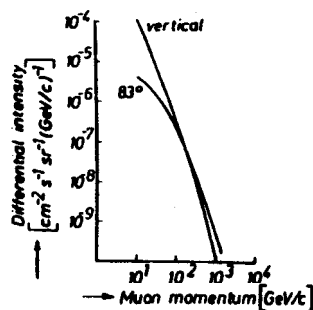
Pig. i0.2: The near horizontal muon spectrum at sea level, and comparison for the vertical spectrum
(Adapted from Allkofer, O. C. et al., 12. International Conference on Cosmic Rays. Hobart (1971), Conference papers, University of Tasmania)

10.3. The charge ratio of muons

The primary cosmic radiation is composed almost entirely of positively charged particles. This charge excess is transformed and diluted by inter-actions in the atmosphere which produce further generations of particles. The mean charge ratio of muons at sea level is found to be

$$r = N(\mu^+)/N(\mu^-) \approx 1.28.$$

This effect is sometimes expressed as a positive excess

$$s_\mu = \frac{N(\mu^+) - N(\mu^-)}{N(\mu^+) + N(\mu^-)}.$$

The positive excess first appears in the pions

$$s_\pi = \frac{N(\pi^+) - N(\pi^-)}{N(\pi^+) + N(\pi^-)} = \frac{Q}{M},$$

The difference $Q = N(\pi^+) - N(\pi^-)$ is the average charge excess given to the secondary pions in the first interaction. It has the approximate value of 1/2, when averaged over all possible interactions of a primary proton with an air nucleus. The sum $M = N(\pi^+) + N(\pi^-)$ is the multiplicity of charged pions. For $M = 5$, $s_\pi = 0.1$ and $r = 1.22$.

If all pions were to decay into muons, a muon charge ratio of the same value would result.

A dilution of the overall excess at sea level occurs for the following reasons:

(1) In addition to protons, the primary cosmic rays consist of heavier nuclei which contain neutrons. The primary proton excess is

$$s_p = \frac{N(p) - N(n)}{N(p) + N(n)} \approx 0.74$$

i.e. 83 % protons and 13 % neutrons.

(2) Secondary nucleons are produced by the hadron cascade which in turn produce secondary pions. If the same fraction of protons and neutrons are knocked out of the air nuclei ($^{16}_8O$, $^{14}_7N$), a zero overall excess results. However, since the secondary nucleons are mainly of low energy, this dilution factor is negligible.

(3) Low-energy muons decay on their way from production to sea level.

(4) High-energy secondary mesons interact instead of decaying, and thus change the effective multiplicity.

The final muon excess is $s_\mu = f \cdot s_p \cdot s_\pi$, where f corresponds to the sum of the different atmospheric effects. The momentum dependence of the
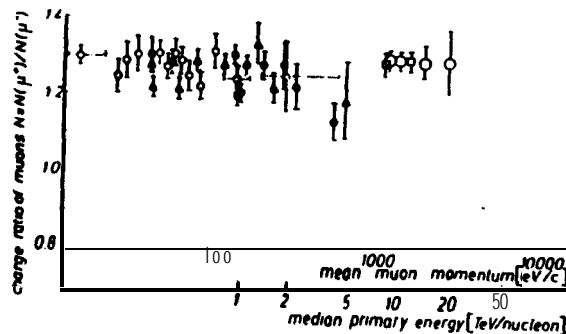
Fig. 10.3: The charge ratio $r = N(\mu^+/\mu^-)$ of muons at sea level (Adapted from Ashley, G. K. et al.: Phys. Rev. Lett. 31 (1973) 1091 and Ayre et al.: J. Phys. A: Gen. Phys. 4 (1971) L89)

charge ratio has been measured many times, up to an energy of $\sim$ 1 TeV, by means of magnetic spectrographs. Such measurements have also been made underground, at energies which correspond to the TeV range when transformed to sea level. Fig. 10.3 shows the measured charge ratio at sea level for a wide range of momentum. Because of low statistics there are large variations in these results. Using the pp-interaction data of the CERN/ISR, the charge ratio has been calculated up to 1500 GeV, assuming Feynman scaling and the hypothesis of limited fragmentation. An approximately constant value is found for the whole momentum range. However, some of the calculations give a high absolute value of $r \approx 1.6$, in contrast to the measured average value of 1.28.

10.4. Depth-intensity relation for muons

Cosmic-ray particles which enter the earth's crust or its oceans, lose energy by several types of interaction. Electrons are quickly absorbed as a result of cascade processes and hadrons are removed by nuclear interactions. Only neutrinos and muons remain.

A study of underground muons is important for several reasons. The relation between depth and muon intensity is of considerable geophysical interest. Muon fluxes have been measured at different depths under rock, and in the sea, down to depths of $\sim 10^6$ g cm^{-2}. From a study of the intensity of muons at different depths, information is obtained about the

electromagnetic processes which reduce the flux. By using the measured intensities and extrapolating the measured electromagnetic cross-sections to the TeV region, muon spectra can be extended to TeV energies.

Finally, the shielding of experiments involving neutrino-interactions is achieved by carrying them out, deep underground. For these measurements, the background muon flux has to be known, because the interaction products are themselves energetic muons.

Starting with the energy-loss relation for muons

$$- dE/dx = a + bE,$$

the mean range can be derived by integration

$$R = -\int_0^E \left(\frac{dx}{dE}\right) dE = \int_0^E \frac{dE}{a + bE} = \frac{1}{b} \cdot \log\left(\frac{a + bE}{a}\right),$$

also

$$E = a/b(e^{bR} - 1) .$$

For low-energy muons $(E_\mu \ll 100 \text{ GeV})$ with $bE \ll a$, this relation simplifies to

$$R = E/a$$

By expressing the integral energy spectrum of muons at sea level as

$$M(> E) = A \cdot E^{-\gamma},$$

the intensity $I(R)$ at depth R can be written as

$$I(R) = M(> E) = A[a/b(e^{bR} - 1)]^{-\gamma} .$$

For $e^{bR} \gg 1$, and using

$$B = \left(\frac{A \cdot a}{b}\right)^{-\gamma},$$

the following depth-intensity relation is obtained

$$I(R) = B \cdot \exp(- bR\gamma) .$$

If the intensity is measured in an inclined direction, at a depth R, the depth-intensity relation is modified by a factor sec Θ

$$I(R, \Theta) = B \sec \Theta \cdot \exp(- bR\gamma \sec \Theta) .$$

For small depths, in the vertical direction, a series expansion of the above equation gives
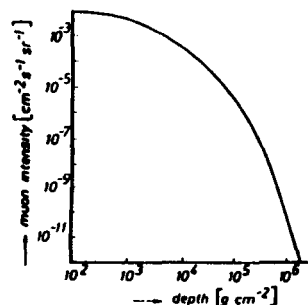
$$I(R) = A(aR)^{-\gamma},$$

Fig. 10.4: Depth-intensity relation of cosmic
ray muons underground
(From Miyake, S.: Rapporteur Paper, 13. Inter-
national Cosmic Ray Conference, Denver (1973))

which shows that the shape of the muon spectrum is reproduced. For
large depths

$$I(R) \propto \exp\left(- bR\gamma\right),$$

corresponding to an exponential decrease of intensity with depth. The
dominant energy-loss process for small thicknesses is ionization, represented
by the factor a, whereas for large depths the electromagnetic processes, b,
are more important. When energy loss occurs by ionization, only small
fluctuations arise between events, because the loss is due to many single
processes. In contrast,the bremsstrahlung mechanism which is dominant at
high energies, is a single process in which a large energy loss can occur, and
as a result large fluctuations are produced in the depth-intensity relation.
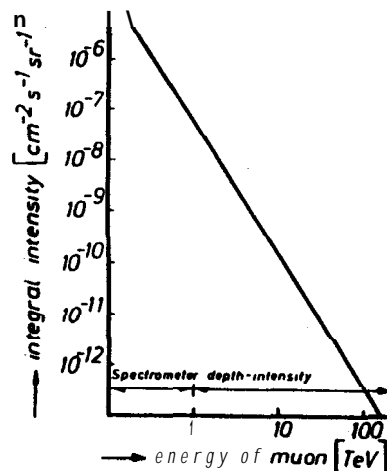
Fig. 10.5: The integral energy spectrum
of muons at sea level in the TeV region
as derived from the depth-intensity
relation
(From Miyake. S.: Rapporteur Paper,
13. International Cosmic Ray Conference,
Denver (1973))

In Fig. 10.4, the depth-intensity relation is shown,down to the greatest
depth presently measured. This figure utilizes measurements made in dif-
ferent absorbers, such as rocks of different density and water, by expressing
the depth in g cm^{-2}. The results lead to the energy spectrum of muons at
sea level up to ~ 100 TeV as shown in Fig. 10.5.

10.5. Electromagnetic interactions of muons

In spite of the low fluxes,cosmic-ray muons on the surface and under-
ground have been used to study electromagnetic interactions; formerly,
because for a long time no muons were available from accelerators and
now, because the cosmic-ray spectrum still extends considerably beyond
the muon energies available from accelerators.

There is one basic difference between the study of muon interactions at
accelerators and in cosmic radiation. The cross-section for an electro-
magnetic process depends upon the incident muon energy, E_μ, the
scattered muon energy, E_μ', and the four-momentum q^2, i.e.
$\sigma_i = \sigma_i(E_\mu, E_\mu', q^2)$. In accelerator experiments the muon energy is
fixed and the variation with E_μ' and q^2 or the energy loss

$$\nu = E_\mu - E_\mu'$$

is studied, i.e.

$$\sigma_i = \sigma_i(q^2, \nu).$$

Because the cross-sections for the different electromagnetic processes
decrease with q^2, the cosmic-ray flux only allows a study at very low
q^2, i.e. $q^2 \rightarrow 0$,

$$\sigma_i = \sigma_i(E_\mu, E_\mu') = \sigma(E_\mu, \nu).$$
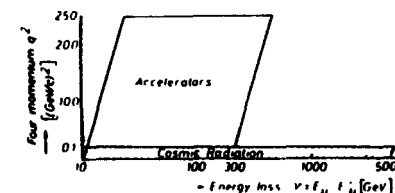

Fig. 10.6: Cross-section domains
for electromagnetic interactions
at accelerators and in cosmic
radiation

Fig. 10.6 shows schematically the domains of present accelerator and
possible future cosmic-ray experiments. The following electromagnetic
interactions have so far been studied in cosmic radiation:

Knock-on mechanism. In this process (see Section 6.3), an electron is liberated from the shell of an atom

$$\mu + A \rightarrow \mu + A + e^- .$$
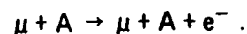
The cross-section is almost independent of the mass of the incident particle.

Bremsstrahlung. Electromagnetic radiation is emitted due to interaction with the electric field of a nucleus (see Section 6.4). In this process energy loss and consequently range, fluctuate strongly.

Direct pair production. A virtual photon converts to a pair of electrons in the field of a nucleus

$$\mu + A \rightarrow \mu + A + e^+ + e^- .$$
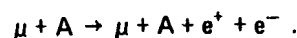
Because the interaction gives rise to three tracks it is called the trident process. The cross-section for muon pair production is less, by a factor of $(m_e/m_\mu)^2$ (see Section 6.8).

Inelastic scattering on nuclei. Here, the muon interacts with the nucleus via a virtual photon, producing nucleons and mesons

$$\mu + A \begin{cases} \rightarrow \mu + A' + (p, n) \\ \rightarrow \mu + A' + (\pi, K) \end{cases}$$
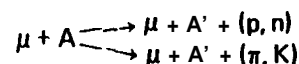
The cross-section for these processes is given by

$$\sigma(E_\mu, \nu) = \int N(E_\mu, \hbar\omega)\, \sigma_{ph}(\hbar\omega, \nu)\, d(\hbar\omega) .$$

$N(E_\mu, \hbar\omega)$ virtual photon spectrum
$\sigma_{ph}(\hbar\omega, \nu)$ photonuclear cross-section

Several types of measurement have been made with differing degrees of precision. They may be classified as follows (see Fig. 10.7):

(1) Shower measurements (Fig. 10.7 A). Muons initiate a local shower which is absorbed in a calorimeter, an assembly of detectors and absorber plates. Hence, ν is evaluated. From a knowledge of the incident intensity, and the target composition and thickness, the cross-section as a function of ν can be obtained, $\sigma(\nu)$. This cross-section is related to the cross-section of interest, $\sigma(E_\mu, \nu)$ by

$$\sigma(\nu) = \int_{E_\mu} N(E_\mu)\, \sigma(E_\mu, \nu)\, dE_\mu .$$

$N(E_\mu)$ energy spectrum of incident muons

A. Shower measurement   B. Shower size measurement

C. Spectrometer + Calorimeter

D. Horizontal air shower HEAS
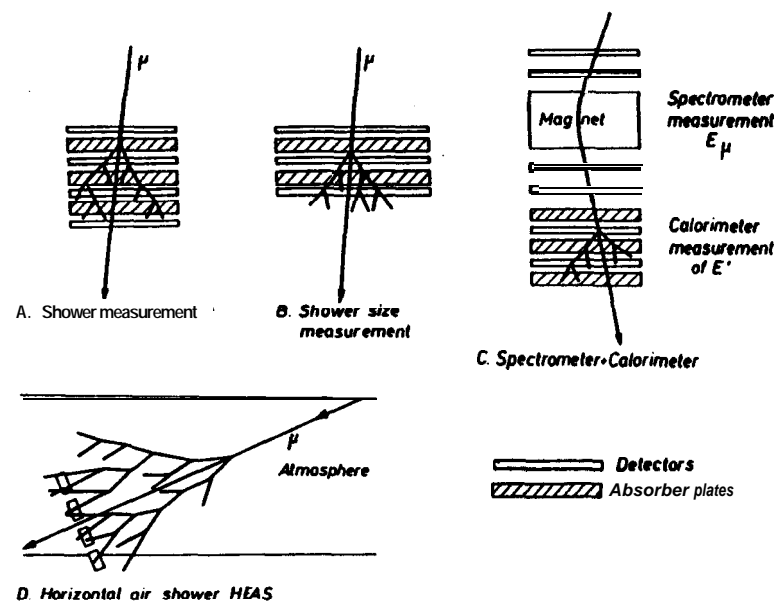
Fig. 10.7: Schematic *representation* of cosmic ray equipment for studying electromagnetic interactions

(2) Shower size measurements (Fig. 10.7 B). In this technique, a part of the shower is measured in a calorimeter of limited size. Only showers of size > s can be measured, and their cross-sections $\sigma(> s)$ obtained. Such a cross-section is related to $\sigma(E_\mu, \nu)$ by

$$\sigma(> s) = \iint N(E_\mu)\; \sigma(E_\mu, \nu)\, f(\nu, s)\, dE_\mu\, d\nu$$

$f(\nu, s)$ probability, that a secondary particle of energy E' produces a shower of size s

This method is less accurate than (1), because less information is measured and more uncertainty is folded in.

(3) Spectrometer measurements (Fig. 10.7 C). The momentum of the muon is measured with a magnetic spectrograph, and the energy transfer obtained by shower measurements, using a calorimeter. Since the probability for each electromagnetic process mentioned above depends upon the
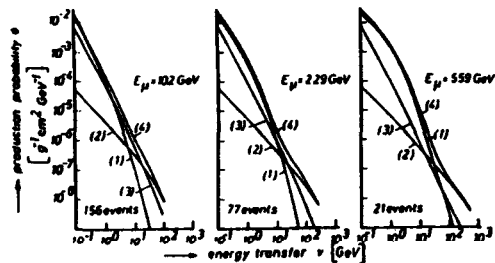
Fig. 10.8: Experimental data for the electromagnetic interactions of muons in cosmic radiation. The curves are the theoretical predictions :(1) pair production, (2) bremsstrahlung, (3) knock-on process, (4) sum of all processes. [From **Allkofer, 0. C., C. Grupen, W. Stamm: Phys. Rev. D 4 (1971) 638)**

incident muon energy, a knowledge of the energy enables the process to be identified.

(4) Horizontal air showers, HAS (Fig. 10.7 D). Primary cosmic-ray particles of high energy produce extensive air showers (see Chapter 11), which are widely distributed laterally. Because the thickness of atmosphere increases with zenith angle, horizontally initiated showers are mainly absorbed in the atmosphere and do not reach ground level. However, by means of bremsstrahlung, high-energy muons can produce electromagnetic cascades in the atmosphere, which are measurable by shower-size methods at sea level. Cross-sections for incident energies of $E_\mu > 10^{14}$ GeV are thereby measured.

Fig. 10.8 shows measured cross-sections for the different processes. In Fig. 10.9 the measured cross-section for muons of energy 1 TeV as a function of energy transfer ν, is shown together with theoretical values. Fig. 10.10 shows the variation of the cross-sections with muon energy.
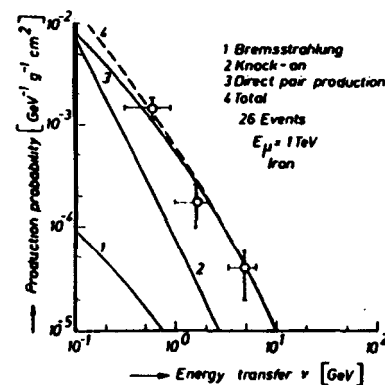
Fig. 10.9: Total cross-section for muom as a function of ν for an incident energy 1 TeV
(From Allkofer, 0. C., C. Grupen: Cosmic Ray Muons in Lectures on Space Physics (Eds. A. Bruzek. H. Pilkuhn). Diisseldorf: Bertelsmann Universitiitsverlag, 19731
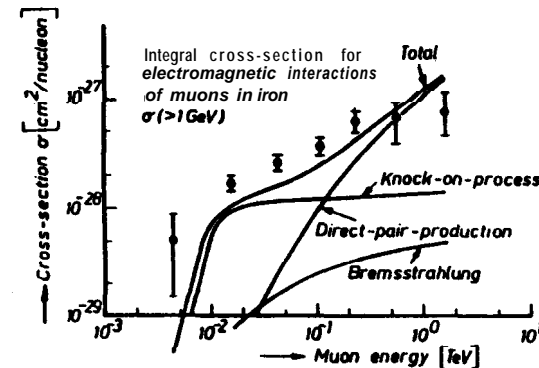
Fig. 10.10: Variation of the integral cross-section for electromagnetic interaction of muons with energy E_μ
(From Allkofer, 0. C., C. Grupen: Cosmic Ray Muons in Lecture on Space Physics (Eds. A. Bruzek, H. Pilkuhnl. Diisseldorf: Bertelsmann Universitiitsverlag 1973)

From the above results, the photonuclear cross-section in the TeV region can be derived. Fig. 10.11 shows the photonuclear cross-section as measured at accelerators in the lower energy range, together with cosmic-ray data at very high energies.
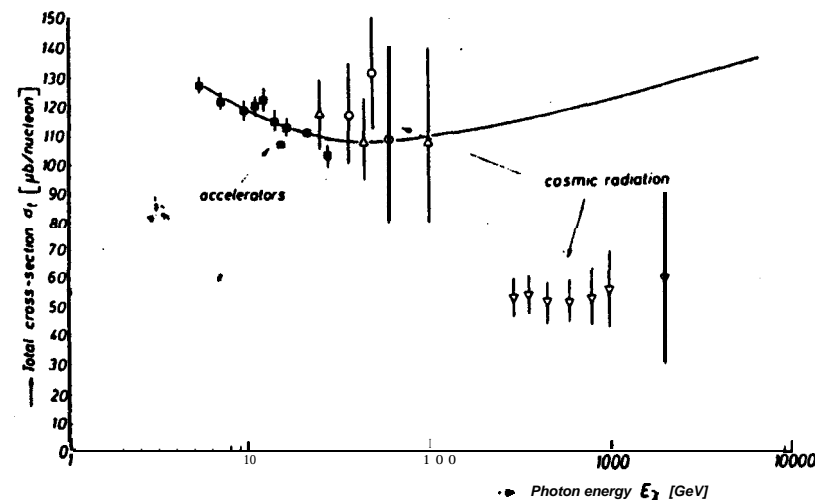
Fig. 10.11: Photonuclear cross-sections measured at accelerators and in cosmic radiation

140

141

19.6. Neutrino interactions

There are two essential reasons why neutrinos are studied in cosmic radiation. Firstly, because calculations of neutrino fluxes from stars should, if possible, be tested by measurements. This is particularly true for the electron-neutrinos produced by thermonuclear interactions in the interior of the sun (see Section 4.81. Secondly, in addition to this astrophysical interest, there is a related particle physics reason. Cross-sections for weak interactions can be investigated at neutrino energies well beyond those available from accelerators.

Solar neutrinos. Electron-neutrinos are produced in the interior of the sun, principally by the mechanism which converts hydrogen to helium. Calculations of their energy spectra have been made (see Fig. 9.23). Because of the very small cross-sections*involved, the detection of these particles requires large pieces of equipment. *Davis* used the inverse beta decay reaction

$$\nu_e + {}^{37}Cl \rightarrow {}^{37}Ar + e^-,$$
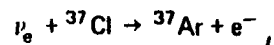
to detect these neutrinos and to measure their flux. The Ar 37 decays by K-capture with a half-life of 35 days. In this experiment a large volume of liquid C_2 Cl, was used, and the detector was situated about 1 500 m underground, to shield against background radiation. It was finally necessary to extract the few radiactive Ar 37 atoms from tons of the liquid in order to identify them.

The measured neutrino flux was nearly a factor of 10 lower than expected, and comparable with the background radiation. There was a finite probability that no electron-neutrinos were detected.

Muon-neutrino interactions The main component of the neutrino flux in the atmosphere and underground is the muon-neutrino. Detectors which are sensitive to this type of particle have been used.

There are three possible interactions which are of interest,

(a)   the quasi-elastic interaction $\nu_\mu + n \rightarrow \mu^- + p$,

(b)   the inelastic interaction $\nu_\mu + K \rightarrow \mu + K' + mesons$; K, K'nuclei,

(c)   production of the intermediate boson W
$$\nu_\mu + K \rightarrow \mu + K + W$$
$$\nu_\mu + K \rightarrow \mu + K' + W + mesons.$$

142
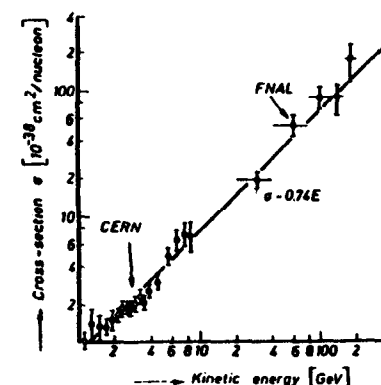
Fig. 10.12: Total cross-section for +-interactions measured et accelerators
(Adapted from Faissner, H.: Naturwissenchaften 62 (1975) 53)

The Fermi theory of weak interactions predicts that the neutrino cross-section increases with energy and so rises indefinitely. However, if the intermediate boson exists there should be a limit at around 250 GeV. Fig. 10.12 shows the measured total cross-section as measured at accelerators which displays a linear increase with neutrino energy.

In order to investigate muon-neutrino interactions at higher energies, cosmic radiation must be used, although, for weak interactions, the low particle flux is a serious disadvantage. The total neutrino-induced muon flux at sea level is $\sim 10^{-13} cm^{-2} s^{-1} sr^{-1}$ compared with the total atmospheric muon flux of $\sim 10^{-2} cm^{-2} s^{-1} sr^{-1}$. It is apparent that neutrino interactions must be performed deep underground.

Cosmic-ray experiments carried out underground have produced a total of about 200 interactions, which gives a ν_μ-flux of (2.6 to 3.5) x 10^{-13} $cm^{-2} s^{-1} sr^{-1}$ in approximate agreement with the expected value. No intermediate boson has been found and a lower limit on its mass is $m_W \geqslant 2.6$ GeV.

References

Allkofer. O.C.. K. Carstensen, et al.: The muon momentum spectra and positive-negative ratios at sea level in the energy range, 10 to 1 500 GeV. 12th International Conference on Cosmic Rays. Hobart (1971) Conference Papers, University of Tasmania.

Allkofer. O.C., K. Castensen, W.D. Dau: The absolute cosmic ray muon spectrum at sea level. Phys. Lett. 36 B, (1971) 425.

Wolfendale. A.W., (ed.) Cosmic rays at ground level. London: The Institute of Physics 1973.

Bruzek. A., H. Pilkuhn tad.): Space Physics. Dusseldorf: Bertelsmann Universitats-verlag 1973.

Ashley, G. K., et al.: Muon charge-ratios measurements and comparision with predictions from hadron scaling. Phys. Rev. Lett. 31 (1973) 1091.

Adair. R. K.: Anomalous muon and hadron charge ratios in secondary cosmic rays. Phys. Rev. Lett. 33 (1974) 115.

Miyake, S.: Rapporteur Paper on muons and neutrinos. 13th International Cosmic Ray Conference, Denver 1973.

Allkofer, 0. C., C. Grupen, W. Stamm: Electromagnetic interactions of high-energy cosmic-ray muons. Phys. Rev. D4 (1971) 638.

Gabathuler, E.: Total photon cross-sections. Rapporteur's talk at the international symposium on electron and photon interactions at high energies, Bonn 1974.

Borog, V. V.. et al.: Energy dependence of the nuclear interaction cross-section of cosmic muons in the range 0.3 to 3 TeV. Canad. Journ. Phys. 46 (1968) 381.

Faissner. H.: Neue Ergebnisse der Neutrino-Experimente. Z. Naturwissenschaften 62 (1975) 53

11. Extensive air showers

11.1. Introduction

When a high-energy hadron enters the atmosphere, it creates, by means of cascade processes, thousands and even millions of secondary particles, which are widely distributed often over several square kilometers. This phenomenon,which involves hadronic, electron-photon and muonic components is called an Extensive Air Shower (EAS). The general features of cascade processes have already been discussed in Chapter 8 and develop ment in the atmosphere in Chapter 9 (see Fig. 9.2).

EAS are of interest for two main reasons; to provide astrophysical infor-mation and to study particle interactions at extremely high energies, beyond 10^{14} eV.

Knowledge of the primary energy spectrum at energies up to 10^{20} eV, comes from EAS measurements. In principal, the chemical composition of primary cosmic radiation at the highest energies can be derived from air-shower measurements, although present results are mutually inconsis-tent. In addition, searches for point sources of cosmic-ray particles in space have been made using EAS. Since most of the primary cosmic-ray particles are deflected by the intergalactic magnetic fields, information about their origin is lost. However, protons with energies beyond about 10^{17} eV are little influenced on the way from their sources, and so EAS detection equipment looks at the highest energies for anisotropies in space. A final interesting point is whether or not the energy spectrum ceases at around 10^{20} eV.

The particle-physics interest in EAS comes from the fact that interactions at accelerators can only be studied up to limited energies, i.e. for protons up to $\sim$ 1 500 GeV. Even if possible future accelerators extend this energy range up to say 10^{14} eV,there will still remain an extensive energy region beyond. Thus phenomena like scale invariance, the increase of multiplicity with energy and the limited fragmentation hypothesis can only be studied in EAS at ultra high energies. The low intensity of cosmic rays, particu-larly at the highest energies, makes the study of EAS very difficult. The only way to detect sufficient events is to use a large apparatus, and consequently the equipment for measuring EAS is often distributed over square kilometers. In Table II.l,the areas at sea level, corresponding to one EAS per month are given, for various incident energies. The numbers clearly demonstrate the experimental problem.

Table 11.1: Average EAS statistics

energy eV	area corresponding to 1 event/month
10^{14}	10 cm^2
10^{15}	300 cm^2
10^{16}	1 m^2
10^{17}	100 m^2
10^{18}	10^5 m^2
10^{19}	1 km^2

11.2. General features

Extensive air showers are initiated by interactions of primary cosmic-ray particles with air nuclei. Most of the secondary particles produced in these interactions are pions. The surviving nucleon – the leading particle – undergoes further interactions on its way through the atmosphere with a mean interaction length of $\lambda \approx 80$ g cm^{-2}. An average of 12 interactions occur each one approximately halving the energy. The hadronic cascade is the basis of an EAS from which the muonic and electromagnetic components are derived and provided for. When π° mesons are produced, they decay immediately into two gamma rays with small opening angle, but the subsequent secondary $e^+ e^-$ · pairs are multiply scattered and hence spread out laterally. The charged pions are mainly of high energy and interact strongly with an interaction length $\lambda_\pi \approx 120$ g cm^{-2}. After several interactions and a consequent energy loss, they decay into muons which are emitted at large angles to the initial direction.
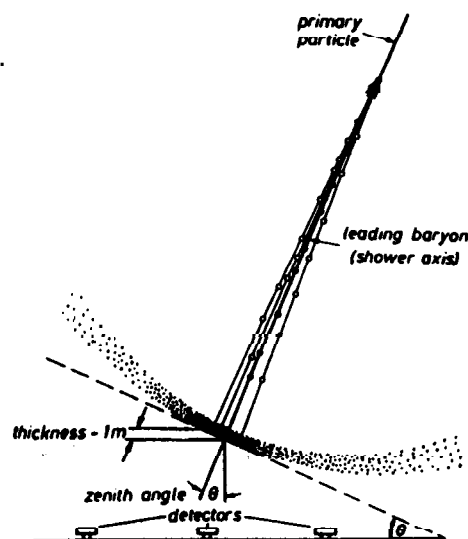
Fig. 11.1 : Schematic representation of an EAS

148

Fig. 11.2: Mean number of charged particles at different distances from the shower core (Adapted from Hillas, A.M.: Cosmic Rays. Oxford: Pergamon Press 19721
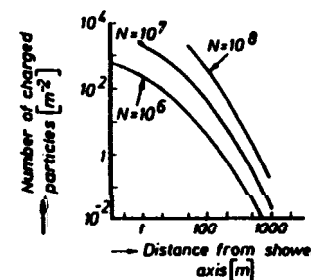
Shower particles become more and more spread out as they proceed through the atmosphere, and all travel with approximately the same velocity, near to the velocity of light. As a result, they are eventually contained within a slightly curved disc, with a diameter of the order of 1 km and a thickness of about 1 m near the axis, increasing to about 100 m at the outside (see Fig. 11.1). The density of shower particles is highest near the core of the shower. Fig. 11.2 gives the number of charged particles per m^2 as a function of distance from the shower core, for EAS of different sizes.

During the development of the shower in the atmosphere, the number of particles increases to a maximum at a depth which is weakly dependent on the primary energy E_0 ($\propto \log E_0$), and then decreases, finally dying out. Fig. 11.3 shows the development of a shower with a primary energy corresponding to an event rate of 10^{-10} m^{-2} s^{-1} sr^{-1}. Because they are travelling relativistically, the particles lose an approximately constant amount of energy per g cm^{-2}, and so the area under the curve of Fig 11.3 down to sea level, is a measure of the energy loss by ionization in the atmosphere. However, a large amount of energy remains when the particles eventually hit the earth's surface. Table 11.2 gives the detailed energy content of two showers, including the amounts of energy which go into the different components.
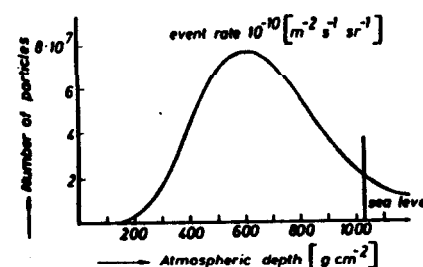
Fig. 11.3: Longitudinal development of a specific shower through the atmosphere (Adapted from Hillas, A.M.: Cosmic Rays. Oxford: Pergamon Press 1972)

147

Table 11.2: Energy content of two showers
(Adapted from Hillas, A. M.: Cosmic Rays. Oxford: Pergamon Press 19721

size at shower maximum	3.9×10^6	7.8×10^7
size at sea level	6.3×10^5	2.0×107
ionization above sea level	4.4×10^{15} eV	8.8×10^{16} eV
energy of soft component at sea level	0.14×10^{15} eV	04×10^{16} eV
energy of hadrons at sea level	0.08×10^{15}	0.2×10^{15}
energy of muons at sea level	0.64×10^{15}	1.3×10^{16}
energy of neutrinos at sea level	0.33×10^{15} eV	0.6×10^{16} eV
Total energv E_n	5.6×10^{15} eV	11.3×10^{16} eV

A simple relation between the number of particles in an EAS, the size number N, and the energy E_0 can be derived from Table 11.2. Hence, $N = k E_0$, where $k = 5 \times 10^{-10}$ for a size number near the shower maximum is used. At sea level, tge factor k is larger, and depends on the primary energy. A very approximate formula is

$$N_{sea\ level} = 10^{-10} E_0 \qquad (E_0 \text{ in eV})$$

The exact relation between shower size N, and primary energy E_{0l} is the crucial factor in the evaluation of energy from measured shower size.

The lateral distribution of a shower differs for the three components. The lateral spead of the hadrons which results from the transverse momenta they receive in production processes is small, because the mean transverse momentum $\langle p_T \rangle$ is small and almost independent of energy. Electrons are mainly spread out by multiple scattering processes. Muons are widely spread, because high energy $\pi^{\pm}$ interact rather than decay, until their energies are only a few GeV, and then they decay. At these low energies the angles of emission are quite large. Fig. 11.4 shows the average lateral distribution of the different components for a shower of size $N = 10^5$.
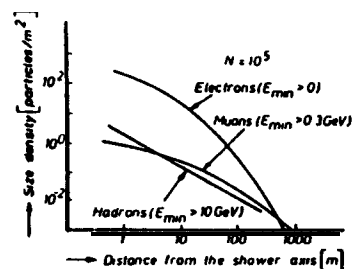
Fig. 11.4: Average lateral distribution of the shower components
(Adapted from Hillas, A. M.: Cosmic Rays. Oxford: Pergamon Press 19721
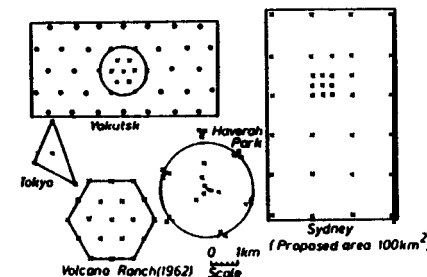
Fig. 11.5: Assemblies of EAS equipment (in use or planned)
(From Turver, K.E.: Extensive Air Showers Above 10^{17} eV, in Cosmic Rays at Ground Level. London: The Institute of Physics 1973)

11.3. Experimental methods

Showers extend over large areas, and so for an exact measurement of shower size it would be necessary to use a detector with an area of some km^2. In practice, to keep the size of the equipment to a minimum, only samples of the shower density are measured. Air shower assemblies are composed of many detectors distributed over a large area, each with a size of several m^2. Fig. 11.5 shows the layout of some detector arrays presently in use. The areas enclosed range from 0.1 to 40 km^2. To identify the various components different types of detector are used. These consist mainly of plastic scintillators and water Cerenkov counters, with areas of 1 to 10 m^2. Most of the arrays measure the area distribution of the electron component, but the muonic component is also used particularly in very large assemblies.

Since the EAS particles are concentrated in a thin disc, their incident direction can be obtained from a measurement of the arrival times of the front particles by several sampling detectors. The sampling method determines the density distribution $\rho(r)$ of the shower, as well as its direction of arrival. The electron distribution is useful for a normalization of the theoretical function which describes electromagnetic cascade development. This function is almost independent of shower size, The lateral distribution of the electron component can be described by the structure function

$$f(r) = \frac{r_M^2 \rho(r)}{N}$$

r_M Moliere radius
N   shower size
$\rho(r)$ electron density

The shower size is obtained by an integration over the density distribution

$$N = \int_0^\infty 2\pi r \rho(r)\, dr .$$

Different approximations for $f(r)$ have been used for different EAS assemblies.

Novel techniques have been proposed to measure EAS at very high energies. A primary particle of $\geqslant 10^{19}$ eV produces an EAS with an energy of more than one Joule which is of course widely spread. A lot of this energy goes into ionization and excitation of the air molecules, which subsequently de-excite with emission of fluorescent light. In principal, this can be detected by ground-based sensors as can the Cerenkov light produced by the relativistic particles in the shower. Of course, large focusing systems would be needed to measure either the fluorescence or Cerenkov light. Additional problems arise because the intensity of the light decreases with distance from the shower core, and only during dark nights could measurements of this kind be performed. The charged particles in an EAS are also a source of radio waves. Radio signals in the MHz range are present in the atmosphere which again, in principal, can be measured with a system of suitably arranged antennae. However, in practice it is estimated that too many antennae would be required.

Another possibility for economic detection of an EAS, would be to use the high electric conductivity which is present in the shower core. This conducting column should be able to reflect radio waves and so a reflected signal would give a measure of the shower size. At present this method has not been successfully carried out.

11.4. Altitude dependence

A quantitative description of longitudinal cascade development which displays an increase to a maximum followed by a decline has been given in Chapter 9. This behaviour applies to the shower cascade in the atmosphere. The maximum of the shower moves nearer to sea level with increasing energy, approximately as log E_0. Accurate calculations of longitudinal shower development and also measurements at various levels in the atmosphere, have been made. Fig. 11.6 shows the measured longitudinal development of several air showers with different energies. It is seen that the maxima of the showers occur relatively high up in the atmosphere, and that they are rather brqad. The cascade curves fluctuate strongly from event to event. Only for the highest energies, i.e. $\sim 10^{20}$ eV, is the shower maximum near to sea level.

The behaviour of the different components in atmospheric shower development is shown in Fig. 11.7. The calculations are for a primary proton of

150
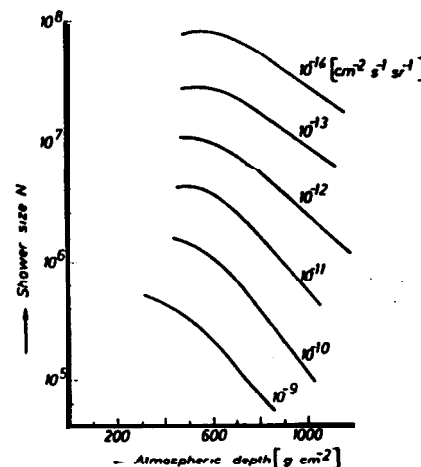
Fig. 11.6: Longitudinal development of air' showers in the atmosphere
(Adapted from Wdowczyk, J.: Extensive Air Showers Below 10^{17} eV. in Cosmic Rays at Ground Level. London: The Institute of Physics 1973)
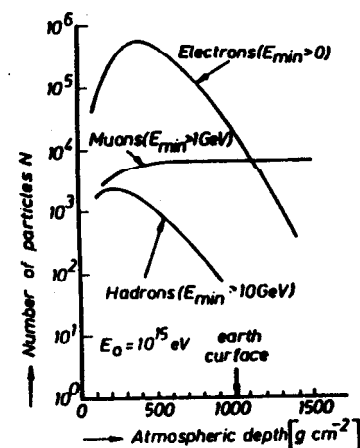

Fig. 11.7: Average longitudinal development of different shower components in the atmosphere
(From Samorski, M., L. Wiedecke: Extensive Air Showers, in Lectures on Space Physics (Eds. A. Bruzek, H. Pilkuhn), Dusseldorf: Bertelsmann Universitatsverlag 19731

energy 10^{15} eV. The size number of the hadrons has a maximum at relatively high altitude, because most of the pions are produced in the initial collisions of the leading baryon. Due to the high inelasticity, about 0.5, the multiplicity and mean energy of the secondary particles are rapidly reduced. The peak in the electron component occurs at about 500 g cm^{-2}, and is theoretically well understood. For muons, the curve reflects the fact that the mean muon lifetime is fairly long because of time dilatation, and that muons do not lose much energy in the atmosphere, the muon component arriving at sea level almost without attenuation.

11.5. The primary energy spectrum

In the energy region beyond $\sim 10^{14}$ eV, EAS are the only source of information about the primary energy spectrum, and various models have been used to reproduce it. The crucial point is the relation between shower size N, and primary energy E_p; the mass of the primary particle also enters into the problem. Some questions of outstanding importance here, are:

– Are there kinks in the primary spectrum,and if so how they can be explained?

– Is the primary spectrum at high energies composed mostly of protons, or is the chemical composition changed by the atmosphere, allowing a larger contribution of heavier nuclei?

– Is the apparent end of the primary spectrum at about 10^{20} eV due to limitations in the measuring techniques, or does it extend to higher energies?

An overall lack of statistics makes it difficult to give accurate answers to these questions. Existing EAS arrays have so far only measured 9 events with an energy greater 5×10^{19} eV, and one doubtfoul event at an energy of 4×10^{21} eV.

In Fig. 4.4, the slope of the integral spectrum $M(E) \propto E^{-\gamma}$ was shown to change from $\gamma = 1.7$ to $\gamma = 2.1$ at a primary energy of $\sim 10^{15}$ eV. This kink can be explained as a galactic cut-off,due to the galactic magnetic field preventing charged particles from escaping into extragalactic space. The Larmor radius r, of a particle moving in a magnetic field H, is given by

$$ r = \frac{P}{300\, ze \cdot H} \qquad \text{p in eV/c, H in Gauss} $$

from which it follows that a particle of unit charge,with a momentum $p \gtrsim 10^{15}$ eV/c, cannot be retained within the galaxy.

For heavier nuclei with higher charges,the cut-off momenta are correspondingly higher p, $\approx Z \cdot 10^{15}$ eV. Thus,the heavier the nucleus the higher its energy spectrum extends. Fig. 11.8 shows schematically, a possible explanation for the steepening of the spectrum around $E_p = 10^{15}$ eV. However, so long as only limited information about the chemical composition in the high energy region is available, this conclusion is of hypothetical value.

The energy spectrum at the highest energies is shown in Fig. 11.9. In contrast to earlier measurements which found a flatening at about 10^{19} eV, the latest results see no large change of slope. The measured data can be expressed as an integral spectrum

$$ M (> E) = 10^{-12} (E/10^{18})^{-1.96}\ \text{m}^{-2}\ \text{s}^{-1}\ \text{sr}^{-1} \ (E\ \text{in eV}) \ . $$

Nothing definitive can be stated about the continuity of the spectrum,but there is a hypothesis that around 10^{20} eV,it is cut-off due to interaction of the primary particles with photons of the 3 K-radiation. The latter particles have a density of ~ 550 cm^{-3} and a mean energy of 7×10^{-4} eV.
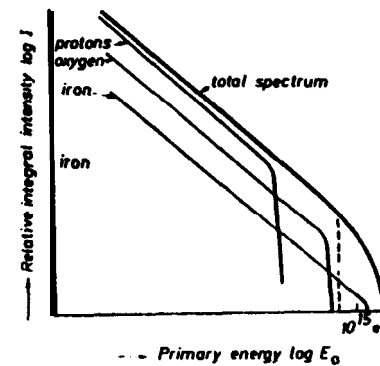
Fig. 11.8: Schematic representation showing the steepening of the primary energy spectrum around $E_p = 10^{15}$ eV.
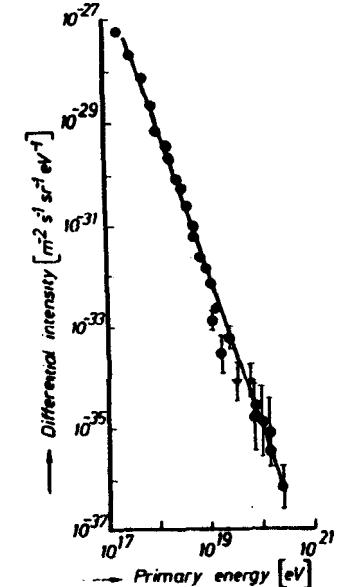
Fig. 11.9: Primary energy spectrum in the ultra high energy region (From Bett, C. J. et al.: J. Phys. A 7 (1974) 8)

At a proton energy of around 3×10^{19} eV,the threshold for pion production is reached and consequently there is a drastic proton energy loss.

Although charged particles of ultra high energy might be expected to retain their initial directions of emission from point sources, due to limited influence of the intergalactic field, no significant evidence for anisotropy has been found. However, statistics are poor.

11.9. Chemical composition

Chemical composition can in principal be studied within the core of a shower because a shower initiated by a heavy nucleus of a atomic weight A, will contain certain of its fragments. In the simplest case,it can be assumed that A independent showers develop, each with a mean energy E_p /A. The development of a shower is strongly influenced by the first interaction and so variations in the first interaction give rise to large fluctuations later. A shower initiated by a proton shows larger fluctuations than a shower initiated by a nucleus A, because in the latter case,the A nucleons simultaneously start different showers (subcores) which in total produce less fluctuations. All measureable shower parameters show a decrease in their fluctuations with A. Thus, a study of the fluctuations of the measurable shower

parameters provides information about the initial chemical composition. The following parameters are involved:

(a) The slope of the lateral distribution of electrons near the shower core. The subcore structure in this component almost disappears due to the fluctuations, but some information can be obtained from the lateral distribution of the electrons.

(b) Muon content. The mean number of muons in a shower N_{μ} increases with A. At the maximum of the shower development

$$\frac{N_{\mu}}{N}(A) = C \cdot A^{0.2} N^{-0.2} .$$

(c) Lateral distribution of muons. The lateral distribution of muons in a shower depends upon the mean transverse momentum $\langle p_T \rangle$, the multiplicity n, and the atomic weight A. An increase of any of these quantities leads to an increase in the number of muons, but it is difficult to separate out their relative contributions.

(d) Hadron energy flow. The fluctuations of the energy flow decrease with increasing A.

The measurements carried out so far are not in mutual agreement, partly due to limitations in resolution. Three possibilities still exist, the primary high-energy particles are all protons, all heavy nuclei or a mixture of the two.

11.7. Particle-physics data from EAS

For the foreseeable future, EAS will continue to be the only source of information about very high energy interactions. However, the information is limited because the number of measurable events is very small, and the interactions cannot be studied directly. The way particle physics is done with EAS, is to postulate models for shower development, and then carry out calculations with the aid of computers, using various sets of parameters for the interaction processes. The simulated showers are then compared with measured values, and thus the optimum model parameters are extracted from the results. Detailed results have not been obtained, because so many parameters have to be taken into account in any model.

A typical set of parameters used for a shower simulation is given in Table 11.3. These data are mostly high-energy extrapolations of accelerator results. These extrapolations become more improbable the higher the primary particle energy. For a particle of energy of 10^{17} eV, the expected

Table 11.3: A typical sat of parameters used for simulation of an EAS (Adapted from Turver, K. E., in Cosmic Rays at Ground Level (Ed. A. W. Wolfendala l. London: The Institute of Physics 19731

nuclear mean free path	λ_p	$= 80 \text{ g cm}^{-2}$
mean nucleon-air inelasticity	K_p	$= 0.5$
pion mean free path	λ_π	$= 120 \text{ g cm}^{-2}$
mean pion-air inelasticity	K_π	$= 1.0$
multiplicity of pions	n	$= 3.75 \, E_p^{1/4} - 1.0$
transverse momentum distribution of secondaries		$f(p_T) \, dp_T = \left(\frac{p_T}{p_0}\right)^{3/2} \cdot \exp\left(-\frac{p_T}{p_0}\right) dp_T$

multiplicity is $\sim$ 5000 if it increase as $E_p^{1/2}$. Alternatively, Feynman scaling ($n \propto \ln E_p$) predicts a multiplicity of $\sim$ 50 at this energy. Fig. 11.10 gives examples of the longitudinal development of electron cascades for showers in the atmosphere. It is seen that the maximum of the shower initiated by the iron nucleus occurs higher in the atmosphere, and the total number of electrons at sea level, is higher for the proton initiated shower.
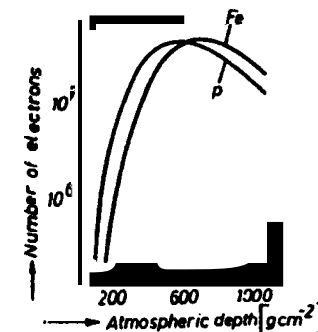

Fig. 11.10: Shower simulation of the longitudinal development of electron-cascades in the atmosphere
p – proton initiated shower
Fe – iron initiated shower
(Adapted from Turvar, K. E.: Extensive Air Showers Above 10^{17} eV, in Cosmic Rays at Ground Level. London: The Institute of Physics 1973)

References

Bruzek, A., H. Pilkuhn (eds.): Lecture on space physics. Dusseldorf: Bertelsmann Universitatsverlag 1973

Wolfendale, A. W.: Cosmic rays at ground level. The Institute of Physics, London (1973)

Cranshaw, T. E.: Cosmic rays. Oxford: Oxford University Press 1963

Hillas, A. M.: Cosmic rays. Oxford: Pergamon Press 1972

Bell, C. J. et al.: The upper end of the observed cosmic ray energy. J. Phys. A 7 (19741 B

Gailbraith, W.: Extensive air showers. London: Butterworths 1958

12. Geomagnetic effects

12.1. Introduction

Primary cosmic rays and most of the secondaries produced in the atmosphere are charged. As a result, their trajectories are bent by the earth's geomagnetic field which leads to a filtering effect; particles need more than a certain minimum momentum or rigidity to reach a particular point on the earth from a particular direction. Since the strength of the geomagnetic field varies from the poles to the equator, this minimum value changes with geomagnetic latitude leading to the *latitude effect,* which is measured for different cosmic-ray components at different altitudes. The cosmic-ray intensity increases from the equator to the poles, but beyond a specific latitude it becomes constant, creating to a knee in the latitude dependence. This knee occurs at different latitudes for different components and is altitude-dependent. A further change in intensity is observed along a specific longitude. This is the result of a variation in the geomagnetic field due to the eccentricity of the geomagnetic dipole moment, and is known as the *longitude effect.* In addition, the interaction of the primary particles, which are positively charged, with the earth's field gives rise to an asymmetry or east-west *effect,* i.e. at a specific angle, a higher intensity is observed from the west than from the east.

These geomagnetic effects can be described by the theory of *Stoermer,* which was developed to explain aurorae but without success, before the former effects were observed. In 1958, the radiation belts were detected by satellite measurements, another phenomenon due to the geomagnetic field.

12.2. The geomagnetic field

The simplest model of the geomagnetic field is the centered dipole approximation. Here, the field is assumed to be equivalent to that of a bar magnet with magnetic moment $\vec{M}$ located at the center of the earth, and oriented from north to south along the geomagnetic axis; the angle between this axis and the axis of rotation being 11.5°. The geomagnetic poles appear at 78.5° N, 69.0° W and at 78.5° S, 111.0° E. If p_1 and p_2 are the pole strengths, the force between them is given by

$$K = \frac{p_1 \cdot p_2}{r^2} \ .$$

r distance between p_1 and p_2; the unit of pole strength is $(cm^{3/2} g^{1/2} s^{-1})$.
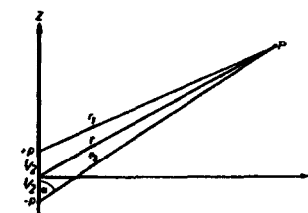
Fig. 12.1: Explanation of the magnetic potential

For a magnetic dipole with pole strengths $\pm p,$ a magnetic potential can be defined in an analogous way to an electric potential, as $\psi = p/r$. The resultant potential at P (Fig. 12.1) is thus

$$\psi = \frac{+p}{r_1} + \frac{(-p)}{r_2} = p \cdot \frac{r_2 - r_1}{r_1 r_2} \ .$$

For the conditions

$$r_1, r_2 \gg l , \ r_1 \approx r_2 \approx r \ \text{and} \ \ r_2 - r_1 = l \cdot \cos \alpha$$

this becomes

$$\psi = \frac{p \cdot l \cdot \cos \alpha}{r^2} \ .$$

Further substitution for the magnetic moment

$$\vec{M} = p \cdot \vec{l} \ ,$$

leads to the expression

$$\psi = \frac{\vec{M} \cdot \vec{r}}{r^3} \ .$$

If the magnetic dipole of the earth was coincident with its axis of rotation $\vec{z}$, the potential would be

$$\psi = \frac{M \cdot z}{r^3} \ ,$$

and the magnetic field strength

$$\vec{H} = - \text{grad} \ \psi = - \left[\frac{\partial}{\partial x}, \ \frac{\partial}{\partial y}, \ \frac{\partial}{\partial z} \right] \frac{Mz}{r^3}$$

$$r = \sqrt{x^2 + y^2 + z^2} \ ,$$

or finally

$$\vec{H} = \left[- \frac{3 \, Mxz}{r^5}, \ - \frac{3 \, Myz}{r^5}, \ - \frac{M(3z^2 - r^2)}{r^5} \right] \ .$$

The magnetic dipole moment of the earth is $M \approx 8.1 \times 10^{25}$ Gauss cm.

123. Stoermer theory

High-energy charged particles are not significantly affected by the geo-magnetic field, whereas particles of much lower energy can have very complex trajectories (see Fig. 12.2). Using the theory originally developed by *Stoermer* to explain the aurorae, it can be shown that there are certain regions around the earth which are inaccessible to charged particles of a given energy and direction.
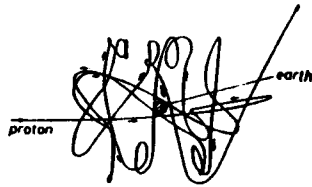

Fig. 12.2: The trajectory of a particle of relatively low energy in the earth's magnetic field
(From Pomerantz, M. A.: Cosmic Rays. New York: Van Nostrand Reinhold Company 1971)

For a charged particle moving in a constant magnetic field two conservation laws must be satisfied, conservation of momentum and conservation of angular momentum.

Starting with the Lorentz equation

$$d/dt \, \vec{p} = ze/c \, (\vec{v} \times \vec{H}),$$

P   momentum
ze   charge of the particle
v   velocity
H   magnetic field

multiplication by $\dot{\vec{r}}$ leads to

$$m/2 \, \frac{d\dot{r}^2}{dt} = ze/c \, (\dot{\vec{r}} \cdot (\dot{\vec{r}} \times \vec{H})) = 0,$$

and hence

$$m\dot{\vec{r}} = \vec{p} = \text{const.}$$

Alternatively multiplication of the Lorentz equation by $\vec{r}$ gives

$$(\vec{r} \times d\vec{p}/dt) = ze/c \, [\vec{r} \cdot (\dot{\vec{r}} \times \vec{H})]$$

or

$$d/dt \, (\vec{r} \times \vec{p}) = ze/c \, [\dot{\vec{r}} \, (\vec{r} \cdot \vec{H}) - \vec{H} \, (\vec{r} \cdot \dot{\vec{r}})].$$

Substituting the last equation of Section 12.2, the z-component becomes

$$d/dt \, (\vec{r} \times \vec{p})_z = ze/c \left[\dot{z} \left(-x \frac{3Mxz}{r^5} - y \frac{3Myz}{r^5} - z \frac{M(3z^2 - r^2)}{r^5} \right) - \right.$$

$$\left. \frac{-M(3z^2 - r^2)}{r^5} \, (\vec{r} \cdot \dot{\vec{r}}) \right] = -zeM/c \cdot \frac{d}{dt} \, (z^2/r^3 - 1/r),$$

from which it follows that

$$(\vec{r} \times \vec{p})_z \, t \, zeM/c \, \frac{r^2 - z^2}{r^3} = D = \text{const.}$$
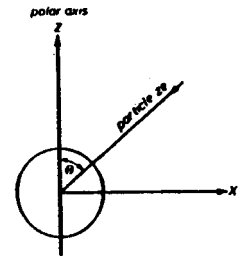
Fig. 12.3: Explanation of cutoff momenta

Now consider the trajectory of a charged particle which is just able to reach the surface of the earth, at vertical incidence, neglecting the atmosphere (see Fig. 12.3). For this condition $\dot{r} = 0$ and $\Theta = 0$. Introducing the spherical polar coordinates

$$x = r \sin \Theta \cos \varphi \quad y = r \sin \Theta \sin \varphi \quad z = r \cos \Theta$$

it follows

$$(\vec{r} \times \vec{p})_z = m \, r^2 \cdot \sin^2 \Theta \cdot \dot{\varphi}$$

with

$$r^2 - z^2 = r^2 \sin^2 \Theta.$$

Then it follows

$$mr^2 \cdot \sin^2 \Theta \cdot \dot{\varphi} + \frac{zeM}{c} \cdot \frac{\sin^2 \Theta}{r} = D.$$

Expressing the velocity in polar coordinates

$$v^2 = r^2 \sin^2 \Theta \cdot \dot{\varphi}^2$$

158

159

or

$$\dot{\varphi} = \pm \frac{v}{r \cdot \sin \Theta} \quad ,$$

and hence, the above equation becomes

$$\pm mvr \cdot \sin \Theta + \frac{zeM}{c} \cdot \frac{\sin^2 \Theta}{r} = D .$$

Using the *Stoermer* unit r_0, which is defined as

$$r_0^2 = \frac{zeM}{cmv} = \frac{\text{magnetic moment}}{\text{rigidity}} \quad ,$$

and making the abbreviations

$$\mu = r/r_0 , \quad \phi = \sin \quad \text{and} \quad D/r_0 \, m \, v = \rho_0$$

The above equation becomes

$$\phi = \mp \frac{\rho^2}{2} \pm \left(\frac{\rho^4}{4} + \rho \rho_0 \right)^{1/2} .$$

Since $\phi \geqslant 0$, the second minus sign can be dropped while the first sign differentiates between the northern and the southern hemispheres. Differentiation with respect top gives ϕ_{max}, i.e.

$$\phi_{max} = \left(\frac{\rho_0}{2} \right)^{2/3}$$

which leads to $\rho_0 = 2$ since $\phi_{max} = 1$.

Thus

$$\phi = \mp \frac{\rho^2}{2} + \left(\frac{\rho^4}{4} + 2\rho \right)^{1/2} .$$

Now

$$\mu = r/r_0 = r \, (zeM)^{-1/2} \cdot (c\rho)^{1/2} \ll 1$$

and

$$\phi^2 \approx 2p = 2 r/r_0 ,$$

giving finally

$$p = \frac{zeM}{4 c R^2} \cdot \sin^4 \Theta .$$

R earth radius

Table 12.1: **Geomagnetic** cut-off momenta for vertically incident protons

geomagnetic latitude λ	0°	15°	30"	45°	60"	75°	90°
cut-off momentump, (GeV/c)	14.9	13	8.4	3.7	0.9	0.07	0

This equation specifies the conditions for a charged particle of momentum p, and incident angle 0, to just reach the surface of the earth.

introducing the rigidity $S = pc /z$ e, is follows that

$$S_{min} = \frac{M}{4 c R^2} \cdot \sin^4 \Theta .$$

The minimum rigidity is largest at the equator $(\Theta = \pi/2)$, and zero at the poles $(\Theta = 0)$. Table 12.1 gives the mean cut-off momenta for protons.

The *Stoermer* unit introduced above, is the radius of the circular orbit described by a particle of momentum mv, in the equatorial plane. Using the radius of the earth

$$r_0 = R = 6.38 \times 10^8 \text{ cm} ,$$

the cut-off momentum for a proton is

$$p_c = 59.6 \text{ GeV/c} .$$

This is the minimum momentum a proton must possess to reach the surface of the earth, at the equator, from the eastern horizon. The corresponding minimum momentum from the west is 10 GeV/c (see Fig. 12.4).
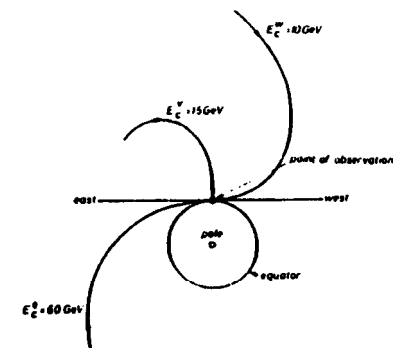
Fig. 12.4: Cut-off momenta at the equator for different directions of incidence

12.4. Propagation in the earth's magnetic field

From the equation for ϕ in the last section, it follows that

$$\sin \Theta = \mp\, r^2/2\, r_0^2 + \left(\frac{r^4}{4\, r_0^2} + \frac{r}{r_0}\, \rho_0 \right)^{1/2} = f(r, p) = f(r, S).$$

This is the track equation for a positively charged particle in the earth's magnetic field, neglecting the atmosphere and also the solid body of the earth, which acts as an absorber. Two regions can be defined for any pair of values of radius and momentum,

permitted region $\quad |\sin \Theta| \leqslant 1$

forbidden region $\quad |\sin \Theta| > 1.$

Since $\rho_0 = D/r_0\, p$, solutions of the above equation are obtained for different momenta, i.e. the permitted and forbidden regions depend on the values of D and po. This is shown in Fig. 12.5, where the two regions are shown in the meridian plane for a specific value of D.
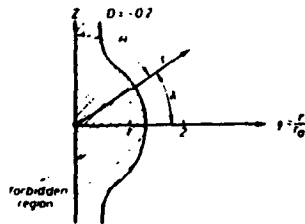
Fig. 12.5: Allowed and forbidden regions due to Stoermer theory
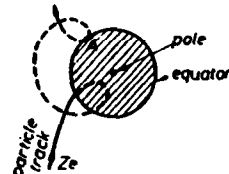
Fig. 12.6: Schematic diagram of the shadow effect

The Stoermer treatment does not take into account complications introduced by the presence of the solid earth. Because the earth is not transparent, what actually happens is illustrated in Fig. 12.6. A particle with a trajectory in the equatorial plane would be detected at point A if the earth was transparent, whereas in reality it is absorbed. This leads to the so called shadow *effect* Numerical calculations of individual orbits *(Lemaitre, Vallarta)* have shown that not all trajectories within the Stoermer cone are allowed, even in the absence of the earth. There is a penumbral region which contains both accessible and inaccessible points, and in addition, there are some allowed orbits which intersect the earth. The results of these calculations are shown in the vertical cut-off diagram (Fig. 12.7), where three regions are defined:
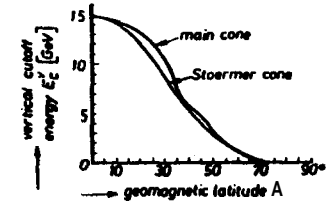
Fig. 12.7: Vertical cutoff energy as a function of geomagnetic latitude

The Stoermer cone: For a fixed position there exists a rigidity below which no particle can be present.

The main cone: For a fixed position there exists a rigidity above which particles with all possible higher rigidities can be present.

The penumbra: This is the intermediate region which contains both, accessible and non-accessible values.

It is difficult to calculate the structure of the penumbra, because in this region only effective cut-off rigidities can be specified. However, the figure shows that there is no penumbra at the poles and near the equator, and so in these regions definite cut-off values can be given.

Several modifications of the simple magnetic dipole model have been carried out. The dipole has been positioned at a distance of 342 km from the geographic center of the earth. More refined calculations have included quadrupole and even higher multipole moments of the field. However, the most precise way to obtain reliable cut-off rigidities is by detailed calculation of actual cosmic-ray trajectories, using as accurate as possible a mathematical representation of the earth's real magnetic field, obtained from a world wide measurement of the magnetic field distribution. The trajactories are then calculated by spherical harmonic analysis. In this approach, the magnetic potential $\psi(r, \Theta, \varphi)$ is developed as a series expansion

$$\psi(r, \Theta, \varphi) = R \cdot \sum_{n=1}^{\infty} \sum_{m-0}^{n} \frac{R}{or}^{n+1} (g_n^m \cos m\, \varphi + h_n^m \sin m\, \varphi)\, P_n^m (\cos \Theta)$$

R earth radius

r distance from the center of the earth

φ geographic longitude

Θ $\pi/2$ − geographic latitude λ

$P_n^m (\cos \Theta)$ associated Legendre functions

g_n^m, h_n^m Gauss coefficients, determined from observational data of the magnetic field

Contributions of quadrupole, octopole and even higher multipole moments can be included in' this representation. The procedure is to consider the reverse of what actually happens, i.e. to shoot negatively charged particles with various rigidities from the earth,and to see if they escape to infinity. Those which succeed,correspond to positive particles approaching the earth from far away. At a particular point on the earth, for a particular direction, the lowest rigidity for which the infinity is reached is the geomagnetic threshold.

Fig. 12.6 shows the penumbra obtained by exact calculation of trajectories at normal incidence, for three geographic locations. Also shown are the allowed (white) and forbidden (black) regions as function of rigidity, and the *Stoermer* and main cones.
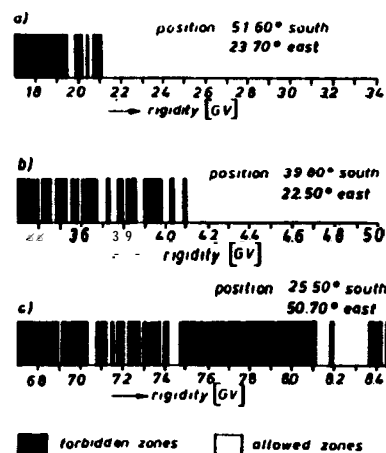
Fig. 12.8: Allowed (white) and forbidden (black) regions of the penumbra for three geographical locations as calculated from individual trajectories, as a function of rigidity

12.5. The latitude effect

A direct consequence of the geomagnetic cut-off is the latitude effect, which is the change of cosmic-ray flux with geomagnetic latitude. Here the earth behaves as a large magnetic spectrometer which analyses the energy spectrum of cosmic-ray particles. Thus, for normally incident particles at the geomagnetic equator, the primary proton energy spectrum below 15 GeV is cut-off, and at a typical latitude, say 50°, all particles with an energy $\lesssim 2.7$ GeV are unable to reach the earth. This leads to an increase of total flux with geomagnetic latitudeand is demonstrated schematically in Fig. 12.9. At the latitude A, the cut-off energy E_c, allows only particles with eneryy
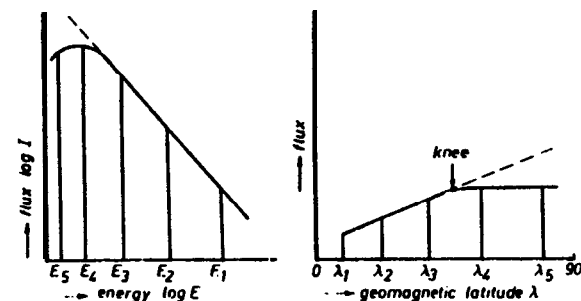
Fig. 12.9: Explanation of the cosmic ray knee in terms of individual trajectories, as a function of rigidity

$E_c \geqslant E_1$ to reach the earth. At λ_2 a much smaller part of the spectrum is cut-off and therefore the flux is higher. Eventually, for $E_c < E_3$,there is no further increase in the flux because the spectrum forms a plateau. Hence, a knee appears in the flux distribution. The total phenomenon is called the latitude effect, and is present in both, the primary and secondary components of cosmic radiation. In Table 12.2 absolute intensities measured outside the atmosphere are given for various latitudes. A maximum flux variation of a factor of 10 is observed.

The latitude effect is present in secondary nucleons and muons, at all levels in the atmosphere. It is larger for nucleons, as measured by the neutron component with neutron monitors, than for muons. The reason for this is that the latitude effect is due to the cut-off of part of the energy spectrum at low energies. Now low-energy muons have only a limited lifetime and consequently a limited path length, s, due to time dilatation,

$$s = \tau_0 \, c \gamma \, .$$

τ_0 muon lifetime
γ Lorentz factor

Table 12.2: Latitude effect for primary particles

| geomagnetic latitude	0°	41°	50°	58°
vertical cut-off energy E_c in GeV	15	5	2.7	1.4
proton flux (cm^{-2} s^{-1} sr^{-1})	2.8×10^{-2}	7.3×10^{-2}	18×10^{-2}	29×10^{-2}
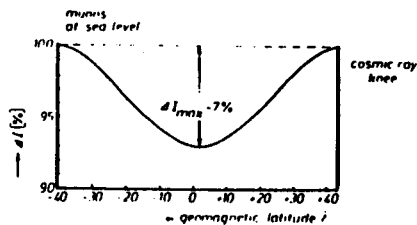
Fig. 12.10: Latitude effect of the muon component at sea level (From Allkofer, 0. C. et al.: METEOR Forschungsergebnisse, Gebr. Born-traeger, **Berlin** 1969)

Thus the minimum energy required to reach sea level from a production height of 16 km is about 2.6 GeV. Fig. 12.10 shows the latitude effect for muons at sea level. The maximum difference between the geomagnetic equator and the knee is only about 7%. Obviously, the latitude effect for muons becomes larger at higher altitudes because more low-energy muons are present. At 5000 m, the maximum difference between the geomagnetic equator and the knee is found to be $\sim$ 33 %.

It is better to express the latitude effect as function of the cut-off rigidity than as a function of geomagnetic latitude. Fig. 12.11 shows the latitude effect for neutrons at sea level, in this representation measured during 1965. The difference in the intensity is about a factor of 2.

In the latitude effect for the secondary components, the atmospheric cut-off due to energy loss by ionization has so far, not been considered. A rela-
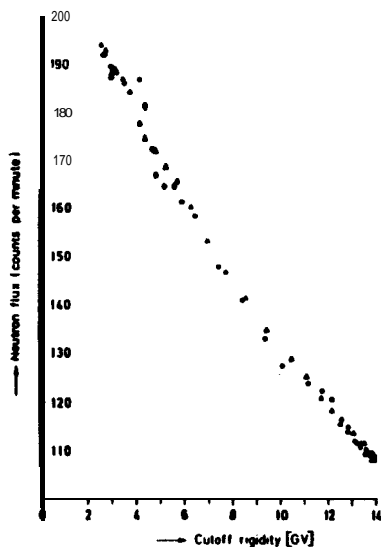
Fig.12.11: Latitude effect for neutrons at sea level (From Allkofer. 0. C. et al.: METEOR Forschungsergebnisse, Gebr. Born-traeger. Berlin 19691

tivistic particle requires a minimum energy of 2.2 GeV to be able to traverse the atmosphere, and consequently there is a knee in the latitude effect for muons. Starting from the equator, where the geomagnetic cut-off prevents muons of less thant 15 GeV from reaching sea level at normal incidence, the muon intensity increases with increasing latitude. Near the latitude of 40°, the cut-off energy becomes equal the atmospheric cut-off, and so for higher latitudes the flux remains constant, because now the atmospheric cut-off is dominant.

The knee of the nucleonic component occurs at a higher geomagnetic latitude, about 55°, and is explained by the low-energy flattening of the energy spectrum, as in the case of the primary component.

12.6. The longitude effect

The total cosmic-ray flux along a constant geomagnetic latitude, at a constant altitude, might naively be expected to have a constant value. However, because the dipole axis of the geomagnetic field is located eccentrically, a variation of the flux does occur; it is called the longitude effect. In Fig. 12.12 the cosmic-ray equator is shown. If a longitude effect did not exist the measured points would lie on the geographic longitude. The maximum sea-level variation around the earth occurs at the equator, and has a value $\sim$ 4%.
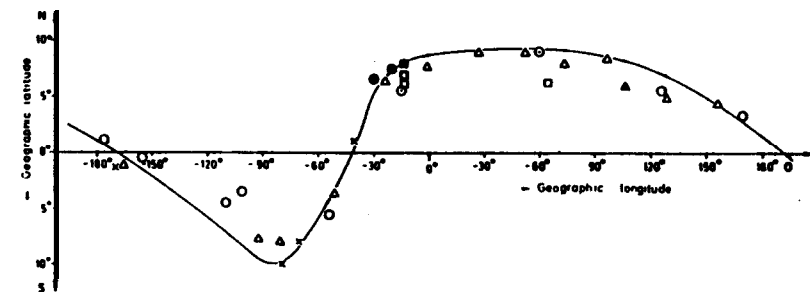
Fig. 12.12: The geomagnetic longitude effect

12.7. East-west effect

When particle fluxes are measured around an azimuth, at a fixed zenith angle, it is found that the fluxes from the south $I_s (\Theta)$ and from the north $I_n (\Theta)$ are equal, but the flux from the west $I_w (\Theta)$ is higher than the flux from the east $I_e (\Theta)$. This east-west effect can be easily explained by the

variation of the geomagnetic cut-off with the angle of incidence. At the equator, the cut-off energy for particles from the east is 60 GeV, whereas from the west it is only 10 GeV. Thus, a larger part of the energy spectrum is cut-off from the east than from the west. The east-west effect depends upon the zenith angle Θ, the altitude h, and the geomagnetic latitude λ. Defining this east-west asymmetry as

$$c = \frac{I_w(\Theta) - I_e(\Theta)}{1/2\,(I_w(\Theta) + I_e(\Theta))} = \epsilon(\Theta, \lambda, h),$$

it follows that

$$\epsilon(h_2) > \epsilon(h_1) \quad \text{for} \quad h_2 > h_1,$$
$$\epsilon(\lambda_2) < \epsilon(\lambda_1) \quad \text{for} \quad \lambda_2 > \lambda_1,$$
$$\epsilon(\Theta_2) > \epsilon(\Theta_1) \quad \text{for} \quad \Theta_2 > \Theta_1.$$

There is a modification of the east-west effect, particularly at large angles, due to the atmosphere. The atmospheric thickness increases with zenith angle,and gives rice to a cut-off of the east-west effect at an angle of $\sim 60°$. For larger angles, the low-energy particles which create the asymmetry are absorbed. Table 12.3 gives some measured values in dependence from λ at $\Theta = 60°$ and at sea level.

Table 12.3: Variation of the east-west offset with latitude

geomagnetic latitude λ	0°	20°	30°	50°
east-west asymmetry c	0.15	0.07	0.05	0.02

12.8. Radiation belts

In 1958, the satellite Explorer I witfi a Geiger-Muller counter on board, measured an unexpectedly high counting rate above an altitude of about 10^3 km. *Van Allen* suggested that this effect was due to charged particles trapped in the geomagneticfield,and a little later this was confirmed with the satellite Explorer III. The theory of *Stoermer* had already predicted the trapping of particles in definite orbits,and in order to prove this beyond doubt,a large scale experiment was carried out within the Argus project, in which a large number of charged particles were created by a nuclear explosion in the atmosphere. The results showed that charged particles were easily trapped within the earth's magnetic field. The motion of the particles in these trapped regions (radiation belts, van Allen belts) is rather complicated, and can be most easily understood if considered as the sum of three components:

(1) a rapid gyration around a field line with a cyclotron period T_C and a radius of gyration R_C (Fig. 12.13). Particles are reflected by the converging magnetic field near the earth and bounce between the mirror points;

(2) latitude oscillations between the mirror points with period T_B;

(3) azimuthal drift motion around the earth, with period of revolution T_r.
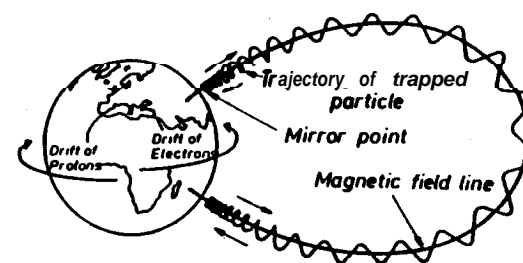
Fig. 12.13: Motion of charged particles in a dipole field

The three periods are energy-dependent, and have the following values:

$$T_C = 10^{-2} \text{ to } 10^{-6}\,\text{s}; \quad T_B = 0.1 \text{ to } 0.7\,\text{s};$$
$$T_R = 0.1 \text{ to } 700\,\text{min.}$$

From the first measurements,it was concluded that two belts were present. However, if lowenergy particles are taken into consideration then the space between the belts also contains trapped particles. It is now more correct to speak about the inner and the outer zone of the radiation belt. The particles observed in the belt are electrons, protons, and small numbers of alpha particles; the latter content being much smaller than in interplanetary space ($N_\alpha/N_p \approx 2.4 \times 10^{-4}$).

Fig. 12.14 shows the configuration of the radiation belt including the flux distributions. They are only symmetrical in the inner region,because the outer region is deformed by the solar wind (see Chapter 13). The electron fluxes are shown on the right side of the figure,and the proton fluxes on the left. The electron belt is composed of two parts, an inner belt at an altitude of about 3000 km above the geomagnetic equator, and an outer belt at an altitude between 15 000 and 25 000 km. Fluxes of up to 10^7 to 10^8 particles $\text{cm}^{-2}\,\text{s}^{-1}$ with energies $\gtrsim 0.5$ MeV have been measured. The proton belt is at an altitude between 2 000 and 13 000 km, and its energy spectrum extends from 10 MeV to 1 GeV.
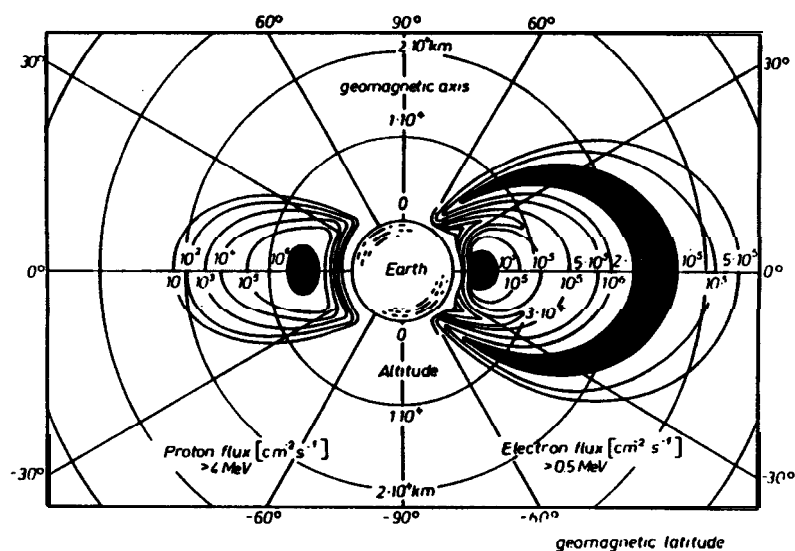
Fig. 12.14: Configuration and flux distribution of the radiation belt

Strong temporal variations are observed in the electron belts, with changes of a factor of 10 during a solar cycle, and additional variations of a factor of 10 to 100 over a period of some months. The proton belt, on the other hand, shows a relatively high temporal stability. Fig. 12.15 shows the proton fluxes at different alitudes for various energy thresholds. Fig 12.16 shows the same for the electron belts, as measured at the end of 1968. The energy spectrum of protons in the inner zone is shown in Fig. 12.17.
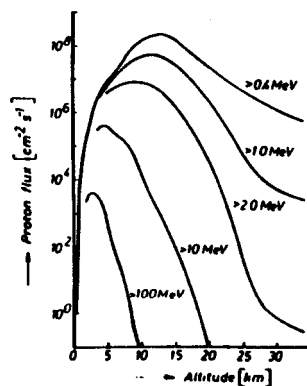
Fig. 12.15: Flux densities of protons in the radiation belt

Fig. 12.16: Flux densitiesof electrons in the radiation belt in December 1966
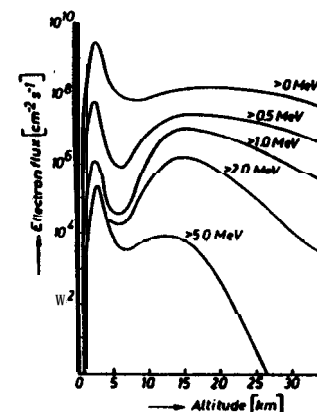
The origin of the particles in the Van Allen belts is not well known. The high-energy protons in the inner belt could be the decay products of neutrons which are produced as secondary particles by interactions in the upper atmosphere,and which are backscattered (albedo neutrons) before they decay. The lifetime of the protons in the radiation belts is determined by the time taken to lose all their energy by successive ionization processes. At 15 000 km,the lifetime for 20 MeV protons is about 3 years, and for 1 MeV electrons about 1 year. There is no explanation of the origin of the electrons or the protons in the outer zone.
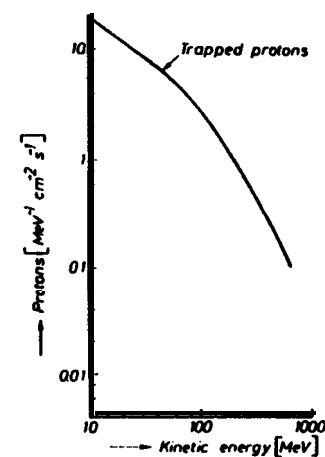
Fig. 12.17: Energy spectrum of protons in the inner zone of the radiation belt

References

Sandstrom, A. E.: Cosmic-ray physics.
Amsterdam: North-Holland Publ. Comp. 1965

Dorman, L. I.: Cosmic revs – variations and space explorations.
Amsterdam: North-Holland Publ. Comp. 1974

Pomerantz, M. A.: Cosmic rays.
New York: Van Nostrand Reinhold Company 1971

Hess, W. N., G. D. Mead: Introduction to space science.
New York: Gordon and Beach 1966

Allkofer, O.C.. R.D. Andresen, E. Bagge, W. D. Dau, H. Funk:
Der Einfluß des Erdmagnetfeldes auf die Kosmische Strahlung. Meteor Forschungs-
ergebnisse, Berlin (1969)

l

13. Solar cosmic radiation

13.1. Introduction

When cosmic radiation was first discovered, the sun was excluded as a possible source, but later on it was found to be a contributor. Measurements made during so called flares from the sun, observe sporadically emitted charged particles of low energy, sometimes with very high fluxes, several orders of magnitude higher than the galactic cosmic-ray flux. Furthermore, interplanetary space is filled with particles of the so called solar wind, which is produced by continuous emission of plasma clouds from the sun. The solar wind transports magnetic fields which influence charged particles of the galactic radiation. Because the intensity of the solar wind undergoes periodic changes, so do its magnetic fields, and hence a modulation effect is observed in the galactic radiation, i.e. a change in the particle flux corresponding to the period of the solar cycle. Due to the continuous flow of the solar wind, the geomagnetic field lines are deformed and the magneto-sphere is built up. In this chapter, solar cosmic radiation and the basic features of the sun will be considered and in the following chapter, the modulation effects induced by the solar cycle. The study of the effect of the sun onto the earth's environment has become a new discipline, solar-terrestrial physics; which is studied extensively with rockets and satellites.

13.2. The sun

In this section, the important features of the sun are discussed, in so far as they are necessary for an understanding of solar-terrestrial relations. Two states of the sun can be considered; the quiet sun, which corresponds to the steady-state condition and the active sun characterized by disturbances and storms.

The sun is at a mean distance of $\sim 1.5 \times 10^{13}$ cm from the earth and has a radius of $\sim 6.96 \times 10^{10}$ cm. Its mass is calculated from the *Kepler* laws to be $M_{\odot} \approx 2 \times 10^{33}$ g, and hence its mean density is ~ 1.41 g cm^{-3}. The light spectrum of the sun is a continuum with about 2 000 absorption lines *(Fraunhofer* lines), and it extends from the short wavelength ultra-violet radiation to the radiofrequency region. The total flux of radiation from the surface of the sun, S, is 1.368 x 10^6 erg cm^{-2} s^{-1}, or expressed in different units, is the solar constant, S = 1.961 cal cm^{-2} min^{-1}. Assuming the radiation to be black-body radiation, the effective temperature of the solar atmosphere is calculated to be T_{eff} = 5 780 K. Table 13.1 lists the most important parameters of the sun.

Table 13.1: Parameters of the sun
(Adapted from Allen, C. W.: Astrophysical Quantities. London: The Athlone Press of
the University of London 1973)

mass	2×10^{33} g $\approx 3.32 \times 10^5$ earth masses
diameter	1.4×10^{11} cm $\approx$ 109 earth radii
mean density	1.41 g cm^{-3}
mean distance earth-sun	1.50×10^{13} cm
energy production	3.7×10^{33} erg s^{-1}
energy flux (solar constant)	1.951 cal cm^{-2} min^{-1}
rotation period	25.38 days

The sun may be divided into four concentric regions, the core, the photo-
sphere, the chromosphere, and the solar corona (Fig. 13.1). The core of the
sun is the region where solar energy is produced, by means of thermonuclear
processes (see Section 3.6). The pressure here is about 10^{11} bar and the
temperature about 1.5 x 10' K. Most of the energy is taken away by
radiation.

The photosphere is the outer limit of the body of the sun, the apparent
surface. Its thickness is only a few hundred kilometers. Most of the solar
light comes from here. The temperature corresponds to black-body radia-
tion with a mean temperature of $\sim$ 6 000 K. Structure details (granules]
are visible under high magnification.

The chromosphere is a dynamic transition region, with a thickness of about
10^9 cm and a strong temperature gradient. The temperature near the
photosphere is about 4 000 K, and increases to a very high temperature near
the corona. Only small amounts of radiation come from this region because
of its low density. These include radiofrequency radiation, ultra-violet
light and X-radiation. The chromosphere is not a homogeneous layer, but
an assembly of close-packed jet-like prominences, called spiculi, with life-
times of several minutes,and velocities of about 20 km s^{-1}. Some of the
prominences reach a height of 10 000 km.
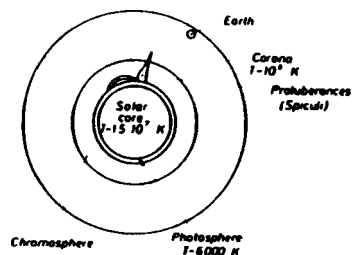
Fig. 13.1: Schematic representation of the
sun

The *corona* has a luminosity about 10^{-6} that of the photosphere. It is the
outermost region of the sun and is composed of highly ionized gases. Its
density decreases with distance from the sun but it has no outer surface;
the earth can be considered as immersed in the solar corona. The temper-
ature of the corona can reach $\sim 10^6$ K, and its radiation extends from the
region of radiowaves to the X-ray region.

13.3. The active sun and the solar cycle

Solar activity corresponds to the presence on the solar surface,of a number
of discrete, local perturbations (active regions) with typical lifetimes of
one day to three months. These active regions have a period of 10 to 14
years, the so called solar cycle (11-year cycle). The most remarkable of the
manifestations are the sunspots. Other features of the active sun include
foculae, prominences, filaments, flares, and the solar wind. All these
phenomena follow the solar cycle.

The solar cycle has been studied over the centuries by obserservations of
sunspots. These are dark regions in the photosphere, with temperatures
about 1000 K cooler than the surrounding medium. Their diameters range
from $\sim 10^2$ km to $\sim 10^5$ km,and their lifetimes are of the order of
months. Strong magnetic fields, about 3000 Gauss, perpendicular to the
sunspots may develop before they become visible. Sunspots occur in pairs
with opposite magnetic polarity, mostly in low solar latitudes, below
$\sim 35°$. The polarities are opposite in the, two hemispheres and reverse
with the solar cycle. They originate at high latitudes and drift towards the
solar equator. Fig. 13.2 shows the variation of the number of sunspots ob-
served since 1750. Fig. 13.3 is a photograph of a sunspot. Associated with
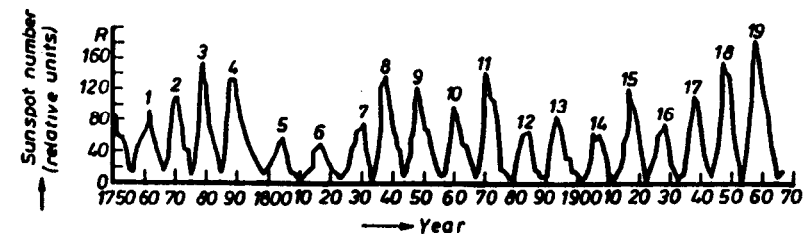the sunspots are foculae, which extend over much larger areas. All sunspots

Fig. 13.2: Variation of the numbers of sunspots since 1750
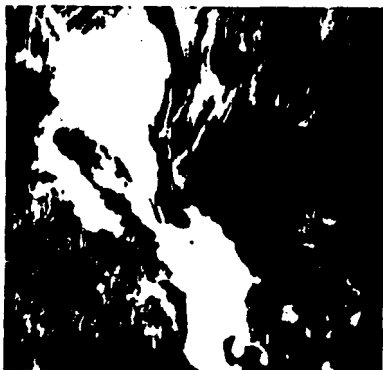(From Kertz, W.: Einfuhrung in dir Geophysik, B1 Hochschultaschenbucher Vol. 535
1971)

Fig. 13.3: Picture of a sunspot
(Reproduced from Mentzel, O. H.,
F. L. Whipple. G. de Vancouleurs:
Survey of the Universe, Englewood
Cliffs, New Jersey: Prentice-Hall 1970)

are surrounded by foculae, but foculae can exist without sunspots, their life-times are longer and they are always associated with magnetic fields.

Prominences are irregular shaped projections of the photosphere into the chromosphere, with maximum dimensions, typically $\sim 10^5$ km. They are cooler and denser than their surroundings, and move with velocities of hundreds of kilometers per second. Their lifetimes are of the order of several weeks. They appear to be shaped by the local magnetic field and are often observed together with sunspots. *Filaments* are special forms of prominences.

Solar flares are sudden and sporadic eruptions of the chromosphere. They develop in minutes with an increase of radiation in specific regions; occasionally, they are associated with particle emission. At times of solar activity, up to 10 events per day can be observed. Their lifetime is 20 to 180 minutes. The increase of the radiation is particularly high in the short-wave region ($< 2\,000$ Å). Four classes of flares are defined according to strength. Even the solar corona reflects the solar cycle. At the maximum of the cycle, the intensity of radiation is twice as great as at the minimum.

13.4. The solar wind

The extension of the solar corona into interplanetary space is called the solar wind, and the region of the solar system which is dominated by the solar wind is called heliosphere. Approximately 10^{12} g of hydrogen per second are transported by the solar wind, which corresponds to $\sim 10^{-4}$ of the solar mass since the beginning of the solar system. The solar wind is also dominated by the solar cycle. Table 13.2 summarizes the mean characteristics of the solar wind in the vicinity of the earth.

Table 13.2: Characteristic features of the solar wind near the earth
(Adapted from Hess, W. N., G. D. Mead (Eds.): Introduction to Space Physics, London: Gordon and Breach 1968)

composition	protons, electrons (+ small numbers of α particles)
flux	5×10^8 particles $cm^{-2} s^{-1}$
velocity	$300 \cdot 800$ km s^{-1}
density	$1 \cdot 20$ particles cm^{-3} (protons + electrons)
thermal energy	10 eV
temperature	10^5 K
proton energy	$0.3 \cdot 3.5$ keV
electron energy	~ 10 eV
magnetic field	$(3 \cdot 15) \times 10^{-5}$ Gauss
electronic conductivity	100 (Ohm $cm)^{-1}$

An explanation of the solar wind was given by *Parker* in 1958. In this theory, the solar wind is treated as a continuous, hydrodynamic streaming of plasma. The expanding coronal gas travels at hypersonic velocity.

The solar wind is a mass flux, which obeys a radial equation of motion, if the rotational velocity of the sun is neglected, i.e. $\Omega = 0$. Thus.

$$\partial v/\partial t + v \cdot \partial v/\partial r = 1/\rho \, \frac{\partial p}{\partial r} - g \, .$$

v mess velocity
p pressure
ρ density
g gravitational constant

For the stationary state $\left(\frac{dv}{dt} = 0 \right)$ this becomes

$$dp = -g\rho \, dr - \rho v \, dv \, .$$

Introducing the relation for adiabatic change of pressure and density

$$dp = v_s^2 \, d\rho \, ,$$

v_s sound velocity

leads to

$$v_s^2 \, d\rho = -g\rho \, dr - \rho v \, dv \, .$$

The amount of material crossing the surface of a sphere of radius r per unit time is

$$4 \pi r^2 \, \rho v = \text{const},$$

and thus

$$\mathrm{d}p/\rho = -2\,\mathrm{d}r/r - \mathrm{d}v/v.$$

Combination of the above equations gives, finally,

$$|1 - v^2/v_s^2|\,\mathrm{d}v/v = |rg/(2\,v_s^2) - 2|\,\mathrm{d}r/r.$$

The value of the parameter $u = rg/2\,v_s^2$ is very important. Here rg has the dimensions of (rotation velocity)^2, corresponding to a satellite at distance r. At the surface of the sun, the velocity has the value 438 km s^{-1}, and at the earth the value 30 km s^{-1}. The velocity of sound v_s, is $\sim$ 170 km s^{-1} in the solar corona where $T \approx 10^6$ K. In the chromosphere $u > 1$, and it diminishes with increasing r to the critical value $u = 1$ at $r = r_K$. Near $r = r_K (1 - 4\,r_{\circ})$, a change of sign in the differential equation occurs corresponding to supersonic flow.

The solar wind transports magnetic fields from the sun out into space. This is possible because the electrical conductivity of the interplanetary plasma is very high. According to the electrical theory, a good conducting medium tends to resist any changes in its internal magnetic fields. If the field is changed, an electromagnetic force is created which gives rise to a current, the associated field of which opposes the change of magnetic field. In finite conducting media such currents are damped. However, the conductivity of the interplanetary medium is so high that the current does not die out, and the solar plasma transports the magnetic field away from the sun. This frozen-in magnetic field remains with the plasma.

The solar wind extends to the distance at which the solar magnetic field density $H_s^2/8\,\pi$, equals the galactic magnetic field density $H_g^2/8\,\pi$. Due to the rotation of the sun, the field lines are not radial but have a spiral form (garden *hose effect*). As the sun rotates with the angular velocity Ω, the following picture results: particles which flow outwards with constant velocity (see Fig. 13.4) follow an Archimedian spiral. The axis $\Theta = 0$ is a fixed reference axis. At time $t = 0$ particles start to stream along some arbitrary axis Θ_0. At an earlier time t the source was at

$$\Theta = \Theta_0 + \Omega t.$$

If the particles are no longer acclerated beyond some distance $r = r_s$, after a further time t, they will reach a distance

$$r = r_s + vt.$$

Elimination of t from the above equations leads to the equation of the *Archimedian spiral*

$$r = r_s + (\Theta - \Theta_0) \cdot v/\Omega.$$
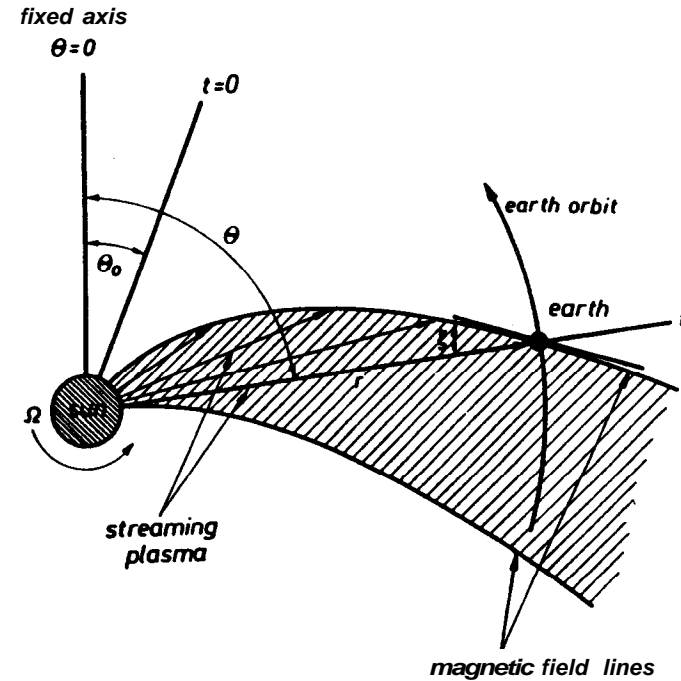
Fig. 13.4: Explanation of the garden hose effect

Of interest here is the stream angle or garden hose angle ζ, which is given by the tangent to the spiral at the radius r, thus

$$\tan \zeta = r\,\mathrm{d}\Theta/\mathrm{d}r = \frac{r\Omega}{v}.$$

Near the earth (r = 1.5 x 10^{13} cm), for Ω = 2.855 x 10^{-6} s^{-1} and v-450 km s^{-1}, ζ has the value 43.8°.
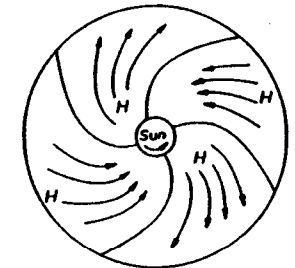
Fig. 13.5: Sector structure of the interplanetary magnetic field

The garden hose spirals are a purely geometrical concept,and give the positions of particles at a fixed time: the particles themselves move only in a radial direction. The frozen-in magnetic fields follow the spiral lines, similar to the stream of water emerging from a rotating lawn sprinkler.

An important feature of the interplanetary magnetic field is its sector structure (Fig. 13.5). The field points predominately towards and away from the sun,during successive periods of about 6 days.

13.5 The magnetosphere

The solar wind blows continuously away from the sun at an average speed of 300 to 500 km s^{-1}. It consists mainly of ionized hydrogen,with approximately equal numbers of protons and electrons, and is therefore electrically neutral. Near the earth,its density is about 1 ion per cm^3. The field contained within the solar wind is of the order of 5 x 10^{-5} Gauss during quiet solar periods, but may increase to many times this value during periods of high solar activity.

An interaction occurs between the magnetic field and the magnetized earth, which leads to a modification of the field fines. On the same side of the earth as the sun,there is a region of pressure build-up called the *magnetosphere.* This has a streamlined shape, and causes the particles coming from the sun to flow around it. On the opposite side of the earth the magnetosphere has an extended tail. Before the structure of the magnetosphere was measured and understood, it was already known that plasma and magnetic fields tend to confine one another. When a streaming plasma encounters an object such as a magnetized sphere, it engulfs it and confines the field to a limited region around the object. The object, in turn, tends to repel the plasma, creating a hole or cavity. The size of the cavity depends upon the energy density of the plasma and the size of the field. Furthermore, if the velocity of the plasma is sufficiently high, i.e. supersonic, a detached shock wave may be produced in the region before the cavity boundary. Such a process is analogous to the formation of a shock wave,in front of an aerodynamic object travelling at supersonic velocity through the atmosphere.

As a result of many measurements and magnetohydrodynamic calculations, the following features of the magnetosphere are known (Fig. 13.6):

(a) The *magnetopause* is the outer boundary of the magnetosphere, and is a region of outwardly decreasing magnetic field with a thickness of about 100 km. It is approximately the limit of the influence of the geomagnetic field. Between the earth and the sun,the magnetopause is a closed region
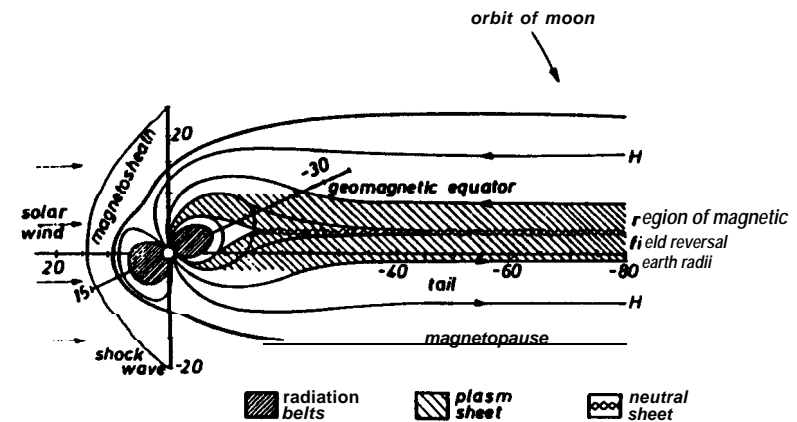
Fig. 13.6: Schematic representation of the magnetosphere
(From Hess. W. N., G. D. Mead: Introduction to Space Science. New York: Gordon and Breach1968)

situated at a distance of 8 to 12 earth radii from the centre of the earth. On the other side of the earth,it has the form of an open tail. The magnetopause is also the region where the pressure of the solar wind is equal to the pressure of the geomagnetic field. At the nearest point to the sun

$$2\,n\,m_p\,v^2 \qquad = H^2/8\,\pi\,.$$

v   velocity of the solar wind
n   particle density
m_p proton mass (= 1.67 x 10^{-24} 9)
H   horizontal magnetic field strength

For n = 5 protons per cm^3 and v = 360 km s^{-1}, the field Is H = 7.4 x 10^{-4} Gauss.

(b) *Shock* wave. The earth and its magnetosphere present an obstacle to the supersonic flow of the solar wind, and as a result,create shock waves in the solar wind upstream of the magnetopause. The speed of sound in the interplanetary medium is $v_s \approx$ 50 km s^{-1} and the solar wind vefocity is about 400 km s^{-1}, which gives a *Mach* number for the flow of $M = v/v_s \approx 8.$

Another important number is the *Alfven* vefocity

$$v_A = H \cdot (4\,\pi\,\rho)^{-1/2} \approx 50 \text{ km s}^{-1}\,,$$

H   magnetic field strength
ρ   density

which has approximately the same Mach number $M_A = v_A/v_s \approx 8$. Since both M and M_A indicate supersonic flow, a shock wave upstream of the magnetopause is expected. Aerodynamically, however, shock waves can only be produced, if the obstacle is large in comparison with the mean free path of the particles which form the fluid. The diameter of the magnetosphere is about 2×10^5 km, and the mean free path of a particle in the solar wind is about 1.5×10^8 km. Therefore no direct interaction between two particles should take place. In this instance, communication is achieved by means of the magnetic field, which causes the low-density plasma to behave like a fluid. All the particles on one magnetic field line are constrained to move together. As the field line is transported towards the magnetosphere by the solar wind, it is deflected and attempts to remain close to its surface.

(c) The magnetosheath or *transition* region. The region behind the shock front is called the magnetosheath or transition region. It contains large local variations of the magnetic field, due to violent turbulences. In this region, the particles are mostly protons with energies between 200 and 600 eV, moving towards and away from the sun. Electrons have also been observed with energies of some keV, which is much higher than in interplanetary space. It is concluded that the shock wave transfers some of the proton energy to the electrons.

(d) *The rail of the magnetosphere.* The side of the magnetosphere away from the sun is the tail region, so called because it bears some resemblance to the tail of a comet. Its magnetic field points towards the sun in the northern hemisphere, and away from the sun in the southern hemisphere. The magnitude of the field is many times less than that of the geomagnetic dipole field; at less than 50 earth radii, r_E, it is about 10^{-4} Gauss. The thickness of the tail is about 500 to 5000 km, and it extends to about 80 r_E. Within the tail, there is a *neutral sheet,* a region where the magnetic field changes direction and becomes very small. This region has up and down motion with velocities of some km s^{-1}. The neutral sheet is embedded in the *plasma sheet,* which has a thickness of 5 to 10 r_E.

13.6. Geomagnetic storms

Intense, world-wide, transient variations of the geomagnetic field are called geomagnetic storms. Such storms start with a sudden increase of the horizontal field component, known as *Sudden Commencement (SC)*. After this initial increase, the magnetic field remains above the pre-storm level for a few hours *(initial phase)*. In the *main phase* a large decrease to

a minimum occurs after a few hours. Finally, over a period of between 10 hours and several days, the field returns to its original value (recovery *phase)*.

The frequency of occurrence of magnetic storms is observed to be correlated with the solar cycle, indicating that they are caused by the sun. Magnetic storms often occur after a solar flare, with a time lag of the order of one or two days. There is general agreement that the cause of a storm is ejected solar plasma. When a transient plasma stream arrives at the boundary of the magnetosphere with a speed substantially greater than that of the solar wind, the magnetosphere suffers a large impact which produces a sudden compression of the magnetic field and also the plasma. The compression is transmitted as a magnetohydrodynamic perturbaiion to the inner regions, and is observed at the earth as a sudden increase in the magnetic field. This phenomenon shows a strong variation with latitude.

Besides the large scale variations, there are variations with much shorter periods and smaller amplitudes. Some of these occur with considerable regularity while others are irregular. The variations are called *geomagnetic micropulsations.* Periods between one second and several minutes have been observed. The shorter pulsations have very small amplitudes, of the order of 10^{-8} Gauss, but the long-period pulsations can have amplitudes as large as several times 10^{-3} Gauss. The pulsations are thought to be due to the solar wind producing- magnetohydrodynamic waves which interact on the geomagnetic field.

13.7. Solar cosmic-ray particles in flares

A solar flare is a very complex phenomenon, which. develops rapidly, in a time of 100 to 1000 seconds, covers a limited region of the solar atmosphere, typically of 10^9 to 10^{10} cm and emits electromagnetic radiation that can extend from wavelengths less than 10^{-10} cm (gamma radiation), up to more than 10^6 cm. It is the source of energetic particles with energies up to some GeV; the highest measured energy being about 50 GeV. In addition, a flare involves a powerful gasdynamic process in which clouds of matter are ejected and shock waves may be generated. The total energy expended in a large flare exceeds 10^{32} erg and a total mass of 10^{16} to 10^{17}g is involved.

Solar cosmic rays originate in solar flares in the sun's chromosphere. So far, every solar cosmic-ray event observed has been correlated moderately well with a solar flare. However, only a small fraction of the flares observed
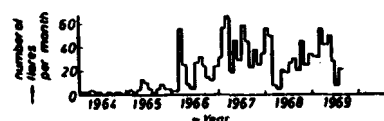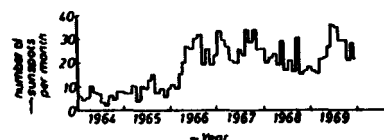
Fig. 13.7: Correlation between sunspot number end solar flare events, during the period 1964 to 1969

produce cosmic rays which can be detected near the earth. The number of flares is inversely proportional to their size. The number of events with very large fluxes is only two to three per year. Correlations of the number and intensity of flares with the number and size of sunspots have been observed for many years. This is shown in Fig. 13.7. The time profile of the particle flux in a flare, measured with a neutron monitor at sea level is shown in Fig. 13.8. A relatively steep rise time of between several minutes and several hours is followed by a decay time of several hours to several days. The biggest flare observed to date occured on the 23rd February 1956. At some ground-level stations, an intensity increase in the nuclear component of up to a factor of 45 was measured. As in galactic cosmic rays, protons are predominant and alpha particles are also present,but the ratio of alpha particles to protons changes from event to event and is a function of energy. Ratios varying from 10 to almost 10^3 have been observed. Heavy nuclei are also present but less abundantly than in galactic cosmic radiation. Their relative abundance in flares reflects the chemical composition of the sun.
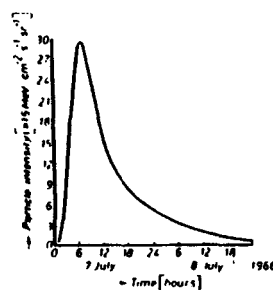
Fig. 13.8: Time profile of a solar flare measured with a neutron monitor at sea level

184

The particle fluxes in solar flares are correlated with other occurences on the sun and induce other effects on the earth. In particular, electromagnetic emissions, ionospheric effects, and absorption effects at high latitudes (Polar Cap *Absorption,* PCA) will be briefly mentioned.

Electromagnetic f/are emission. The sources of optical flare emission are the chromosphere and the corona. The solar disc is commonly viewed with the light of the H_α-line, i.e. the first line in the *Balmer* series with λ = 6563 Å. In general, the maximum brightness only lasts a few minutes. The light increase in the visible region is accompanied by ultra-violet light, X-rays, gamma rays, and radio emission.

Waves and shocks produced by flares. In a flare event, the chromosphere shows a large number of variations which are apparently closely related to the flare process: filament activation, which often occurs before the flare onset, prominence ejections during the development of large flares and blast waves, originating in the flare and travelling along the solar surface.

Ionospheric effects. The arrival of radiation increases the electron density in the upper atmosphere by photoionization, causing *Sudden Ionospheric Disturbances* (SID). This results in electromagnetic radiation effects including the short-wave fade-outs of radio transmissions. The arrival of the charged particles in the atmosphere, also causes a large increase of electron density in the ionosphere and as a consequence there is an attenuation of the normal radio noise. This ionization is especially strong near the poles, where low-energy protons of 5 to 20 MeV. the most abundant in flare processes, can also enter. The effect is called *Polar Cap Absorption* (PCA). In a typical PCA event, the presence of low-energy flare particles is recorded a few hours after the maximum brightness of the flare.

Energy spectrum. The energy spectrum of solar cosmic rays does not remain constant during an event. The highest-energy particles, say $\gtrsim$ 1 GeV, are the earliest arrivals after the flare with delay times of only a few minutes. Lower-energy particles then appear in increasing numbers, while the higher-energy numbers decrease and then disappear. Hence, the energy spectrum is different at different times of observation. The energy or rigidity spectrum is described over a wide energy range by an exponential relation

$$N(S, t) = I_0(t)\, e^{-S/G(t)} .$$

$S = pc/ze$ rigidity
$I_0(t)$ flare parameter characterizing the intensity of the flare
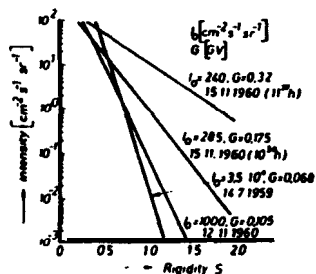$G(t)$ flare parameter characterizing the slope of the spectrum

185

Fig. 13.9: Some typical flare spectra
(From Allkofer, 0. C.. M. Simon: Atompraxis 16
(1970) 1)

The slope of the spectrum is steeper for flares with small values of G than
with large values. Values of G range from 40 MV to 400 MV and values of
I_0 from 2 to 10^3 protons cm^{-2} s^{-1} sr^{-1}. The spectra steepen with time.
The fluxes of high-energy particles are frequently some 10^3 times higher
than the galacticcosmic-ray flux. The integral flux in a single event may
exceed 10^{12} particles per cm^2. Some rigidity spectra at particular times
are shown in Fig. 13.9, and Fig. 13.10 shows some spectra at the maximum
intensities, measured by satelliteduring 1968/69. Finally, in Fig. 13.11 the
different properties of some solar energy spectra and the galactic spectrum
is shown,indicating high flux and low energy in the solar radiation and low
flux but high energy in the galactic component.
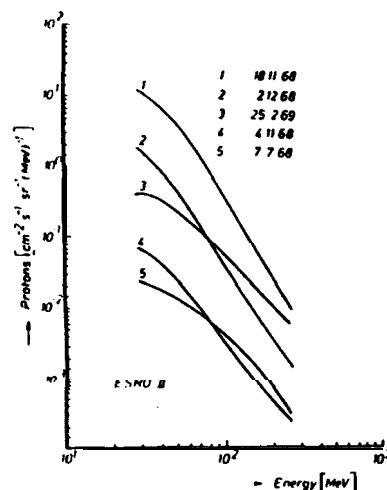
Fig. 13.10: Differential energy
spectra of flares at the maximum of
intensity. measured with an ESRO
satellite during 1968/69.
(From Engelmann, J.: in Proceedingsof
the International Congress on Protection
against Accelerator and Space Radiation,
CERN-Report 71 • 16 (1971))
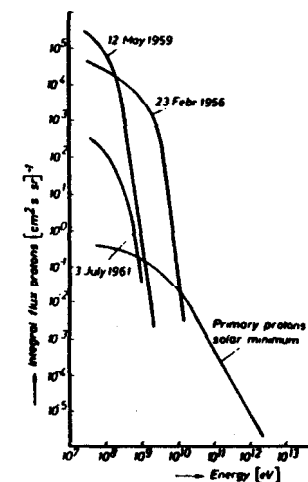
Fig. 13.11: Comparison of f fare energy spectra
with the galactic spectrum

Propagation. It has been observed that flares originating in the western
hemisphere of the sun, are more likely to produce solar particles capable
of reaching the earth, than flares in the eastern hemisphere. Also, the north-
ern hemisphere is more effective than the southern one. The explanation of
the east-west asymmetry is schematically illustrated in Fig. 13.12. The
plasma ejected by the flare carries the magnetic field of the sunspot with
it, and the lines of force are arranged in Archimedian spirals. A magnetic
bottle is formed,which prohibits the escape of low-energy solar cosmic
rays from the inside,and penetration of galactic cosmic rays from the
outside. When the earth is included within the magnetic bottle, there is
easy access from the western hemisphere of the sun, because the field lines
guide the solar particles, whereas particles originating in the eastern hemi-
sphere must cross the field lines. Thus, the latter particles diffuse towards
the earth more slowly. Flares from the eastern hemisphere have a corres-
pondingly slow rise time,whereas flares from the western hemisphere are
characterized by a rapid rise time. In all cases some diffusion occurs, and so
even the flares from the western hemisphere produce particles which
arrive much later by diffusion (indirect radiation). The field in the magnetic
bottle reduces the galactic flux at the earth (Forbush decrease, see Chapter
14.).

Production meachnism. The mechanism by which particier are accelerated
to the energies observed in a solar flare is not yet fully understood although
various models have been proposed. The largest flares have volumes of
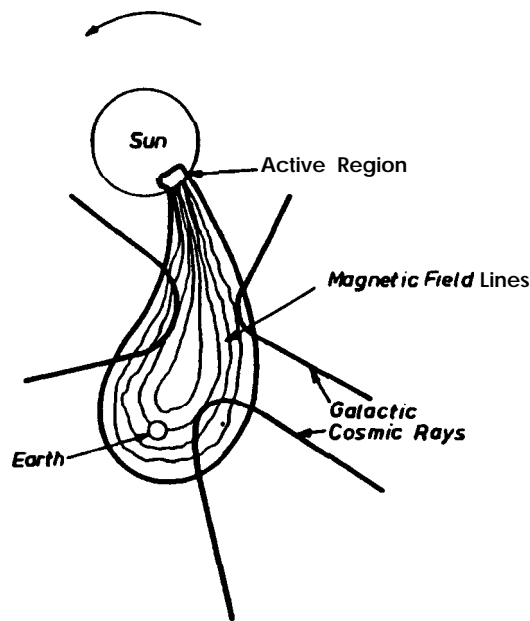
Fig. 13.12: Magnetic bottle model for explanation of flare behaviour

about 10^{29} cm^3, and field strengths of about 1 000 Gauss are involved. Thus an energy density $\rho = H^2/8\,\pi$ erg cm^{-3}, corresponding to a magnetic energy of 10^{33} erg within the volume of the flare, is calculated. This is sufficient to account for the total energy release in a large flare.

References

Kertz. W.: Einfiihrung in die Geophysik. Mannheim: BI Hochschultaschenbiicher Ed. 535.1971

Pomerantz, M. A.: Cosmic Rays. New York: Van Nostrand Reinhold Company 1971

Hess, W. N.: G. D. Mead: Introduction to space science. New York: Gordon and Beach 1968

Unsold, A.: Der neue Kosmos. Berlin: Springer-Verlag 1974

Bruzek, A., H. Pilkuhn: Lectures on Space Physics. Dusseldorf: Bertelsmann Universitatsverlag 1973

Pomerantz. M.A., S. P. Daggal: The sun and cosmic rays. Symposium on solar-terrestrial phenomeny for cycles 18-20. AGU Fall Meeting (1973).

14. Time variations of cosmic radiation

14.1. Introduction

Since the earliest days of research into cosmic radiation, time variations have been extensively studied. Although, to a first approximation, the sea-level flux can be considered as constant, analysis over a period of many years has shown that fluctuations in the intensity exist, which are partly periodic, and partly aperiodic. The observed periodic changes have periods of hours, days, and even years, and are all due to a modulation process caused by the sun. The aperiodic variations also have their origin in the sun. Hence, the *Forbush descrease,* a reduction of the flux, is often observed after solar flares. Additional variations are observed due to meterological effects such as changes of temperature, pressure and season. Finally, long-term variations of the primary radiation over thousands or millions of years are of great interest; such information can be obtained from analysis of meteorites.

14.2. Meteorological variations

Atmospheric variations are studied mainly by means of the sea-level flux of muons and nucleons, the latter via the neutron component. Secondary components are produced in the atmosphere which either decay further or are absorbed. If there is a large scale variation of the atmosphere, it shows up in the sea-level fluxes as a modulation effect.

Although in principal, the behaviour of the whole atmosphere should be taken into consideration, modulation of the nucleon component is well described by pressure variations in the main production layer of nucleons, i.e. the first interaction length of the atmosphere. Thus the variation of the nucleonic component at sea level is correlated with pressure variations in the 100 millibar layer of the atmosphere. The fractional change in the intensity of this component $\Delta I/I$, which has been measured with a neutron monitor at sea level, is given by

$$\Delta I/I = -\alpha_N\,\Delta p.$$

Δp pressure variation of the 100 millibar layer

If the pressure of the production layer is higher than some reference pressure p_0, i.e. $\Delta p = (p - p_0) > 0$, then the neutron flux is reduced, because the particles then have to traverse a great& thickness of atmosphere (g cm^{-2}) down to sea level. The barometric pressure coefficient α_N has the value 0.96% per mm Hg.

The muonic component is modified by the atmosphere in a more compli-
cated way, since muons are unstable particles with relatively short life-
times. The pressure effect of the 100 millibar layer still exists, but is less
significant for muons because they are attenuated less in the atmosphere.
Muons only lose energy by ionization, whereas nucleons lose large amounts
of energy in nuclear interactions. The relation

$$(\text{I/I)}, = -\alpha_\mu \, \mathrm{D}p$$

also applies to muons with barometric pressure coefficient α_μ of 0.215%
per mm Hg.

A further atmospheric effect arises due to the limited lifetime of the muon.
When the altitude of the main production layer is changed, the path lengths
of muons to sea level and consequently their survival probabilities are also
changed. If $H = H - H_{0},$ is the positive change in altitude of the 100 milli-
bar layer (H_0 reference level) then

$$(\Delta I/I)_H = -\beta \, \Delta H \, .$$

The decay coefficient β has a value of about 5% per 10^3 m of atmosphere.

Yet a third atmospheric effect is due to the competition between inter-
action and decay for charged pions (see Section 9.12), the probabilities for
both processes being dependent on the density of the atmosphere. When
there is a rise in temperature of the region between the 100 millibar layer,
where most of the pions are produced, and the 200 millibar layer, where
they mainly interact or decay, the density falls and consequently more
pions decay giving a higher muon flux. Hence,

$$(\Delta I/I)_T = \gamma \quad T.$$

T temperature change in the region between 100 and 200 mbar

This effect is positive in contrast to the others. The atmospheric tempera.
ture coefficient is measured to be 7 = 0.1% per 1 °C.

The total variation of the muonic component at sea level is given by

$$\Delta I = - \, I \, (\alpha_\mu \, \Delta p + \beta \, \Delta H - \gamma \, \Delta T) \, .$$

For an exact analysis, the variation of the coefficients a, β and 7 with atmos-
pheric depth must be considered, and also the variation of these partial
coefficients with muon energy, i.e. a. β, 7 = $f(E_\mu$, HI. In order to detect
other modulation effects, which may have smaller amplitudes, the atmos-
pheric effects, which are of no special interest must be welt determined and
removed.
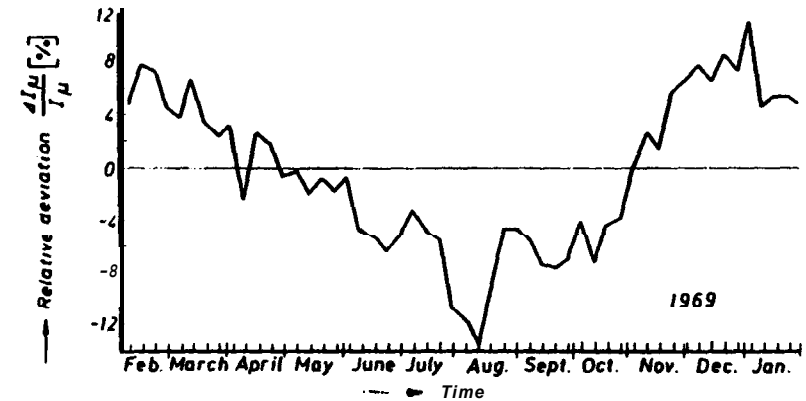
Fig. 14.1: Seasonal variation of the cosmic-ray muon flux
(From Allkofer, 0. C., H. Jokisch: Il Nuovo Cimento 15A (1973) 371)

There exists a large seasonal effect for nucleons and muons, due to a seasonal
variation of the production layer. For muons this corresponds to a combi-
nation of barometric and temperature effects. Fig. 14.1 shows the seasonal
variation of the cosmic ray muon flux at sea level during 1969.

14.3. Durnal variation

For many years, the cosmic-ray intensity measured on the earth has been
observed to undergo periodic fluctuations with a period of one solar day.
The variation is sinusoidal, and has a maximum soon after noon, local time
(see Fig. 14.2). This maximum has been measured at many different stations
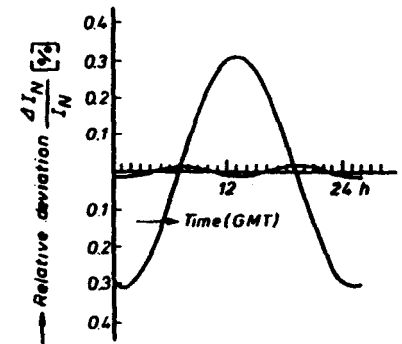
Fig. 14.2: Diurnal variation of the nu-
cleonic component measured at sea level
(Reproduced from Sandstrom, A. E.:
Cosmic Ray Physics. Amsterdam:
North-Holland Publ. Camp., 1965)

at the same local time. Its amplitude is about 0.3% for the nucleonic component and about 0.1% for muons.

An important characteristic of any modulation process is its variation with energy or rigidity, since the origin of the modulations is always the interaction of cosmic-ray particles with the interplanetary magnetic field. Thus modulation is rigidity-dependent, and the fractional change in intensity can be expressed as

$$\Delta I\,(S)/I\,(S) = KS^{-} \,.$$

This is called the variational spectrum. For the diurnal variation, ≈ 0, up to a limiting rigidity $S_{||}$ above which the diurnal anisotropy disappears. Thus

$$I\,(S)/I\,(S) = K \quad \text{for} \quad S < S_1$$
$$I\,(S)/I\,(S) = 0 \quad \text{for} \quad S > S_1\,.$$

S, changes during the solar cycle, and has a value of about 55 GV at the solar minimum and 100 GV at the solar maximum.

The origin of the modulation is believed to be the interaction of the solar wind with the magnetic field. Since the magnetic field co-rotates with the sun, so also do the low-energy cosmic-ray particles spiraling around the magnetic field lines. As a result, the particles moving in the same direction as the earth's orbital motion have a flux excess of about 0.4% compared with those moving in the opposite direction. Under these conditions, the cosmic-ray particles are continuously overtaking the earth, and this should produce a directional anisotropy. Calculations are in approximate agreement with the observed amplitude and its variation with geomagnetic latitude.

Fourier analysis finds that the diurnal variation is not quite sinusoidal, but contains a second harmonic, a semi-diurnal variation (also shown in Fig. 14.2). Its amplitude is less than 0.1%.

If cosmic ray intensity is not isotropic within the volume of our galaxy, then the rotation of the earth should cause a periodic fluctuation of any measured flux with a period of one sideral day. Thus by searching for sideral variations, anisotropic sources might be detected. However, because of the interstellar magnetic field only the original directions of high energy particles are conserved. For energies up to 10^{15} eV, a sideral variation with an amplitude of a few times 10^{-2} % has been detected, and for energies up to 10^{17} eV, an amplitude of about 1% has been found.

192

14.4. Forbush decreases

By continuous monitoring of the cosmic-ray intensity, it was found that on many occasions, on a world-wide scale, the cosmic-ray intensity decreased by between a few per cent and about 20%. This decrease occurs relatively fast, within a few hours, and then the intensity recovers to the original level within the order of days or several weeks. These events are known as *Forbush decreases* or F-events. The superposition of several F-events is called cosmic-ray storm. Fig. 14.3 shows an F-event measured with a neutron monitor. In contrast to the diurnal cosmic-ray variation, which is a local time effect, the *Forbush decrease* is a universal-time effect, i.e. the event is observed almost simultaneously all over the world. F-events often occur in association with geomagnetic storms, but there is not a one-to-one correspondence, either one may happen without the other. Both of these effects are usually observed about one day after a solar flare.

Although exact details are not yet well known, the general mechanism responsible for a F-event is generally believed to be a solar-wind effect. At the time of occurence of a solar flare, the ejected magnetic plasma cloud may have a higher velocity than the normal plasma stream. This stream which has a velocity of about 1000 km h^{-1}, produces a blast wave, and arrives at the earth in a typical time of the order of one day. A magnetic bottle is formed (see Fig. 13.12) which, due to the high electrical conductivity, transports the field present in the vicinity of the sunspot area where the flare originated. When the earth is included within the magnetic bottle, its magnetic field deflects away low-energy galactic cosmic-ray particles, preventing them from reaching it. The magnetic bottle also causes the geomagnetic field to increase during a geomagnetic storm (see Section 13.6).
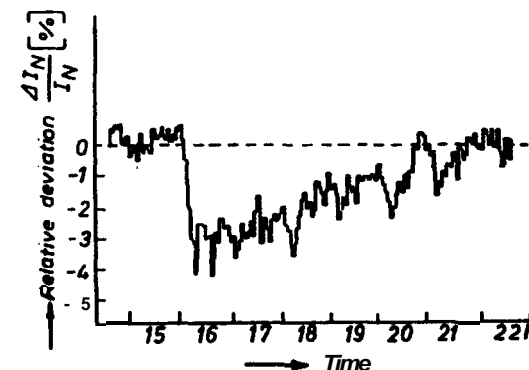
Fig. 14.3: *Forbush decrease, measured with a neutron monitor* (Reproduced from Pomerantz. M. A.: Cosmic Rays. New York: Van Nostrand Reinhold Company 197 1 I

193

14.6. 27-day recurrences of variations

If an abnormal value of the cosmic-ray flux is observed one particular day, on the average, a similar effect may be observed 27 days later. The 27-day recurrence of geomagnetic storms is a well known phenomenon. Forbush decreases have a similar recurrence pattern, and the effect also appears in the amplitude of the diurnal variation. Because this interval is the same as the 27-day rotational period of the sun, the recurrences can be explained as a solar effect. Thus, the same sunspot zones reappear with this periodicity. Characteristic features of specific sunspot areas are repeated every 27 days.

14.6. 11-year variation

By monitoring the cosmic-ray flux over a large number of years, it has been found that the average flux varies with a period of about 11 years. This period is equivalent to the 1 l-year cycle of solar activity and is anticorrelated with the cycle of sunspot appearances. Fig. 14.4 shows the variation of the muon and neutron components measured during 1965/72. The peak-to-peak variation in this period is 14% for the neutron flux, and 4.5% for the muon flux. Variations of up to 30% have been measured for neutrons. The modulation effect of the solar cycle also appears in the primary component of cosmic radiation. Hence the primary energy spectrum is modulated at low energies according the 1 l-year cycle as shown in Fig. 14.5. The differential proton flux at 1 GeV, can vary by a factor of 5 over the solar cycle.

The anti-correlation between solar activity and galactic cosmic-ray flux, can also be explained as due to the solar wind. The solar wind, with its magnetic fields changes with the 1 l-year cycle, i.e. at solar active periods the solar-wind intensity increases, and during quiet periods it decreases. Thus, the magnetic field strength in the solar plasma clouds changes with the solar
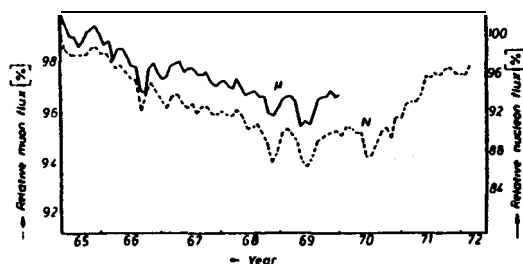
Fig. 14.4: The 11 -year variation of the muon and neutron components at sea level (From Allkofer, 0. C.: H. Jokisch: Il Nuovo Cimento 15A 1197313711

194
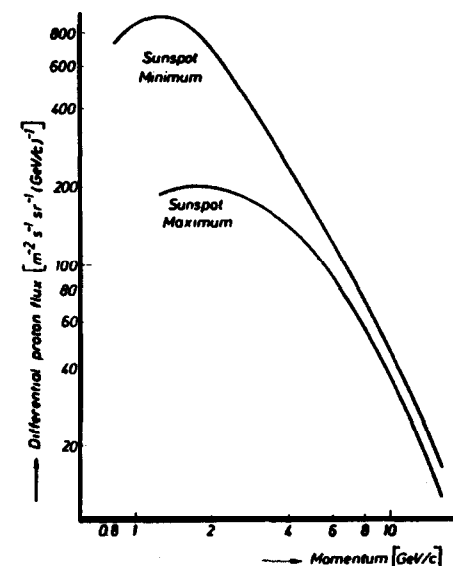
Fig. 14.5: Modulation of the primary galactic energy spectrum due to the solar cycle (Adapted from Schopper, E.. E. Lohrmann, G. Mauck: Nukleonen in dar Atmosphare, Handbuch dar Physik, Kosmische Strahlung II, 372 Berlin: Springer Verlag 1967)

cycle. At the solar sunspot maximum, the flux of galactic cosmic radiation is strongly reduced, i.e. more particles are deflected by the magnetic bottle, and do not reach the earth.

14.7. Longperiod variations

Cosmic-ray particles produce both, stable and unstable isotopes by nuclear interactions in the atmosphere. In general, isotopes are produced in the earth's crust, in the atmosphere and in meteorites. The production of C 14 in the atmosphere, and its use for determining the age of plants and animals has already been mentioned in Section 9.9. The following nuclides have been detected in the atmosphere, the oceans and in marine sediments:

He 3, Be 10, Si 32, Cl 36, Ar 39, Mn 53, Ni 59, and Kr 81.

Analysis of stable and radioactive nuclides produced by nuclear reactions in meteorites, yields information on the flux behaviour of cosmic radiation over the ages. If a meteorite is irradiated by a constant flux of cosmic-ray protons, the radioactive isotopes produced build up to a saturation value in a time approximately equal to the mean lifetime of an isotope, while the stable isotopes continue to accumulate indefinately. Assuming that the present cosmic-ray flux has prevailed throughout the irradiation the production rate of certain nuclides can be calculated. The components com-

195

pared in flux evaluations are (a) short-lived and long-lived nuclides produced in similar nuclear reactions, (b) radioactive and stable nuclides, (c) products with widely different mass numbers. If the cross-sections for two specimens are similar, the relative production rate is given by the ratio of the cross-sections, independently of the detailed nature of the bombarding flux. The nuclides produced in meteorites by cosmic-ray protons are summarized in Table 14.1. Their half-lives extend from two weeks to millions of years. If the cross-sections are known, the bombardment age can be calculated. An ideal case for comparison is the pair of isotopes Cl 36 and Ar 36. About 60% of all the Ar 36 atoms formed in an iron meteorite result from the decay of radioactive Cl 36.

From the comparisons of nuclide pairs, it has been established that the flux of cosmic radiation has been the same over the past 500 years and the same to within ± 10% over the past 500 000 years. Constancy over a period of 10^9 years is within a factor of two.

Table 14.1: Nuclidas produwd in meteorites
(Adapted from Honda, M., I. R. Arnold: Effects of Cosmic Rays on Meteorites. In Handbuch der Physik. Vol. LVI/2 (Ed. K. Sitte) Berlin: Springer Verlag (1967)

short-lived	intermediate	long-lived	stable
Mn 52 (5.7d)	Mn 54 (300d)	Mn 53 $(2.10^6 a)$	Cr 53; Cr 54
V 48 (16d)	V 49 (330d)	K 40 $(1,3 \cdot 10^9 a)$	V 50; Cr 50
Sc 46 (84d)	Ca 45 (165d)	Cl 36 $(3 \cdot 10^5 a)$	sc45: ca 43
Ar 37 (35d)	Ca 41 $(8 \cdot 10^4 a)$	Al 26 $(7.4 \cdot 10^5 a)$	Ca 46; K 41
Be 7 (53d)	Ar 39 (260d)	Be 10 $(2.5 \cdot 10^6 a)$	Ar 48; S36
	Na 22 (2.6a)		Ne 20; Ne 21
	C 14 $(5.6 \cdot 10^3 a)$		Ne 22; He3
	H 3 (12.3a)		He 4; Ar 36
			Ca42

References

Dorman, L.I.: Cosmic rays: variation and space exploration. Amsterdam: North-Holland Publishing Company 1974

Sandstrom, A. E.: Cosmic-ray physics. Amsterdam: North-Holland Publishing Company 1965

Pommerantz, M. A.: Cosmic rays. New York: Van Nostrand Reinhold Company 1971

Allkofer, O.C., H. Jokisch: A survey on the recent measurement of the absolute vertical cosmic-ray muon flux at sea level. Il Nuovo Cimento 15A (1973) 371.

16. Biophysical significance of cosmic radiation

15.1. Introduction

When cosmic-ray particles interact with tissue, they produce a radiation , dose similar to a radioactive source. At sea level, and at mountain altitudes, this dose is negligible compared with doses from environmental radioactivity. The integral cosmic-ray flux and hence the dose rate increases with altitude, the latter much more rapidly, due to the changing composition of cosmic radiation. At the cruising altitude of the subsonic jets, about 10 km, the dose rate is already about a factor of 70 higher than at sea level. However, the cosmic radiation from solar flares is almost completely absorbed higher in the atmosphere, and heavy nuclei play a minor role at this level, because they are more or less completely fragmented in higher atmospheric layers.

At the higher altitudes of the Supersonic Transports (SST), the situation is different because the composition of the galactic component differs from that at the subsonic level, the solar flares are more efficient, and a small number of heavy nuclei are still present. The dose rate is about a factor 5 more than at the subsonic level, and about 400 times higher than at sea level.

In free space, there is no longer any shielding against solar flares, and an additional radiation hazard appears when the radiation belts have to be crossed. For long, manned space flights, the effects of all the cosmic ray components have to be considered.

A useful sub-division of the radiation hazards due to cosmic radiation is as follows:

– radiation dose produced by galactic radiation
– local radiation injuries due to heavy nuclei of the galactic component
– total radiation hazard due to solar flares
– occasional very high dose rates due to strong solar flares.

15.2. Basic definitions of radiation dose units

When a charged particle traverses material such as tissue, it loses energy by ionization and excitation, $(- dE/dx) \propto z^2/v^2$ (z charge of the particle, v velocity of the particle). The radiation damage increases with the charge z, of the bombarding particl.e, and decreases with its velocity v. Thus, stopping heavy ions at the end of their range are particularly dangerous. Particles

can also interact with atomic nuclei in matter, causing breakup or emission of mesons and hyperons. Low-energy secondary particles also have a high ionization density. Since neutrons undergo nuclear interactions and produce secondary particles, they too have a similar effect. The toxicity of a specific type of particle increases with Linear Energy *Transfer,* LET, i.e. more ions are produced within a given distance.

There are three basic units of radiation dose,

(a)   The roentgen (r) is the absorbed dose of X- or gamma radiation which produces 1 esu (electrostatic charge unit) in 1 cm^3 of air (= 1.293 mg), thus

$$1 \text{ r} \triangleq 2.06 \times 10^9 \text{ ion pairs.}$$

The amount of energy produced per g differs from one medium to another. In air 1 r $\triangleq$ 67.6 erg g^{-1} and in tissue 1 r $\triangleq$ 94 erg g".

(b)   The rad (radiation absorbed dose) is a definition based upon absorbed energy

$$1 \text{ rad} \triangleq 100 \text{ erg g}^{-1};$$

for tissue, 1 rad $\approx$ 1 r.

(c)   A dose unit which takes into consideration the degree of toxicity. If two different kinds of charged particles produce the same rad dose, they have different radiotoxidities if they differ in LET, since toxiditv depends on the distribution of ionization along the particle trajectory. A quality factor QF, is introduced,which increases with LET (see Fig. 15.1). The dose unit which takes into consideration the differences in LET is the rem (roentgen equivalent man),

$$\text{rem} = \text{QF} \times \text{rad} .$$

This is the most convenient unit for describing the biological radiation hazard.
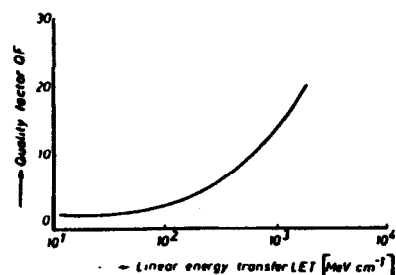
Fig. 15.1: Variation of the quality factor QF with linear energy transfer LET for a charged particle

Table 15.1: Natural and artificial environmental radiation doses

type of irradiation	mean dose rate (mrem a^{-1})
external irradiation	50
cosmic rediation	30
internal irradiation	50
medicine (diagnostics and therapy)	130
technical applications	2
radioactive fallout from nuclear explosions	20
professional exposure (reactors, x-ray therapy, redionuclides)	2
total	250 - 300

Heavy nuclei have high QF values, because of their high charges, whereas stopping particles have high QF values, because of their low velocities. Strongly interacting particles, such as protons and neutrons produce secondaries with high charge and low velocity, and consequently also have high QF values. Heavy nuclei have the highest QF values with QF $\lesssim$ 20.

It is useful to know for comparison,what radiation dose people receive from the environment. A natural component is present due to radioactivity and an artificial one due to medicin and technical applications.. Table 15.1. gives a summary of average yearly doses. The mean radiation dose per year is seen to be 250 to 300 mrem. The amount of radiation damage is strongly dependent upon which organ of the body is exposed to radiation; there are different tolerance levels for different organs. A differentiation is made between:

(a)   *somatic effects* which manifest themselves directly in the tissue of the whole organism, and may occur soon after the exposure (minutes to weeks) or much later (months or years),

(b)   generic injuries, which manifest themselves statistically in the whole population, and from which the legally allowed limits for radiation doses are deduced, and

(c)   *fruit damage,* i.e. damage to a foetus or embryo in the early stages of development, where there is a special sensitivity due to rapid cell division. In the latter case a high dose rate can produce malformations.

15.3. Radiation hazard at the level of supersonic transport

The cruising altitude of SST flights will be between 17 and 23 km. In order to evaluate the radiation hazard, the particle fluxes of the galactic com-
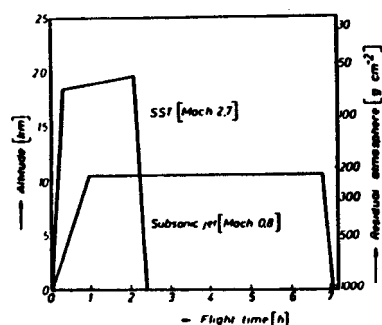
Fig.15.2: Typical flight profiles for a subsonic jet, and a supersonic transport, on a flight from Paris to New York.

ponent, in particular the flux of heavy nuclei, and the radiation produced by solar flares have to be considered separately. Fig. 15.2 shows the typical flight profiles of a subsonic and a supersonic aircraft, on a flight from Paris to New York and Fig. 15.3 gives the fluxes of the main cosmic-ray components present at subsonic and SST levels.

in principle, hadronic and electromagnetic cascade multiplication can take place in the wall of the aircraft. However, because the characteristic lengths for these processes in aluminum (interaction length λ_{AI} = 32.3 cm and radiation length X_{AI}^{o} = 9.1 cm) exceed the wall thickness, they can be neglected for dose rate evaluation.

(a)   Galactic radiation. Table 15.2 gives the fluxes of the main cosmic-ray components at the highest SST level of 23 km, at the subsonic level and at sea level. The radiation dose has been both calculated and measured at the SST level. Variations in the results have been obtained due to the latitude effect, an altitude effect and a change with the 11-year cycle. Values be-
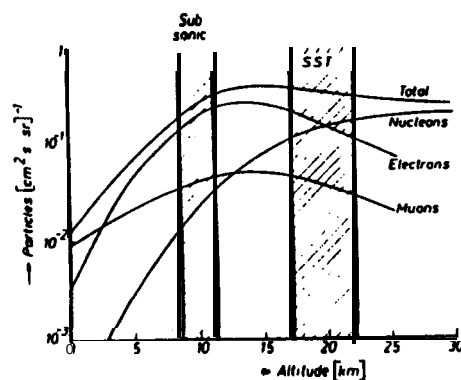
Fig. 15.3: Flux composition at the level of SST and at subsonic level

Table 15.2: Comparison of the main particle fluxes et sea level, subsonic level, end SST level
(Adapted from Allkofer. 0. C., M. Simon: Atompraxis 16 (1970) 1)

particles $(cm^{-2} sr^{-1} s^{-1})$	SST 123 km)	subsonic (10 km)	see level
nuclaons	0.17	0.02	1 0 - 4
electrons	0.10	0.20	4 x 10-3
muos	0.03	0.04	0.01

tween 1 and 4 mrem h^{-1} have been measured. At a cruising altitude of 20 km, a dose rate of 2 mrem h^{-1} is a reasonable average figure. A duty time of 20 hours per month at SST altitude, leads to a dose rate of 480 mrem a year.

(b)   *Dosimetric significance of heavy nuclei.* The intensities of heavy nuclei are very low, because the primary flux is only about 1% of its initial value, and because fragmentation occurs in the upper atmosphere (see Section 9.10). However, it is generally believed that single hits of low-energy or stopping nuclei in tissue, can produce a high local damage because of the large amount of eneigy deposited. Such stopping tracks of heavy nuclei are called enders or thin down hits. The number of stopping nuclei for different charge groups have also been both, measured and calculated. Fig. 15.4 shows the omnidirectional flux of stopping nuclei per cm^3 of tissue, for different atmospheric depths, at the solar minimum. From these
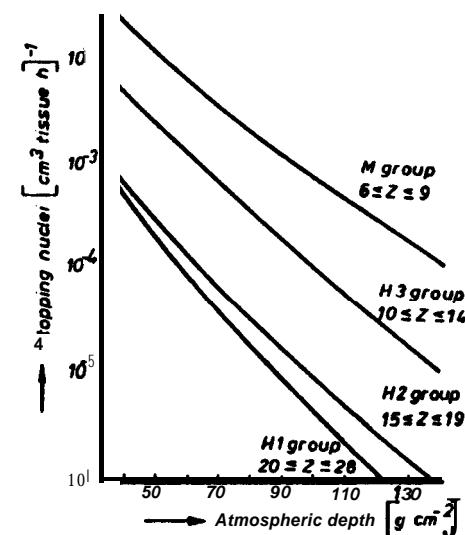
Fig. 15.4: Omnidirectional flux of stopping nuclei per cm^3 of tissue, for different atmospheric depths at solar minimum
(From Allkofer, O.C., W. Heinrich: Health Physics 27 (1974) 543)
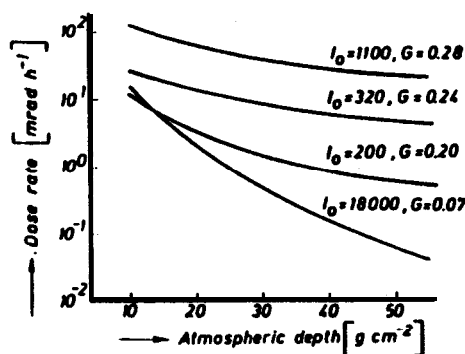
Fig. 15.5: Dose rate versus atmospheric depth at solar minimum
(From Allkofer, 0. C., M.Simon: Atompraxis 16 (1970) 1)
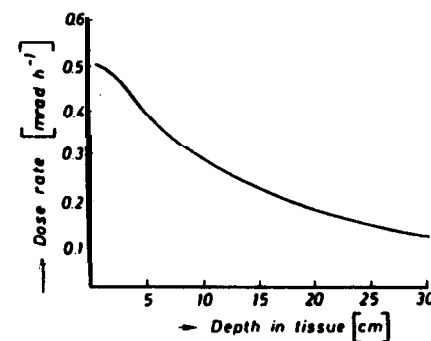

Fig. 15.6: Depth dose distribution produced by average flare events at SST level
(From Allkofer. O.C., M. Simon: Atompraxis 16 (1970) 1)

values, the number of stopping nuclei within a sphere of tissue of diameter 12 cm. simulating a human body, has been calculated for different charge groups, at an altitude of 20 km. For nuclei with charge $Z \geqslant 6$, a value of 5.6×10^{-3} stopping nuclei per cm^3 of tissue per hour was obtained. The radiation hazard caused by these low fluxes can barely be evaluated, although a possible collision with an embryo during organogenesis could have a serious result. Taking a value of 1 cm^3 for the embryo, and a duty time of 40 h per month, the probability of such a hit for a pregnant crew member is 20% per month, at an altitude of 20 km. At the altitude of 16 km the probability is reduced by a factor of 10. For passengers the probability is lower, because less time is spent at SST level, although the total risk increases with the number of passengers.

(c)   *Solar flares.* There is at present no direct experimental information on the time profile of the radiation surge at SST altitude during large solar flares. Only those flares which are able to produce extraordinarily high intensities at SST altitude are important. Such flares occur during the time of the active sun, with a frequency of about 12 per year. Fig. 15.5 shows the variation of proton dose rate near the polar region, at different altitudes, for some typical flares. Flares produce no effects in the equatorial region because of the high geomagnetic cut-off. Secondary neutrons produced in the atmosphere by flare protons, contribute 20 to 50% of the dose rate, depending on the flare parameters. Occasionaly events of very high flux occur, such as the event of the 23 rd February 1956 in which dose rates of some rems were produced at SST level. The frequency of high-intensity events producing dose rates of some 100 mrem h^{-1}, is about 2 per year. In addition to the high-intensity flares, there are other flares which produce an average radiation dose of about 1 mrem h^{-1}, the same order of magnitude as the dose rate from the galactic component. To give an idea of the di-

stribution of the dose rate in ittuse, the depth-dose distribution is shown in Fig. 15.6, for a typical flare event. It is seen that the calculated, interior dose rates are only slightly smaller than those on the surface. Fig. 15.7 shows possible biological doses, in mrem h^{-1}, near polar regions, for different flare parameters. About 60% of all measured events lie within the enclosed region.
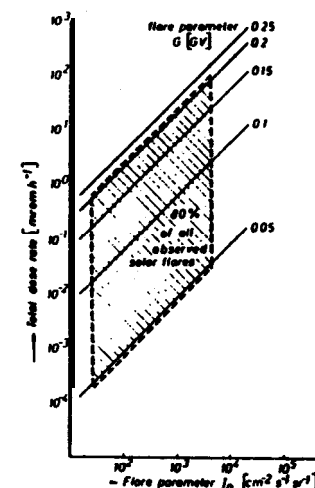
Fig. 15.7: Dose rate distribution of observed flare events as a function of the typical flare parameters I_0 and G
(From Allkofer, O.C., M. Simon: Atompraxis 16 (1970) 1)

16.4. Radiation doses in free space

In free space as at SST level, there exist the galactic component containing protons and heavy nuclei, the solar flares, here producing higher dose rates because there is no atmospheric shielding, and the radiation belts. In order to evaluate the dose rates in free space, several kinds of particles (electrons, protons, heavy nuclei), with various energies must be considered. Dose

Table 15.3: Radiation doses in free space
(Adapted from notes for the Advanced Radiological Protection Course of the Harwell
Post-Graduate Education Centre, A.E.R.E., Harwell, Didcot, Oxfordshire. England)

radiation	dose rate	remarks
galactic radiation	0.01 • 0.05 red d^{-1} 0.07 • 0.30 rem d^{-1}	a 10-day Apollo mission -0.5 rad
radiation belts	protons: 1 • 10 rad h^{-1} (behind a shielding of 1 cm Al) electrons: $10^2 \cdot 10^3$ rad h^{-1} fat surface)	traversing the radiation belts -0.5 rad almost completely absorbed by the walls of the spacecraft
solar flares	12 • 350 rad per event at surface 1 • 15 rad at 2 cm depth of tissue	the very strong event of 23.2.56, ~1000 rad in tissue
heavy ions (Z > 10; LET > 550 MeV cm- ^{1}	10.9 • 1.71 x 103 particles $m^{-2} d^{-1}$	1.5 hits cm^{-2} for a 10-day Apollo moon mission

rates in free space are important for astronauts, particularly on long-term
missions. Some dose rates for different sources are given in Table 15.3.
The reason for the wide range of values is that there are modifications due
to the influence of the magnetosphere, the solar cycle and the geomagnetic
cut-off.

(a)   *Galactic radiation.* Possible hazards due to the galactic radiation are
a shortening of the lifespan and an increased possibility of contracting
cancer. The only results available are for mice. Applying these values to
man, the values for radiation damage given in Table 15.4 are obtained. The

Table 15.4: Shortening of lifespen due to irradiation by the galactic component in
free space
(Adapted from Schafer, H. J.: Biophysics 5, (1969) 315 and Tobias C. A. et al.:
AGARD Conference Preprint 95 (1971) C6)

radiation	LET (MeV cm^{-1})	lifetime shortening (d rad^{-1})	
		accute irradiation	chronic irradiation
primary protons. alphaparticles and high-energy secondary particles	35	12	3
heavy ions (3 ≼ Z ≼ 28), low-energy secondary particles and neutrons	36	24	24

consequent shortening of life for astronauts is on average about 0.25% of
the mission time. Using observational data obtained at clinics, where pa-
tients have been treated by radiotherapy, it is predicted that the probability
for contracting leukaemia is doubled in space missions.

(b)   Solar *flares.* At the advent of a solar flare, astronauts would be irra-
diated for a period of about one day. The wails of the space vehicle would
provide some shielding. Fig. 15.8 shows the integral percentage of flare
events behind 2 cm and 40 cm of aluminum. Because most flare particles
are of relatively low energy, they do not penetrate far into the human body.
Nevertheless, very strong flares produce appreciable doses at a depth of sever-
al cm of tissue; at 5 cm the dose is reduced about 20% of that on the surface.
The blood-producing organs situated near the skin, might receive as much
as 30 rem during a strong flare event, and so in addition to the chronical
injuries produced by galactic radiation, further radiation injuries can occur.
The very strong flare of 23 rd February 1956, produced a radiation dose in
free space of about 1900 rem.

(c)   *Radiation belts.* The potential hazards of irradiation in the radiation
belts are also difficult to evaluate, because high fluxes of low-energy partic-
les are present. At various locations within the radiation belts, protons
produce dose rates of between 1 and 10 rad h^{-1}, behind 1 cm Al, an ap
preciably higher dose rate than that of the galactic radiation. During a
space mission, the radiation belts are usually crossed by the spacecraft in
less than one hour and so the resultant dose rate is less than the accumula-
ted dose of galactic radiation, during a 10-day mission to the moon. Be-
cause the energy of the electrons in the radiation belts is very low, most
of them are absorbed in the walls of the space vehicles.
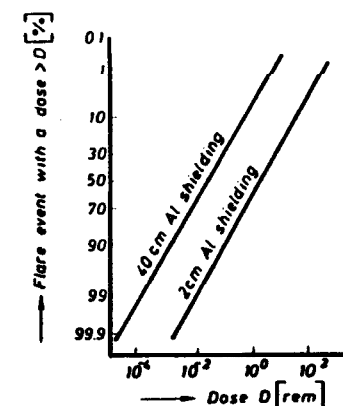
Fig. 15.8: Integral distribution of flare
events as a function of dose rate, for two
thicknesses of shielding

Table 16.5: Number of nerve-cells destroyed due to hits by heavy ions
[Adapted from Schafer, H. J.: Biophysics 5,315 (1969) and Tobias C. A. et al., AGARO Conference preprint 95 (1971) C6)

cell5	number of cells destroyed per 10^6 cells	
	Apollo mission (12 days)	2 year space mission
cerebellum	0.50 • 0.65	40 • 50
netskin ganglies cells	0.64 • 5.7	50 - 500
cerebrum	2 - 1 4	16 - 120
shell of cerebrum (BETZ cells)	18-83	1050 • 6600
spinal cord	26-200	2000 - 16000

Fig. 15.9: Picture of some artemia salina eggs with a particle track detected in a plastic detector

(d) *Heavy ions.* **The radiation hazard due to heavy nuclei has to be evaluated in terms of single events as at SST level. A comparison of the number of hits in space and at an SST level of 20 km, finds that the crew members of an aircraft during 20 years of service will receive the same number of hits as astronauts on a 10-day trip to the moon. The influence of heavy ions was studied during the Apollo mission to the moon where astronauts saw light flashes with closed eyes. Laboratory experiments found that such flashes were due to hits on the retina of the eye. When a low-energy heavy ion hits a cell nucleus it is very probable that the cell nucleus will be destroyed because of the large amount of energy deposited. Furthermore, because the region of ionization around the particle path increases with the charge of an ion, it is probable that every cell struck by a heavy ion will be destroyed. Table 15.5 shows the numbers of sensitive organ cells destroyed during the moon mission of Apollo 12 and for a hypothetical long-term mission of two years. The lower limit is calculated under the assumption that a hit on any part of a cell destroys it. Under normal environmental conditions nerve-cells also die, making it difficult to evaluate real radiation damage. Certainly, for future long-time missions in space, such effect must be taken into consideration. Experiments have even shown that roots of hairs become grey, if they are hit by a heavy ion.**

In order to obtain direct information about the biophysical significance of the radiation hazard of heavy ions, the *biostack experinient* **was performed. During the manned Apollo 16 and 17 missions to the moon, a biostack was carried in the capsule. Such an object consists of several layers of biophysical specimens, alternately stacked between track-sensitive detectors. Some of the specimens were shrimp eggs (Artemia Salina). Fig. 15.9 shows two of the eggs under magnification, together with the track of a heavy**
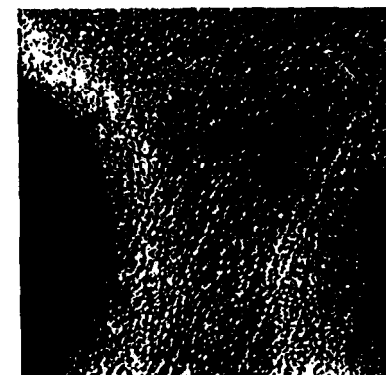
ion, which has penetrated one of the eggs and been measured in a plastic detector. Preliminary results found a high reduction in larval emergence and hatching, plus the beginnings of developmental anomalies in the struck eggs.

References

International congress on protection against accelerator and space radiation. CERN-report CERN 71-16 (1971).

Allkofer. O.C.: Dosimetry at SST altitude. Invited paper at the 8th international conference of nuclear photography and solid state track detectors, Bukarest (1972).

Allkofer. O. C., W. Heinrich, M. Simon: Strahlenbelastung bei bemannten Raumflugen. Umschau in Wissenschaft und Technik 72, Heft 19, (1972) 284

Bruzek, A., H. Pilkuhn: Lectures on Space Physics. Dusseldorf : Bertelsmann Universitatsverlag, 1973.

Allkofer. O. C, W. Heinrich: Measurement of cosmic-ray heavy nuclei at supersonic transport altitudes and their dorimetric significance. Health physics 27 (1974) 543.

Schafer, H. J.: Die gelaktische Strahlendoris im freien Planetenraum. Biophysic 5 (1969) 315.

Tobies, CA., T. F. Budinger, J.T. Leith. A. M. Mamoon, P. Chapman: Visual phenomena induced by cosmic rays and accelerated particles. AGARD conference preprint 95 (1971) C6.

Bucker, H., G. Horneck. E. Reinholz, W. Ruther, E. H. Graul, H. Planel, J.P. Soleilhavoup, P. Cuer, R. Kaiser, J.P. Massue, A. Pfohl. W. Enge, K.P. Bartholoma, R. Beaujean. K. Fukui, O.C. Allkofer, W. Heinrich, E. V. Benton, E. Schopper. G. Henig. J. U. Schott, H. Francois, G. Portal. H. Kuhn, 0. Herder, W. Wollenhaupt, G. Bowman: Biostack experiment, Apollo 17: preliminary science report, NASA SP-330, 251 (1974).

16. Applications of cosmic radiation

Although cosmic-ray particles have the highest energies observed in our universe, they are of little practical use. The whole field of cosmic radiation, in its astrophysical, geophysical and high-energy physics aspects is an almost pure science. However, a small number of applications have been made. The radiation dose considerations for SST flights and manned space missions, discussed in Chapter 15, represent a field of study of some relevance to society. If scientists had not carried out research in this field, a potential danger for man might have remained unknown. In the following three sections, some examples of uses of cosmic radiation will be briefly described.

16.1. Temperature measurement in the atmosphere

The muon flux at sea level varies according to changes in meteorological parameters (see Section 14.2.). One of these parameters is the atmospheric temperature. To a first approximation, sea level flux variations depend only on temperature variations of the 200 millibar layer

$$I_\mu = I_0 (1 + \alpha \, \Delta T) \, .$$

b   mean intensity
T temperature change
α temperature coefficient (%/°C)

From this relationship, the mean temperature change of a specific layer in the upper atmosphere is determined to be

$$\Delta T = \frac{1}{\alpha} \cdot \frac{\Delta I}{I} \, .$$

In a more refined treatment, the variation of temperature coefficient with muon energy and the altitude in the atmosphere, are taken into account. Fig. 16.1 shows the partial temperature coefficient as a function of atmospheric depth for three muon energy ranges (a) $0.2 \leqslant E_\mu \leqslant 0.35$ GeV, (b) $E_\mu \geqslant 0.5$ GeV, and (c) $E_\mu \geqslant 1.2$ GeV. Using the above relations, the behaviour of the temperature in the i-th layer of the atmosphere, at time t, can be written as

$$T_i(t) = \beta_{1\,i} \, I_1(t) + \beta_{2\,i} \, I_2(t) + \beta_{3\,i} \, I_3(t) \, .$$

$T_i(t)$ time-dependent temperature of layer i
β_{1i} temperature coefficient of layer i for $0.2 < E_\mu \leqslant 0.35$
β_{2i} temperature coefficient of layer i for $E_\mu \geqslant 0.6$ GeV
β_{3i} temperature coefficient of layer i for $E_\mu > 1.2$ GeV
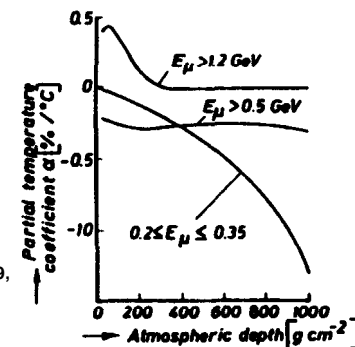
Fig. 16.1: Partial temperature coefficients of muons at different energies as a function of arrnospheric depth
[Adapted from Miyazaki. Y., M. Wada: Acta Physica Academiae Scientiorium Hungaricae 29, Suppl. 2 (1970) 591]

$I_1(t)$, $I_2(t)$ and $I_3(t)$ are the measured muon fluxes for the corresponding energy ranges.

Using detectors with an area of about 10 m^2, the temperature has been measured at three-hours intervals, with a precision of 1 to 2 °C.

16.2. Search for hidden chambers in the pyramids

Part of the energy spectrum of low-energy muons at sea level, is cut off if they traverse a finite amount of absorbing material. By using a high-angular resolution muon detector, in an underground laboratory in mountainpthe angular variation of the muon flux can be measured, and hence the contours of the mountains above can be seen by "the light of the muons". In principle, the muon flux can therefore be used to search for caves in mountains or hidden chambers in pyramids. Three pyramids built about 2 500 B.C. are situated at Giza, near Cairo. The largest is 145 m high. One of them, Cheop's pyramid, shows great complexity in construction, with many internal passages, galleries and chambers, whereas in another, Chephren's pyramid, only one buriel-chamber has been discovered. Using wire spark chamber detectors, attempts have been made to detect unknown chambers in this pyramid, by looking for anomalies in the muon angular distribution. Calculations showed that a chamber of reasonable size would be seen in spite of multiple scattering by thestones of the pyramid. It was estimated that the path length of a muon in limestone could be determined to an accuracy of 1 m in 100. Only a limited volume of the pyramid has been studied so far, and 2×10^6 tracks have been analyzed. No chamber has been detected. Analysis of the results has shown that it is reasonable to use the cosmic-ray muon flux for applications of this kind.

16.3. Sea wave and tide recording

Since the cosmic-ray flux at sea level is almost constant, a detector of convenient size can measure the thickness of absorbing material above it. If this detector is installed in the sea, the underwater flux determines the water layer thickness above the detector. In this way, direct information of the tide gauge is obtained, knowing the relation between cosmic-ray flux and water depth. A scintillation counter of ~ 4 m^2, measuring over a period of some minutes leads to errors of 1 to 2 cm in the value of the depth. The values are in agreement with those obtained by conventional methods. Fig 16.2 shows the recorded tide gauge using cosmic radiation and using a conventional mechanical system.
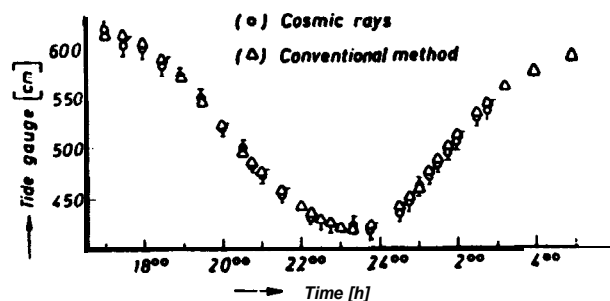
Fig. 16.2: Tide gauge measured by (a) cosmic rays and (b) a conventional, mechanical tide racordar
(From Allkofer, O. C., M. Simon: Ocean Engineering 2 (1972) 123)

As the thickness of the water layer above the detector varies, due to sea wave movements, so does the measured flux and hence a sea wave record can be made. For the analysis of sea waves it must be realized that sea motion is a stochastical process and that there are a finite number of data for analysis. Such an analysis is performed by an autocorrelation method. Some results are shown in Fig. 16.3. The data correspond to a power spectrum of sea waves as measured by cosmic rays and by a mechanical wave recorder. The power spectrum indicates the dominance of particular wave frequencies, and determines the dominant sea wave period to be 4.3 ± 0.3 s, with a mean wave height of 30 to 64 cm. Comparison shows that the cosmic-ray method is as good as the mechanical system. The important advantages of the former method,which is new, are the fact that the
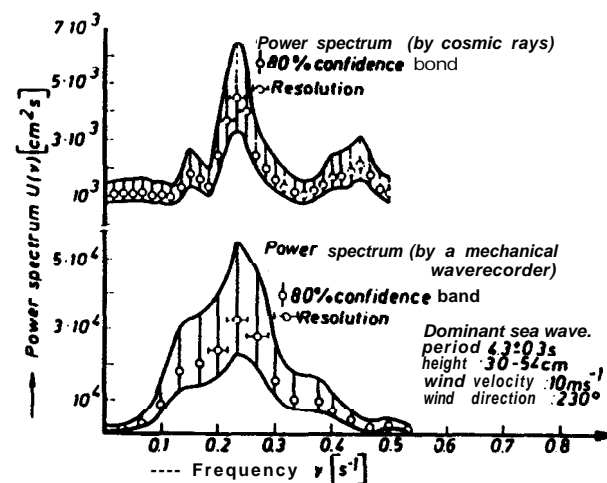
Fig. 16.3: Power spectra computed from cosmic-ray data (top), and from a conventional wave recording system (bottom)
(From Allkofer, O. C.. M. Simon: Ocean Engineering 2 (1972) 123)

measurements can be performed on-line from an off-shore location,and that it can be used even with ice-drift in winter time, since the detector is always below the surface of the water.

References

Miyazaki, Y., M. Wada: Simmulation of cosmic-ray variation due to temperature. Acta Phys. Acad. Sc. Hung. 29, Suppl. 2 (1970) 691

Alvarez. L.W., J.A. Anderson. F. El. Badwei. J. Burkhard. A. Fakhry, A. Girgis, A. Gonaid. F. Hassan. D. Iverson, F. Lynch. Z. Miligy, A. H. Mousse. M. Sharkawi, L. Yazolino: Search for hidden chambers in the pyremids. Science 167 (1970) 832

Allkofer, O.C.. M. Simon: A cosmic-ray sea wave and tide recording system. Ocean Engineering 2 (1972) 123

Review of the literature

Below in chronological order are listed books related to the field of cosmic radiation and review articles relevant to or closely associated with the field, published in HANDBUCH DER PHYSIK, PROGRESS IN COSMIC RAY PHYSICS. and ANNUAL REVIEW OF NUCLEAR SCIENCE. The review articlesare classified according to the volume of the periodical and not according to specific subjects.

Books

Montgomery, 0. J. X.: Cosmic Ray Physics. Princeton: Princeton University Press 1949

Jinossy, L.: Cosmic Rays (2nd ed.). Oxford: At the Clarendon Press 1956

Heisenberg, W. (ed.) (2nd ed.): Vortrage uber Kosmische Strahlung. Berlin: Springer 1953 ·

Rossi, B. (2nd ed.): High Energy Particles, Englewood Cliffs: Prentice Hall 1956

Gailbraith, W.: Extensive Air Showers. London: Butterworths 1956

Ramakrirhnan, A.: Elementary Particles and Cosmic Rays. Oxford: Pergamon Press 1962

Hopper, V. D.: Cosmic Radiation and High Energy Interactions. New Jersey: Prentice-Hall Inc. 1964

Cranshaw, T. E.: Cosmic Rays. Oxford: Oxford University Press 1963

Wolfendale, A. W.: Cosmic Rays. London: George Newnes LTD 1963

Peters. B. (ed.): Cosmic Rays, Solar Particles, and Space Research. Proceedings of the International School of Physics "Enrico Fermi", Course XIX. Varenna 1961. New York: Academic Press 1963

Ginrburg, V. L., S. I. Syrovatskii: The Origin of Cosmic Rays. Oxford: Pergamon Press 1964

Rossi. 6.: Cosmic Rays. Englewood Cliffs: Mc Graw Hill 1964

Sandstroem. A. E.: Cosmic Ray Physics. Amsterdam: North-Holland 1965

Hess, W. N., G. D. Mead (eds.): Introduction to Space Science (2nd ed.). New York: Gordon and Breach 1966

Ginzburg. V. L.: The Astrophysicsof Cosmic Rays (2nd ed.). Jerusalem: Israel Program for scientific Translations 1969

Roederer, J. G.: Dynamicsof Geomagnetically Trapped Radiation. Berlin: Springer 1970

Hayakawa, S.: Cosmic Ray Physics (Nuclear and Astrophysical Aspects). New York: John Wiley 1969

Pomerantr. M. A.: Cosmic Rays. New York: van Nostrand 1971

Greisen, K.: The Physics of Cosmic X-Ray, X-Ray and Particle Sources. London: Gordon and Breach Science Publishers 1971

Hillas. A. M.: Cosmic Rays. Oxford: Pergamon Press 1972

Bruzek. A.. H. Pilkuhn teds.): Lectures on Space Physics. 2 Volumes. Dusseldorf: Bertelrmann Universitatsverlag 1973

Wolfendale, A. W. (ed.): Cosmic Ray Physics at Ground Level. London: The Institute of Physics 1973

Dorman. L.: Cosmic Rays: Variations and space Explorations. Amsterdam: North-Holland 1974

Khristiansen. G. B.: Extensive Air Showers. Moscow: University of Moscow 1974 fin russian)

Rochester, G. D., A. W. Wolfendalr.: The origin of the Cosmic Radiation. London: Philosophical Transactions of the Royal Society 1975 Series A. Volume 277 No 1270

Apparao, K. M. V.: Composition of Cosmic Radiation. London: Gordon and Breach Science Publishers 1975

Review articles

Handbuch der Physik XLVI/1, Berlin: Springer Verlag 1961

Morrison, P.: The Origin of Cosmic Rays.

Vallarta, M. S.: Theory of the Geomagnetic Effectsof Cosmic Radiation.

Ray, E. C.: Experimental Results of Flights in the Stratosphere.

Sitte. K.: Penetrating *Showers*.

Cocconi, G.: Extensive Air Showers.

Fowler. G. N., H. H. Wills. A. W. Wolfendale: The Hard Component of r-Mesons in the Atmosphere.

Handbuch der Physik XLVI/2. Berlin: Springer Verlag 1967

Nishimura, J.: Theory of Cascade Showers.

Fujimoto. Y., S. Hayakawa: Cosmic Rays and High-Energy Physics.

Webber. W. R.: The Spectrum and Charge Compositon of the Primary Cosmic Radiation.

Gould, R. J.: High Energy Photons and Neutrinos from Cosmic Sources.

Ouenby. J. J.: The Time Variations of the Cosmic Ray Intensity.

Schopper. E.. E. Lohrmann, G: Mauck: Nukleonen in der Atmosphare.

Lal, D.: Cosmic Ray Produced Radioactivity on the Earth.

Honda, M.: Effects of Cosmic Rays on Meteorites.

Annual Review of Nuclear Sciece, Pala Alto: Annual Reviews Inc.

Alpher. R. A., R. C. Herman: The Origin end Abundance Distribution of the Elements. Ann. Rev. Nucl. Sci. 2 (1953) 1

Salpeter, E. E.: Energy Production in Stars. Ann. Rev. Nucl. Sci. 2 (1953) 41

Biermann, L.: Origin and Propagation of Cosmic Rays, Ann. Rev. Nucl. Sci. 2 (19531335

Leprinca-Ringuet. L.: Mesons and Heavy unstable Particles in Cosmic Rays. Ann. Rw. Nucl. Sci. 3 (1953) 39.

Sarabhai. V., N. W. Nerurkar: Time Variations of Primary Cosmic Rays. Ann. Rev. Nucl. Sci. 6 (1956) 1

Neher. H. V.: The Primary Cosmic Radiation. Ann. Rev. Nucl. Sci. 6 (1958) 217

Cameron, A. G. W.: Nuclear Astrophysics. Ann. Rw. Nucl. Sci. 8 (1958) 239

Greisen, K.: Cosmic Ray Showers, Ann. Rev. Nucl. Sci. 10 (1960) 83

Ney, E. P.: Experiments on Cosmic Rays and Related Subjects during the International Geophysical Year. Ann. Rev. Nucl. Sci. 10 (1960) 461

Arnold, J. R.: Nuclear Effects of Cosmic Rays in Meteorites. Ann. Rev. Nucl. Sci. 11 (1961) 349

Burbidge, G.: Nuclear Astrophysics. Ann. Rw. Nucl. Sci. 12 (1962) 507

Anderson, K. A.: Energetic Particles in the Earth's Magnetic Field. Ann. Rev. Nucl. Sci. 18 (1966) 291

Chin. Hong-Yee: Neutrinos in Astrophysics and Astronomy. Ann. Rev. Nucl. Sci. 18 (1966) 591

Friedman. H.: X Rays from Stars and Nebulae. Ann. Rw. Nucl. Sci. 17 (1967) 317

Lal, O.. H. E. Suers: The Radioactivity of the Atmosphere and Hydrosphere. Ann. Rw. Nucl. Sci. 18 (1968) 407

Shapiro, M. M., R. Silberberg: Heavy Cosmic Ray Nuclei. Ann. Rev. Nucl. Sci. 20 119701323

Progress in Cosmic Ray Physics. fed. Wilson, J.G.) Amsterdam: North-Holland

Camerini, U.. W. 0. Lock, D. H. Perkins: The Analysis of Energetic Nuclear Encounters Occurring in Photographic Emulsions. Prog. Cosm. R. Phys. 1 (1957) 3

Butler. C. C.: Unstable Heavy Cosmic Ray Particles. Prog. Cosm. A. Phys. 1 (1957) 65

Michel, L.: Coupling Properties of Nucleons, Mesons and Leptons. Prog. Cosm. R. Phys. 1 (1957) 127

Peters. 8.: The Nature of Primary Cosmic Radiation. Prog. Cosm. R. Phys. 1 (19571193

Neher, H. V.: Recent Data on Geomagnetic Effects. Prog. Cosm. R. Phys. 1 (1957) 245

Puppi, G., N. Oallaporta: The Equilibrium of the Cosmic Ray Beam in the Atmosphere. Prog. Cosm. R. Phys. 1 (1957) 315

George. E. P.: Observations of Cosmic Rays Underground and Their Interpretation. Prog. Cosm. R. Phys. 1 (1957) 392

Eliot. H.: The Time Variationsof Cosmic Ray Intensity. Prog. Cosm. ft. Phys. 1 (1957) 452

Sard, R. 0.. M. F. Crouch: Nuclear Interactionsof Stopped r-Mesons. Prog. Cosm. R. Phys. 2 (1954) 3

Wilson, J. G.: Experimental Data on the Heavy Unstable Particles. Prog. Cosm. R. Phys. 2 (1954) 57

Dymond. E.G.: The Penetrating Component of Cosmic Radiation in the Upper Atmosphere. Prog. Corm. R. Phys. 2 (1954) 112

Messel, H.: The Development of a Nucleon Cascade. Prog. Corm. R. Phys. 2 119541145

Voyvodic, L.: Particle Identification with Photographic Emulsions, and Related Problems. Prog. Cosm. R. Phys. 2 (1954) 217

Greisan. K.: The Extensive Air Showers. Prog. Corm. R. Phys. 3 (1956) 3

Bridge. H. S.: Experimental Results on Charged K-Masons and Hyperons. Prog. Cosm. R. Phys. 3 (1956) 145

Thomson, R. W.: Decay Processes of Heavy Unstable Neutral Particles. Prog. Cosm. R. Phys. 3 (1956) 265

Puppi, G.: The Energy Balance of Cosmic Radiation. Prog. Cosm. R. Phys. 3 119561341

D'Espagnat. B., J. Prentki: Some Theoretical Aspects of the Strong Interactions of the New Particles. Prog. Cosm. R. Phys. 4 (1958) 3

Walker, W. D.: The Properties and Production of K-Mesons. Prog. Cosm. R. Phys. 4 (1958) 73

Fowler, G. N.. A. W. Wblfendale: The Interactions of μ-Mesons with Matter. Prog. Cosm. R. Phys. 4 (1958) 107

Singer, S. F.: The Primary Cosmic Radiation and its Time Variation. Prog. Cosm. R. Phys. 4 (1958) 205

Ginzburg, V. L.: The Origin of Cosmic Radiaton. Prog. Corm. R. Phys. 4 (1958) 339

Lundby, A.: Weak Interactions. Prog. Cosm. R. Phys. 5 (1960) 4

Gammel. J. L.. R. M. Thaler: Phenomenology of the Nucleon-Nucleon Interaction. Prog. Cosm. R. Phys. 6 (1960) 99

McConnell, J.: Theory of Antinucleons. Prog. Cosrn. R. Phys. 5 (1960) 207

Perkins, D. H.: Obarservationson Cosmic Ray "Jet" Interactions in Nuclear Emulsions. Prog. Cosm. R. Phys. 5 (1960) 259

Tennent. R. M.: The Absorption and Decay of Negative Muons. Prog. Corm. R. Phys. 5 (1960) 367

Lal, D., 8. Peters: Cosmic Ray Produced Isotopes and Their Application to Problems in Geophysics. Prog. Cosm. R. Phys. 8 (196213

Webber, W. R.: Time Variations of Low Rigidity Cosmic Rays During the Recent Sunspot Cycle. Prog. Cosm. R. Phys. 8 (1962) 77

Singer, S. F.. A. M. Lenchek: Geomagnetically Trapped Radiation. Prog. Corm. R. Phys. 8 (1962) 247

Dorman, L. I.: Geophysical and Astrophysical Aspects of Cosmic Radiation. Prog. Cosm. R. Phys. 7 (1963) 1

Martin. A.: Analyticity in Potential Scattering. Prog. Cosm. R. Phys. 8 (1965) 3

Ne'eman, Y.: Strong Interactions Symmetry. Prog. Cosm. R. Phys. 8 11965169

Nikolif. M. M.: Experimental Information on Negative Kaons. Prog. Cosm. R. Phys. 8 (19651 125

Tenner, A. G., G. F. Wolters: Resonances. Prog. Corm. R. Phys. 8 (1965) 241

Parker, E. N.: The Dynamical Origin of the Solar Wind and Cosmic Ray Variations. Prog. Cosm. R. Phys. 9 (1967) 3

Jelley. J. V.: brencov Radiation from Extensive Air Showers. Prog. Cosm. R. Phys. 9 (1967) 41

Menon. M. G. K., P. V. Ramana Murthy: Cosmic Ray Intensities deep Underground. Prog. Cosm. R. Phys. 9 (1967) 163

Murzin. V. S.: Principles and Applications of the Ionization Calorimeter. Prog. Cosm. R. Phys. 9 (1967) 247

Hatton, C. J.: The Neutron Monitor. Prog. Corm. R. Phys. 10 (1971) 3

Miesowicz, M.: Fireball Model of Meson Production. Prog. Cosm. R. Phys. 10 (1971) 103

Allan, H. R.: Radio Emission from Extensive Air Showers. Prog. Cosm. R. Phys. 10 (19711171

Oda, M., M. Matsuoka: Cosmic X-Rays. Prog. Cosm. R. Phys. 10 (1971) 305

Progress in Nuclear Physics. London: Pergamon Press.

Waddington. C. J.: The Composition of the Primary Cosmic Radiation. Prog. Nuc. Phys. 8 (1960) 1

INDEX